Investigation of intrinsic defects and versatility of Zn-doping in SnO_2 thin films using pulsed laser deposition

Yoann Bernard Henri Porte

A thesis submitted in fulfilment of the requirements for the degree of Doctor of Philosophy

Imperial College London

Department of Materials

April 2016

Foreword

This thesis is the result of my own investigation and work, carried out in the Department of Materials, Imperial College London, between November 2012 and March 2016. All contributions from others has been appropriately referenced and cited throughout. All the experimental work reported here has been carried out by me, with the exception of the following:

- The Kelvin probe data was extracted by Dr Hendrik Faber,(Anthopoulos groups, Dept. of Physics)
- The XPS data collection and analyses was carried out by Dr Freddy Oropeza-Palacio and Dr Ignacio Villar Garcia (Payne group, Dept. of Materials)
- Solar cell devices were fabricated and tested by Maurizio Morbidoni (McLachlan group).
- The dilatometry analysis was performed by Richard Sweeney (Research officer, Dept. of Materials).

The work presented in this thesis has also been published in the following paper.

Y. Porte, R. Maller, H. Faber, T. Anthopoulos, H. Alshareef and M. McLachlan, "***Exploring and controlling intrinsic defect formation in SnO_2 thin films***", J. Mat. Chem. C, **2016**, 4, 758-765. **DOI:** 10.1039/C5TC03520A

Acknowledgements

Firstly, I would like to thank the King Abdullah University of Science and Technology for the financial support and my supervisor Dr Martyn McLachlan for his help and support during these three and a half years. I want to thank also Dr Peter Petrov for his help in the LCN and Dr Joseph Franklin for his guidance at the beginning of this project.

I am really grateful to Hendrik Faber for the time spent on the Kelvin probe measurements with me, and a special thanks to Freddy Oropeza-Palacio for the useful discussion and XPS analysis as well as Ignacio (Nacho) Villar Garcia for his contribution to the XPS measurements.

My thanks goes to all the McLachlan group, Maurizio Morbidoni and Jiaqi Zhang for their help in the fabrication of devices despite the short amount of time, Rob Maller, Jorge Costa Dantas Faria, Claire Burgess, Becky Kilmurray, Bob Xu and Tian Du, but also Xuemei Zhang and Daniel Price for all the fun times in the office, the climbing sessions and forcing me to go out from time to time.

I also would like to express my gratitude to my friends from France for their support during this experience, Kiki, Vince, Thieum, Scott, Riton, Pedro, Loic, Louis, Émilie and Ivan, thank you for being there despite the distance.

A particular thanks to my family for their unconditional support not only through the PhD but also everything else, my parents Dominique and Isabelle, my brother and sister, Maxime and Maeva.

Finally, I would like to express a special thanks to my partner Mélody for supporting me during these 4 years, helping me going through the hard times and most of all being a part of my life. Thank you.

Abstract

n-type transparent conducting oxides (TCOs) have been studied extensively and are now commercially available. The development of p-type counterparts lags someway behind, despite the opportunity preparing such materials offers. Interest in tin oxide (SnO_2) thin films and their applications has grown significantly over recent years, particularly for the preparation of p-type TCOs. However for this to be realised, limitations such as the ionisation energy of acceptor defects and the existence of compensating mechanisms must be overcome.

Even though the effectiveness of acceptor doping is essential, the presence of compensating defects as the film growth environment changes is critical for stable p-type TCOs. Here a growth study of SnO_2 deposited using pulsed laser deposition (PLD) reveals intrinsic acceptor defects have limited contribution to the conductivity as theoretically predicted. The conductivity remains n-type despite significant variation in the oxygen content of the growth environment and temperature - which is attributed to the large concentration of tin interstitial defects.

To limit donor defect concentration, elevated temperature and oxygen pressure were set as the growth conditions with the introduction of Zn as an acceptor dopant. Here, the introduction of Zn acceptors changes the behaviour of intrinsic defects such that measured charge carrier concentrations increase by some 3-orders of magnitude compared with undoped films, suggesting the presence of compensating mechanisms. n-type behaviour persists, even after oxygen annealing, and film resistivity also increases. This is attributed to the formation more acceptor defects that act as electron compensation centres.

Zn is reported to act not only as an acceptor in SnO_2 but also to enhance n-type conductivity: here this behaviour is also confirmed. By studying the electrical, optical and structural properties of Zn doped SnO_2, films of surprisingly low resistivity (2.9×10^{-3} Ω.cm) were formed, which exhibited preferential (200) on Zn addition. An observed decrease in bandgap was found when Zn doping was increased, from 3.6 eV in undoped films down to 3.4 eV in crystalline films and 3.2 eV in amorphous films. The work is concluded by investigating low deposition temperature where low resistivity highly transparent films are formed at temperatures as low as 100 °C

Table of contents

List of figures

Chapter 1

Chapter 4

Appendix 3

Abbreviations

AC	Alternating current
AFM	Atomic force microscope
at.%	Atomic percent
ATO	Antimony-doped tin oxide
AXXC	Annealed at XX °C
BE:	Binding energy
BHJ	Bulk hetero-junction
BZ	Brillouin zone
BZB	Brillouin zone boundary
CB	Conduction band
CBM	Conduction band minimum
CMA	Cylindrical mirror analyser
CMOS	Complementary metal-oxide semiconductor
CMVB	Chemical modification of the valence band
CN	Coordination number
CPD	Contact potential difference
DC	Direct current
e^-	Electron
EDX	Energy dispersive X-ray spectroscopy
E_g	Band gap
FEGSEM	Field emission gun scanning electron microscopy
FF	Fill factor
FTO	Fluor-doped tin oxide

FWHM	Full width half maximum
h	Plank constant
HOMO	Highest occupied molecular orbital
ICBA	Indene-C60 Bisadduct
ITO	Indium tin oxide
J_{sc}	Short-circuit current
k_B	Boltzmann constant
KE	Kinetic energy
KP	Kelvin probe
KPFM	Kelvin probe force microscopy
LUMO	Lowest unoccupied molecular orbital
NA	Non-annealed
O-rich	Oxygen rich
O_i	Oxygen interstitial
OLED	Organic light-emitting diode
OPV	Organic photovoltaic
O_{Sn}	Oxygen antisite
P3HT	Poly(3-hexylthiophene-2,5-diyl)
PCBM	Phenyl-C61-butyric acid methyl ester
P_D	Background oxygen deposition pressure
PLD	Pulsed Laser Deposition
PV	Photovoltaic
SC	Semiconductor
SCL	Space-charge layer

SEM	Scanning electron microscope
Sn_i	Tin interstitial
Sn_O	Tin antisite
SnO	Tin monoxide
SnO_2	Tin oxide
Sn-rich	Tin rich
TC	Texture coefficient
TCO	Transparent conducting oxide
T_D	Deposition temperature
TFT	Thin film transistor
UHV	Ultra-high vacuum
UV-Vis	Ultraviolet-visible spectroscopy
VB	Valence band
VBM	Valence band maximum
V_O	Oxygen vacancy
V_{oc}	Open-circuit voltage
V_{Sn}	Tin vacancy
XPS	X-ray photoelectron spectroscopy
XRD	X-ray diffraction spectroscopy
Zn_{Sn}	Zn substituted on Sn site
ZTO	Zn-doped SnO_2

Introduction

Transparent conducting oxides (TCOs) have been widely investigated and are now implemented in a variety of optoelectronic applications such as solar-cells, light-emitting devices, flat panel displays and thin film transistors.[1–4] Tin oxide (SnO_2) is one of the most studied material for TCOs applications. SnO_2 is a wide band gap intrinsic n-type semiconductor. Its electrical properties can be enhanced by introducing extrinsic dopants, *e.g.* F or Sb, reaching resistivity down to 2-3 $x10^{-4}$ Ω.cm.[5–7] Even though these n-type TCOs, along with indium tin oxide (ITO) and aluminium zinc oxide (AZO), have been developed to an industrial extent, the progress on p-type TCOs with competitive electrical performances is still far behind.

Over the past years the interest in p-type conducting SnO_2 has been. Unlike Cu-based p-type metal oxides, high n-type conductivity has already been achieved in SnO_2. Therefore, the development of p-type conductivity within this material would constitute a leap forward to the fabrication of p-n homo-junction for smart windows and UV-light-emitting diodes, and fully transparent complementary metal-oxide semiconductor (CMOS) based devices. [8–10]

However p-type doping of TCOs, in particular SnO_2, has been very controversial. While several authors[11–14] reported successful p-type doping of SnO_2, Scanlon and Watson[15] theoretically predicted efficient p-type conductivity cannot be achieved in SnO_2. One of the key issues in the development of such material is the presence of compensating defects. The intrinsic defects responsible for the n-type conductivity in SnO_2 have raised interest since Kiliç and Zunger's work on "Origins of coexistence of conductivity and transparency in SnO_2".[16] Further studies are essential as They would contribute to the improvement of n-type conductivity and helps understand the limitations of p-type conductivity development through compensation mechanisms. Even though several models have been suggested, some controversy persists between the different studies on the preferential formation of donor defects and their contribution to the conductivity.

To the author's knowledge, no experimental studies linking the theoretical predictions to the environmental effects during the film deposition have been reported in undoped SnO_2. Moreover, within the experimental work devoted to the p-type doping of SnO_2, there is a little consideration towards the presence of compensating mechanisms. Despite the

theoretical work done in the field no correlation has been carried out experimentally between the growth environment and its impact on the doping efficiency and the formation of compensating defects. These factors are considered essential when forcing a change of conductivity within a material.

Among the existing cation acceptor dopant such as Zn, In, Ga or Al in SnO_2, Zn is the most versatile. The introduction of Zn dopant in SnO_2 has been reported to improve the n-type conductivity in certain conditions but also to show acceptor dopant behaviour as well.[17,18] The impact of the growth environment on the SnO_2 system, undoped firstly and then doped with Zn, will be investigated. This study will focus on the behaviour of acceptor defects in environments supposedly favourable for their formation which will be reflected on the electrical properties of the films. The pulsed laser deposition (PLD) technique is the deposition method of choice for this type of study. Even though it is inherently unsuitable for large-scale deposition, PLD represents an essential asset in the understanding of thin film performances relating to their structure by allowing excellent control over the growth environment.

Chapter 1: Literature review

1. Fundamentals

1.1. Band theory and origin of semiconductors

In order to describe the characteristics of semiconductor (SC) materials and their band structure, the Drude model and the free electron model are used in a first place and finally the nearly free electron model is introduced to take into consideration the effect of the periodic potential in the lattice.

1.1.1. The Drude model

The Drude model was proposed by Paul Drude in 1900 to explain electron transport properties in a material.[19] Drude supposed the electrons move in straight lines and are scattered through collisions of negligible duration. He assumed the electrons do not collide between each other but with the positive ion cores (nuclei). Two terms are introduced; the scattering time, τ, which represents the average time between collisions and the mean free path, l, which is the average distance travelled by electrons between collisions. Without an electric field, the global velocity is around zero as the collisions induce random change of directions as showed on Figure 1.1.a.

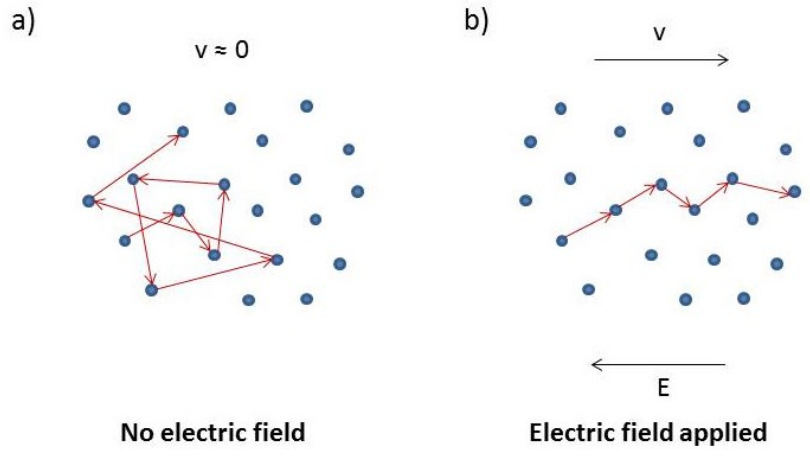

Figure 1. 1: Electrons mean free path (in red arrows) described with the Drude model a) without electric field and b) when an electric field is applied. The nuclei are represented in blue circles, v is the global velocity and E the electric field.

However in the presence of an electric field, E, the electrons experience a force –eE and their movement is more oriented in the opposite direction of the applied electric field.

Therefore the velocity, v, is also in the opposite direction of E and the drift velocity v (the average electrons velocity) can be expressed as,[19]

Equation 1.1 $$v = \frac{-eE\tau}{m}$$

Where m is the mass of the electron and e the charge of an electron. The current density, J, is then described as,[19]

Equation 1.2 $$J = -nev = \frac{ne^2\tau E}{m}$$

With n the number of free electrons per unit volume acting as a charge carrier. Since the electrical conductivity σ is given by J=σE, and the mobility μ is function of v they can be expressed as,[19]

Equation 1.3 $$\sigma = \frac{ne^2\tau}{m} \quad \text{and} \quad \mu = \frac{|v|}{E} = \frac{e\tau}{m}$$

1.1.2. The free electron model

Electrons can be described as particles with a momentum p and an energy E but according to the wave-particle duality expressed by de Broglie they can also be treated as a wave with a wavelength λ and a frequency. From the de Broglie equivalence electrons are assigned a wave-vector, k, function of the electron momentum p, [20]

Equation 1.4 $$p = \frac{h}{\lambda} = \hbar k \qquad \text{and} \qquad k = \frac{2\pi}{\lambda}$$

Where h is the Plank constant and ħ the reduced Plank constant with ħ = h/2π. The valence electrons can be then be treated as quantum mechanical waves using a wave function ψ but the periodic potential of the crystal is ignored. The system treated is a one dimensional "box" of free electrons of length L along the x axis. The potential inside the box is zero and the temperature is at absolute zero. The Schrodinger equation and its solution in this case are given in Equation 1.5.[21]

Equation 1.5 $$-\frac{\hbar^2}{2m}\frac{d^2\psi}{dx^2} = E\psi \text{ and } \psi = e^{ikx}$$

The energy, E, can then be expressed as a function of k by replacing ψ by its solution in the Schrodinger equation, [20,21]

Equation 1.6 $$E = \frac{\hbar^2 k^2}{2m}$$

Due to the periodic boundary condition (ψ(x=0) = ψ(x=L)), k possible values are given by, [21]

Equation 1.7

$$e^{ikL} = 1 \text{ -> } k = \frac{2\pi n}{L}$$

With n an integer. Therefore the allowed energy states for the electron are function of k^2 and are positioned every k = 2πn/L as shown on Figure 1.2.

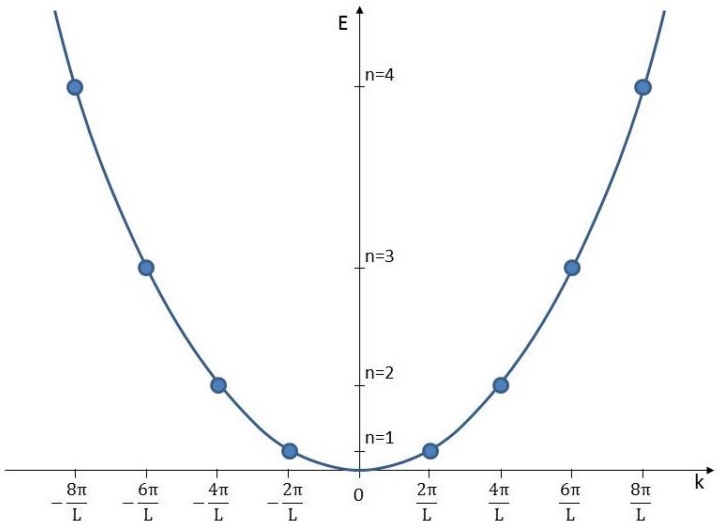

Figure 1. 2: Permitted energy (represented in blue circles) for the electrons function of k in reciprocal space for a 1 dimensional box of free electrons and of length L. Diagram inspired from [21].

According to Pauli's exclusion principle, no two electrons with the same spin can occupy the same quantum state simultaneously, therefore only two electrons are allowed for each state.

The Drude model and the free electron model works well with metals but cannot describe precisely other materials. Therefore the nearly-free electron model is introduced.

1.1.3. The nearly-free electron model

In a real crystal the electrons are not completely free and are affected by the periodicity of the lattice. Because of the positive nuclei in the lattice, a periodic potential, U(x) (U(r) in one dimension), which varies as 1/x near the nuclei is shown on Figure 1.3.

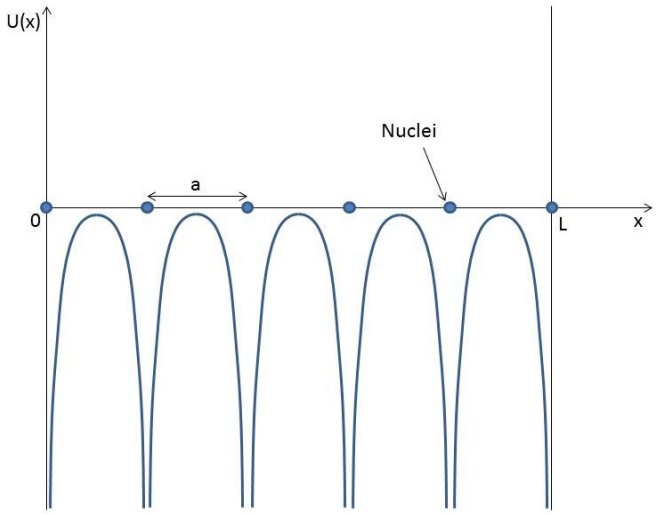

Figure 1. 3: One dimension representation of the periodic potential of the lattice (represented in blue line) in a box of length L. The distance between each nuclei is a.

The Schrodinger equation is modified due to the presence of the periodic potential function, U(x). [21]

Equation 1.8

$$-\frac{\hbar^2}{2m}\frac{d^2\psi}{dx^2} = (E - U(x))\psi$$

Bloch showed that the solution of this type of equation can be written in the form: [21]

Equation 1.9

$$\psi = U(x)e^{ikx}$$

This is known as the Bloch function where U(x) is a periodic function with the periodicity of the lattice in the x direction, as seen on Figure 1.3. The result of this solution is that for certain wave-vectors, the electron waves will scatter from U(x) and interfere creating energy gaps. These gaps occur at $k = n\pi/a$ where a is the distance between two nuclei and n an integer. Therefore the allowed energy for the electrons inside this one dimensional box vary proportionally to k^2 between the nuclei as for the free electron model but due to the periodicity of the lattice forbidden energy appears at $n\pi/a$, as shown on Figure 1.4. [21,22]

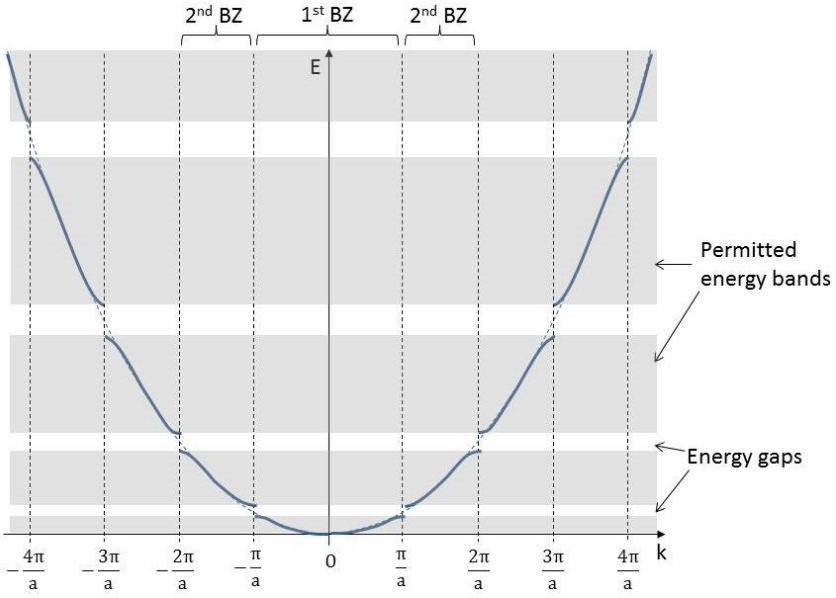

Figure 1. 4: 111 – Permitted energy of the nearly free electrons in one dimension function of the wave-vector k. a represents the distance between two nuclei. The allowed energy states are represented by light grey bands and the Brillouin zones (BZ) are delimited by the black dotted lines.

The zone for which $-\pi/a < k < \pi/a$ is defined as the first Brillouin zone (BZ) and contain the first allowed energy levels. The Brillouin zone boundaries (BZB) show where the energy gaps are positioned along the k axis. At the BZB, $dE/dk = 0$. The concept of bands of allowed energies can then be introduced. Their representation is known as flat band diagram, Figure 1.5.[21]

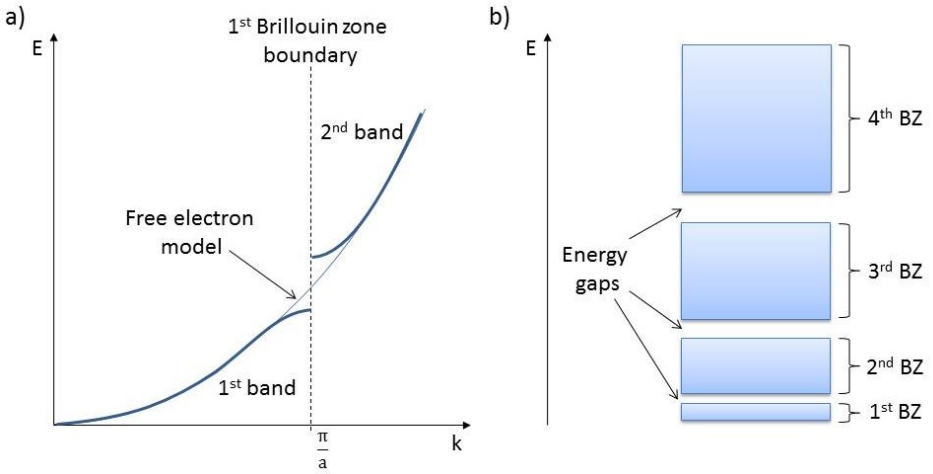

Figure 1. 5: Diagram representing; a) the permitted energy of the nearly free electrons in one dimension function of the wave-vector k around the first Brillouin zone boundary (BZB) in thick dark blue line, a being the distance between two nuclei. b) The "flat band" diagram extracted from the nearly free electron model exhibiting the forbidden energy gaps and the bands of allowed energy constituting the different Brillouin zones.

1.1.4. Fermi level and electronic conductivity

By extending the model of the free electron to a three dimensional cubic box of size L (volume V), the solution of the Schrodinger equation is in the form $\psi = e^{i(k_x x + k_y y + k_z z)}$ which leads to an expression of the allowed energy levels similar to the one dimension solution $E = \frac{\hbar^2 k^2}{2m}$ but now $k^2 = k_x^2 + k_y^2 + k_z^2$. Therefore the equal value of E lies on the surface of a sphere of radius k and volume V_f,[21]

Equation 1.10

$$V_f = \frac{4}{3}\pi k^3$$

The sphere constituted of free electrons of constant energy in a k-space is called the Fermi sphere. The number of electrons filling the sphere can then be expressed as N(E), the number of electronic states with an energy E or less, [21]

Equation 1.11

$$N(E) = 2 * \frac{vol.of\ the\ sphere}{vol.per\ k\ state} = \frac{V}{3\pi^2}\left(\frac{2mE}{\hbar}\right)^{\frac{3}{2}}$$

The solution of the Schrodinger's equation points a non-uniformity of the distribution of the energy level in space, therefore the notion of density of states, D(E), is introduced. D(E) represents the density of electronic states per unit energy,[21]

Equation 1.12

$$D(E) = \frac{dN}{dE} = \frac{V}{2\pi^2}\left(\frac{2m}{\hbar^2}\right)^{\frac{3}{2}} E^{\frac{1}{2}}$$

In this case D(E) is proportional to $E^{1/2}$.

At T=0 K, the lowest energy states in the Fermi sphere are doubly filled; while at T>0 K, most of the electronic states within the Fermi sphere remain occupied and some are thermally promoted just above the Fermi surface. In order to consider the effect of the temperature, the Fermi-Dirac distribution function, f(E), is introduced and gives the occupation probability of an energy level,[21]

Equation 1.13

$$f(E) = \frac{1}{\exp\left(\frac{E-\mu}{k_B T}\right)+1} = \frac{1}{\exp\left(\frac{E-E_F}{k_B T}\right)+1}$$

Where μ is the chemical potential of the system and k_B the Boltzmann constant. At T = 0 K, $\mu = E_F$ and at T > 0 K, $\mu \approx E_F$. Thus μ is substituted by E_F in Equation 1.13. Finally the occupation density of states Z(E) is defined as the product of the Fermi-Dirac distribution function f(E), and the density of states D(E),[21]

Equation 1.14

$$Z(E) = D(E)f(E)$$

The highest occupation density of states occurs near the Fermi level. The total number of valence electrons N is then extracted combining Equation 1.11 and 1.14,[21]

Equation 1.15 $$N = \int_0^{\infty} D(E)f(E)dE$$

This equation will be used later to show the position of the Fermi level in a semiconductor.

1.1.5. Semiconductors

From the nearly free electron model and depending on the energy levels filled by the electrons in a material three main class can be observed as shown on Figure 1.6.

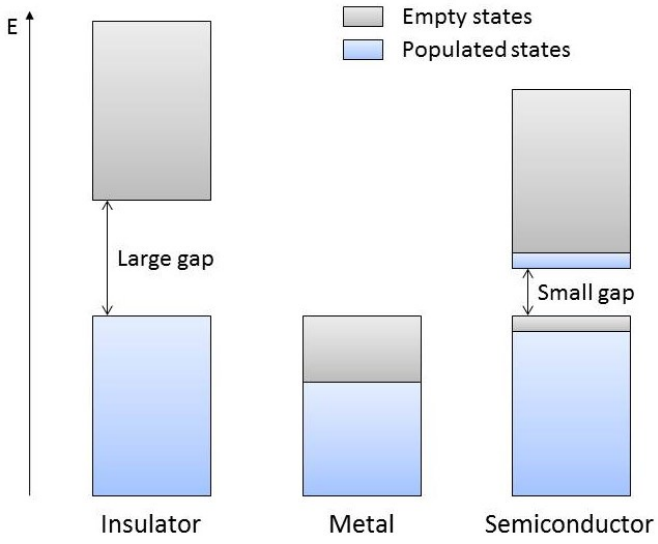

Figure 1. 6: Flat band diagram in the case of an insulator, a metal and a semiconductor function of the energy E. The empty energy levels are represented in grey while the populated ones are in blue.

Insulator materials have a poor conductivity due to the band fully occupied and the large band gap preventing the electrons from being excited to higher energy levels. Metals are good conductors, since their band is partially filled, electrons can be easily excited to higher energy levels by applying an electric field. Finally the semiconductor class of materials display a moderate conductivity (at T > 0 K). Their occupied band is nearly full and their small energy gap allows the thermal excitation of electrons across the gap. The lower band constituted of mainly occupied states is called the Valence band (VB) and the upper band constituted of mainly vacant states is called the Conduction band (CB). The gap of energy separating the VB from the CB is called the band gap, E_g. The size of E_g is determined by the lattice periodic potential U(r). When U(r) is small E_g is small while a large value of U(r) give a large band gap. [21]

When a photon is incident on a semiconductor, it is absorbed by the material if the energy of the photon is high enough to promote an electron of the valence band into the conduction band ($E_{photon} \geq E_g$). The electrical properties of a semiconductor are dominated by the smallest band gap that at T = 0 K separates the highest occupied states at the valence band maximum (VBM) from the lowest energy empty states at the conduction band minimum (CBM). If energy transition between the VBM and the CBM involves no variation of wave-vector k (they are at the same position in the k-space) the band gap is called direct. However if the highest occupied states of the VB possess a different wave-vector k than the lowest unoccupied stated of the CB, the transition must involve a phonon to conserve momentum and the band gap is called indirect, as shown on Figure 1.7.[21,23]

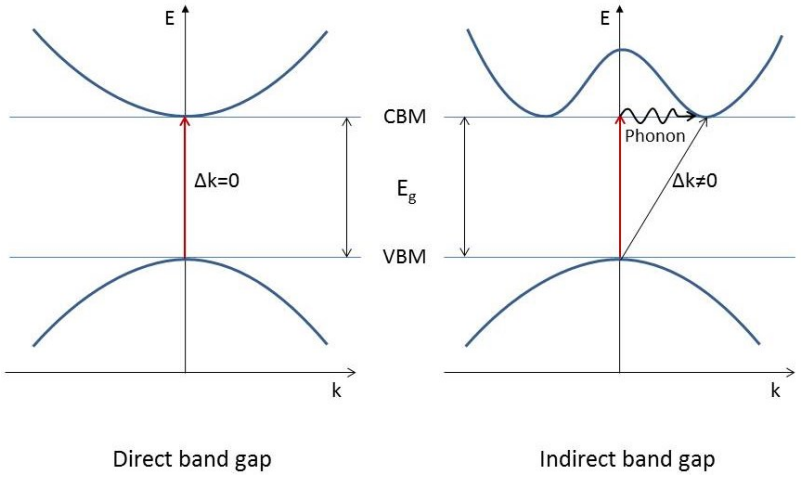

Figure 1. 7: Interband transitions in a semiconductor in the case of direct band gap and indirect band gap. The vertical red arrow represents the energy given by an incident photon during the absorption process while the wiggly arrow in the indirect band gap diagram represents the absorption or the emission of a phonon.

Due to the electron-ion interactions, the mass of the electrons is different from the mass of the free electrons. Therefore the electron effective mass m_e is introduced as a variable to explain the shape of the bands and can be expressed by deriving Equation 1.6, [21]

Equation 1.16

$$\frac{1}{m_e} = \frac{1}{\hbar^2}\frac{d^2E}{dk^2}$$

m_e is inversely related to the curvature of E(k) therefore the mass of electrons changes with it. Electrons in band with strong curvature are light while electrons in bands with a smaller curvature are heavier. The effective mass also affects the mobility of the electrons, as seen in Equation 1.3, therefore a lower effective mass leads to a higher mobility and thus a greater conductivity. With a lower effective mass, the charge carriers are also more easily promoted to higher energy levels.

In a semiconductor, two types of charge carriers are distinguished; the electrons which are promoted from the top of the VB to the bottom of the CB and the holes which are absence of electrons (vacant energy states) and that appear at or near the top of VB. The holes respond like electrons but possess a positive charge and an effective mass m_h.

By using Equation 1.15 and integrating the occupation density of states Z(E) in the case of electrons and holes the carrier concentrations n and p respectively can be calculated,[21]

Equation 1.17
$$n = 2\left(\frac{m_e k_B T}{2\pi\hbar^2}\right)^{\frac{3}{2}} exp\left(\frac{E_F - E_C}{k_B T}\right)$$

Equation 1.18
$$p = 2\left(\frac{m_h k_B T}{2\pi\hbar^2}\right)^{\frac{3}{2}} exp\left(\frac{E_V - E_F}{k_B T}\right)$$

The combination of n and p results in an equation for the Fermi energy level,

Equation 1.19
$$E_F = \frac{E_V + E_C}{2} + \frac{3}{4} k_B T ln\left(\frac{m_h}{m_e}\right)$$

At absolute zero, the Fermi energy level lies at the middle of the band gap. At finite temperature (T > 0 K), E_F deviates from the middle of the band gap, generally the mass of the holes is greater than the mass of the electrons therefore the Fermi energy increases with the temperature. However the deviation is generally very small and it is of common approximation to state that the Fermi energy level of an intrinsic semiconductor lies midway between the VB and the CB.

In an intrinsic semiconductor, in order to maintain charge neutrality, the charge carrier concentration is given by $n_i = p = n$. Therefore by multiplying Equation 1.17 and 1.18 we obtain,[21]

Equation 1.20
$$n_i = 2\left(\frac{k_B T}{2\pi\hbar^2}\right)^{\frac{3}{2}} (m_e m_h)^{\frac{3}{4}} exp\left(\frac{-E_g}{2k_B T}\right)$$

The intrinsic carrier concentration depends on the size of the band gap and is also a function of the temperature. Therefore the size of the band gap determines the amount of free electrons that can be promoted to the conduction band at room temperature and participate in the conductivity.

1.2. Defects in solids, nature, formation and consequences

Most metal oxide semiconductors such as ZnO, In_2O_3 and SnO_2 possess a large band gap. Therefore their intrinsic conductivity cannot be achieved only through the thermal excitation of electron from the valence band. In an ideal ionic crystal, each atom is located

at its regular lattice site and all sites are occupied. However in a real crystal lattice, the structure deviates from the perfect atomic arrangement. This deviation from stoichiometry has an impact on important properties in metal oxides such as the electronic transport, the melting point and the optical properties. Various types of defect can be found in the lattice, such as vacant lattice sites, interstitial atoms, impurity atoms, dislocations and stacking fault.[24]

In the scope of this thesis the interest is brought upon the point defects in the lattice. Those types of defect can either be intrinsic (in a pure material) or extrinsic (due to the addition of impurity or dopant). Intrinsic point defects are deviations from the ideal structure and emerge from the displacement or the removal of lattice atoms. Two categories of point defects are distinguished; stoichiometric and non-stoichiometric defects. Stoichiometric defects are defects which maintain the stoichiometry and do not contribute to the electrical conductivity.[25] The most commons are the Schottky defects which constitute of a vacant cation and a vacant anion (in the case of metal binoxide three defects are considered, a vacant metal atom and two vacant oxygen atoms), and the Frenkel pair defect where a cation and an anion atom are displaced from their regular sites into interstitial sites. In the case of Schottky defects, the ions leave their lattice and relocate at the crystal surface.[24] Non-stoichiometric defects are defects causing a change in the stoichiometry of the material leading to the formation of charge carriers. Such defects participate in the electrical conductivity and can be distinguished into three classes: the vacancies representing a vacant atom, the interstials where an atom sits in an interstitial site and the antisites which represents atom that substituted on the site of a different atom. The various defects mentioned are shown on Figure 1.8.

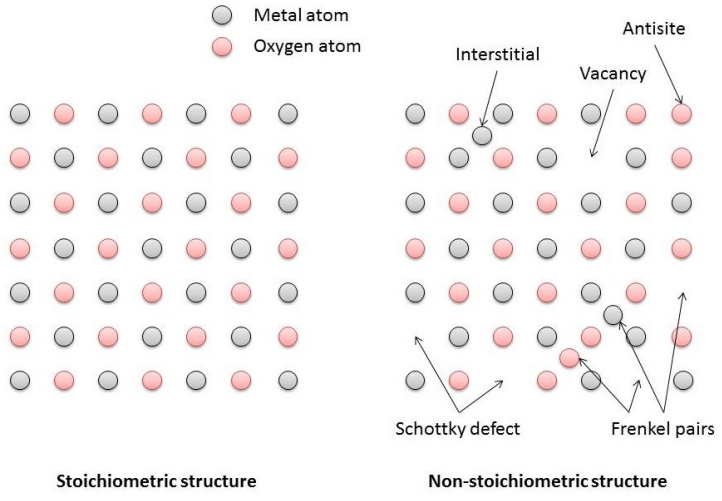

Figure 1. 8: Schematic representation of the point defects present in the non-stoichiometric metal oxide structure. The metal atoms are represented by grey circles while the oxygen atoms are in red.

Those type of defect are often described with Kröger–Vink notations.[26,27] The structure of these notations is composed of three parts; the main body indicating if the defect is either a vacancy (V) or an ion, the subscript indicating the site the defect occupies (either a regular lattice site or an interstitial "i") and the superscript which gives the effective charge of the defect ($\circ$ for a positive charge, / for a negative charge and x for a neutral charge). In the case of SnO_2 the main types of defect found are:

- V_{Sn} or V_O: tin or oxygen vacancy.
- Sn_i or O_i: tin or oxygen interstitial.
- Sn_O or O_{Sn}: a tin atom on an oxygen site and an oxygen atom on a tin site, *i.e.* antisites.

The change in free energy of the crystal by the formation of 1 mole of a defect is given by Equation 1.21.[28]

Equation 1.21 $$\Delta G_D = \Delta H_D - T\Delta S$$

Where ΔG_D is the free energy of a crystal by a defect formation, ΔH_D the energy required to form 1 mole of defect D and S the entropy of the system. As the distribution of the created defects on the vailable sites N_{sites} increases with the entropy S of the system, ΔG_D reaches a minimum at a defect concentration N_D given by, [28]

Equation 1.22 $$N_D = N_{sites}\, exp\left(-\frac{\Delta H_D}{k_B T}\right)$$

N_D represents the amount of defects per unit volume in thermal equilibrium and its equation can also be written as,[29]

Equation 1.23 $$c = N_{sites}\, exp\left(-\frac{E^f}{k_B T}\right)$$

Where c is the concentration of defects in thermal equilibrium and E^f the formation energy of the defect D. Equation 1.23 points out that the defect concentration is the highest for those with the lowest formation energy. The formation energy is dependent on the Fermi energy level and on the chemical potential (*i.e.* partial pressure) of the species concerned.[30] For example, the formation energy E^f of an oxygen vacancy (V_O) in SnO_2 in charge q is given by,[29]

Equation 1.24 $$E^f(V_O{}^q) = E_{tot}(V_O{}^q) - E_{tot}(SnO_2) + \mu_O + q(E_F + E_{VBM})$$

Where $E_{tot}(V_O{}^q)$ is the total energy of the supercell containing the V_O in charge q and $E_{tot}(SnO_2)$ the total energy of a SnO_2 perfect crystal in the same supercell. E_F is the Fermi

energy level, E_{VBM} the energy of the VBM and μ_O the chemical potential of oxygen. The formation energy of the defect depends on the relative abundance of element in the environment; in this case the formation energy of an oxygen vacancy depends on the amount of oxygen in the environment expressed through the chemical potential (μ_O). E^f also depends on the difference in charge between the defect and the lattice site it occupies. The greater this difference, the higher the formation energy of the defect will be. The charge of the defect is determined by the position of the Fermi energy level in the band gap.[28]

When formed, non-stoichiometric intrinsic as well as extrinsic defects introduce carriers into localised energy levels within the band gap and thus in this case are electrically active. Therefore the energy required to promote an electron into the conduction band does not depend solely on the band gap size but on the energy level of the defects created. Point defects creating an energy level just below the CBM are considered donor defects due to the fact that they will donate an electron to the conduction band. Semiconductors whose main type of charge carrier is electrons and which possess a major concentration of donor-type defects are called n-type semiconductors. Other defects will form an energy level just above the valence band; those are considered acceptor defects because they will accept the transfer of some electrons from the valence band and hence create vacancies. In the case of semiconductor possessing mainly acceptor type defects and whose major carriers are hole are called p-type semiconductors. The two concepts of donor and acceptor energy levels are illustrated on Figure 1.9.[24]

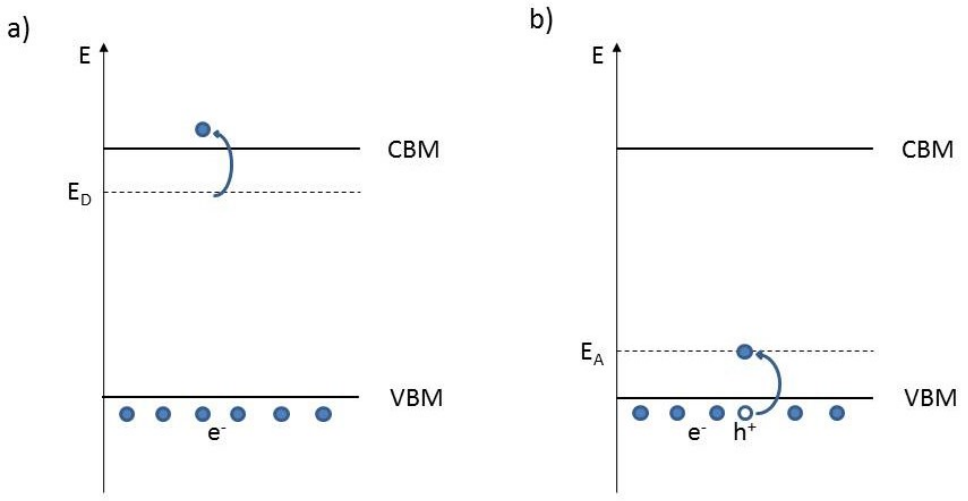

Figure 1. 9: Schematic representation of an energy diagram showing a) the creation of a donor energy level E_D below the conduction band and b) the creation of an acceptor energy level E_A above the valence band. Electrons are represented in blue filled circles and hole in empty circle. VBM and CBM are respectively the valence band maximum and the conduction band minimum.

The crucial energy required to excite an electron (respectively a hole) into the CB (respectively VB) is now the energy difference between E_D (respectively E_A) and the CBM (respectively VBM) rather than the band gap. Therefore charge carriers are more easily excited and the conductivity of the material is increased. Depending on the position of the defect energy level, these excitations can even occur at room temperature.

These types of defect are often electrically active, however their charge is dependent on the position of the Fermi level and on what is called the transition level of the defect $\varepsilon_D(q/q')$. $\varepsilon_D(q/q')$ represents the Fermi energy level at which the formation energy of charge state q and q' for a defect are equal and is given by,

Equation 1.25
$$\varepsilon_D(q/q') = \frac{E^f(D^q;E_F=0) - E^f(D^{q'};E_F=0)}{q-q'}$$

Where $E^f(D^q;E_F=0)$ and $E^f(D^{q'};E_F=0)$ are the formation energies of the defect D in charge q and q' respectively when E_F is at the valence band maximum. The impact of this parameter is that if E_F is below $\varepsilon_D(q/q')$, the charge q is stable while if E_F is above it the charge q' is stable, as shown on Figure 1.10.[29]

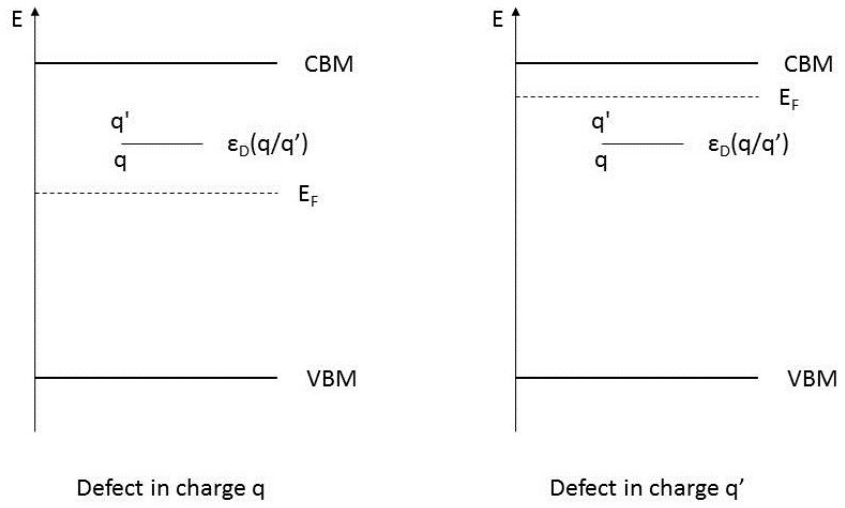

Figure 1. 10: Schematic representation of the transition level $\varepsilon_D(q/q')$ of a defect D related to the position of the Fermi energy level E_F.

From this point two kinds of defects are distinguished; shallow level defects with a transition level positioned such that it is likely to be thermally ionized at room temperature (close to a band edge, either CBM or VBM), and deep level defects whose transition level is such that it is unlikely to be ionized at room temperature.[29]

2. The case of SnO_2

Tin oxide exists in many different forms such as SnO_2, SnO and Sn_3O_4.[31] These different phases are shown on the phase diagram of Sn-O on Figure 1.11.

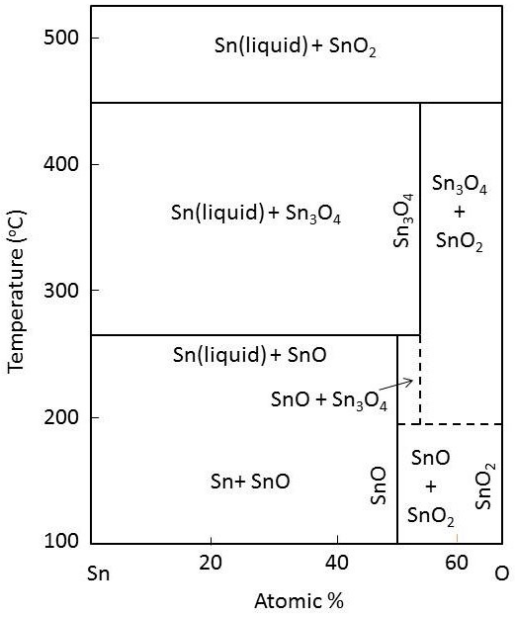

Figure 1. 11: Sn-O phase diagram at 1 atm extracted from Ref [32]

Out of these phases, SnO_2 and SnO are the most common forms. Their existence reflects one of the key characteristics of tin which is its dual valency. Tin is both stable in its Sn(II) or Sn(IV) oxidation state. Even though they differ only by a degree of oxidation in term of stoichiometry, their properties are greatly changed. SnO_2 is an intrinsic n-type wide band gap semiconductor while SnO have a smaller band gap (≈2.6-3 eV) but is also a p-type intrinsic semiconductor.[33] The other existing state Sn_3O_4 is formed of an intermediate phase between SnO and SnO_2 where Sn is present both in Sn(II) and Sn(IV) states. Among these phases, SnO_2 is the most abundant of tin oxide.

2.1. General properties and structure

SnO_2 is found in nature as a mineral called Cassiterite. SnO_2 possesses a rutile crystal structure with a tetragonal unit cell of symmetry $P4_2/mnm$ and with a = b = 4.737 Å and c = 3.186 Å.[33] Each tin atom is surrounded by six oxygen atoms while the oxygen atoms are three-fold coordinated as shown on Figure 1.12.a. Other metal oxides possess a similar structure such as TiO_2, PbO_2, VO_2 and RuO_2.[33]

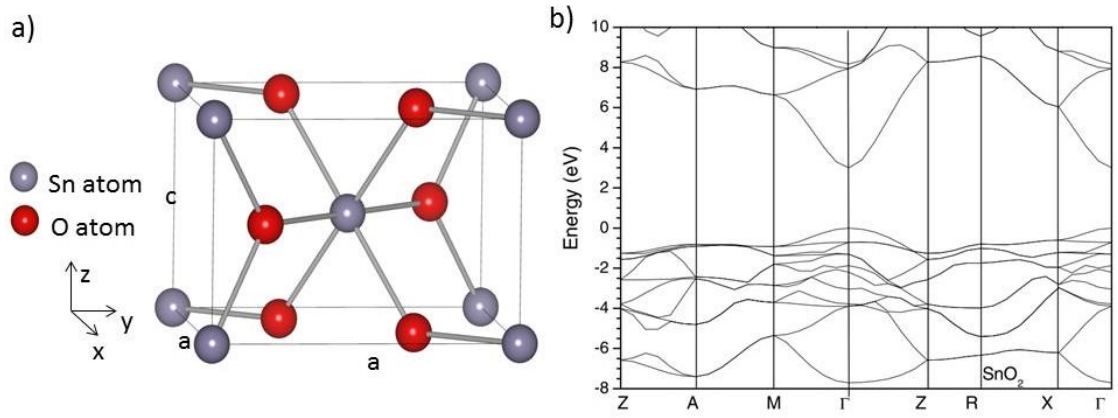

Figure 1. 12: a) Schematic of SnO_2 rutile structure where a = 4.737 Å and c = 3.186 Å. b) Band structure of SnO_2 taken from ref [34].

SnO_2 is a n-type intrinsic semiconductor with a direct band gap of 3.6 eV, hence is transparent in the visible spectral region. Its larger band gap compared to SnO arises from the shorter Sn-O bonds formed (2.07 Å in SnO_2 and 2.23 Å in SnO)[33] due to Sn^{4+} being more electronegative than Sn^{2+}. In SnO_2, the valence band maximum (VBM) is mostly constituted of O 2p states while its conduction band minimum (CBM) is formed of Sn 5s states. The band structure of SnO_2 is shown on Figure 1.12.b with direct band gap at the Γ point. The strong dispersion of the s-like conduction band induces light effective electron mass for charge carrier transport and thus a high mobility of the electrons.[35] Undoped SnO_2 exhibit resistivity of 10^{-3}-10^{-2} Ω.cm with charge carrier (electron) concentration about 10^{19}-10^{20} cm^{-3} and mobility around 5-30 $cm^2/V.s$).[36] These electrical properties can be enhanced through the use of extrinsic dopants (Sb or F). The combination of both high electrical conductivity and optical transparency in SnO_2 makes it a good candidate for a wide range of applications such as; conducting electrodes, transparent transistors, photovoltaics, sensors, LEDs and smart windows.[1,36–41] In its stoichiometric form SnO_2 is an insulator, thus its conductivity arises due to non-stoichiometry. The origins of its conductivity are still a matter of extensive debate and discussed in the next section. SnO_2 can also be doped with various elements to improve its functional properties such as Sb or F to enhance its conductivity[42], and Ag or Pd to improve its gas sensitivity[41,43].

2.2. Origin of conductivity in SnO_2

2.2.1. Intrinsic defects

As mentioned in section 1.2, two types of defect are distinguished; donor type defects which introduce energy levels close or in to the CB and give electron to the system, and acceptor type defects which form energy levels close or in the VB and accept electron from

the system (they produce holes). Since SnO_2 is an intrinsic n-type semiconductor, the major defects are donor type defects. The possible defects in SnO_2 are oxygen vacancies (V_O), tin interstitials (Sn_i), tin vacancies (V_{Sn}), oxygen interstitials (O_i), tin antisite (Sn_O) and oxygen antisite (O_{Sn}). The latest two (Sn_O and O_{Sn}) are not considered since their formation energy is too high and thus have a low contribution to the non-stoichiometry.[16] The formation of the common four defects present in SnO_2 can be described using Kröger-Vink notations. The following equations represent the formation of the defects in their fully ionised state.[25]

Equation 1.26
$$O_O^x \rightarrow V_O^{\circ\circ} + 2e^/ + \frac{1}{2}O_2$$

The formation of an oxygen vacancy in Equation 1.26 gives two extra electrons to the system while a tin interstitial gives four extra electrons,

Equation 1.27
$$V_i^x + Sn_{Sn}^x \rightarrow Sn_i^{\circ\circ\circ\circ} + 4e^/$$

Since both defects induce the formation of electrons they are donor type defects. On the contrary, tin vacancies accept electron from the system and therefore produce four holes,

Equation 1.28
$$Sn_{Sn}^x \rightarrow V_{Sn}^{////} + 4h^\circ + Sn$$

Similarly the oxygen interstitials generate two extra holes,

Equation 1.29
$$V_i^x + \frac{1}{2}O_2 \rightarrow O_i^{//} + 2h^\circ$$

Therefore tin vacancies and oxygen interstitials are considered acceptor-type defects.

As explained in section 1.2, the formation energy of these point defects is function of the Fermi energy level E_F and the chemical potential μ (representative of the environmental conditions). When doing theoretical calculations, two environmental limits are generally analysed; Sn-rich/O-poor conditions when the oxygen chemical potential reach the limit for the decomposition of SnO_2 into SnO ($\mu_O \approx -3$ eV), and Sn-poor/O-rich limits when the oxygen chemical potential reaches $\mu_O = 0$ eV. Since the oxygen chemical potential is linked to the oxygen partial pressure, these limits represent the two extreme experimental conditions in the preparation of SnO_2 thin films. In order to understand the origin of n-type conductivity in SnO_2 and the impact of each point defect, three parts are involved; i) the case of donor-type defects, ii) the case of acceptor-type defects and iii) summary of the main defects presents.

The formation energy of the different defects is generally displayed in the form a diagram function of the Fermi energy level as shown on Figure 1.13 below.

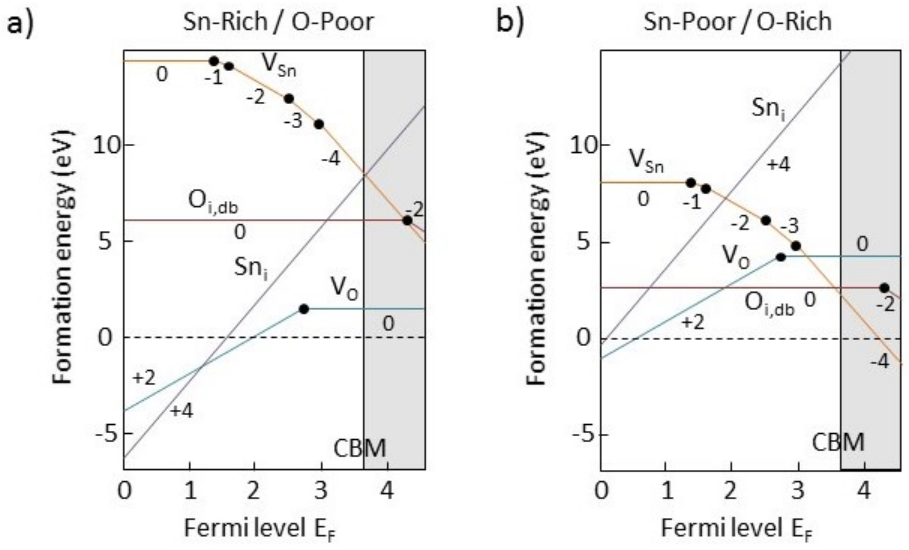

Figure 1. 13: Formation energies of the different point defect present in SnO_2 function of the Fermi energy level under a) Sn-rich/O-poor environment and b) Sn-poor/O-rich environment. The origin for the Fermi level is taken at the VBM and the grey band corresponds to the CB. The black dots represent the transition energy levels ε(q/q') of the defects where q is the charge of the defect when E_F is below it and q' the charge of the defect when E_F is above. $O_{i,db}$ represents the dumbbell oxygen defect (explained below). Diagram taken from [44].

No clear plot of the formation energy has been established yet as it varies with the calculation methods employed by the different teams of researchers. Therefore the representation of the defect formation energies function of the Fermi level varies from an author to another but in order to have a visual representation of the relative positions of the defect formation energy I chose to use the diagram made by Péter Ágoston.[44]

2.2.1.1. Donor-type defects

Under Sn-rich/O-poor conditions, Kiliç and Zunger[16] calculated the formation energy of oxygen vacancies to be higher than tin interstitials when the Fermi level is close to the CBM (which is the case in n-type semiconductors). They found that Sn_i produce a shallow donor level, with its lowest transition level at $\varepsilon(Sn_i)(4+/3+) = E_{CBM} + 203$ meV. This put the defect state directly in the conduction band, thus when formed Sn_i are instantly ionised and participate to the conductivity. This is thought to be due to the outer electrons of the tin which are weakly bound to the nuclei. They also calculated that V_O possess a donor level just below the CBM with its transition level at $\varepsilon(V_O)(2+/0) = E_{CBM} - 114$ meV. Therefore oxygen vacancies would only be ionized when the Fermi energy level lies below this transition level. This is in agreement with what Samson and Fonstad previously

observed experimentally.[45] They measured the first ionisation state to lie 30 meV below the CBM and a second state 150 meV below the CBM corresponding to the second ionisation level. When the Fermi level is close to the VBM (case of a p-type SC), both Sn_i and V_O possess negative formation energies which means they would form spontaneously. With the Fermi level in the middle of the band gap, which is the case for pure intrinsic SC, they estimated Sn_i to have a negative formation energy while V_O have a positive formation energy. This would lead to an easier formation of tin interstitials and thus the abundance of Sn_i in the system. While Kiliç and Zunger[16] established tin interstitials as the main source of n-type charge carrier in SnO_2, their argument was discussed by Singh *et al.*[46]. In their calculations, Singh *et al.* concluded that the V_O and Sn_i are not responsible for the n-type conductivity in SnO_2. They calculated Sn_i formation energy was too high which would lead to a concentration of Sn_i negligible under equilibrium conditions and that despite the lower formation energy of V_O, its lower charge transition level makes it unlikely to contribute to the conductivity. Instead they introduced hydrogen impurities as a cause of n-type conductivity in SnO_2, but this part is later discussed in section 2.2.2. Godinho *et al.*[25] studied the structural impact of the defect in SnO_2. They found that oxygen vacancies are the main cause of non-stoichiometry due to the multi-valence of the tin with possible reduction of some Sn(IV) ions to Sn(II) as charge compensation mechanism. The presence of Sn(II) states in SnO_2 has been previously reported.[47,48] Péter Ágoston[44] showed similarly that V_O possesses the lowest formation energy in these environmental conditions and thus would be the dominant defect compared to Sn_i which possesses a higher formation energy.

Under Sn-poor/O-rich conditions, the formation energy of donor type defects are increased as the environment is less favourable to their formation. However V_O remains one of the defect with the lowest formation energy as observed in figure 1.11.[44] When the Fermi level is close to the VBM (p-type conditions), the formation energy of V_O and Sn_i are the lowest ones and can reach a negative formation energy. This means these defects are very likely to form spontaneously under oxygen rich conditions when the Fermi level moves towards the valence band.

When either a Sn_i or an V_O is formed in SnO_2, the lattice may undergo some change in term of dimension considering the strain caused by these defects. In the case of the oxygen vacancy, the differences in lattice relaxation behaviour have been found to be dependent on the V_O charge state. [46] When V_O is in neutral state (V_O^0), Singh *et al.*[46] estimated a relaxation inward by 2.5 % of the three tin atoms surrounding the vacancy, which induces a compression of the lattice. However when in its doubly charged state (V_O^{2+}), the three

nearest tin atoms have been found to relax outward by 10 % which induces an extension of the lattice. A similar displacement was estimated by Godinho *et al.*[25] and the repulsion of the neighbouring tin atoms around the oxygen vacancy is thought to be due to Coulombic repulsion. In the case of Sn_i, in its neutral state a large displacement of the lattice is observed due to its covalent radius (1.40 Å).[16] In its 4+ state, due to the important charge of the interstitial, considerable electrostatic size effects exists.[44] In TiO_2 the four closest oxygen atom closest to the Ti_i relax away from the interstitial by 0.24 Å.[49] Since TiO_2 possess a rutile structure similar to SnO_2 it seems rational to relate the titanium interstitial size effect to Sn_i. Therefore regarding its charge Sn_i would cause an extension of the lattice size in SnO_2.

2.2.1.2. Acceptor-type defects

Compared to the determination of donor-type main defects in SnO_2 less controversy have appeared in the literature concerning the acceptor defects as the authors seem to agree on their behaviour. Since SnO_2 is an intrinsic n-type semiconductor the main defects cannot be acceptor type defects. It can be observed on Figure 1.11 that V_{Sn} and O_i clearly possess higher formation energy in Sn-rich/O-poor conditions.

However the case of n-type conductivity is less obvious in Sn-poor/O-rich environment. Regarding the tin vacancies, their formation energy decreases in this environment but remains higher than the oxygen interstitials formation energy.[25] Godinho *et al.* assimilated the high formation energy of V_{Sn} to the high energy required to remove an electron from an oxygen 2p state due to the high electronegativity of the oxygen. Even though they can be present as a minority, they cannot be responsible for the non-stoichiometry in SnO_2.[44] In the case of the oxygen interstitials, their formation energy is greatly lowered in oxygen-rich conditions, even below that of V_O which would make them the dominant defect. However the incorporation of the doubly charged oxygen in an interstitial site results in a large outward relaxation of the neighbouring oxygen atoms.[50] In order to release the stress caused by the O_i, the elastic strain can be decreased by releasing two electrons and forming what is called a neutral oxygen dumbbell on a regular lattice site. This phenomena has also been explained by Godinho *et al.*[25], and Scanlon and Watson[15]; instead of the expected O^{2-} interstitial (O_i^{2-}), the oxygen atom relaxes towards an oxygen from the lattice to displace it and form a peroxide species (O_2^{2-}). The similar effect was observed in ZnO as well.[51] The dumbbell oxygen defect formation can be written as follow,[44]

Equation 1.30
$$O_i^{//} + O_O^0 \rightarrow (O_2)_O^0 + 2e^/$$

The ionisation level of this defect lies too deep in the conduction band to be active as an acceptor defect and be considered as part of the conductivity.[15,25] As a consequence of the poor formation of V_{Sn} and O_i, V_O will be the dominant defect in these conditions.

2.2.1.3. Summary

Considering all the possible point defects in SnO_2 the donor-type defects have been found to be the main defects in SnO_2 due to their lower formation energy. This is not surprising as SnO_2 is intrinsically a n-type semiconductor. Even under oxygen-rich condition, the acceptor defects are not stable in the structure. Despite what has been found by Kiliç and Zunger[16], Sn_i is not the defect responsible for most of the n-type conductivity, since V_O has been shown to have a lower formation energy.[15,25,44] Despite being contradicted by Singh *et al.*[52], the conductivity is likely to be linked to the existence of shallow donor levels near the CB and formed by oxygen vacancies.[45,53–55]

2.2.2. Hydrogen impurities

Although not intrinsic to SnO_2, hydrogen is often present in the various growth environment and is particularly hard to remove from it.[46] In 1973, Samson and Fonstad[45] observed a rapid increase of the carrier concentration in SnO_2 thin films exposed to H_2 atmosphere. This lead them to assume the existence of a new donor level created by the hydrogen species which increases the conductivity. In 2000, Van de Walle[56] demonstrated theoretically that hydrogen acts as a shallow donor and occupies an interstitial site in ZnO as H_i^+ and this was confirmed experimentally by Hofmann *et al.*[57] in 2002. Kiliç and Zunger[58] generalized the study to wide band gap oxide and especially the case of SnO_2 and MgO. They admit the existence of a "hydrogen pinning level" lying around 3 eV below the vacuum level and estimated that material whose CBM lies below this level are likely to be donor-doped through the incorporation of hydrogen in the lattice. In the case of SnO_2 the hydrogen pinning level lies in the CB, therefore the defect created by hydrogen incorporation is constantly ionized and H donates electron to the system. The effect of hydrogen as an impurity in SnO_2 were also studied by Singh *et al.*[46] where they believed the conductivity in SnO_2 to be caused by hydrogen and not Sn_i or V_O intrinsic point defects. They found H_i to be a shallow donor with a ionization level lying in the CB. However the formation energy of H_i do not take the oxygen partial pressure in consideration and the conductivity of SnO_2 have been known to decrease when the environment becomes oxygen-rich. Singh *et al.* explained the oxygen dependence with the presence of substitutional hydrogen on the oxygen site (H_O^+). H_O acts as a shallow donor with a formation energy only slightly higher than H_i.

Hydrogen donor impurities (H_i^+ and H_O^+) have often been responsible for a part of the n-type conductivity in SnO_2 due to their low formation energy defects and their shallow donor behaviour.[15,46,58] However their incorporation is difficult to control in the growth process and they are particularly hard to detect. Thus the control that can be brought through the growth conditions is mainly used to influence the formation intrinsic point defect such as Sn_i, V_O, V_{Sn} and O_i in SnO_2.

2.2.3. Extrinsic defects

Even though the type of conductivity of a semiconductor is determined by its intrinsic defects behaviour, it can be either enhanced or modified through extrinsic doping. In the case of n-type (respectively p-type) transparent conducting oxides (TCOs) the aim is to increase the concentration of charge carriers in the system by doping with higher (respectively lower) valency elements. Since SnO_2 is intrinsically n-type, extrinsic doping using donor impurities is easier than with acceptors. The most common n-type dopants for SnO_2 are Sb^{5+} which substitute on Sn^{4+} site and F^- on O^{2-} site.[59] When Sb^{5+} substitutes on Sn^{4+} site, four electrons are used in the bonding and an extra electron remain loosely bound to the dopant. This electron can be easily ionised and participate to the conductivity under an applied electric field. With these types of doping resistivity in the range of 10^{-4} Ω.cm can be achieved with charge carrier concentration in the order of 10^{21} cm^{-3} and mobility between 1-20 $cm^2/(V.s)$[5–7,60,61] Other n-type dopants such as Mo[62], Ta[63] and Cl[64] are used but they are not as efficient as F or Sb. When selecting a dopant, the ionic radii has to be considered, it should be close to the ionic radii of the host atom to minimize lattice distortion and preserve the transport properties.[59] Another important parameter is the oxidation state of the dopant. While the inclusion Sb^{5+} on Sn^{4+} induce the formation of a free electron, Sb^{3+} results in the formation of an acceptor state (a hole).

Therefore another category of dopants, known as acceptor dopants, induce the formation of holes in SnO_2. Since SnO_2 is intrinsically n-type, to change its type of conductivity would mean to neutralise the existing electrons and induce holes via extrinsic doping. As mentioned previously, intrinsic defects such as V_{Sn} or O_i cannot be dominant in SnO_2 which makes the fabrication of p-type SnO_2 thin films difficult. However it has been shown that extrinsic dopants such as Li[65], Al[13], Ga[11], In[14], N[66], Sb[67] and Zn[68] could be used to induce p-type conductivity through the formation of acceptor-like states in SnO_2. Even though the conductivities achieved are not comparable to F- or Sb-doped SnO_2 films, the progress made in this field is important. The achievement of p-type SnO_2 could be a milestone in the field of transparent electronic. The progress achieved and the possibility

of such type of doping is more developed in section 2.4 of this chapter and later in chapter 4 (specifically on Zn-doped SnO_2).

2.2.4. Limitation mechanisms

The conductivity of a material is a product of the concentration of free charge carriers (n) and the carrier mobility (μ), as shown in Equation 1.31,

Equation 1.31 $$\sigma = en\mu$$

Generally, not only one type of charge carrier is present in a semiconductor, therefore its conductivity depends on the concentration and the mobility of both type of carriers, this is taken into account by,

Equation 1.32 $$\sigma = en\mu_n + ep\mu_p$$

Where n and p are the concentrations of electron and holes respectively, and μ_n and μ_p their respective mobilities. The previous sections were focused on the charge carriers present in SnO_2 through intrinsic defects and/or extrinsic dopants. In this part the factors affecting the mobility of the charge carrier are discussed. To simplify the study, the mobility of only one type of charge (electrons) is studied as the limitation mechanisms are the same for both type of charge carriers.

As described by the Drude model in section 1.1.1, the electron mobility μ_n correspond to the speed at which electrons can travel through the system under an applied electric field. Therefore μ_n is expressed as the ratio between the drift speed $|v|$ and the electric field E, and is given in $m^2/(V.s)$. μ_n is then driven by the effective mass m_e^* of the electrons and the mean free time between scattering τ, as taken from Equation 1.1.

Equation 1.33 $$\mu_n = \frac{|v|}{E} = \frac{e\tau}{m_e^*}$$

It was previously mentioned that the effective mass of the charge carriers is related to the curvature of the band (CB for electrons and VB for holes). One of the reason SnO_2 is a good n-type semiconductor is because of the dispersive nature of its CB which result in low electron effective mass, while its VB is flat and lead to high hole effective mass.[35] In transparent conductive oxides (TCOs) the mobility of the charge carriers is limited by different scattering mechanism such as, ionized impurity scattering, lattice scattering and grain boundary scattering.[69]

If the scattering mechanisms occur independently, the Matthienssen rule can be applied and the overall mobility (μ) can expressed as a function of the mobilities resulting from the different scatterings (μ_{ii} for ionized impurities, μ_L for lattice scattering and μ_{gb} for grain boundaries),[70]

Equation 1.34

$$\mu = \left[\frac{1}{\mu_{ii}} + \frac{1}{\mu_L} + \frac{1}{\mu_{gb}}\right]^{-1}$$

2.2.4.1. Ionized impurity scattering

TCOs contain a large amount of defects either intrinsic or from dopants which are usually ionised. These ionised impurities generally act as strong scattering centres for the mobile charge carriers. The path of a passing electron is deflected when passing by a ionised impurity, either through a repulsive (negatively charged impurity) or an attractive (positively charged impurity) interaction. This type of scattering becomes predominant in degenerate semiconductors due to the large amount of ionised impurities (carrier concentration > 10^{19} cm^{-3})[71,72] For degenerate SC, the mobility of the charge carriers when scattered by ionised impurities (μ_{ii}) does not depend on temperature but is function of the material constants such as its dielectric constant ε and the electron effective mass m_e^*, and is inversely proportional to the concentration of ionised scattering centres and their charge. In the case of non-degenerate SC, the factors affecting the mobility are the same except for a contribution from the temperature.[73]

Overall, μ_{ii} decreases when the amount of ionised impurities increases which is consistent with more scattering centres being formed. This scattering mechanism is dominant at high concentration of charge carrier (common in TCOs).[74]

2.2.4.2. Lattice vibration scattering

Lattice vibration scattering arises from the atoms vibrating due to thermal motion. The vibration of the atoms gives rise to acoustic or optical phonons which acts as scattering centres for electrons. The scattering effect from the acoustic and the optical phonons can be grouped as lattice vibration scattering. Therefore the mobility resulting from the lattice vibration scattering (μ_L) is inversely proportional to the temperature T. As T increase the atoms vibrate more and the scattering from the resulting phonons increase, thus a decrease of the mobility. However when at low temperature this type of scattering is insignificant compared to others such as impurity scattering.[69,73]

2.2.4.3. Grain boundary scattering in polycrystalline TCOs

Polycrystalline TCOs are formed of crystallites of different growth orientation joined by grain boundaries. The grain boundaries constitute crystallographically disturbed regions and contain lattice defect trapping states. These defect trapping states are filled by the charge carriers in the grain and balance the charge. This leads to the formation of a depletion region and the creation of a potential barrier which decrease the carrier mobility between the crystallites.[69,75] The carrier transport across grain boundaries has been described by Seto[76] where he created a simple model to describe the mobility affected by the grain boundaries (μ_{gb}),[75]

Equation 1.35
$$\mu_{gb} = \mu_0 exp\left(-\frac{E_b}{k_B T}\right)$$

Where E_b is the height of the energetic barrier and μ_0 the mobility inside the grain expressed as,[75]

Equation 1.36
$$\mu_0 = \frac{eL}{\sqrt{2\pi m^* k_B T}}$$

Where L is the grain size and e the charge of an electron. The height of the barrier is function of the size of the depleted region (x_d) and the carrier concentration N as shown in Equation 1.37.[75]

Equation 1.37
$$E_b = \frac{e^2 N}{2\varepsilon} {x_d}^2$$

At low carrier concentration, the depletion region extends to a distance $x_d = L/2$ on each side of the grain leading to a complete depletion of the grain. The potential barrier becomes,[75]

Equation 1.38
$$E_b = \frac{e^2 N L^2}{8\varepsilon}$$

This means the potential barrier increases with increasing carrier concentration. However, the barrier height increases only until all the traps are filled and the maximum height barrier corresponds to the point where the carrier where $N = N_t/L$, where N_t is the charge trap density at the grain boundary. This maximum of E_b corresponds to a minimum of mobility μ_{gb} based on Equation 1.35. Further increase in the carrier concentration leads to added carriers which are not trapped and decrease the height of the barrier. The width of the depletion region decreases to $x_d = N_t/2N$ which induces a consequent change in the barrier height,[75]

Equation 1.39

$$E_b = \frac{e^2 {N_t}^2}{8\varepsilon N}$$

Once the trap states are filled, the potential barrier decreases which lead to an increase in the mobility. Grain boundary scattering is a dominant scattering mechanism for films with low carrier concentration (< 5 x10^{-18} cm^{-3}) and relatively small grain size when compared to the mean free path of free electrons which is only a few nm.[69] However when considering TCOs with high carrier concentration and good quality crystallites grain boundary scattering has a much smaller contribution on the mobility compared to other scattering mechanisms.

2.3. Applications

2.3.1. Transparent conducting oxides (TCOs)

Transparent conducting oxides (TCOs) are metal oxides which exhibit both high electrical conductivity and high optical transparency. They are used extensively, mainly as transparent electrode, in solar cells, flat panel displays, organic light-emitting diodes (OLEDs), low-emissivity windows and oven windows.[36–40] Thin films suitable for TCO applications are expected to exhibit a resistivity < 10^{-3} Ω.cm and a transparency in the visible region greater than 80 %. Generally the films fulfilling these conditions are degenerated semiconductors with high carrier concentration (above 10^{20} cm^{-3}) and band gap above 3 eV to avoid any absorption in the visible region. The first TCO growth was reported in 1907 by Badeker with conductive thin films of CdO. Then first report on the most used TCO, Indium Tin Oxide (ITO), was carried by Rupperecht in 1954, followed by others such as SnO_2 and ZnO.[30,77] ITO films are composed of In_2O_3 doped with about 10 at.% Sn and generally exhibit resistivity in the order of 10^{-4} Ω.cm with high optical transparency (80-95 %).[78] In the past 20 years, little progress has been made on the improvement of ITO electrical conductivity and the reason is ITO is not suitable for the expanding optoelectronic market owing to its cost and scarcity.[60] As a replacement, the interest has been brought on binary oxides such as ZnO and SnO_2, and other ternary or multicomponent oxides such as Cd_2SnO_4, $CdSnO_3$ and Zn_2SnO_4.[2,36,60] ZnO and SnO_2 are the best candidates since the application of Cd based compounds are limited due to Cd toxicity and others do not reach the resistivity attained by ZnO or SnO_2 compounds.[60] The most comment dopants for these metal oxides are Al:ZnO (AZO), F:SnO_2 (FTO) and Sb:SnO_2 (ATO). Although AZO films possess slightly better electrical performances with resistivity of 8.5 x10^{-5} Ω.cm[42], ATO and FTO films resistivity approach ITO performances with resistivity around 2-3 x10^{-4} Ω.cm. ATO and FTO films seem to exhibit similar properties with carrier concentrations about 1-2 x10^{21} cm^{-3}, however FTO show slightly

larger mobility (20 $cm^2/(V.s)$) compared to ATO (10 $cm^2/(V.s)$).[5–7] FTO films are already used as electrodes in devices such as solar cells to replace the ITO.[79,80]

Whilst most of the TCOs developed are crystalline, amorphous TCOs have a potential use for flat panel displays or solar cells on flexible substrates. The inconvenience with crystalline TCOs is often their high deposition temperature required (300-400 °C).[74] However amorphous thin films can be obtained at temperature below 150 °C (which is often the temperature limit for flexible substrates) while maintaining a high mobility. This is due to ns orbitals of metal ions constituting the CB of most metal oxides (ZnO, SnO_2) which form transport path for mobile carriers even in amorphous state where the disorder is higher.[77] Amorphous TCOs such as $AgSbO_3$, Cd_2GeO_4 and Cd_2PbO_4 showed high electron mobility of 10 $cm^2/(V.s)$ which is large compared to a-Si:H (< 1 $cm^2/(V.s)$).[81,82]

Another field of applications yet to be explored concern the TCO based devices. With the development of p-type TCO with electrical and optical properties on pair with their n-type counterpart, new devices could be developed such as UV-light emitting diodes (LEDs), transparent thin film transistors or functional windows which transmit visible light and generate electricity through the absorption of UV photons.[30,77] The first (UV)-LED was fabricated in 2000 and was based on a p-n heterojunction made of p-$SrCu_2O_2$ and n-ZnO.[83] However even though a lot of work has been carried on n-type TCOs, the development of their p-type counterpart is still recent and needs to be improved. The aim is brought on the development of semiconductor which could support either n- or p-type doping function of the dopant used in order to be used as p-n homojunction. Therefore two methods have been developed: the research for new p-type metal oxides which could be n-doped and the introduction of p-type conductivity in already developed n-type TCOs such as SnO_2 and ZnO. This matter is more detailed in section 2.4 of this chapter.

2.3.2. Gas sensors

Gas sensors are devices recording the changes in environment through the use of a material whose properties depend on the ambient gas. In such devices, the variations in electrical conductivity are recorded to analyse the environmental changes. The most common materials for gas sensing applications are ZnO and SnO_2. These systems are based on the surface conductivity of these materials. When a molecule adsorbs at the surface of SnO_2, electrons can be transferred if the Fermi level lies below its lowest lying unoccupied orbitals. The resulting charge at the surface need to be compensated which lead to an electron depletion or accumulation (depending on the type of charge) leading to the

formation of a space charge region and inducing a surface band bending. [33](more details about space charge region in chapter 2) Due to the presence of an accumulation/depletion zone, the overall conductivity is altered and used as a signal for gas sensing devices. In polycrystalline SnO_2, the formation of Schottky barriers at grain boundaries (see section 2.2.4 of this chapter) can also amplify the gas sensing response.[84] Dopants can also be used to increase the gas response. In SnO_2 the most commonly used are Ag and Pd.[41,43] Under atmospheric conditions these additives are present as Ag_2O and PdO which lead to a larger work function of oxidised additives compared to SnO_2 and thus an upward band bending (electron depletion translated by a decrease in conductivity). However when exposed to combustible gas, the environment becomes reducing and the additives change from oxides to metals, decreasing their work function and thus the band bending (increase of conductivity).

2.3.3. Solar cells

FTO and undoped SnO_2 have been reported to be used in CdS/CdTe solar cells. Due to its high electrical conductivity, good optical transparency and work function close to that of CdS FTO is a good cathode candidate for CdS contact. However since the carrier collection in CdS is insufficient[85] the light absorbed is lost. To reduce the amount of light absorbed by the CdS layer and improve the short-circuit current, the thickness of the CdS layer can be decreased. However since its thickness is extremely small (100 nm) compared to the CdTe thickness (3-7 μm)[86] the CdS layer may contain pin-holes leading to direct contact between FTO and CdTe and thus the formation of micro-junction decreasing the overall efficiency.[85,87–89] To avoid the loss in open-circuit voltage and field factor caused by these pin-holes, the use of a highly resistive layer such as undoped SnO_2 is required between the FTO and the CdS layers. The use of SnO_2 as a buffer layer reduce the atom diffusion form the TCO during the device fabrication, improve the surface morphology (reduce the amount of pin-holes) and minimise the contact area between CdTe and FTO.[87,89] Great improvement have been reported when using SnO_2 as a buffer layer with a cell efficiency increase from 4 to 11 % for FTO/CdS/CdTe/Cu/Au and FTO/SnO_2/CdS/CdTe/Cu/Au respectively.[89] Solar cells fabricated with FTO/SnO_2 cathode contact were reported to achieve up to 15.2 % efficiency with open-circuit current of 0.84 V, short-circuit current density of 23 mA/cm^2 and field factor of 78 %.[87]

2.4. P-type doping in SnO_2

Despite the numerous application using TCOs, very little work has been carried on TCO based devices.[30] Most TCOs are n-type while p-type TCOs with equivalent properties

still need to be developed. As specified previously, to be used as TCO a conductive film must have a band gap greater than 3.1 eV (the visible photon energy being between 2.1 and 3.1 eV), a transparency superior to 80 % in the visible region and a conductivity higher than 1000 S/cm (resistivity lower than 10^{-3} Ω.cm).[30] The development of good p-type TCOs is essential in the fabrication of p-n homo-junction[8,9], *i.e.* for functional windows which transmit light in the visible region and generate energy through the absorption of ultra-violet (UV) photons, and fully transparent CMOS.[10] The first p-type TCO was a NiO thin film developed by Sato *et al.*[90] in 1997 with a resistivity of 0.14 Ω.cm and transparency of only 40 % in the visible. Since then, a great deal of effort has been put into the development of a good p-type TCO and two main approaches can be distinguished: i) chemical modification of the valence (CMVB) and ii) ion implantation.[15]

2.4.1. Chemical modification of the valence band (CMVB)

The first method was proposed by Kawazoe *et al.*[8] in 1997 when they successfully made p-type Cu_2O thin films doped with Al to increase the band gap. They suggested that the problem in the development of p-type conductivity lies in the strong localisation behaviour of the top of the valence band on oxygen atoms. The wide band gap in metal oxide is due to a significant ionic character of the bond between metal and oxygen atoms.[9] Generally the energy of the O 2p states lies lower than those of the valence orbitals of the metallic cations. Therefore when a hole is produced, it is localised on an oxygen atom due to the high electronegativity of oxygen and constitutes a deep acceptor level with a high energetic barrier to overcome. As a way to counter this problem, Kawazoe and Hosono suggested to hybridize the metal orbitals with O 2p orbitals to have a more dispersed VBM and decrease the ionic character of the bond, *i.e.* bring more covalency.[8,9,77] In this approach, the material must fulfil several conditions:

- The energy of the metal valence orbitals must be close to those of the O 2p to reduce the localisation of the VB edge on the oxygen and decrease the ionic character of the bond.[9]
- The oxygen atoms have to adopt a tetrahedral coordination to increase the covalency of the bonds.[8]
- The metallic cations should have a close d-shell electronic configuration to avoid d-d transitions which induce a loss of transparency and a strong coloration of the films.[9]
- The band gap of the material needs > 3 eV to avoid absorption in the visible region.[9]

Cu and Ag have been identified as good cation candidates due to their valence orbitals approaching the energy of the O 2p states (around 6 eV for O 2p while 10-11 eV for Cu^+ and Ag^+). The first $CuAlO_2$ TCO based on this approach[8] possessed a resistivity of 1 Ω.cm but a mobility of 10 $cm^2/(V.s)$. From this point two main families of Cu-based p-type TCOs appear: $CuMO_2$ (with M = Al, Ga, In, Cr, Sc…) which possess a delafossite structure and $SrCu_2O_2$, LaCuOCh (where Ch is a chalcogen: S, Se, or Te) with a non-delafossite structure.[4] The first UV-LED was fabricated in 2000 by Ohta *et al.*[83] and was composed of a p-n junction of p-$SrCu_2O_2$ and n-ZnO. So far the lowest p-type resistivity achieved is attributed to the delafossite type $CuCr_{0.95}Mg_{0.05}O_2$ deposited by Nagarajan *et al.*[91,92] reaching 4.5 $x10^{-3}$ Ω.cm. However the highest hole concentration achieved is attributed to Hiramatsu *et al.*[93] with $LaCuOS_{1-x}Se_x$:Mg reaching 2.2 $x10^{20}$ cm^{-3} and a resistivity of 7.1 $x10^{-3}$ Ω.cm. $LaCuOS_{1-x}Se_x$:Mg is the first degenerate p-type TCO. A summary of the p-type TCOs developed over the past 20 years can be observed in Table 1.1.

Table 1. 1: Outlook of the performance of the different p-type TCOs developed the resistivity, mobility, carrier (hole) concentration, transparency in the visible range and optical band gap.

Year	Material	Resistivity Ω.cm	Carrier concentration cm^{-3}	Mobility $cm^2/(V.s)$	Transparency %	Band gap eV	Ref
1984	$CuAlO_2$ (Bulk)	$5.9x10^2$	-	< 0.1	-	-	[94]
1993	NiO	$1.4x10^{-1}$	$1.3x10^{19}$	-	40	-	[90]
1997	$CuAlO_2$	1	$1.3x10^{17}$	10	-	3.5	[8]
1998	$SrCu_2O_2$:K	$2.1x10^1$	$6.1x10^{17}$	0.46	-	3.3	[95]
	In_2O_3-Ag_2O	$8.8x10^{-3}$	$4.2x10^{19}$	17	20	-	[96]
1999	ZnO:Ga:N	2	$4x10^{19}$	0.07	90	-	[97]
2001	$NiCo_2O_4$	$6x10^{-2}$	-	-	40-60	-	[98]
	$CuGaO_2$	$1.6x10^1$	$1.7x10^{18}$	0.23	80	3.6	[99]
	$CuInO_2$:Ca	$3.6x10^2$	-	-	-	3.9	[100]
	$CuCrO_2$	1	-	-	-	-	[91]
	$CuCr_{0.95}Mg_{0.05}O_2$	**$4.5x10^{-3}$**	**-**	**-**	**50**	**3.1**	[92]
	$CuScO_2$	$3.3x10^2$	-	-	40	3.3	[92]
	$CuYO_2$:Ca	$9.5x10^{-1}$	-	-	50	3.5	
2002	$CuNi_{2/3}Sb_{1/3}O_2$:Sn	$2.0x10^1$	-	-	60	3.4	[101]
	$AgCoO_2$	5	-	-	40-60	4.1	
	ZnO:Sb	$8x10^{-3}$	$5x10^{20}$	1.5	-	-	[102]
	ZnO:As	-	$3x10^{17}$	-	-	-	[103]
2003	**$LaCuOS_{1-x}Se_x$:Mg**	**$7.1x10^{-3}$**	**$2.2x10^{20}$**	**4**	**-**	**-**	[93]
2004	ZnO:N	-	$2x10^{20}$	8	-	3.3	[104]
2005	LaCuOS	-	$<10^{19}$	0.5	-	3.2	[105]
	LaCuOSe	$4.2x10^{-2}$	$2x10^{19}$	8	-	2.9	
2006	$SrCu_2O_2$:Ca	$1.2x10^1$	-	-	-	3.2	[4]
	ZnO:Li	5.9	$6.0x10^{17}$	1.8	-	-	[106]
	ZnO:P	$2x10^{-2}$	$3.8x10^{19}$	6.9	-	-	[107]
2007	ZnO:As	$5x10^{-2}$	$4x10^{19}$	2	-	-	[108]
	ZnO:Sb	4.2	$1.9x10^{17}$	-	80-85	3.26	[109]
2008	$CuYO_2$	$1.3x10^{-1}$	-	-	60	3.15	[110]
2009	ZnO:As	-	$6x10^{17}$	-	-	-	[111]
2011	$CuAlO_2$	$5.5x10^{-1}$	$5x10^{19}$	-	-	-	[112]
2012	$Cu_{1-x}Pt_xFeO_2$	$8x10^{-2}$	$4x10^{19}$	-	>50	3.45	[113]
2015	$CuCrO_2$:Mg	$6.3x10^{-1}$	10^{21}	-	63	3.3	[114]

2.4.2. Ion implantation

2.4.2.1. General method

Ion implantation is a method using intrinsic n-type metal oxides and dope them with acceptor dopants to induce p-type conductivity. The development of p-type metal oxides using this technique would be an important milestone in the transparent electronic field as it would allow the fabrication of wide band gap p-n homojunctions.[10] The principle lies on the formation of holes via cation (respectively anion) substitution with lower valency atoms or via defect complex. A good example is the case of ZnO. ZnO has been one of the most studied candidates for p-type ion implantation doping. Successful p-type conductivity of ZnO has been reported when doped with As[108,111], Sb[109], P[107], Li[106] and N[104].[115] In the case of As, Sb and P the p-type conductivity was thought to result from the formation of shallow M_{Zn}-$2V_{Zn}$ defect complex where M is either As, Sb or P.[116] Li (respectively N) acts as an acceptor dopant when substituted on Zn site (respectively O) due to its lower vacancy (Li^{+} or N^{3-}). The ion implantation methods requires to take into consideration both the dopant impurities used and the intrinsic defects present in the host matrix to achieve p-type conductivity.[117] Therefore it is necessary to characterise the material and its defects in order to investigate the most suitable growth conditions. The understanding of the role and formation of intrinsic defects would be of great value in the development of p-type films. The use of thermal annealing is often required in order to active electrically the dopants after implantation. In the process of p-type doping of ZnO using As or Sb as dopant the use of an oxygen-rich environment and/or a post-deposition thermal annealing was required.[118,119] The key issues in this approach lie within the choice of the dopant, the optimisation of growth conditions and the control over native defects to avoid compensation effects. The advantage in making p-type ZnO, In_2O_3 or SnO_2 is that these materials can be easily incorporated in p-n homojunction using their n-type counterpart.

2.4.2.2. The case of SnO_2

It has been discussed previously that the main intrinsic defects present in SnO_2 are donor type defects and thus the intrinsic conductivity is n-type. Even an extreme oxygen-rich environment, supposedly favourable for p-type defects, is not enough to place them as major defects. In these conditions and considering the Fermi level to lie around the CBM, their formation energy is greatly lowered to a point that V_{Sn} and O_i would form more easily than V_O or Sn_i. However their formation would induce a shift of the Fermi level towards the VBM, zone where the formation energy of donor defects (V_O and Sn_i) becomes negative, *i.e.* the defects form spontaneously. Therefore the development of intrinsically p-

type SnO_2 films is impossible due to the lower formation energy of the donor intrinsic defects, even in oxygen-rich environment where the formation energy of p-type defects is decreased. The only possibility to induce p-type conductivity in SnO_2 remains in the control of the n-type defects coupled with the implantation of extrinsic acceptor defects.

Singh *et al.*[46] looked at the use of group IA (Li), group IIIA (In, Ga, Al), group IIIB (Zn) as cation dopant and group V (N) as anion dopant due to their lower valency inducing the formation of one (or more) hole(s) as the dopant substitutes on Sn or O site (depending on the dopant). They found that while N and Li give rise to deep acceptors with a strong tendency of Li for self-compensation through inclusion in interstitials, other dopants such as In, Ga, Al and Zn would exhibit a preferential doping on Sn sites and act as shallow acceptors in SnO_2. Over the past 10 years the research on p-type doping of SnO_2, even though not as investigated as p-type ZnO, has progressed and p-type SnO_2 has been successfully developed with the use of either In, Ga, Al, Zn, Sb or N as acceptor dopant but also using Al-N or In-Ga as co-dopants. The dopants were selected for their lower valency than Sn (or O) but also for their close ionic radius regarding the site they are to occupy ($r(Sn^{4+})$ = 0.69 Å, $r(In^{3+})$ = 0.80 Å, $r(Ga^{3+})$ = 0.62 Å, $r(Al^{3+})$ = 0.54 Å, $r(Sb^{3+})$ = 0.76 Å, $r(Zn^{2+})$ = 0.74 Å, and $r(O^{2-})$ = 1.38 Å and $r(N^{3-})$ = 1.46 Å). The effective p-type SnO_2 thin films developed are listed in table 1.2.

Li doping has been proven successful[65,120,121], however only through the use of a very high amount of dopant in the SnO_2 lattice (> 40 at.%). The inclusion of Li^+ on Sn^{4+} site should induce the formation of 3 hole states above the VBM. However considering the level of doping required to induce the change of conductivity (26 at.% Li[65]) and the amount required to highest hole concentration it is not surprinsing to observe some self-compensation effect. This effect has been reported in Li-doped ZnO films.[106] When placed in an interstitial, Li^+ acts as a donor and compensates the hole created. Even though the number of electrons produced with Li_i is low against the number of holes created with Li_{Sn} (1 electron against 3 holes), the energy required to form the acceptor defect is much higher than that of Li_i.[15] The use of Li as an acceptor dopant seems to be limited due to this self-compensation effect which limits the amount of uncompensated holes achievable.

Al is one of the best candidates for p-type doping of SnO_2. So far the lowest resistivity achieved was about 3.6 $x10^{-2}$ Ω.cm with a mobility as high as 26 $cm^2/(V.s)$ and was achieved by Bagheri-Mohagheghi and Shokooh-Saremi.[13] The type of conductivity appears to switch from n to p-type at doping level of 7.5 at. % with the optimum p-type

conductivity at 8.4 at.% Al. Ahmed *et al.*[122] reported shift to p-type conductivity happening around 12 at.% Al.

Table 1. 2: Outlook of the performance of the different p-type SnO_2 thin films deposited showing the dopant used, the amount, the deposition technique used, the deposition temperature (T) with or without presence of annealing (A), resistivity, mobility, carrier (hole) concentration, and optical band gap.

Dopant	Amount at. %	Deposition technique	Deposition temperature (°C)	Resistivity Ω.cm	Carrier concentration cm^{-3}	Hall mobility $cm^2/(V.s)$	Band gap eV	Ref
Li	75	Spray	480	$1.6x10^{-1}$	$1.1x10^{18}$	-	3.6	[65]
	41.5	Spray	500	$8.34x10^{-1}$	-	-	3.6	[120]
Al	8.4	Spray	480	$3.6x10^{-2}$	$6.7x10^{18}$	26	4.1	[13]
	19	Dip coating	A400	$7.3x10^{-1}$	-	-	4.2	[122]
	-	Sputtering + thermal diffusion	RT A450	$8.1x10^{-1}$	$7.2x10^{18}$	1.1	-	[123]
Ga	20 (Si)	Sputtering	700	$2.8x10^{-3}$	$3.2x10^{18}$	700	-	[11]
	20 (Q)		750	3.3	$7.9x10^{18}$	0.24		
	20	Sputtering	RT A600	1.2	$2.6x10^{19}$	<1	4	[124]
	20	Sputtering	RT A650	10^2	$8.8x10^{18}$	0.14	3.8	[125]
	15	Sol-gel	A520	1.5	$1.7x10^{18}$	6.3	3.8	[126]
In	10	Dip coating	RT A500	$2.1x10^{1}$	$1.9x10^{17}$	1.6	-	[14]
	20	Spray	RT A600	-	$3.1x10^{16}$	0.43	-	[127]
N	-	Sputtering + thermal oxidation	RT A350	$1.4x10^{-1}$	$1.3x10^{19}$	3.6	-	[66]
	P_{N2} = 97.2 %	Sputtering	400	$4.4x10^{-1}$	$3.2x10^{14}$	1.33	3.7	[128]
Sb	3	Thermal growth	A900	-	$1.5x10^{17}$	22	-	[67]
	20	Sputtering	200 A700	$1.7x10^{-1}$	$5.8x10^{19}$	0.64	3.5	[129]
	20	PLD	700 A500	$8.7x10^{-1}$	10^{19}	0.65	3.7	[130]
Zn	20	Sputtering	200 A600	3.6	$3.3x10^{19}$	0.52	3.8	[68]
	25	Spray	340	6.3	-	11	3.46	[12]
	25	Spray	340	3.8	$9.5x10^{17}$		3.8	[131]
	-	Sputtering + thermal diffusion	A400	7.4	$2.4x10^{17}$	35	-	[132]
Al-N	25 at% AlN	Sputtering	RT A450	$6.9x10^{-1}$	10^{18}	-	-	[133]
	Al 14.8 N 1.9	Sputtering	A450	$3.7x10^{-1}$	$4x10^{19}$	0.25	-	[134]
In-Ga	In 9.2 Ga 10.8	Spray	350 A500	$1.7x10^{-1}$	$9.5x10^{17}$	39.2	-	[135]

On first sight it would appear that Ga might be the best p-type dopant for SnO_2 as Yang *et al.*[11] mentioned a resistivity of 2.8 $x10^{-3}$ Ω.cm. However they admitted that those films were deposited on silicon substrate and that it could influence the Hall measurement. Instead they measured a resistivity of 3.3 Ω.cm for the films deposited on quartz, the

carrier concentration was slightly higher than for the Si substrates. During Hall/resistivity measurements the use of a non-conductive substrate is required to avoid any unwanted contribution from the substrate. The main difference lied in the mobility which achieved a ridiculous 700 $cm^2/(V.s)$, way above the mobility observed in n-type SnO_2 films[42], for the films deposited on Si which clearly shows the contribution of the Si substrate in the measurements. The minimum amount of doping required to turn the material p-type was about 10 at.% Ga[126] while the optimum conductivity was generally achieved around 20 at.% Ga.[11,124,125] The presence of Ga in the interstitial position has also been reported by Pei *et al.*[136]. They have been detected by photoluminescence and are thought to act as compensation centre for the p-type conductivity.

While the inclusion of Sn^{4+} in In_2O_3 lattice result in the formation of highly conductive n-type TCO, *e.g.* ITO, the inclusion of In^{3+} in SnO_2 lattice can induce p-type conductivity in the film. This has been reported by Ji, He *et al.*[14] and Ji, Zhao *et al.*[127], however the hole concentration achieved is too low (10^{16}-10^{17} cm^{-3}) compared to other dopants and the lowest resistivity was about 2.1 $x10^1$ Ω.cm. Hole concentration about 4 $x10^{18}$ was achieved by Ji *et al.*[127] for a doping concentration of 20 at.% In however very low mobility was obtained (3 $x10^{-3}$ $cm^2/(V.s)$). Mao *et al.*[135] attributed the low mobility present in both In and Ga p-type SnO_2 films to the lattice distortions caused by the inclusion of these dopants. In order to reduce the strain on the lattice they coupled In (inducing an expansion of the lattice) with Ga (inducing a compression of the lattice) through a In-Ga co-doping method. Their results show promising mobility as high as 3.9 $x10^1$ $cm^2/(V.s)$ with doping of 9.2 at.% In and 10.8 at.% Ga.

N is the only anion p-type acceptor dopant which has shown successful p-type doping in SnO_2. It is an attractive method especially for vacuum deposition technique where the amount of N dopants could be controlled through the gas pressure in the chamber. Mobilities higher than 1 $cm^2/(v.s)$ and hole concentration as high as 1.3 $x10^{19}$ cm^{-3} have been achieved.[66,128] However the presence of a compensation mechanism might limit the optimisation of the p-type conductivity. The incorporated nitrogen possesses different chemical states: atomic nitrogen (β-N) which replaces an oxygen and constitutes an acceptor defect, and molecular nitrogen (γ-N_2) which is constituted of N_2 molecules at O sites forming a double donor.[66,128] Such compensation mechanism has been observed in the p-type N-doped ZnO films where the atomic nitrogen defects were also compensated by N-acceptors-N_2 complexes.[137] The use of N coupled with Al as co-dopants for p-type SnO_2 has been tested but even though the lowest resistivity achieved was 3.7 $x10^{-1}$ Ω.cm, the mobility is 100 times lower than with simply Al doping.[13,134]

Even though Sb is well known as a n-type dopant for highly conductive SnO_2 due to its oxidation state Sb^{5+} creating an extra electron when placed on a Sn^{4+} site, Sb also possesses a lower oxidation state Sb^{3+}. When Sb^{3+} successfully substitutes on a Sn site, it forms an acceptor defect and generates a hole in the lattice. The lowest resistivity achieved was 1.7 $x10^{-1}$ Ω.cm with a hole concentration as high as 3.3 $x10^{19}$ cm^{-3} and was reported by Ni *et al.*[129]. The films conductivity switches to p-type when annealed above 600 °C however the conductivity changes back to n-type above 800 °C of annealing, this is attributed to the formation of donor defects such as oxygen vacancies. The annealing is required to get rid of the remaining intrinsic n-type defects present in the films and electrically activate the acceptors.[129]

Zn is among the favourable p-type dopant suggested by Singh *et al.*[46]. p-type conductivity has been achieved either by using spray pyrolysis[12,131] or by magnetron sputtering[68,132]. The optimum doping seems to lie around 20-25 at. % Zn. The highest hole concentration achieved was 3.3 $x10^{19}$ cm^{-3}[68] while the highest mobility reached 3.5 $x10^{1}$.[132] Since both these results have not been achieved within the same films, it remains possible to improve both the hole concentration and their mobility. So far the lowest resistivity achieved is 3.56 Ω.cm.[68] Even though the formation energy required for the substitution of Zn^{2+} on Sn^{4+} site is than with dopant such as Al, Ga or In due to the double holes formed, successful doping can still be achieved through annealing of the films.[46] However, above annealing temperature of 800 °C the films have been found to switch back to n-type conductivity.[68]

Even though p-type conductivity of SnO_2 has been reported, high annealing temperature are generally required to activate the acceptor dopants coupled with high amount of dopant in the lattice. Lany and Zunger[138] studied the formation of p-type defects in ZnO, In_2O_3 and SnO_2 system and found that acceptor dopant (Ga, Al and In in the case of SnO_2) causes the formation of localised holes centred on the oxygen site close to the dopant. While they estimated the acceptor ionisation levels, $\varepsilon_A(0/-1)$, to lie at 0.85, 0.76 and 0.58 eV above the VBM for Al, Ga and In respectively, Scanlon and Watson[15] suggested they might lie deeper in the band gap. They considered Al, Ga, In, Li and N as deep acceptors in SnO_2 while in interstitial they would constitute shallow donors (except for N). Even though the formation energy of the dopant in interstitial position is higher than in substitutional position in oxygen-rich conditions, the Fermi level might still be trapped around mid-gap for the Al, Ga and In dopants. They concluded that under either oxygen-rich or tin-rich conditions it would not be possible to achieve good p-type conductivity. The localisation of holes on the oxygen sites in SnO_2 is not a surprise as the valence band is mostly formed of

O 2p states whose orbitals lie at 6 eV while the valence orbitals of SnO_2 (Sn 4d) lie at 24 eV.[9] The difference in electronegativity is too important and thus to have a chance to obtain p-type conductivity, dopants with valence orbitals lower in energy (closer to the O 2p states) must be considered to reduce the localisation on the oxygen. While Ga $3d^{10}$ and In $4d^{10}$ lie around 20 eV, Zn^{2+} valence orbitals lie lower at 15 eV.[9] Furthermore, even though the formation of Zn_{Sn} acceptor defects requires more energy than with Ga, Al or In, when successfully substituted it allows the generation of two holes in the lattice. On overall p-type conductivity of SnO_2 thin films with acceptor dopants has been achieved. The conductivity achieved does not surpass the Cu-based p-type metal oxide developed so far, however unlike the Cu-based oxides which still requires a reliable n-type counterpart for the formation of p-n homo-junction, highly conductive n-type SnO_2 has already been developed. Furthermore one of the main issues in Cu-based oxides, aside the conductivity improvement, is the low transparency in the visible region due to the low band gap of these oxides. This problem is almost inexistent in SnO_2 p-type thin films since SnO_2 is wide band gap semiconductor to begin with. But the development of p-type conductivity in intrinsic n-type metal oxides remains a challenge as the stability of the holes in the system is questioned through the formation of donor-type defects.

Even though the best results have been achieved through Al and Ga doping for p-type SnO_2 thin films, the interest is brought to the use of Zn as acceptor dopant. Interesting results have been reported[68,12,131,132] but the possible achievement of p-type conductivity must still be questioned. Yet no experimental report focused on the type of environment required for the growth of these films. Singh *et al.*[46] and Pan *et al.*[134] insisted on the importance of the growth conditions and especially Singh *et al.* who suggested the existence of optimum conditions lowering the formation energy of the acceptor defects and at the same time raising the formation energy of donor defects high enough to achieve p-type conductivity. A final parameter which has not been discussed much in the reported studies despite its importance is the position of the Fermi level of the films and the charge neutrality limit (CNL) in SnO_2. The CNL corresponds to the energy at which the character of defects formed changes respectively to the E_F position. Below the CNL, the donor-like character of the defects will be predominant while when E_F lies above it the acceptor-like character of the defects is favoured.[59,139–141] In most semiconductor this limit lies close to the middle of the band gap, however in TCOs such as ZnO, In_2O_3 and SnO_2 the CNL lie close (ZnO) or above the CBM (In_2O_3) and (SnO_2).[139,141,142] The CNL lying above the CBM in SnO_2 can be seen as a consequence of the large size and electronegativity mismatch between the tin and the oxygen atoms.[141] The position of the CNL in the CB of

SnO_2 is one of the reasons n-type doping can be easily achieved while p-type doping is difficult. So far few studies have reported the position of the Fermi level for their p-type thin films developed and most of the studies reporting successful p-type conductivity did not take into account the CNL limitation.

2.5. Use of Zn as dopant

The use of Zn as a dopant grew interest in the 1990s with the introduction of new multicomponent oxides as potential TCOs material. These materials were mainly derived from binary oxides such as ZnO, CdO, In_2O_3 and SnO_2. Some of the new ternary compounds introduced were Zn_2SnO_4[143], $ZnSnO_3$[17], $Zn_2In_2O_5$[144], $MgIn_2O_4$[145], $CbSb_2O_6$:Y[146], $GaInO_3$[147] and $In_4Sn_3O_{12}$[148]. The $ZnSnO_3$ and Zn_2SnO_4 were introduced by Minami *et al.*[17,149] and by Enoki *et al.*[143] showing interesting resistivity as low as 4 $x10^{-3}$ Ω.cm for $ZnSnO_3$. However, as it can be noticed, the introduction of such large amount of Zn (> 30 at.%) induces a phase change from SnO_2 to either $ZnSnO_3$ or Zn_2SnO_4. Since then the research has continued on these ternary oxides but the interest was also brought to the use of Zn in smaller quantities maintaining the phase of the material. In these kinds of study the amount of Zn doping varies between 0 and 30 at.%.[150–152] Even though the amount of doping is high, no sign of other phases than SnO_2 rutile were measured. The $ZnSnO_3$ and $ZnSnO_4$ phases seem to appear above 33 at.%. Based on the valence of Zn(II), with the introduction of Zn^{2+} species in SnO_2 a decrease of the conductivity is expected through the Zn substitution on Sn site and the formation of 2 holes. However some studies revealed an improvement of the electrical conductivity with resistivity down to 2 $x10^{-3}$ Ω.cm for Zn doping between 10-20 at.%.[153–155] The most noticeable change was not in the carrier concentration (about 10^{19}-10^{20} cm^{-3}) but in the stability of the mobility up to 24 $cm^2/(V.s)$ with 11 at.% of Zn in SnO_2. Along the improvement in mobility observed in some cases, the addition of Zn seems to induce a reduction of the crystalline size of the film along with a slight decrease of the band gap.[150,153,156,157] A few results found in literature are highlighted in table 1.3.

The conductivity of the Zn-doped SnO_2 thin films seems to depend on the deposition technique used. Apart from Singh *et al.*[154] who obtained a low resistivity of 8.94 $x10^{-3}$ Ω.cm by spray pyrolysis, the most conductive films seem to arise from sputtering deposition technique.[18][153] With the addition of Zn a change in crystalline growth has also been observed in several studies. The (110) preferred orientation in undoped SnO_2 changes to either the (101) or the (200) orientation as more Zn is added. [150,153,156,157] Even though the (101) orientation has been the most reported with

addition of Zn, it should be noted that both the (101) and (200) are oxygen deficient surfaces. In all reports, the deposition temperature was kept below 500 °C and no post-annealing treatment or further oxidation process was carried. By refereeing to the previous reports on p-type conductivity, it can be observed that the inclusion of Zn in SnO_2 can either compensate the charge carrier and induce p-type conductivity or improve the n-type conductivity of the films function of the deposition parameters.

Table 1. 3: Outlook of the properties of Zn-doped SnO_2 thin films the phase, the dopant concentration, the deposition technique used, the deposition temperature, main growth orientation, resistivity, mobility, carrier (electron) concentration and optical band gap.

Phase	Doping level at. %	Technique	Temperature °C	Main orientation	Resistivity Ω.cm	Mobility $cm^2/(V.s)$	Carriers concentration cm^{-3}	Eg eV	Ref
$ZnSnO_3$	33	Sputtering	300	-	$4x10^{-3}$	10	10^{20}	-	[158]
Zn_2SnO_4	80	Sputtering		-	$1.7x10^{-2}$	-	-	-	[143]
SnO_2	20	Sputtering	250	(101)	$1.12x10^{-2}$	7.02	$1.44x10^{20}$	-	[153]
	15	Sol-gel	450	(110), (101)	-	-	-	3.68	[159]
	8.7	Spray	400	(110), (101), (211)	$8.94x10^{-3}$	5.34	-	4.07	[154]
	16.8	Sol-gel	480	-	$4.35x10^{0}$	-	-	3.69	[151]
	24.3	Spray	400	(200)	-	-	-	3.71	[157]
	10	Spray	350	(200) $+Zn_2SnO_4$	$6.64x10^{3}$	-	-	3.58	[152]
	11	Sputtering	450	Amorphous	$2x10^{-3}$	24	$1x10^{20}$	-	[18]
	12	CVD	300	Amorphous	$1.5\ x10^{-2}$	1.5	$3\ x10^{20}$	3.82	[155]

2.6. Deposition methods

Various deposition techniques have been developed for the fabrication of SnO_2 thin films. The preference of one technique over another depends on the expectations and the conditions set by the user. In the scope of this thesis, the interest is brought upon the control of dopant inclusion and intrinsic defects, with a fine control over the growth environment but still with a reasonable growth rate and good film quality.

Deposition techniques working in atmosphere are generally used for low cost and large area processing. Spray pyrolysis is among the most commonly used for SnO_2.[140] With this technique a soluble salt (tin chloride $SnCl_2$ or $SnCl_4$) is mixed with a solvent (methanol/water) and sprayed onto a heated surface leading to the thermal decomposition of the salt and oxidation into the formation of SnO_2. During the deposition the environment is not controlled, and even though most of the oxygen source comes from the solvent used, the stoichiometry remains difficult to control.[140] Owing to its lower chemical reactivity than Zn in oxidising environment[60], the spraying of SnO_2 leads to non-stoichiometric films with rather low resistivity (about 10^{-3} Ω.cm).[64,160] The large

amount of defects (mainly V_O and Sn_i) through spray pyrolysis deposition accounts for its large use in n-type SnO_2 TCOs, however the lack of control of the amount of donor-type defects and of the environment would be problematic in this study. The same problems apply for other in air-technique such as sol-gel deposition.

To control the growth environment the use of a vacuum system and/or a gas carrier is often required. Four systems are highlighted: chemical vapour deposition (CVD), molecular beam epitaxy (MBE), magnetron sputtering and pulsed laser deposition (PLD). CVD involves the deposition of a thin film on a substrate from a gas phase. The environment is controlled through the use of gas phases for the reaction. The species interact with the heated surface of the substrate and the decomposition product then deposits on the surface. This technique allows the formation of films with low defect density and high chemical purity.[2] The growth rate is tuneable however one of the main issue of the technique is the toxicity of the precursor used.[161] MBE is a technique allowing a very fine control over the growth of single-crystal epitaxial films in high vacuum. The slow evaporation of elements in different crucibles is controlled by fast shutters to control the growth process along with the composition, dopant concentration and thickness.[162] However MBE's operation is complex and the throughput is limited partly due to slower deposition rates to achieve good quality crystals. Magnetron sputtering is widely used for the deposition of large area coating in industry. The sputtering process consists of the bombardment of highly energetic particles (generally ions from an inert gas such as Ar) on a target surface. The ion bombardment leads to the ejection of target species (Sn) towards the substrate, the oxidation of the tin can be controlled through the use of background oxygen gas.[2,140] The inclusion of dopant is controlled either through the background gas or within the target composition. Magnetron sputtering is the most suitable deposition method for the processing of TCO in industry which gathers good environment control and high quality films. Finally PLD, even though it is not a suitable technique for large area applications, is a technique allowing a fine control of the growth and the environment leading to good quality films. The system is composed of a laser (source of energy) focused on a ceramic target, leading to the instant evaporation of the material on the surface of a target and formation of a plasma plume depositing the desired material on the substrate placed parallel to the target. The system is in vacuum and a background gas (oxygen) is used to control the energy of the plasma species and the stoichiometry of the films. The highly energetic plasma plume allows the formation of good quality crystalline thin films even at low temperature and with a high growth rate (> 10 nm/min).[163] Furthermore the doping is controlled through the target

composition as PLD allows a stoichiometric transfer of the cation species due to the non-equilibrium of the process.

PLD technique meets the requirement for a study involving fine control of the growth, doping and the environment. Even though this technique is not suited for industrial applications it remains an excellent tool for the investigation of thin film properties with a broad panel of deposition conditions.

References

[1] R.E. Presley, C.L. Munsee, C.H. Park, D. Hong, J.F. Wager, D.A. Keszler, "Tin oxide transparent thin-film transistors", J. Phys. D. Appl. Phys. 37 (2004) 2810–2813.

[2] G.J. Exarhos, X.-D. Zhou, "Discovery-based design of transparent conducting oxide films", Thin Solid Films. 515 (2007) 7025–7052.

[3] H. Liu, V. Avrutin, N. Izyumskaya, Ü. Özgür, H. Morkoç, "Transparent conducting oxides for electrode applications in light emitting and absorbing devices", Superlattices Microstruct. 48 (2010) 458–484.

[4] S. Sheng, G. Fang, C. Li, S. Xu, X. Zhao, "P-Type Transparent Conducting Oxides", Phys. Status Solidi. 203 (2006) 1891–1900.

[5] E. Elangovan, K. Ramamurthi, "A study on low cost-high conducting fluorine and antimony-doped tin oxide thin films", Appl. Surf. Sci. 249 (2005) 183–196.

[6] H. Kim, R.C.Y. Auyeung, A. Piqué, "Transparent conducting F-doped SnO2 thin films grown by pulsed laser deposition", Thin Solid Films. 516 (2008) 5052–5056.

[7] A.V. Moholkar, S.M. Pawar, K.Y. Rajpure, C.H. Bhosale, J.H. Kim, "Effect of fluorine doping on highly transparent conductive spray deposited nanocrystalline tin oxide thin films", Appl. Surf. Sci. 255 (2009) 9358–9364.

[8] H. Kawazoe, M. Yasukawa, H. Hyodo, M. Kurita, H. Yanagi, H. Hosono, "P-type electrical conduction in transparent thin films of CuAlO2", Nature. 389 (1997) 939–942.

[9] H. Kawazoe, H. Yanagi, K. Ueda, H. Hosono, "Transparent p-Type Conducting Oxides : Design and Fabrication of p-n Heterojunctions", MRS Bull. (2000) 28–36.

[10] S. Sohn, H. Kim, Transparent Conductive Oxide (TCO) Films for Organic Light Emissive Devices (OLEDs), in: S.H. Ko (Ed.), Org. Light Emit. Diode - Mater. Process Devices, InTech, 2011: pp. 233–274.

[11] T. Yang, X. Qin, H. Wang, Q. Jia, R. Yu, B. Wang, et al., "Preparation and application in p–n homojunction diode of p-type transparent conducting Ga-doped SnO2 thin films", Thin Solid Films. 518 (2010) 5542–5545.

[12] K. Ravichandran, K. Thirumurugan, N. Jabena Begum, S. Snega, "Investigation of p-type SnO2:Zn films deposited using a simplified spray pyrolysis technique", Superlattices Microstruct. 60 (2013) 327–335.

[13] M.-M. Bagheri-Mohagheghi, M. Shokooh-Saremi, "The influence of Al doping on the electrical, optical and structural properties of SnO2 transparent conducting films deposited by the spray pyrolysis technique", J. Phys. D. Appl. Phys. 37 (2004) 1248–1253.

[14] Z. Ji, Z. He, Y. Song, K. Liu, Z. Ye, "Fabrication and characterization of indium-doped p-type SnO2 thin films", J. Cryst. Growth. 259 (2003) 282–285.

[15] D.O. Scanlon, G.W. Watson, "On the possibility of p-type SnO2", J. Mater. Chem. 22 (2012) 25236.

[16] Ç. Kılıç, A. Zunger, "Origins of Coexistence of Conductivity and Transparency in SnO2", Phys. Rev. Lett. 88 (2002) 095501.

[17] T. Minami, H. Sonohara, S. Takata, H. Sato, "Highly Transparent and Conductive Zinc Stannate Thin Films Prepared By Rf Magnetron Sputtering", Jpn. J. Appl. Phys. 33 (1994) L1693–L1696.

[18] J.H. Ko, I.H. Kim, D. Kim, K.S. Lee, T.S. Lee, B. Cheong, et al., "Transparent and conducting Zn-Sn-O thin films prepared by combinatorial approach", Appl. Surf. Sci. 253 (2007) 7398–7403.

[19] J.S. Blakemore, The Drude model, in: Solid State Phys. Second Ed., Cambridge university press, 1985: pp. 158–162.

[20] J.S. Blakemore, The quantized free electron theory, in: Solid State Phys. Second Ed., Cambridge university press, 1985: pp. 170–201.

[21] R.E. Hummel, "Electronic Properties of Materials fourth edition", Springer, 2000.

[22] J.S. Blakemore, The band theory of solids, in: Solid State Phys. Second Ed., Cambridge university press, 1985: pp. 202–234.

[23] M. Fox, "Optical Properties of Solids", Oxford university press, 2001.

[24] J.L.G. Fierro, "Metal Oxides chemistry and applications", Taylor & Francis Group, 2006.

[25] K.G. Godinho, A. Walsh, G.W. Watson, "Energetic and Electronic Structure Analysis of Intrinsic Defects in SnO2", J. Physic Chem. C. 113 (2009) 439–448.

[26] F.A. Kröger, "The Chemistry of the Imperfect Crystals", Amsterdam: North Holland, 1974.

[27] F.A. Kröger, H.J. Vink, "Relations between the Concentrations of Imperfections in Crystalline Solids", Solid State Phys. - Adv. Res. Appl. 3 (1956) 307–435.

[28] K. Ellmer, A. Klein, B. Rech, "Transparent Conductive Zinc Oxide: Basics and Applications in Thin Film Solar Cells", 2007.

[29] A. Janotti, C.G. Van de Walle, "Fundamentals of zinc oxide as a semiconductor", Reports Prog. Phys. 72 (2009) 126501.

[30] A.N. Banerjee, K.K. Chattopadhyay, "Recent developments in the emerging field of crystalline p-type transparent conducting oxide thin films", Prog. Cryst. Growth Charact. Mater. 50 (2005) 52–105.

[31] S. Cahen, N. David, J.M. Fiorani, A. Maitre, M. Vilasi, "Thermodynamic modelling of the O-Sn system", Thermochim. Acta. 403 (2003) 275–285.

[32] S. Cahen, N. David, J.M. Fiorani, A. Maitre, M. Vilasi, "Thermodynamic modelling of the)-Sn system", Thermochim. Acta. 403 (2003) 275–285.

[33] M. Batzill, U. Diebold, "The surface and materials science of tin oxide", Prog. Surf. Sci. 79 (2005) 47–154.

[34] J. Robertson, "Disorder and instability processes in amorphous conducting oxides", Phys. Status Solidi. 245 (2008) 1026–1032.

[35] O.N. Mryasov, A.J. Freeman, "Electronic band structure of indium tin oxide and criteria for transparent conducting behavior", Phys. Rev. B. 64 (2001) 233111.

[36] K.L. Chopra, S. Major, D.K. Pandya, "Transparent conductors—A status review", Thin Solid Films. 102 (1983) 1–46.

[37] I. Hamberg, C.G. Granqvist, "Evaporated Sn-doped In2O3 films: Basic optical properties and applications to energy-efficient windows", J. Appl. Phys. 60 (1986) R123.

[38] H. Hartnagel, A.L. Dawar, A.K. Jain, C. Jagadish, "Semiconducting Transparent thin films", IOP Publishing Ltd., Bristol and Philadelphia, 1995.

[39] D.S. Ginley, C. Bright, "Transparent Conducting Oxides", MRS Bull. 25 (2000) 15–18.

[40] B.G. Lewis, D.C. Paine, "Applications and Processing of Transparent Conducting Oxides", MRS Bull. 25 (2000) 22–27.

[41] N. Yamazoe, Y. Kurokawa, T. Seiyama, "Effects of Additives on Semiconductor Gas Sensors", Sensors Actuators B Chem. 4 (1983) 283–289.

[42] H. Agura, A. Suzuki, T. Matsushita, T. Aoki, M. Okuda, "Low resistivity transparent conducting Al-doped ZnO films prepared by pulsed laser deposition", Thin Solid Films. 445 (2003) 263–267.

[43] S.C. Tsang, C.D.A. Bulpitt, P.C.H. Mitchell, A.J. Ramirez-Cuesta, "Some new insights into the sensing mechanism of palladium promoted tin (IV) oxide sensor", J. Phys. Chem. B. 105 (2001) 5737–5742.

[44] P. Agoston, Point defect and surface properties of In2O3 and SnO2: A comparative study by first-principles methods, Technische Universit, 2011. http://tuprints.ulb.tu-darmstadt.de/2781/.

[45] S. Samson, C.G. Fonstad, "Defect structure and electronic donor levels in stannic oxide crystals", J. Appl. Phys. 44 (1973) 4618.

[46] A.K. Singh, A. Janotti, M. Scheffler, C.G. Van de Walle, "Sources of Electrical Conductivity in SnO2", Phys. Rev. Lett. 101 (2008) 055502.

[47] D. Maestre, J. Ramírez-Castellanos, P. Hidalgo, A. Cremades, J.M. González-Calbet, J. Piqueras, "Study of the Defects in Sintered SnO2 by High-Resolution Transmission Electron Microscopy and Cathodoluminescence", Eur. J. Inorg. Chem. 2007 (2007) 1544–1548.

[48] M. Fang, X. Tan, X. Cao, L. Zhang, P. Liu, Z. Jiang, "Impurity induced formation of Sn2+ ions in SnO2 and the photoluminescence property", J. Phys. D. Appl. Phys. 40 (2007) 7648–7651.

[49] H. Iddir, S. Öğüt, P. Zapol, N.D. Browning, "Diffusion mechanisms of native point defects in rutile TiO2 : Ab initio total-energy calculations", Phys. Rev. B. 75 (2007) 073203.

[50] P. Ágoston, C. Körber, A. Klein, M.J. Puska, R.M. Nieminen, K. Albe, "Limits for n-type doping in In2O3 and SnO2: A theoretical approach by first-principles calculations using hybrid-functional methodology", J. Appl. Phys. 108 (2010) 053511.

[51] A. Janotti, C.G. Van de Walle, "Native point defects in ZnO", Phys. Rev. B. 76 (2007) 165202.

[52] A.K. Singh, A. Janotti, M. Scheffler, C.G. Van de Walle, "Sources of Electrical Conductivity in SnO2", Phys. Rev. Lett. 101 (2008) 055502.

[53] J. Prades, J. Arbiol, A. Cirera, J. Morante, M. Avella, L. Zanotti, et al., "Defect study of SnO2 nanostructures by cathodoluminescence analysis: Application to nanowires", Sensors Actuators B Chem. 126 (2007) 6–12.

[54] J. Robertson, "Defect levels of SnO2", Phys. Rev. B. 30 (1984) 3520–3522.

[55] P. Ágoston, K. Albe, R.M. Nieminen, M.J. Puska, "Intrinsic n-Type Behavior in Transparent Conducting Oxides: A Comparative Hybrid-Functional Study of In2O3, SnO2, and ZnO", Phys. Rev. Lett. 103 (2009) 245501.

[56] C.G. Van de Walle, "Hydrogen as a Cause of Doping in Zinc Oxide", Phys. Rev. Lett. 85 (2000) 1012–1015.

[57] D.M. Hofmann, A. Hofstaetter, F. Leiter, H. Zhou, F. Henecker, B.K. Meyer, et al., "Hydrogen: A Relevant Shallow Donor in Zinc Oxide", Phys. Rev. Lett. 88 (2002) 045504.

[58] C. Kılıç, A. Zunger, "N-Type Doping of Oxides By Hydrogen", Appl. Phys. Lett. 81 (2002) 73.

[59] J. Robertson, B. Falabretti, "Handbook of Transparent Conductors", Springer US, Boston, MA, 2011.

[60] T. Minami, "Transparent conducting oxide semiconductors for transparent electrodes", Inst. Phys. Publ. 20 (2005) 35–44.

[61] M. Mwamburi, E. Wäckelgard, A. Roos, "Preparation and Characterisation of Solar Selective SnOx:F Coated Aluminium Reflector Surfaces", Thin Solid Films. 374 (2000) 1–9.

[62] B. Stjerna, E. Olsson, C.G. Granqvist, "Optical and electrical properties of radio frequency sputtered tin oxide films doped with oxygen vacancies, F, Sb, or Mo", J. Appl. Phys. 76 (1994) 3797.

[63] S.W. Lee, Y.-W. Kim, H. Chen, "Electrical properties of Ta-doped SnO2 thin films prepared by the metal–organic chemical-vapor deposition method", Appl. Phys. Lett. 78 (2001) 350.

[64] C. Agashe, S.S. Major, "Effect of F, Cl and Br doping on electrical properties of sprayed SnO2 films", J. Mater. Sci. Lett. 15 (1996) 497–499.

[65] M.-M. Bagheri-Mohagheghi, M. Shokooh-Saremi, "Electrical, optical and structural properties of Li-doped SnO 2 transparent conducting films deposited by the spray pyrolysis technique: a carrier-type conversion study", Semicond. Sci. Technol. 19 (2004) 764–769.

[66] S.S. Pan, S. Wang, Y.X. Zhang, Y.Y. Luo, F.Y. Kong, S.C. Xu, et al., "p-type conduction in nitrogen-doped SnO2 films grown by thermal processing of tin nitride films", Appl. Phys. A. 109 (2012) 267–271.

[67] J.M. Wu, "A room temperature ethanol sensor made from p-type Sb-doped SnO2 nanowires", Nanotechnology. 21 (2010) 235501.

[68] J.M. Ni, X.J. Zhao, J. Zhao, "Structural, Electrical and Optical Properties of p-Type Transparent Conducting SnO2:Zn Film", J. Inorg. Organomet. Polym. Mater. 22 (2011) 21–26.

[69] D.H. Zhang, H.L. Ma, "Scattering mechanisms of charge carriers in transparent conducting oxide films", Appl. Phys. A Mater. Sci. Process. 62 (1996) 487–492.

[70] N. Tsuda, K. Nasu, A. Yanase, K. Siratori, "Electronic Conduction in Oxides", Springer Berlin Heidelberg, 1991.

[71] K. Ellmer, R. Mientus, "Carrier transport in polycrystalline transparent conductive oxides: A comparative study of zinc oxide and indium oxide", Thin Solid Films. 516 (2008) 4620–4627.

[72] J.R. Bellingham, W.A. Phillips, "Intrinsic performance limits in transparent conducting oxides", J. Mater. Sci. Lett. 11 (1992) 263–265.

[73] J.S. Blakemore, "Solid State Physics second edition", Cambridge university press, 1985.

[74] T. Minami, "New n-Type Transparent Conducting Oxides", MRS Bull. 25 (2000) 38–

44.

[75] K. Ellmer, R. Mientus, "Carrier transport in polycrystalline transparent conductive oxides: A comparative study of zinc oxide and indium oxide", Thin Solid Films. 516 (2008) 4620–4627.

[76] J.Y.W. Seto, "The electrical properties of polycrystalline silicon films", J. Appl. Phys. 46 (1975) 5247.

[77] H. Hosono, "Recent progress in transparent oxide semiconductors: Materials and device application", Thin Solid Films. 515 (2007) 6000–6014.

[78] S. Ishibashi, "Low resistivity indium–tin oxide transparent conductive films. II. Effect of sputtering voltage on electrical property of films", J. Vac. Sci. Technol. A Vacuum, Surfaces, Film. 8 (1990) 1403.

[79] H.M. Yates, P. Evans, D.W. Sheel, S. Nicolay, L. Ding, C. Ballif, "High-performance tandem silicon solar cells on F:SnO2", Surf. Coatings Technol. 230 (2013) 228–233.

[80] H.M. Yates, P. Evans, D.W. Sheel, S. Nicolay, L. Ding, C. Ballif, "The development of high performance SnO2:F as TCOs for thin film silicon solar cells", Surf. Coatings Technol. 213 (2012) 167–174.

[81] H. Hosono, M. Yasukawa, H. Kawazoe, "Novel oxide amorphous semiconductors: transparent conducting amorphous oxides", J. Non. Cryst. Solids. 203 (1996) 334–344.

[82] K. Shimakawa, S. Narushima, H. Hosono, H. Kawazoe, "Electronic transport in degenerate amorphous oxide semiconductors", Philos. Mag. Lett. 9 (1999) 755–762.

[83] H. Ohta, K. Kawamura, M. Orita, M. Hirano, "Current injection emission from a transparent p-n junction composed of p-SrCu2O2/n-ZnO", Appl. Phys. Lett. 77 (2000) 475–477.

[84] V. Lantto, T.T. Rantala, T.S. Rantala, "Atomistic understanding of semiconductor gas sensors", J. Eur. Ceram. Soc. 21 (2001) 1961–1965.

[85] C.S. Ferekides, R. Mamazza, U. Balasubramanian, D.L. Morel, "Transparent conductors and buffer layers for CdTe solar cells", Thin Solid Films. 480-481 (2005) 224–229.

[86] V. Krishnakumar, A. Barati, H.J. Schimper, A. Klein, W. Jaegermann, "A possible way to reduce absorber layer thickness in thin film CdTe solar cells", Thin Solid Films. 535 (2013) 233–236.

[87] B. a. Korevaar, a. Halverson, J. Cao, J. Choi, C. Collazo-Davila, W. Huber, "High efficiency CdTe cells using manufacturable window layers and CdTe thickness", Thin Solid Films. 535 (2013) 229–232.

[88] Z. Fang, X.C. Wang, H.C. Wu, C.Z. Zhao, "Achievements and challenges of CdS/CdTe solar cells", Int. J. Photoenergy. 2011 (2011) 8.

[89] O. Vigil-Galán, D. Jiménez-Olarte, G. Contreras-Puente, M. Courel, "SnO2 buffer layer deposition for thin film solar cells with superstrate configuration", J. Renew. Sustain. Energy. 7 (2015) 013115.

[90] H. Sato, T. Minami, S. Takata, T. Yamada, "Transparent conducting p-type NiO thin films prepared by magnetron sputtering", Thin Solid Films. 236 (1993) 27–31.

[91] R. Nagarajan, A.D. Draeseke, A.W. Sleight, J. Tate, "p-type conductivity in CuCr(1−x)MgbxO2 films and powders", J. Appl. Phys. 89 (2001) 8022.

[92] R. Nagarajan, N. Duan, M.K. Jayaraj, J. Li, K.A. Vanaja, A. Yokochi, et al., "p-Type conductivity in the delafossite structure", Int. J. Inorg. Mater. 3 (2001) 265–270.

[93] H. Hiramatsu, K. Ueda, H. Ohta, M. Hirano, T. Kamiya, H. Hosono, "Degenerate p-type conductivity in wide-gap LaCuOS(1-x)Se(x) (x=0-1) epitaxial films", Appl. Phys. Lett. 82 (2003) 1048–1050.

[94] F.A. Benko, F.P. Koffyberg, "Opto-Electronic Properties of CuAlO2", J. Phys. Chem. Solids. 45 (1984) 57–59.

[95] A. Kudo, H. Yanagi, H. Hosono, H. Kawazoe, "SrCu2O2: A p-type conductive oxide with wide band gap", Appl. Phys. Lett. 73 (1998) 220.

[96] T. Minami, K. Shimokawa, T. Miyata, "P-type transparent conducting In2O3-Ag2O thin films prepared by rf magnetron sputtering", J. Vac. Sci. Technol. A Vacuum, Surfaces Film. 16 (1998) 1218–1221.

[97] M. Joseph, H. Tabata, T. Kawai, "p-Type electrical conduction in ZnO thin films by Ga and N codoping", Japanese J. Appl. Physics, Part 2 Lett. 38 (1999) 1205–1207.

[98] C.F. Windisch, K.F. Ferris, G.J. Exarhos, "Synthesis and characterization of transparent conducting oxide cobalt–nickel spinel films", J. Vac. Sci. Technol. A Vacuum, Surfaces, Film. 19 (2001) 1647.

[99] K. Ueda, T. Hase, H. Yanagi, H. Kawazoe, H. Hosono, H. Ohta, et al., "Epitaxial growth of transparent p-type conducting CuGaO2 thin films on sapphire (001) substrates by pulsed laser deposition", J. Appl. Phys. 89 (2001) 1790.

[100] H. Yanagi, T. Hase, S. Ibuki, K. Ueda, H. Hosono, "Bipolarity in electrical conduction of transparent oxide semiconductor CuInO2 with delafossite structure", Appl. Phys. Lett. 78 (2001) 1583.

[101] J. Tate, M.K. Jayaraj, A.D. Draeseke, T. Ulbrich, A.W. Sleight, K.A. Vanaja, et al., "p-Type oxides for use in transparent diodes", Thin Solid Films. 411 (2002) 119–124.

[102] T. Aoki, Y. Shimizu, a. Miyake, a. Nakamura, Y. Nakanishi, Y. Hatanaka, "p-type ZnO layer formation by excimer laser doping", Phys. Status Solidi Basic Res. 229 (2002) 911–914.

[103] C. Morhain, M. Teisseire, S. Vézian, F. Vigué, F. Raymond, P. Lorenzini, et al., "Spectroscopy of Excitons, Bound Excitons and Impurities in h-ZnO Epilayers", Phys. Status Solidi B. 229 (2002) 881–885.

[104] A. Tsukazaki, A. Ohtomo, T. Onuma, M. Ohtani, T. Makino, M. Sumiya, et al., "Repeated temperature modulation epitaxy for p-type doping and light-emitting diode based on ZnO", Nat. Mater. 4 (2004) 42–46.

[105] T. Kamiya, K. Ueda, H. Hiramatsu, H. Kamioka, H. Ohta, M. Hirano, et al., "Two-dimensional electronic structure and multiple excitonic states in layered oxychalcogenide semiconductors, LaCuOCh (Ch=S, Se, Te): Optical properties and relativistic ab initio study", Thin Solid Films. 486 (2005) 98–103.

[106] J.G. Lu, Y.Z. Zhang, Z.Z. Ye, Y.J. Zeng, H.P. He, L.P. Zhu, et al., "Control of p- and n-type conductivities in Li-doped ZnO thin films", Appl. Phys. Lett. 89 (2006) 87–90.

[107] Z. Gen, P. Wu, H. Gong, "Control of p- and n-type conductivities in P-doped ZnO thin films by using radio-frquency sputtering", Appl. Phys. Lett. 88 (2006) 1–3.

[108] C. Yuen, S.F. Yu, E.S.P. Leong, S.P. Lau, K. Pita, H.Y. Yang, et al., "Room temperature deposition of p -type arsenic doped ZnO polycrystalline films by laser-assist filtered cathodic vacuum arc technique", J. Appl. Phys. 101 (2007) 1–7.

[109] W. Guo, A.Allenic, Y.B. Chen, X.Q. Pan, Y. Che, Z.D. Hu, et al., "Microstructure and properties of epitaxial antimony-doped p-type ZnO films fabricated by pulsed laser deposition", Appl. Phys. Lett. 90 (2007) 1–3.

[110] R. Manoj, M. Nisha, K.A. Vanaja, M.K. Jayaraj, "Effect of oxygen intercalation on properties of sputtered CuYO2 for potential use as p-type transparent conducting films", Bull. Mater. Sci. 31 (2008) 49–53.

[111] J.C. Fan, C.Y. Zhu, S. Fung, Y.C. Zhong, K.S. Wong, Z. Xie, et al., "Arsenic doped p-type zinc oxide films grown by radio frequency magnetron sputtering", J. Appl. Phys. 106 (2009) 073709.

[112] B.L. Stevens, C.A. Hoel, C. Swanborg, Y. Tang, C. Zhou, M. Grayson, et al., "DC reactive magnetron sputtering, annealing, and characterization of CuAlO2 thin films", J. Vac. Sci. Technol. A Vacuum, Surfaces, Film. 29 (2011) 011018.

[113] C. Ruttanapun, W. Prachamon, A. Wichainchai, "Optoelectronic properties of Cu1-xPtxFeO2 (0<x<0.05) delafossite for p-type transparent conducting oxide", Curr. Appl. Phys. 12 (2012) 166–170.

[114] A. Barnabé, Y. Thimont, M. Lalanne, L. Presmanes, P. Tailhades, "p-type conducting transparent characteristics of delafossite Mg-doped CuCrO2 thin films preparation by RF-sputtering.", J. Mater. Chem. C. (2015) 6012–6024.

[115] O. Maksimov, "Recent Advances and Novel Approaches of P-Type Doping of Zinc Oxide", Rev. Adv. Mater. Sci. 24 (2010) 26–34.

[116] W.-J. Lee, J. Kang, K.J. Chang, "p-Type Doping and Compensation in ZnO", J. Korean Phys. Soc. 53 (2008) 196–201.

[117] G. Brauer, J. Kuriplach, C.C. Ling, A.B. Djurišić, "Activities towards p-type doping of ZnO", J. Phys. Conf. Ser. 265 (2011) 012002.

[118] T. Aoki, Y. Shimizu, A. Miyake, A. Nakamura, Y. Nakanishi, Y. Hatanaka, "p-type ZnO layer formation by excimer laser doping", Phys. Status Solidi Basic Res. 229 (2002) 911–914.

[119] C. Morhain, M. Teisseire, S. Vézian, F. Vigué, F. Raymond, P. Lorenzini, et al., "Spectroscopy of Excitons, Bound Excitons and Impurities in h-ZnO Epilayers", Phys. Status Solidi B. 229 (2002) 881–885.

[120] D.P. Joseph, P. Renugambal, M. Saravanan, S.P. Raja, C. Venkateswaran, "Effect of Li doping on the structural, optical and electrical properties of spray deposited SnO2 thin films", Thin Solid Films. 517 (2009) 6129–6136.

[121] A. Chaparadza, S.B. Rananavare, "Towards p-type conductivity in SnO2 nanocrystals through Li doping.", Nanotechnology. 21 (2010) 035708.

[122] S.F. Ahmed, S. Khan, P.K. Ghosh, M.K. Mitra, K.K. Chattopadhyay, "Effect of Al doping on the conductivity type inversion and electro-optical properties of SnO2 thin films synthesized by sol-gel technique", J. Sol-Gel Sci. Technol. 39 (2006) 241–247.

[123] J. Zhao, X.J. Zhao, J.M. Ni, H.Z. Tao, "Structural, electrical and optical properties of p-type transparent conducting SnO2:Al film derived from thermal diffusion of Al/SnO2/Al multilayer thin films", Acta Mater. 58 (2010) 6243–6248.

[124] F. Finanda, H.C. Ma, H.Y. Lee, "Characteristics of p-type gallium tin oxide (GTO) thin films prepared by RF magnetron sputtering", Ceram. Progress. Res. 13 (2012) 181–185.

[125] Y. Huang, Z. Ji, C. Chen, "Preparation and characterization of p-type transparent

conducting tin-gallium oxide films", Appl. Surf. Sci. 253 (2007) 4819–4822.

[126] C.-Y. Tsay, S.-C. Liang, "Fabrication of p-type conductivity in SnO2 thin films through Ga doping", J. Alloys Compd. 622 (2015) 644–650.

[127] Z. Ji, L. Zhao, Z. He, Q. Zhou, C. Chen, "Transparent p-type conducting indium-doped SnO2 thin films deposited by spray pyrolysis", Mater. Lett. 60 (2006) 1387–1389.

[128] S.S. Pan, G.H. Li, L.B. Wang, Y.D. Shen, Y. Wang, T. Mei, et al., "Atomic nitrogen doping and p-type conduction in SnO2", Appl. Phys. Lett. 95 (2009) 222112.

[129] J. Ni, X. Zhao, X. Zheng, J. Zhao, B. Liu, "Electrical, structural, photoluminescence and optical properties of p-type conducting, antimony-doped SnO2 thin films", Acta Mater. 57 (2009) 278–285.

[130] S. Yu, W. Zhang, L. Li, D. Xu, H. Dong, Y. Jin, "Fabrication of p-type SnO2 films via pulsed laser deposition method by using Sb as dopant", Appl. Surf. Sci. 286 (2013) 417–420.

[131] K. Thirumurugan, K. Ravichandran, "Role of solvent volume on the structural and transparent conducting properties of SnO2:Zn films", J. Mater. Sci. Mater. Electron. 25 (2014) 3594–3600.

[132] J. Ni, X. Zhao, J. Zhao, "P-type transparent conducting SnO2:Zn film derived from thermal diffusion of Zn/SnO2/Zn multilayer thin films", Surf. Coatings Technol. 206 (2012) 4356–4361.

[133] Y.S. Liu, C.I. Hsieh, Y.J. Wu, Y.S. Wei, P.M. Lee, C.Y. Liu, "Transparent p-type AlN:SnO2 and p-AlN:SnO2/n-SnO2:In2O3 p-n junction fabrication", Appl. Phys. Lett. 101 (2012) 122107.

[134] S.S. Pan, G.H. Li, "Recent Progress in p-Type Doping and Optical Properties of SnO2 Nanostructures for Optoelectronic Device Applications", Recent Pat. Nanotechnol. 5 (2011) 138–161.

[135] Q. Mao, Z. Ji, L. Zhao, "Mobility enhancement of p-type SnO2 by In-Ga co-doping", Phys. Status Solidi. 247 (2010) 299–302.

[136] X. Pei, D. Ji, J. Ma, T. Ning, Z. Song, Y. Tan, et al., "Structural and Photoluminescence Properties of SnO2:Ga Films Deposited on α-Al2O3 (0001) by MOCVD", J. Lumin. 130 (2010) 1189–1193.

[137] E.-C. Lee, Y.-S. Kim, Y.-G. Jin, K.J. Chang, "Compensation mechanism for N acceptors in ZnO", Phys. Rev. B. 64 (2001) 085120.

[138] S. Lany, A. Zunger, "Polaronic hole localization and multiple hole binding of acceptors in oxide wide-gap semiconductors", Phys. Rev. B - Condens. Matter Mater. Phys. 80 (2009) 085202.

[139] S.K. Vasheghani Farahani, T.D. Veal, J.J. Mudd, D.O. Scanlon, G.W. Watson, O. Bierwagen, et al., "Valence-band density of states and surface electron accumulation in epitaxial SnO2 films", Phys. Rev. B. 90 (2014) 155413.

[140] D.S. Ginley, H. Hosono, D.C. Paine, eds., "Handbook of Transparent Conductors", Springer, 2011.

[141] P.D.C. King, T.D. Veal, P.H. Jefferson, J. Zúñiga-Pérez, V. Muñoz-Sanjosé, C.F. McConville, "Unification of the electrical behavior of defects, impurities, and surface states in semiconductors: Virtual gap states in CdO", Phys. Rev. B. 79 (2009) 035203.

[142] B. Falabretti, J. Robertson, "Electronic structures and doping of SnO2, CuAlO2, and CuInO2", J. Appl. Phys. 102 (2007) 123703.

[143] H. Enoki, T. Nakayama, J. Echigoya, "The Electrical and Optical Properties of the ZnO-SnO2 Thin Films Prepared by RF Magnetron Sputtering", Phys. Stat. Sol. 129 (1992) 181.

[144] T. Minami, H. Sonohara, T. Kakumu, S. Takata, "Highly Transparent and Conductive Zn2In2O5 Thin Films Prepared by RF Magnetron Sputtering", Jpn. J. Appl. Phys. 34 (1995) L971–L974.

[145] H. Un'no, N. Hikuma, T. Omata, N. Ueda, T. Hashimoto, H. Kawazoe, "Preparation of MgIn2O4- X Thin Films on Glass Substrate by RF Sputtering", Jpn. J. Appl. Phys. 32 (1993) L1260–L1262.

[146] K. Yanagawa, Y. Ohki, T. Omata, H. Hosono, N. Ueda, H. Kawazoe, "Preparation of Cd1-xYxSb2O6 thin film on glass substrate by radio frequency sputtering", Appl. Phys. Lett. 65 (1994) 406–408.

[147] J.M. Phillips, J. Kwo, G.A. Thomas, S.A. Carter, R.J. Cava, S.Y. Hou, et al., "Transparent conducting thin films of GaInO3", Appl. Phys. Lett. 65 (1994) 115–117.

[148] T. Minami, Y. Takeda, S. Takata, T. Kakumu, "Preparation of transparent conducting In4Sn3O12 thin films by DC magnetron sputtering", Thin Solid Films. 309 (1997) 13–18.

[149] T. Minami, "Transparent and conductive multicomponent oxide films prepared by magnetron sputtering", J. Vac. Sci. Technol. A Vacuum, Surfaces, Film. 17 (1999) 1765.

[150] A. Tripathi, R.K. Shukla, "Blue shift in optical band gap of sol–gel derived Sn1−xZnxO2 polycrystalline thin films", J. Mater. Sci. Mater. Electron. 24 (2013) 4014–4022.

[151] J.S. Bhat, K.I. Maddani, A.M. Karguppikar, "Influence of Zn doping on electrical and optical properties of multilayered tin oxide thin films", Bull. Mater. Sci. 29 (2006) 331–337.

[152] V. Bilgin, S. Kose, F. Atay, I. Akyuz, "The effect of Zn concentration on some physical properties of tin oxide films obtained by ultrasonic spray pyrolysis", Mater. Lett. 58 (2004) 3686–3693.

[153] J. Zhao, J. Ni, X. Zhao, Y. Xiong, "Preparation and characterization of transparent conductive zinc doped tin oxide thin films prepared by radio-frequency magnetron sputtering", J. Wuhan Univ. Technol. Sci. Ed. 26 (2011) 388–392.

[154] R. Singh, M. Kumar, S. Shankar, R. Singh, A.K. Ghosh, O.P. Thakur, et al., "Effects of Sb, Zn doping on structural, electrical and optical properties of SnO2 thin films", Mater. Sci. Semicond. Process. 31 (2015) 310–314.

[155] Y. Jiang, W. Sun, B. Xu, M. Yan, N. Bahlawane, "Unusual enhancement in electrical conductivity of tin oxide thin films with zinc doping.", Phys. Chem. Chem. Phys. 13 (2011) 5760–5763.

[156] S. Tian, Y. Gao, D. Zeng, C. Xie, "Effect of Zinc Doping on Microstructures and Gas-Sensing Properties of SnO2 Nanocrystals", J. Am. Ceram. Soc. 95 (2012) 436–442.

[157] S. Vijayalakshmi, S. Venkataraj, M. Subramanian, R. Jayavel, "Physical properties of zinc doped tin oxide films prepared by spray pyrolysis technique", J. Phys. D. Appl. Phys. 41 (2008) 035505.

[158] T. Minami, S. Takata, H. Sato, H. Sonohara, "Properties of transparent zinc-stannate conducting films prepared by radio frequency magnetron sputtering", J. Vac. Sci. Technol. A. 13 (1995) 1095.

[159] A. Tripathi, R.K. Shukla, "Blue shift in optical band gap of sol–gel derived Sn1−xZnxO2 polycrystalline thin films", J. Mater. Sci. Mater. Electron. 24 (2013) 4014–4022.

[160] M.G. Takwale, V.G. Bhide, "Correlation between the structural and electrical transport properties of Sn02 films", J. Mater. Sci. 24 (1989) 2628–2636.

[161] K. Choy, "Chemical vapour deposition of coatings", Prog. Mater. Sci. 48 (2003) 57–170.

[162] K. Seshan, "Handbook of Thin-Film Deposition Processes and Techniques", 2002.

[163] R. Eason, "Pulsed Laser Deposition of Thin Films: Applications-Led Growth of Functional Materials", John Wiley & sons, 2006.

Chapter 2: Experimental

1. Deposition technique: Pulsed laser deposition (PLD)

Lasers have been used as an energy source for evaporative film growth since their discovery. The first PLD experiments were carried out by Smith and Turner in 1965[1] and Hass and Ramsey in 1969[2] where they experimented the preparation of semiconductors and dielectric films. However it was only in the late 1980s that PLD became more investigated with the work of Dijkkamp *et al.*[3] on high-temperature superconductors. Their research showed stoichiometric cation transfer from the target to the substrate, high deposition rates (0.1 nm per pulse) and the presence of droplets on the substrate surface. The development of PLD has continued over the past 20 years and it is now a refined technique for thin-film deposition research. Nowadays, PLD is used in the deposition of insulators, metals, semiconductors, polymers and biological materials.[4] PLD is now established as a reliable method for the deposition of highly crystalline thin film with controlled cation stoichiometry.

1.1. Principle of PLD

PLD is a vacuum deposition technique using laser as a source of energy. Unlike sputtering the source of energy is placed outside the vacuum chamber, making it easier to manage. The setup is described schematically on Figure 2.1 and 2.2.

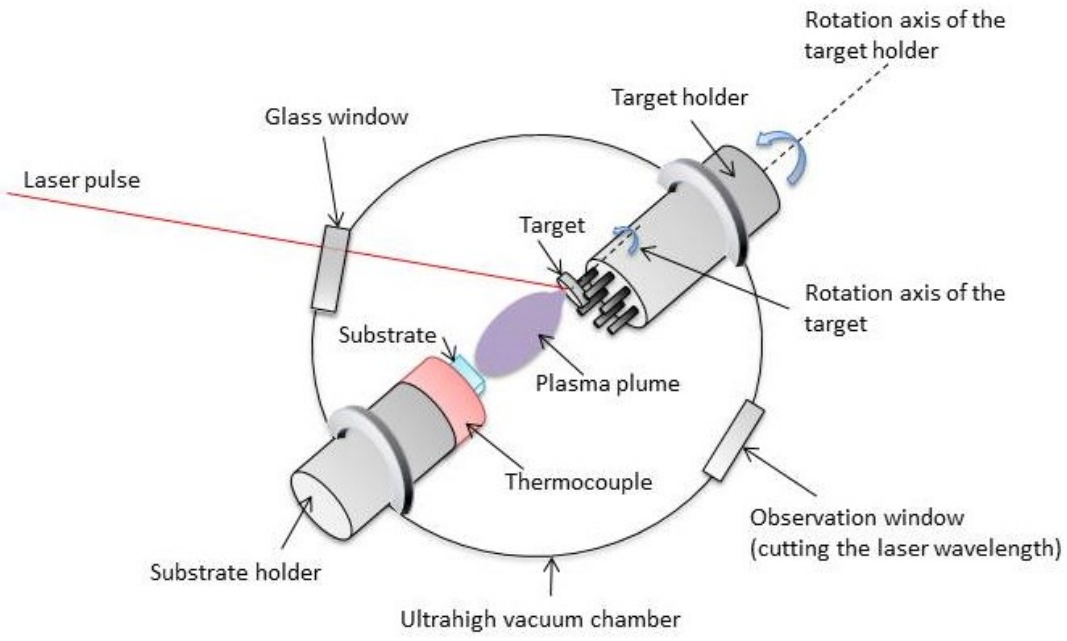

Figure 2. 1: Schematic of a Pulsed Laser Deposition system

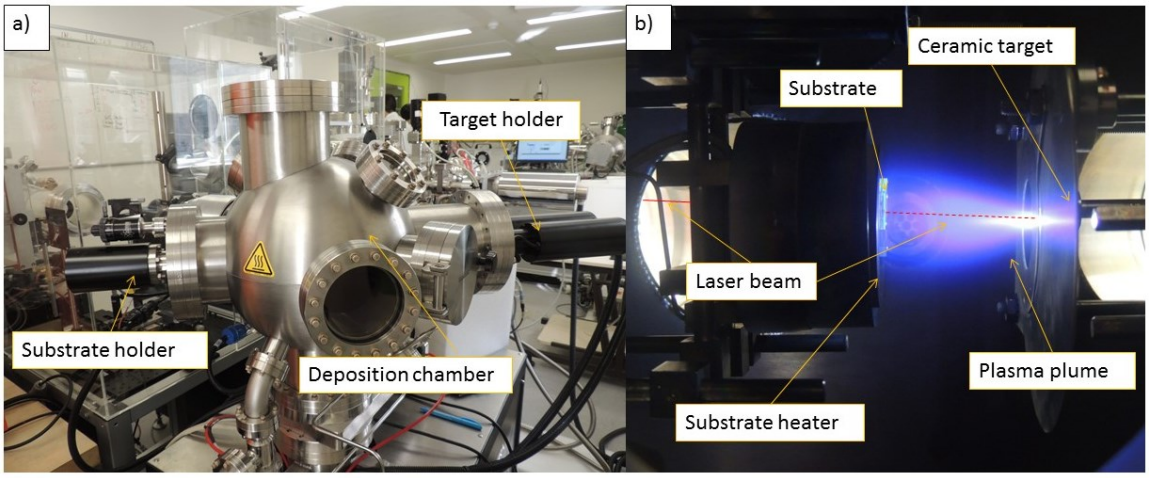

Figure 2. 2: Photograph showing the major components of a) the PLD growth system and b) the inside of the PLD chamber during operation.

The laser is oriented inside the vacuum chamber using optics and a window transparent to the laser wavelength. The deposition process can be described in three steps; ablation, plume expansion and condensation.

i. Ablation

The high energy laser is focused on a narrow spot (around 1-20 mm^2) of the rotating target. The target is placed so that it is struck at an angle of 45° by the pulsed and focused laser beam. Incident photons are absorbed by the material close to the surface.[5] The penetration depth varies with the optical properties of the material and the wavelength of the laser. In the case of non-metals (in the context of this thesis metal oxides), the energy absorbed is transferred to the surrounding material leading to a localized heating and thus causes the surface to melt and evaporate with subsequent emission of ions, neutral atoms molecules and electrons. Because of the non-equilibrium nature of the ablation process the cation stoichiometry of the target is preserved in the deposited films which constitutes one of the main advantages of the PLD.[4] In order to avoid local overheating and melting of the target, the target is rotated and the pulse length is kept short (< 20 ns) as the temperature generated would exceed the melting point of many materials, *i.e.* SnO_2, T_m = 1630 °C.

ii. Plume expansion

Since the ablation process occurs on a shorter time scale than the pulse duration (the energy relaxation time is on the order of 10^{-12} s[6], compared to the 10^{-9} s of the pulse), the

laser continues to interact with the evaporated material and ionises it. The formation of ionised gas particles leads to the formation of a plasma plume which expands away from the target. Laser radiation is also absorbed by the plasma by inelastic free electron scattering leading to increased heating and expansion of the plasma. Due to atom collisions in the plasma and atom ions at the surface of the target the plasma emits lights by Bremsstrahlung radiation which explains the luminous shape escaping from the target. The plasma plume is highly-directional (the thickness distribution from a stationary plume is quite non-uniform) and can interact with a background gas (if present) which would react with and slow down the plume.[4]

iii. Condensation

During this final step, the highly energetic species condense on a substrate placed on a heater, parallel to the target and at a few centimetres (2-10 cm). The nature of the growth depends on the surface energies between the film and the substrate. The growth at the surface of the substrate is explained by an organisation which tends to decrease the surface free energy. The film will grow in the orientation leading to a minimum of the surface free energy.[4] The quality of the crystallinity increases when the temperature increases. A lot of thin film deposition techniques require the use of high substrate temperature in order to increase the diffusion of the deposited particles and thus improve the crystallinity. However PLD technique offers good quality of crystallinity even at low deposition temperatures.[7,8] This is due to the high kinetic energy of the species; the surface mobility of the species is enhanced enabling the growth of crystalline films.

1.2. Effect of deposition parameters

During the growth of metal oxides such as SnO_2 some parameters play an important role and have to be carefully considered. Those are; the target, laser wavelength, laser repetition rate, laser energy density, background gas, target-substrate distance and substrate temperature.

1.2.1. Target

In order to reduce the risks of particulate inclusion in the deposited films the density of the target used should be higher than 90 %.[9] The target is generally made of a powder mix of the desired components which is then pressed as a pellet and sintered at high temperature. The stoichiometry of the target often represents the stoichiometry of the film. Due to the difficulty in the sintering process of SnO_2, additives such as Zn can be added to improve the densification process.[10,11] (described in Appendix 1) Because of

the stoichiometric transfer of cations from target to film a single phase target is not necessarily required to obtain a single phase thin film. This main advantage facilitates the preparation of doped films by PLD through the easy doping control during the target preparation.

After being exposed to multiple laser ablations, changes in the target surface stoichiometry are possible. Claeyssens *et al.*[12] observed that post-ablated ZnO target surface shows enrichment in Zn due to material backscattering from the plasma plume and recondensation on the target. The less volatile component gets recondensed first. In this case Zn, leading to a Zn:O ratio greater than unity. This phenomenon causes the stoichiometry of the films to change as the target is more exposed to the laser thus causing the films to be more metal-rich. In order to maintain the stoichiometry the target can be polished regularly or another solution is to compensate the metal-rich environment by increasing the amount of oxygen background gas in the chamber.

1.2.2. Laser wavelength

An efficient ablation requires a non-equilibrium excitation of the volume at temperature much higher than the evaporation temperature of the material. To do so, the laser pulse has generally a short duration, is high in energy density and highly absorbed by the material. If the energy delivered by the laser is not high enough, it will result in a volume heating and the formation of a liquid pool that lasts for hundreds of nanoseconds. Due to this it is possible that the subsurface volume will boil, which will cause the ejection of micrometre-sized droplets. The optical absorption coefficient is essential in the surface boiling effect. If this coefficient is too low (material specific), the energy delivered by the laser will not be enough to vaporize the material which will result in a heating process. Even by using low wavelength laser, the formation of liquid droplets cannot be completely avoided. To limit this boiling effect and to have a vaporization of the material, the energy delivered by laser has to be larger than the band gap of the target material. This effect can also be reduced by using highly dense ablation target.[5,13,14]

1.2.3. Repetition rate

In PLD laser pulses are used in order to minimize the dissipation of the laser energy beyond the volume of the ablated surface of the target. This helps to avoid the destruction of the target and phase segregation.[15]

1.2.4. Laser energy density or fluence

At low fluence or low absorption at the laser wavelength, the target is only heated by the laser and the ejected flux of material comes from the thermal evaporation of the target species. As the fluence increases, an ablation threshold appears when the laser energy absorption is higher than the energy needed for evaporation. This ablation threshold depends on the absorption coefficient of the material and on the wavelength used. When the fluence exceeds the ablation threshold, the laser beam is absorbed by the ablated species which results in the formation of a plasma (the plume). However if the laser fluence is too high, the film is degraded due to the bombardment of high energetic species and the presence of ejected droplets can also be observed on the film due to the formation of liquid pool on the surface of the target.[4]

1.2.5. Background gas

In PLD, a background gas is generally used for two main reasons. The first one is the formation of thin-film materials that requires reactive species (*e.g.* oxygen for oxides). The stoichiometry of the films plays an important role in their physical properties. As seen in the previous sections, the conductivity of metal oxide thin films is influenced by the oxygen vacancy concentration. The background gas pressure can be controlled over a wide range of pressures and thus, when using oxygen for metal oxide deposition, the conductivity of the film can be controlled through the oxygen incorporation during the film deposition. It is also possible to include a cooling-down step after the high-temperature deposition by putting a high oxygen pressure in order to incorporate more oxygen in the film.[4] The second role of the background gas is to reduce the kinetic energy of the ablated species which are typically on the order of several hundred electron volts. The background gas allows moderating the plume energy to much less than 1 eV. The vapour formed by laser ablation compresses the surrounding background gas. Interaction with the ambient gas slows the plume expansion.[16]

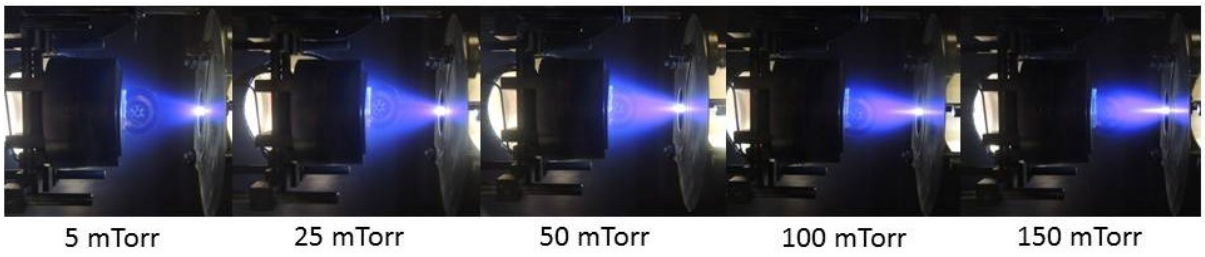

Figure 2. 3: Photographs of the plasma plume taken during the deposition at different oxygen pressure.

Figure 2.3 shows the effect of the background gas pressure on the plasma plume. As the oxygen pressure increases, the shape of the plume becomes narrower and is more focused towards its centre.

1.2.6. Target-substrate distance

The distance between target and substrate defines the optimal deposition of the film. If we consider the particulate-gas collisions, the effects of the background pressure and target-substrate distances are related. When the background gas pressure increases, the plume dimensions decrease due to the increase of interactions, see Figure 2.3. Kwok *et al.*[17] found a relation linking the pressure P, the target-surface distance d and a positive exponent function of the material γ,

Equation 2.1 $$P * d^{\gamma} = constant$$

1.2.7. Substrate temperature

The nucleation process changes with the surface energies between the substrate and the condensed species, but it is also greatly dependant on the substrate temperature. The energy from the substrate temperature helps the organisation and diffusion of the atoms on the surface of the substrate and thus increases the crystallinity of the film. Due to the presence of highly energetic species, PLD allows the growth of crystalline films at low temperature. However, when the oxygen pressure (P_D) is increased, the incident particles are slowed down which decrease their kinetic energy and thus a higher substrate temperature is required to obtain crystalline films. The substrate temperature depends on the desired material and on the crystallinity, however if the deposition is performed at too elevated temperatures there is a possibility that the films particles re-evaporate from the surface. [4]

1.3. Issues and practical considerations

Despite the advantages offered by PLD the system presents significant issues, the challenge of large area deposition. Since the plume is highly directional, the uniformity of the deposition is only possible over around 4 cm^2. Uniform deposition have been performed on 20 cm diameter substrates, however as the size of the substrate increases, higher laser power is required to only achieve average film growth rates.[4] Another problem occurring with PLD is the presence of droplet on the film due to localised melting of the target. These particles can be up to 1 μm large which can be critical in many thin films applications. Also the fundamental process of PLD is not fully understood due to the strong non-equilibrium, the modelling of this process is difficult.

1.4. Summary and system used

PLD is a very precise deposition technique with a simple setup for film formation. The advantages of this technique includes the stoichiometric transfer from the target to the film, the possibility to deposit under a wide range of oxygen pressure and thus to control the electrical conductivity, a high deposition rate and a good control of doping (preparation of the target) and film growth. PLD is not a technique suited for industrial application. However, because of its precise control over the dopant incorporation in the metal oxide lattice and on the film growth, it is a perfect tool to study the deposition, doping and the properties of tin oxide thin films.

In this work a KrF excimer laser was used as the external source of energy. The laser beam was oriented in the vacuum chamber through a system of lenses. The specifications of the laser and the range of parameters used are listed in table 1.1.1.

Table 2. 1: List of laser and deposition parameters used in this work.

Laser parameters	Wavelength	248 nm
	Repetition rate	8 Hz
	Pulse length	25 ns
	Fluence	2.17 J.cm^2
	Beam spot size	0.185 cm^2
Deposition parameters	Target – substrate distance	5 cm
	Background pressure	5*10^{-2} mTorr
	Deposition oxygen pressure	5-300 mTorr
	Substrate temperature	50-700 °C

2. Characterisation

2.1. Morphology and structure

2.1.1. Profilometer

The profilometer is a topographic tool used mostly for the thickness measurement of thin films. The principle is similar to the AFM. A stylus is put in contact with a material and then moved horizontally across the surface of the sample. The stylus does not raster the surface like AFM but moves in only one direction. As the stylus operates in contact mode, the topographic variations of the sample induce a vertical displacement of the stylus which is measured and recorded. The resulting data is a profile line specific of the topography of the sample along the scanned area.[18]

In this work a Dektak 150 stylus profilometer was used. Each thickness point was averaged from several measurements and 5 thickness points were extracted on the samples deposited by PLD in order to average the thickness over the whole sample. To expose a sharp step between the deposited film and the substrate, droplets of TiO_2 paste (TiO_2 powder suspended in isopropanol) were placed on the edges of the substrate and in the centre before the deposition. The TiO_2 was then removed by rinsing with isopropanol to expose the thickness gap.

2.1.2. X-ray diffraction (XRD)

2.1.2.1. Principle

X-ray diffraction (XRD) is a non-destructive technique using X-rays to extract information about the crystal structure and phase of a material. The principle of the technique lies upon an incident beam of X-rays being diffracted at a certain angle when interacting with the sample and if the condition of the Bragg's law is respected constructive interferences will be produced. The X-rays are generated when a potential is applied between a tungsten coil and a metal sheet (in our case copper). Electrons are emitted from the tungsten coil and accelerated toward the copper sheet. When striking upon the copper sheet, some of the inner electrons of the copper atoms are knock out due to the shock leaving the atoms in an excited state. In order to stabilise the system, an outer electron immediately takes the place of the missing one. This stabilisation is followed by the emission of X-rays characteristics of the nature of the electronic transition, Figure 2.4.[19]

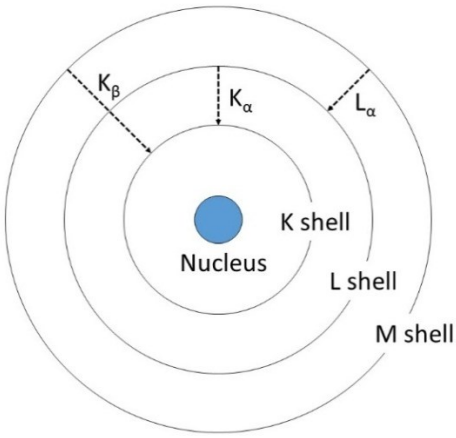

Figure 2. 4: Electronic transitions in an atom. The emissions are assigned to the movement of an outer electron toward the lower shell to replace the missing one and stabilize the atom. The energy and wavelength of the emission are characteristic of the initial and final shell of the moved electron.

The K_α radiation corresponds to the energy emitted during the relaxation of an electron from the L shell to the K shell. It is the most commonly used due to its short wavelength

and high energy. Other radiations are emitted corresponding to the other transitions. Each of these relaxations phenomena is emitted at a particular wavelength and is characteristic of the material. In the case of copper, the K_α is emitted at 1.541 Å. It is also important to note that X-rays are also emitted due to the sudden deceleration of the tungsten electrons. The wide range of X-rays emitted is known as the continuous spectrum.[19]

When interacting with the atoms of the sample, the sinusoidal nature of the X-ray in the incident beam causes the electrons to oscillate around their mean position. As a result an electromagnetic wave of the same wavelength and frequency as the incident X-rays is produced in all directions. Since the principle of the measurement is to measure a signal when the diffracted waves lead to constructive interference, the detector is placed at an angle of reflection equal to the incident angle (θ) of the source. Therefore the detector has to move twice as fast as the source and the resulting angle is given as 2θ. The principle of Bragg's diffraction is shown on Figure 2.5. Constructive interferences are produced when two waves are in phase. Therefore for interferences to occur, the difference in path of two beams, initially in phase, must be equal to a whole number of wavelengths in order to maintain the phase relationship. This happens when the angle θ meets the conditions of the Bragg's equation,[19]

Equation 2.2 $$n\lambda = 2d\ sin\theta$$

Where λ is the wavelength of the X-rays, d the spacing between two consecutive crystalline planes, θ the Bragg angle and n a whole number.

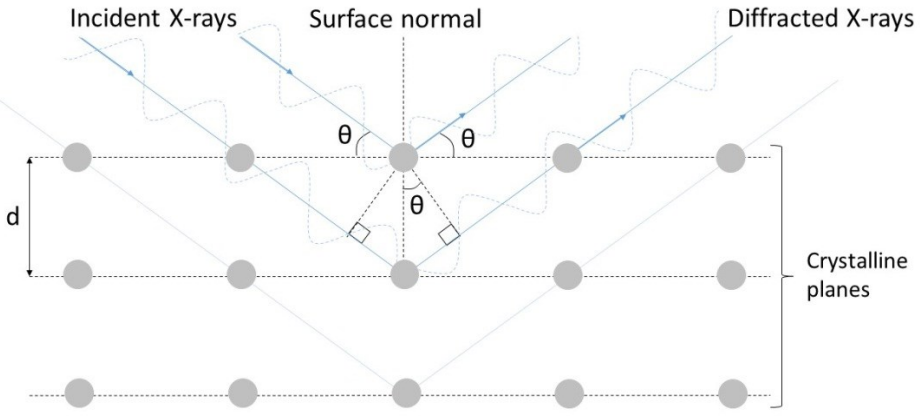

Figure 2. 5: Schematic representation of the Bragg diffraction occurring in crystalline lattice. The incident X-rays are diffracted at an angle θ and then sent in the detector. d is the lattice spacing. The phase of the X-ray wave is represented in dotted blue line. Picture inspired from [19].

The constructive interferences are collected at the detector and a series of peaks appearing at the Bragg angles and whose intensity is related to the amount of crystalline planes of the same Miller indices parallel to the surface. Each peak obtained is characteristic of a d-spacing related to a specific plane. All the d-spacings of a material are specific to its structure, therefore the XRD of a crystalline sample allows to extract the structural and compositional identity of the material. The composition is not quantitative but qualitative since the identification is based on the distance between crystalline planes and some materials only show few or no degree of crystallinity, *e.g.* amorphous films.

2.1.2.2. Practical considerations and data extracted

It can be seen from Equation 2.2 that the Bragg angle is dependent on the incident wavelength and it has been shown previously that other type of radiations are generated from the source, like K_β (λ=1.392 Å). The use of a filter is required to remove the unwanted radiation from the source, leaving only the K_α radiation. However, the filter is not perfect and small amount of K_β manages to pass through. This results in the apparition of additional peaks from diffraction of the same crystallographic plane, as seen on Figure 2.6,

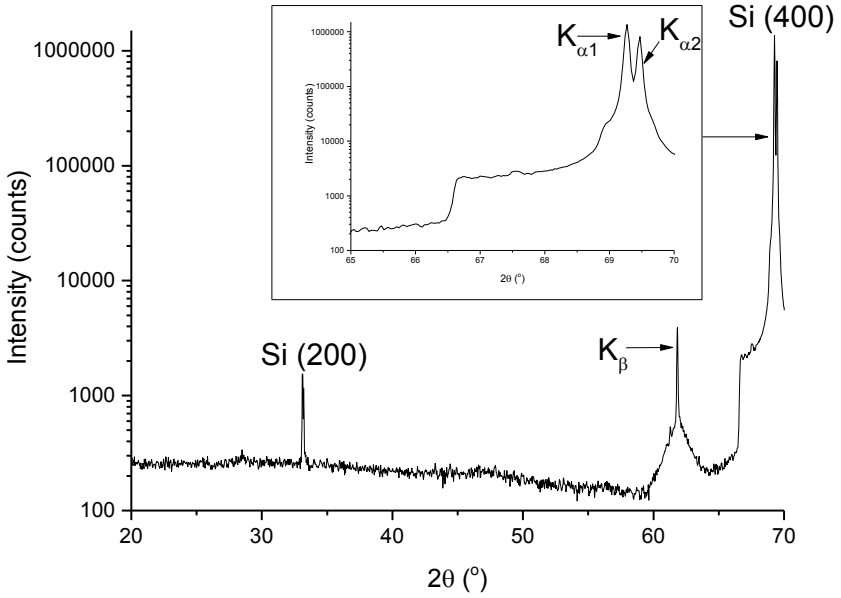

Figure 2. 6: XRD data for the Si reference oriented (100) showing the peaks originated from the $K_{\alpha1}$, $K_{\alpha2}$ and K_β. θ_B represents the Bragg angle.

As the wavelength of K_β radiation is shorter than that of K_α it causes the peak to appear at a lower angle. Since the filter absorbs a large amount of the initial K_β radiation this peak is only seen with high degree of crystallinity, in this case a single crystal. It is also important to note that the K_α radiation is in fact composed of two radiation which can't be separated

by the filter, $K_{\alpha1}$ (λ = 1.541 Å) and $K_{\alpha2}$ (λ = 1.544 Å) with the intensity of $K_{\alpha1}$ twice that of $K_{\alpha2}$. This causes the peaks to split, this effect is more notable at high angle.

As the d-spacing in a crystal is related to lattice parameters it is possible to extract them for a specific crystalline plane. In the case of tetragonal structure, the lattice parameters are given by, [19]

Equation 2.3

$$\frac{1}{d^2} = \frac{h^2+k^2}{a^2} + \frac{l^2}{c^2}$$

Where d is the lattice spacing, h, k and l the Miller indices of the crystalline plane involved and a and c the lattice parameter of the tetragonal lattice.

If we consider a perfect infinite crystal, the diffraction would only occur at Bragg angles. However in a non-ideal finite crystal it is not exactly the case and it results in a peak broadening due to the detection of diffraction signal over a range of angles, as seen in Figure 2.7.

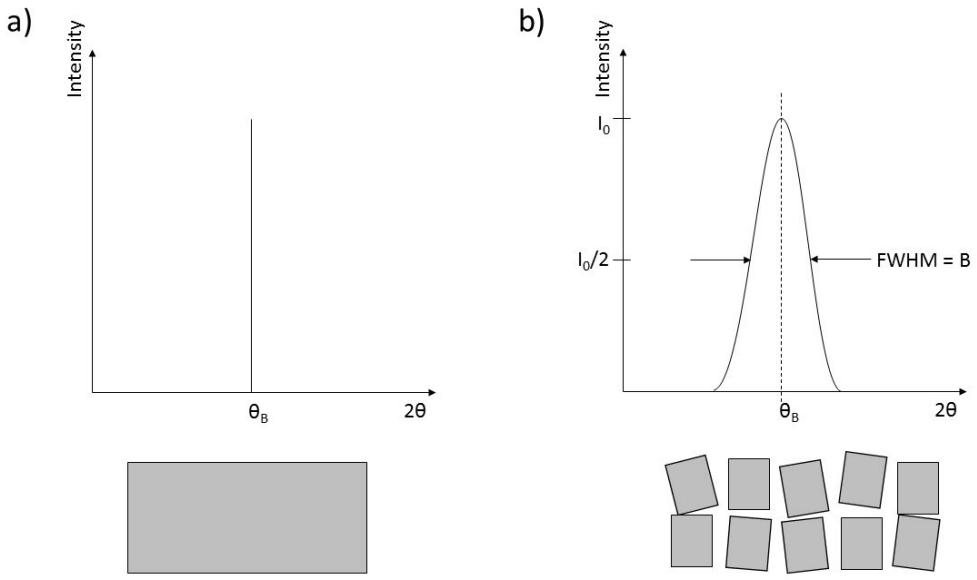

Figure 2. 7: Schematic representing the shape of the diffraction peak for a) in a perfect crystal and b) in a non-ideal crystal with different crystalline sizes with B the Full width half maximum, I_0 the maximum intensity of the peak and θ_B the Bragg angle. The crystal shape is represented in grey below the XRD data.

The broadening of the peak is related to the crystallite size and can be extracted by using the Scherrer equation, [19]

Equation 2.4

$$\tau = \frac{K\lambda}{(B-B_0)\cos\theta_B}$$

Where τ is the mean crystallite size, λ the wavelength of the source, B the full width half maximum (FWHM) of the peak, B_0 the instrument broadening (0.08 obtained from silicon standard), θ_B the Bragg angle and K a dimensional shape factor (generally 0.9). In the case of small crystallite size the peak is broadened while for single crystal a straight line is obtained.

2.1.2.3. Measurements

The system used in this work was a Panalytical X'Pert Prowith with a Cu X-ray source and is equipped with a 0.04 rad Soller slits in order to reduce the radiations from the background. The system was operated at a tension of 40 kV and a current of 40 mA. The data were acquired using a step size of 0.034 ° 2θ. Films deposited on a substrate were levelled by being pressed on sample holder and then rotated at 60 rpm during the measurements. Powders were pressed and levelled on a different substrate holder and no spinning was used during the measurements. In order to avoid the presence of the wide amorphous peak present in quartz, the films were deposited on monocrystalline silicon substrates.

2.1.3. Scanning Electron Microscopy (SEM)

The scanning electron microscope (SEM) is a tool using an electron beam to create a magnified image of the sample. The working principle is similar to optical microscope but using electrons instead of photons as the source. Since the electron wavelength (1.2 Å for an accelerating voltage of 10 kV[20]) is much smaller than the visible light wavelength (around 4000 Å) the maximum resolution obtained with electrons as a source is greatly increased for higher magnification imaging.

The electron beam is produced using the field emission gun by holding a potential difference between the field emission tip and an anode which extracts the electrons from the tip. The electrons are then accelerated by applying a voltage (the acceleration voltage) between a cathode and a second anode. Condenser lenses are used to remove the high angle electrons, scan coils are used to raster the beam across the sample and an objective lens focuses the beam on the surface of the sample. When electrons interact with matter, two types of scattering can occur: elastic and inelastic scattering. With an elastic scattering the trajectory of the electron is changed but not its kinetic energy or its velocity. In the case of inelastic scattering, an incident electron collides and moves an electron from the shell of an atom from the sample and put the electron in an excited state. As a result, various effects can occur such as production of secondary electrons, backscattered

electrons, X-rays emission, and Auger electrons. These effects are shown on Figure 2.8.[21]

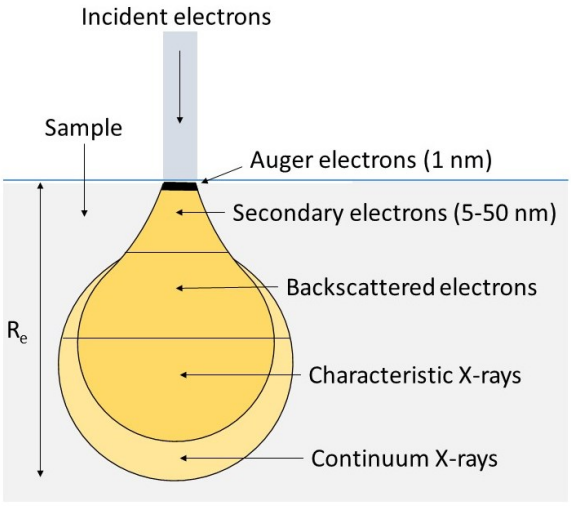

Figure 2. 8: Spatial resolution and depth of the Auger electrons, secondary electrons, backscattered electrons and X-rays produced when an incident electron beam is focused on the surface of a sample. R_e represents the electron depth penetration. Figure adapted from [20].

In SEM, the focus is typically brought on secondary electrons. Because of their low energy (5 eV), only those very near to the surface (< 10 nm) can exit the sample and be collected. Therefore their production gives information on the topography of the sample. As we have seen other effects emerge from the interaction between incident electrons and the sample. The backscattered electrons are highly energetic electrons originating from the electron beam that have been reflected or back-scattered by the sample. Their production depends directly on the atomic number of the atom it had interacted with. The relaxation of excited atoms can give rise to X-rays and Auger electrons.[20,21] The penetration depth of the electron beam in the surface of the sample is given by the Kanaya-Okayama formula, with R_e the penetration depth, M the atomic weight, E the beam energy, Z the atomic number and ρ the density.[22]

Equation 2.5

$$R_e = \frac{0.0276\, M\, E^{1.67}}{Z^{0.89}\, \rho}$$

In this study we used a LEO 1525 Field emission gun scanning electron microscopy (FEGSEM). The accelerating voltage used was fixed at 5 kV with a chamber vacuum around 10^{-5} Torr. The beam is rastered over the surface and the intensity of the secondary electron produced is gathered by the detector on a screen in the form of a map corresponding to the topography of the surface. In order to avoid charge building effects on the surface which could be caused by resistive materials, the samples were coated by a

thin conductive layer of metal (Cr or Au). Another alternative is to decrease the accelerating voltage to reduce the charging effect.

2.1.4. Energy Dispersive X-ray Spectroscopy (EDX)

Energy dispersive X-ray spectroscopy (EDX) is carried out typically in SEM, however the focus is not on the secondary electrons but on the emitted X-rays. The principle is similar to the generation of X-ray from a copper sheet in XRD. When the sample is bombarded by incident electrons, an electron from the inner shell is ejected from the atom on the surface, Figure 2.4. The electron vacancy is then filled by an electron from the outer shell which is followed by an emission of X-rays. For each radiation emitted, their wavelength and energy are specific of the type of electronic transition and of the element emitting the X-ray. Therefore by knowing the energies associated to the different elements it is possible to determinate the composition of the sample.[21] As EDX relies on the same type of structure as SEM, they are often coupled in the same system as to obtain topographic and compositional information. Similarly to SEM, the electron beam is rastered across the sample and the measured X-rays intensities are displayed by energy. These peaks are then compared to a database and assigned to elements.[21] The composition is estimated by comparing the intensities of the different radiations measured for all elements.

The resolution is governed by the penetration depth and the spreading of the electron beam, Figure 2.8. For a typical conditions (acceleration voltage of 20 kV), the depth resolution is about 2 μm.[21] This means in the case of thin film the choice of the substrate is crucial as the film thickness generally does not exceed 500 nm. In this work we used quartz substrates to avoid the noise from the presence of the secondary elements often found in floated glass substrates. Other solutions to avoid this problem would be to increase the film thickness of to decrease the accelerating voltage (Equation 2.5).

EDX is a good elemental analysis technique for qualitative analysis but is limited in term of quantitivity as the overall accuracy is around 2 %.[21] It is generally considered reliable when the amount of element present in the film is above 3 at.%. Otherwise the peak intensity would be too small and could not be distinguished from the noise produced by the continuum spectrum.

In this work the system used was a JSM 6400 operated at 20 kV acceleration voltage under high vacuum. The samples were generally coated with a thin conductive layer of metal (Au or Cr) in order to avoid charging effect on the surface of the sample.

2.1.5. X-ray photoelectron spectroscopy (XPS)

2.1.5.1. Principle

X-ray photoelectron spectroscopy (XPS) is an elemental analysis technique first developed by Dr Siegbahn and his coworkers.[23] XPS is an essential tool for surface analysis as it allows determination of the elemental composition plus the oxidation state and the electronic configuration of a material. This technique is based on the photoelectric effect shown on Figure 2.9.

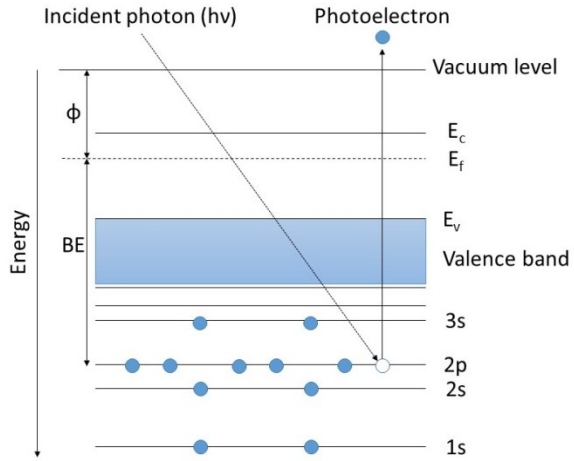

Figure 2. 9: Energy level representation for the emission of a photoelectron when an incident photon removes a core electron from a semi-conductor. E_v and E_c are respectively the energy of the valence band maximum and the conduction band minimum. E_f is the Fermi energy level of the system, φ the work function and BE the binding energy associated to the ejected electron. The electrons are represented by blue circles. Diagram inspired from [24].

The sample is irradiated by a monoenergetic X-ray beam. The incident X-rays interact with the atoms at the surface of the sample and some core electrons are knocked out of the structure. The photoelectrons emitted possess a kinetic energy (KE) directly related to their binding energy (BE). Therefore by collecting their KE in a detector it is possible to determine the elements present on the surface of the sample as they possess characteristic BE. The main setup of an XPS system is constituted of a monoenergetic source of X-ray using light element such as Al ($E_{K\alpha}$ = 1.4866 keV) or Mg ($E_{K\alpha}$ = 1.2566 keV).[20] The ejected electrons then pass through a cylindrical mirror analyser (CMA). The CMA is formed of two concentric metal cylinders set at different potentials. The inner part is set at 0 V while the outer part is set at a positive voltage, creating an electric field inside the

CMA. Due to this electric field, three cases are distinguished; if an electron enter the CMA with a velocity (KE) too high it will collide with the inner cylinder and if the velocity is too low it will collide with the outer cylinder. Only electrons with the right kinetic energy pass through the CMA and are collected in the detector, Figure 2.10.

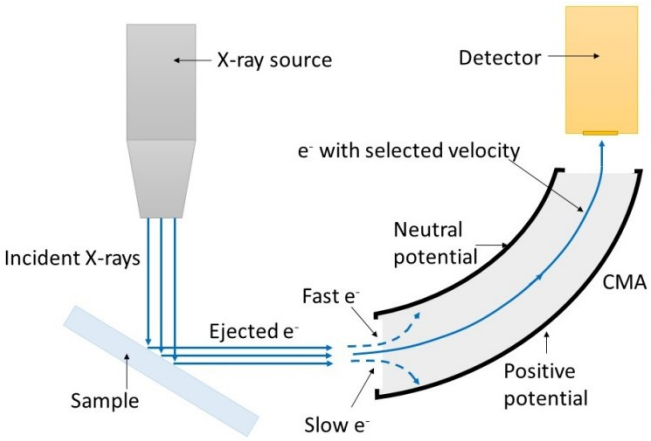

Figure 2. 10: Schematic of a typical XPS setup with diagram displaying the behaviour of electrons depending on their kinetic energy inside the CMA.

The cylinder voltage is changed in order to vary the accepted kinetic energy and for each KE the amount of electron passing through the CMA to the detector is counted. The kinetic energy KE is related to the binding energy BE by,[20]

Equation 2.6 $$BE = h\nu - KE - \phi$$

Where hν is the energy of the photons from the source, ϕ is the work function of the analyser and KE the kinetic energy measured by the detector. Using this equation and by varying the kinetic energy measured it is possible to gather the different binding energies measured and to assign them to their respective elements and electronic transitions.

XPS is a surface analysis technique. Though the X-rays penetrate the sample surface up to micrometres the photoelectrons collected are only obtained from 10-100 Å depth below the surface. This is due to other collisions happening with the electron emitted from the lower layers of the surface. As the photoelectrons are emitted they might collide with electrons from the upper layers giving electrons with lower energies. The number of electrons collected from this phenomenon is much lower than the photoelectron emitted from the top layers however some still manage to pass through the CMA and constitute a background noise.[24] Another type of electron also emitted during a XPS analysis is the Auger electrons. These electrons are produced when a vacancy left by an electron knocked out of the atom is filled by an electron of higher energy. The excess of energy needs to be

evacuated and a third electron, the Auger electron, moves out of the atom with the excess of energy.[24]

2.1.5.2. Data extraction

All XP spectra were recorded using a K-alpha$^+$ XPS spectrometer equipped with a MXR3 Al K_α monochromated X-ray source ($h\nu$ = 1486.6 eV). X-ray gun power was set to 72 W (6 mA and 12 kV). With this X-ray settings, the intensity of the Ag $3d_{5/2}$ photoemission peak for an atomically clean Ag sample, recorded at 20 eV pass energy (PE), was 5 x10^6 counts/s and the full width at half maximum (FWHM) was 0.58 eV. Binding energy calibration was made using Au $4f_{7/2}$ (84.01 eV), Ag $3d_{5/2}$ (368.20 eV) and Cu $2p_{3/2}$ (932.55 eV). No charge compensation was used to analyse the samples. Survey scans were acquired using 200 eV pass energy, 1 eV step size and 100 milliseconds (50 ms x 2 scans) dwell times. All high resolution spectra for the valence band were acquired using 20 eV pass energy, 0.1 eV step size and 1 second (50 ms x 20 scans = 1000 ms) dwell times. Samples were prepared by pressing the sample onto the holder with a metal pin and analysed at an electron take-off angle normal to the surface with respect to the analyser. Pressure during the measurement of XP spectra was ≤ 1 x10^{-8} mbar. The work function of the samples was determined by measuring the spectrum cut-off and Fermi edge whilst applying a bias of -30 V to the sample. The cut-off was acquired using 5 eV pass energy, 0.05 eV step size and 1 second (50 ms x 20 scans = 1000 ms) dwell time, and the Fermi edge was acquired using 40 eV pass energy, 0.05 eV step size and 1 second (50 ms x 20 scans = 1000 ms) dwell time.

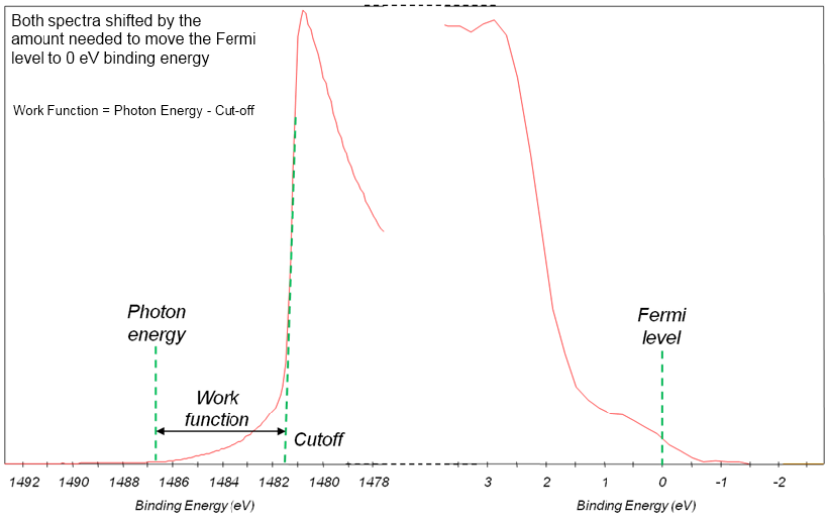

Figure 2. 11: Example of spectrum cut-off (left) and Fermi edge (right) shifted to align the Fermi level at 0 eV binding energy. The work function is determined with the photon energy and the cut-off. Figure taken from K-Alpha$^+$ Surface Analysis operating manual.

The work function (ϕ) of the sample is extracted with the cut-off of the spectrum as shown in Figure 2.11 and using Equation 2.7.

Equation 2.7 $$\emptyset = h\nu - (E_{kin\ cut-off} + E_{Fermi\ edge})$$

Where hν is the energy of the X-ray (1486.6 eV), $E_{kin\ cut\text{-}off}$ the kinetic energy of the spectrum cut-off and $E_{Fermi\ edge}$ the Fermi edge energy deviation from 0 eV binding energy.

2.2. Opto-electronic properties

2.2.1. Hall effect measurements

The Hall effect measurement method is commonly used to determine the carrier density, type, resistivity and mobility of a semiconductor. The Hall effect has been discovered by Dr Edwin Hall in 1879 when he placed a gold foil into a magnetic field and applied an electrical current to it. He observed the presence of a transverse voltage across the material, phenomenon known as the Hall effect.[20]

2.2.1.1. Basic principle

The Hall effect happens when an electrical current is applied to a material under a perpendicular magnetic field. A magnetic force F_M perpendicular to the magnetic field is formed and deviates the charge carrier from the main flow. This magnetic force F_M is given by Equation 2.8.[20]

Equation 2.8 $$F_M = q(vB)$$

Where v is the drift velocity of the charge carriers, q their charge and B is the magnetic field. The magnetic force pushes the charge carriers at the edge of the sample which results in a potential difference across the sample perpendicular to both the current flow and the magnetic field. This potential difference is known as the Hall voltage V_H. The effect is represented schematically on Figure 2.12.

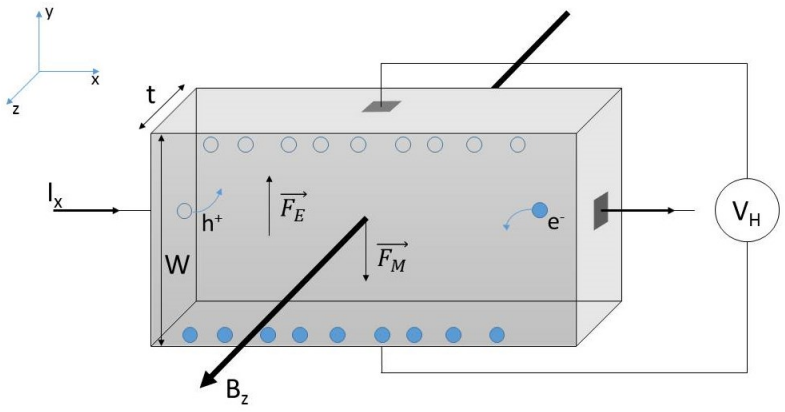

Figure 2. 12: Schematic of the Hall effect in n-type semiconductor of thickness t and width W. I_x is the current applied in the x direction and B_z the magnetic field applied in the z direction. The charge carriers are pushed to the edges of the sample opposite to the y direction due to the magnetic force F_M. This charge carrier build-up induces an electric force F_E opposite to F_M along the y axis and a potential difference V_H is measured.

The charge carrier accumulation on one side of the sample creates an electric field E_y resulting in an electric force F_E opposite to F_M and in the same direction as the Hall voltage is measured. The steady state resulting from the magnetic force, F_M, and the opposed electric force, F_E, is given by,[20]

Equation 2.9 $$F_M + F_E = -qv_xB_z + qE_y = 0$$

Considering the relationship between the drift velocity of the charge carriers (v_x) and the current given in Equation 2.10, S being the surface of homogenous width W and thickness t,[20]

Equation 2.10 $$I_x = Sqnv_x$$

The electric field can then be expressed as a function of I, the current acting through the material in the x direction, in Equation 2.11.[20]

Equation 2.11 $$E_y = \frac{IB_z}{Wtqn}$$

Where W is the width of the sample and t its thickness. The Hall voltage can then be given by,[20]

Equation 2.12 $$V_H = WE_y = \frac{IB_z}{tqn} = -\frac{R_HIB_z}{t}$$

In the case of an n-type semiconductor, the Hall coefficient is inversely proportional to the charge carrier density,[20]

Equation 2.13

$$R_H = -\frac{1}{qn}$$

It can be observed from Equations 2.12 and 2.13 that the Hall voltage is negative when the main charge carriers are electrons. The case is the opposite if the major carriers are holes and the Hall voltage would then be positive. Therefore the sign of the Hall voltage gives information about the nature of the carrier present in the material.

Given that I, B_z, t and V_H are all measurable, the hall coefficient, R_H, can be calculated and thus the charge carrier density of the material, n, can be extracted. From the Hall coefficient the Hall mobility can also be calculated,[20]

Equation 2.14

$$\mu = \frac{|R_H|}{\rho}$$

ρ is the resistivity of the material and can be extracted using the van der Pauw methodology, discussed in a few paragraphs.

Alongside the Hall effect another factor is known to influence the measured parameters, the Hall scattering factor, r_H. Therefore Equation 2.13 is scaled upon this factor,[20]

Equation 2.15

$$R_H = -\frac{r_H}{qn}$$

Considering the change in R_H all the other equation have to take this change in consideration and the drift carrier mobility, μ, is now defined as the Hall mobility, μ_H. The Hall scattering factor is specific of the material and as it is often unknown it is assumed to be 1. However in the case of SnO_2 it has been found to be about 1.01 at 300K [25] leaving the assumption of $r_H = 1$ correct in our case.

2.2.1.2. Sample geometry and resistivity

In 1958, van der Pauw found that the Hall effect measurement could be performed on samples of arbitrary shape as long as the contacts are as small as possible, located at the periphery of the sample and the sample is free of isolated holes and with a uniform thickness.[26] Even though the measurement is theoretically possible on an arbitrary shape, a symmetrical configuration is preferred. Several sample configurations have been tested such as circle, clove leaf and cross but the easiest one to use is the square as substrates are easier to produce in this shape, Figure 2.13.

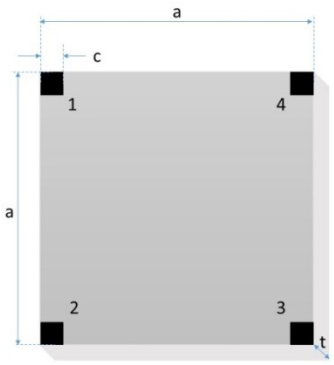

Figure 2. 13: Schematic representation of a possible symmetrical van der Pauw geometry used in Hall measurement. The main sample is a grey square of width a and thickness t. The four contacts of width c, represented by black squares, are dispersed at the four corner of the sample. Each contact is identified by a number.

In order to extract the resistivity ρ of the sample displayed in the previous figure, the system measures the resistances within the sample without applying a magnetic field. Equation 2.16 details the calculations.[20]

Equation 2.16
$$\rho = \frac{\pi t}{ln2}\frac{(R_A+R_B)}{2}f$$

Where t is the thickness, uniform across the sample, and f the correctional factor which is equal to 1 when a perfectly symmetrical sample is used with the contacts orthogonal to each other.[27] This shows the importance of having a homogenous sample when measuring the resistivity and thus the mobility (Equation 2.14).

R_A and R_B are the resistance measured by applying current between two adjacent contacts and by measuring the voltage difference between the two remaining contacts, *e.g.* for R_A current applied between contact 1 and 2 ($I_{1,2}$) and voltage measured between contact 3 and 4 (V_3-V_4). [20]

Equation 2.17
$$R_A = \frac{V_3-V_4}{I_{1,2}} \quad \text{and} \quad R_B = \frac{V_4-V_1}{I_{2,3}}$$

2.2.1.3. Additional factors and measurements methods

Considering an ideal Hall effect measurement, the Hall voltage should be zero when no magnetic field is applied. However during a real measurement the conditions are not ideal and the measured voltage, V_m, contains errors within the system. Amongst these are the misalignment voltage V_o and the thermoelectric voltage V_{TE}. The misalignment voltage is due to an asymmetry between the contacts or within the sample[28], while the thermoelectric voltage is a result of temperature gradient within the Hall sample.[27]

In order to remove the effect of the misalignment and thermoelectric voltage from the measured voltage, it is necessary to use a method based on, respectively, current and field reversal. As the thermoelectric voltage is independent of the current, and by reversing the current and taking the difference of the two measured voltages it is possible to remove it from the measured voltage. The same principle can be applied for the misalignment voltage, considering the thermoelectric voltage is already removed. V_o is independent of the magnetic field however the Hall voltage is not and thus by measuring the voltage at two different magnetic fields V_o can be extracted and removed from the V_m equation.

Two types of Hall measurement can be distinguished, DC and AC. DC type of measurement is suited for high mobility materials. When measuring low mobility materials, the misalignment voltage becomes larger than the Hall voltage which leads to a large electrical noise.[27] The minimum mobility that a DC measurement system can measure is 0.1 $cm^2/(V.s)$. However this limit can be overcome by using a low frequency AC Hall measurement system can go down to 10^{-3} $cm^2/(V.s)$.[27]

In AC Hall measurements, the magnetic field is sinusoidal and develops a time dependency, thus the Hall voltage becomes time dependent with the magnetic field expressed as $B_z = B\cos(\omega t)$, t being the time and ω the frequency.

Equation 2.18

$$V_H = \frac{R_H I B_z \cos(\omega t)}{t}$$

The main advantage of an AC Hall measurement over a DC is the possibility to extract the misalignment voltage from the measured voltage even at low mobility. This results in less error during the measurements and the opportunity to analyse low mobility samples.

For the measurements the films were deposited on squared 1 x 1 cm^2 quartz samples and the contact were made on the four corners of the samples using metallic indium. The resistivity of the films was measured using the Van der Pauw method. AC Hall measurements were performed using a Lakeshore 8400 system with AC current between 10 nA and 50 mA, and with fixed sinusoidal magnetic field of 1.19 T and of frequency 50 or 100 Hz.

2.2.2. Thin film transistors (TFTs)

Thin-film transistors (TFTs) are three-terminal field-effect devices which modulates the current flowing in a semiconductor placed between two electrodes (the drain and the source). In order to control the flow of current through the semiconductor, a third electrode (the gate) is added and a dielectric layer is placed between the gate and the

semiconductor. TFTs are a kind of MOSFET (Metal-Oxide Semiconductor Field-Effect Transistor). The electrical characteristics of a TFT are represented by the field effect mobility (μ), the threshold voltage (V_t), the On/Off ratio and the subthreshold swing (S). Because fast switching is a key role of TFTs in electronic devices, the aim is to achieve high mobility, threshold voltage close to zero and subthreshold swing as small as possible.[29]

2.2.2.1. Operation principle

A voltage is applied across the gate which modulates the current flowing between the source (S) and the drain (D) electrodes through electrostatic coupling. The source electrode provides carriers injection into the semiconductor and the drain electrode extracts them. When a bias voltage (V_G) is applied between the gate and the source, an equal and opposite amount of charge is created at both interfaces of the dielectric layer. The dielectric behaves as a capacitor and an electric field is emitted. If a voltage is applied between the drain and the source electrode (V_D), charges from the source accumulate at the semiconductor/dielectric interface due to the electric field. The charges are then driven through the semiconductor layer forming a channel. This accumulation of mobile charges occurs at a gate voltage known as the threshold voltage (V_t).

Considering a n-type semiconductor and in the case of a perfect transistor, if the polarization is negative ($V_G < 0$) there is an accumulation of holes (a p-type conducting channel) at the interface semiconductor-dielectric. In that case no electron can flow through the channel and the transistor is considered off. Without gate polarization ($V_G = 0$) no conduction channel is formed between the source and drain so the transistor is still off. When the gate polarization becomes negative ($V_G > 0$) electrons accumulate at the semiconductor dielectric interface creating a n-type conducting channel between the source and the drain. Electrons can now flow through the channel and the drain current I_D starts to increase. Before the drain voltage ($V_D > 0$ for a n-type SC) is applied, the accumulation of charges at the interface SC/dielectric is constant. However when V_D is applied a potential gradient increasing from the source to the drain appears in the channel. As long as V_D does not exceed the voltage difference between the gate voltage and the threshold voltage ($V_D < V_G - V_t$), the system is considered in the linear regime, Figure 2.14.a.[30] Further increase in V_D decreases the accumulation region from the drain until that region is depleted of carrier. When this region is fully depleted, the channel is said pinched-off and no further increase in the drain current I_d can be observed. This is the saturation regime and at this point $V_D \approx V_G - V_t$, Figure 2.14.b. [29,31]

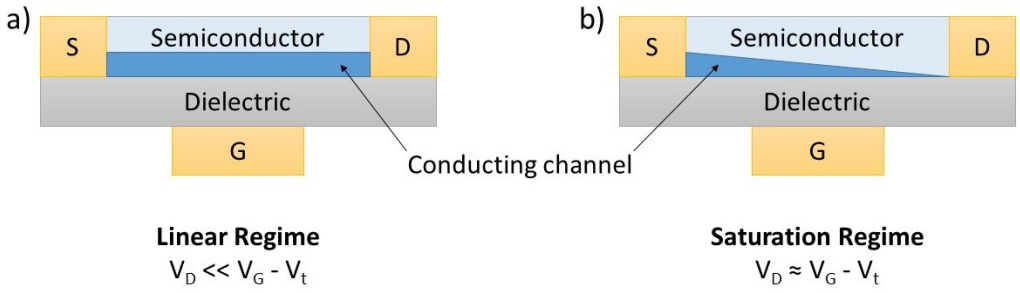

Figure 2. 14: Schematic representation of a TFT device operating in a) linear regime with a constant channel and b) saturation regime with the area close to the drain pinched off. G, S and D are respectively the gate, source and drain electrodes of the device.

2.2.2.2. Device characterisation

The most important characteristics of a TFT are the mobility (μ), the On/Off ratio, the turn-on voltage (V_{on}) and the subthreshold swing (S). In this work, TFT are only used to determine the type of carriers as well as the saturation mobility of thin films. These information can be extracted by measuring the transfer (I_D function of V_G) and output characteristics (I_D function of V_D) shown in Figure 2.15.

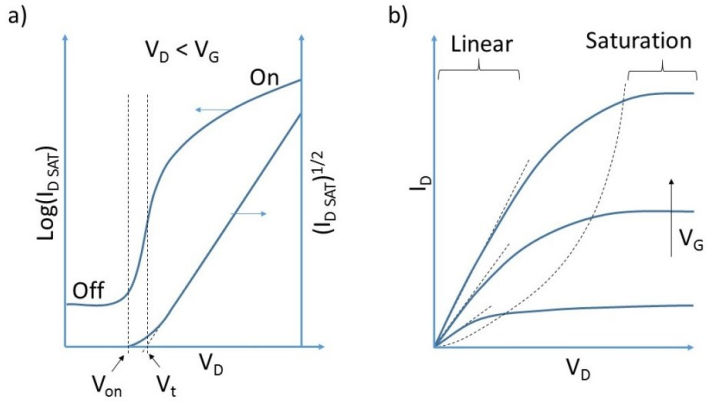

Figure 2. 15: a) Transfer characteristics of an ideal TFT showing how to report V_{on} and V_t using the square root of I_D. b) Output characteristics of an ideal TFT showing the linear and saturation regime at different gate voltages. The trend line shows the evolution of the pinch-off voltage (V_t) values when V_G increases. Figure from [32].

The threshold voltage V_t corresponds to the gate voltage V_g for which the conductive channel is formed close to the dielectric-semiconductor interface. This value can be easily determined by plotting the square root of I_d function of V_g. In the saturation regime ($V_d \approx V_g - V_t$) the saturation mobility (μ_{sat}) can be extracted with,[32]

Equation 2.19

$$\mu_{sat} = \frac{L}{WC_i}\frac{d^2 I_{D\,sat}}{dV_G{}^2} = \frac{2L}{WC_i}\left(\frac{d\sqrt{I_{D\,sat}}}{dV_G}\right)^2$$

Where W is the width of the channel, L the length of the channel, C_i the capacitance per unit area, I_{Dsat} the saturated drain current and V_g the gate voltage. μ_{sat} is often used to describe the efficiency of a TFT and is the field effect mobility, μ_{FET}.

2.2.2.3. Device architecture and system used

Several types of TFT architecture are possible, in this work coplanar bottom gate configurations were used. The films were deposited on OFET structures with Au source/drain, SiO_2 (230 nm) gate-insulator and Si gate from Fraunhofer. The Substrates were generation 5 OFETS meaning their channel width is fixed at 2 mm. Each substrate was composed of 4 sets of channel length (2.5, 5, 10 and 20 µm) each composed of 4 OFETs. To avoid multiple depositions and to reduce the amount of substrates used the OFETs were cut in 4 (one piece for every channel length) and deposition was performed on 2 pieces at the same time (20 and 10 µm channel length). The pieces with a 20 µm channel were annealed at 600 °C while those with a 10 µm channel were annealed at 700 °C. The system used for the measurements was a MMR probe station combined with an Agilent 4155 C. The measurements were controlled using the software Desktop Easy Expert.

2.2.3. Kelvin probe force microscopy (KPFM)

2.2.3.1. Operating principle

The Kelvin probe force microscopy technique is based on the AFM system and was proposed by Nonnenmacher *et al.*[33] in 1991. KPFM is a tool used to measure the local conductive potential difference (CPD) between a conductive AFM tip and a sample. This CPD (V_{CPD}) is defined as the difference between the work function of the tip ϕ_t and the sample ϕ_s over the electric charge e, as shown in Equation 2.20.[34]

Equation 2.20
$$V_{CPD} = \frac{\phi_t - \phi_s}{-e}$$

The system layout is simple, the sample is placed on a conductive substrate as to avoid charging effect and is connected to a movable platform. A conductive tip is then brought above the surface of the sample at a distance d. Three cases can then be observed as shown on Figure 2.16,

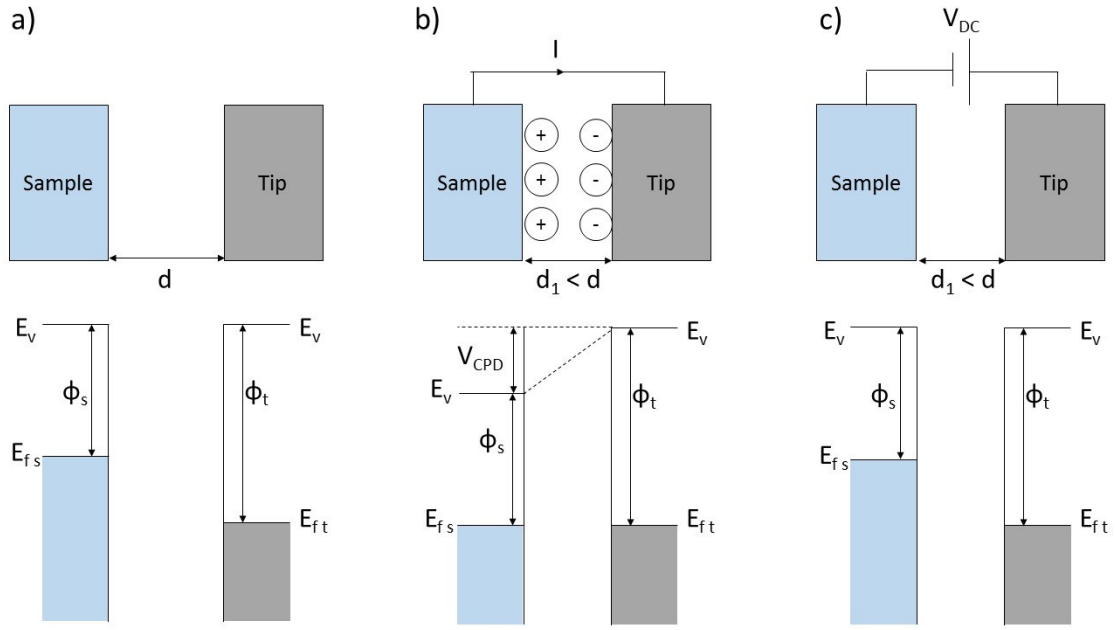

Figure 2. 16: Schematic representation of the variations of the energy levels with the distance between the conductive tip of$_s$ the Kelvin probe (represented in grey) and the sample (represented in light blue). On top are represented the distance between tip and sample, while the bottom part is dedicated to their energy level diagrams. Three different cases are shown; a) the distance d between tip and sample is too large and no electrical connection occurs, b) the distance is reduced to d_1 and electrical contact happens with a line-up of the Fermi levels and the apparition of internal voltage V_{CPD} the contact potential difference, c) The distance d_1 is kept but an external bias V_{DC} is applied which cancel the internal voltage V_{CPD} and therefore the previous electric force. Φ_s and Φ_t represent the work function of the sample and tip, respectively. $E_{f\,s}$ and $E_{f\,t}$ are the Fermi level energies of the sample and tip, respectively, and E_v the vaccum energy level. Schematic based on Melitz et al.[34]

In the first case, Figure 2.16.a, the distance between the tip and the sample is too large and no electrical connection is established. When the distance is decrease up to a point where the tip and the sample are close enough to permit electron tunnelling, electrical contact occurs, the Fermi level energies line-up and the system reaches an equilibrium, Figure 2.16.b. Both surfaces become charged and a potential difference appears, V_{CPD}, between the tip and the sample. Due to the presence of charges on the surface of the tip and the sample, an electric force acts on the contact area. However this force can be compensated by applying an external bias, V_{DC}, between the tip and the sample with the same magnitude as V_{CPD} but in the opposite direction. Knowing V_{CPD} from the applied voltage V_{DC} it is possible to extract the work function ϕ_s of the sample if the work function of the tip ϕ_t is known using Equation 2.20.[34,35]

During the measurement an AC voltage (V_{AC}) is applied to the tip along with a DC voltage (V_{DC}). The AC voltage generates oscillating electrical forces between the tip and the sample

and those are nullified when V_{DC} compensate V_{CPD}. The electrostatic force present between the tip and the sample is shown in Equation 2.21.

Equation 2.21
$$F_{es}(z) = -\frac{1}{2}\Delta V^2 \frac{\partial C(z)}{\partial z}$$

Where C is the capacitance along the direction z normal to the sample surface and ΔV is the potential difference between sample potential and the voltage applied at the tip. As the external bias is composed of V_{DC} and $V_{AC}\sin(\omega t)$ where ω is the frequency and t the time, ΔV is expressed by,

Equation 2.22
$$\Delta V = (V_{DC} \pm V_{CPD}) + V_{AC}\sin(\omega t)$$

By replacing ΔV from Equation 2.22 by its developed term in Equation 2.21, the electrostatic force can be expressed in three parts,[34]

Equation 2.23
$$F_{es} = F_{DC} + F_{\omega} + F_{2\omega}$$

Equation 2.24
$$F_{DC} = -\frac{\partial C(z)}{\partial z}\left[\frac{1}{2}(V_{DC} \pm V_{CPD})^2\right]$$

Equation 2.25
$$F_{\omega} = -\frac{\partial C(z)}{\partial z}(V_{DC} \pm V_{CPD})V_{AC}\sin(\omega t)$$

Equation 2.26
$$F_{2\omega} = \frac{\partial C(z)}{\partial z}\frac{1}{4}{V_{AC}}^2[cos(2\omega t) - 1]$$

F_{DC} induces a static deflection on the tip and $F_{2\omega}$ is used for capacitance microscopy [34]. However F_{ω} is used to measure V_{CPD}. When V_{DC} reaches the complementary value of V_{CPD}, the oscillating electrical forces between the tip and the sample are nullified and thus the work function difference between the tip and the sample can be extracted.

2.2.3.2. Considerations with semiconductors

It is also important to note that Equation 2.25 is valid only when using a metallic tip and sample. In the case of a semiconductor the measurement may be affected by the presence of a space-charge layer (SCL).[20,34] When a positive (negative) charge is put at the surface of a material, the surrounding electrons (holes) rearrange to compensate the extra charge. They screen it such that deeper in the material the electric field created from the charge disappear. The screening range is governed by the electron (hole) concentration. In the case of metals with carrier concentration about 10^{22} cm^{-3} the screening length is on the order of atomic distance while for SC the carrier concentration is much lower (about < 10^{20} cm^{-3}) resulting in a much larger screening range (about 10 nm depending on the carrier concentration).[36] The screening region is called the space-charge layer (SCL). In

the bulk of a material the Fermi level is governed by the bulk doping level and intrinsic defects. Considering the case of a n-type SC, the formation of acceptor-like surface states is possible and their position with respect to the Fermi level is fixed. Since E_F is close to the CBM in n-type SC, E_F would be far above the acceptor surface states (close to the VBM) and thus they would be fully ionised (filled with electron). This charge build-up on the surface is not stable and a deformation of the band structure is required to compensate them. A band bending of the bands near the surface places E_F below the donor defect transition level (E_D) and allows the defect states to be depleted of electrons, thus compensating the negative charge formed by the acceptor states. The position of the Fermi level at the surface and the amount of band bending are determined by the charge neutrality. In n-type SC, three cases of SCL can be distinguished: depletion, inversion and accumulation. They are illustrated on Figure 2.17. The depletion type of SCL is the case explained before where the presence of acceptor-like surface states induce an upward band bending decreasing the density of n-type charge carrier near the surface with respect to the bulk. The inversion SCL occurs at higher density of acceptor surface states at lower energies in the band gap. In this case the band bending becomes so strong that the intrinsic energy E_i cross E_F. The intrinsic energy level E_i is defined by,

Equation 2.27

$$E_i = \frac{E_C + E_V}{2} - \frac{1}{2} k_B T ln\left(\frac{N^C_{eff}}{N^V_{eff}}\right)$$

Where E_C and E_V are the energies of the CBM and VBM, and N^C_{eff} and N^V_{eff} the effective Cb and VB density of states respectively.

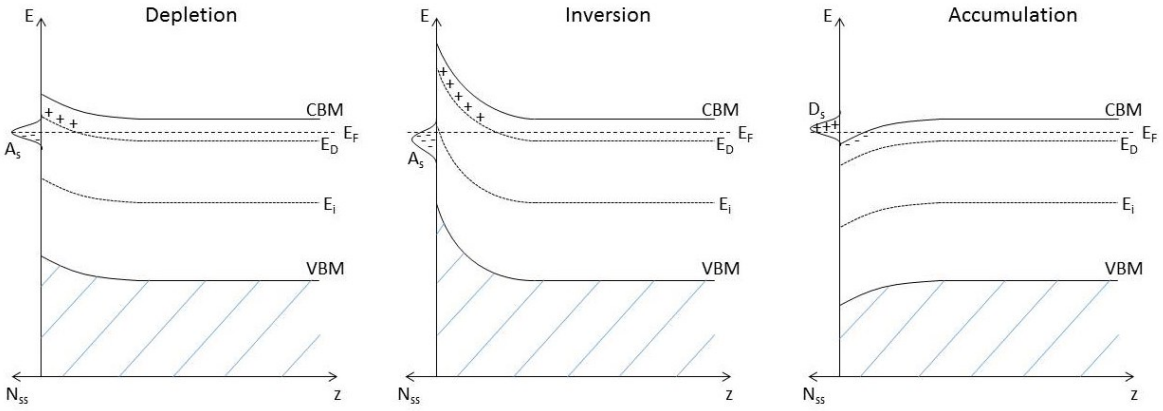

Figure 2. 17: Band diagram function of the thickness with respect to the SC surface in the case of depletion, inversion and accumulation SCL in a n-type SC. E_i and E_D represents the intrinsic and donor defect levels respectively. N_{SS} is the density of surface states, and A_S and D_S the surface acceptor and donor states respectively. Diagram taken from ref [36].

When $E_F > E_i$ the SC is considered n-type but when $E_F < E_i$ the SC is p-type. When E_i crosses the Fermi level, the type of carrier changes from electrons (bulk) to holes (surface), thus the name of inversion SCL. The last type of SCL is an accumulation of electron which requires the presence of donor-type surface states (D_S). If these states are high enough in energy (above E_F) they are ionised and carry a positive charge which is compensated by an electron accumulation in the CB below the surface, inducing a downward band bending. When dealing with a p-type SC, the situation is reversed.

The presence of surface band bending induced by surface states affect the Kelvin probe (KP) measurement by changing the work function ϕ at the surface as shown on Figure 2.18.

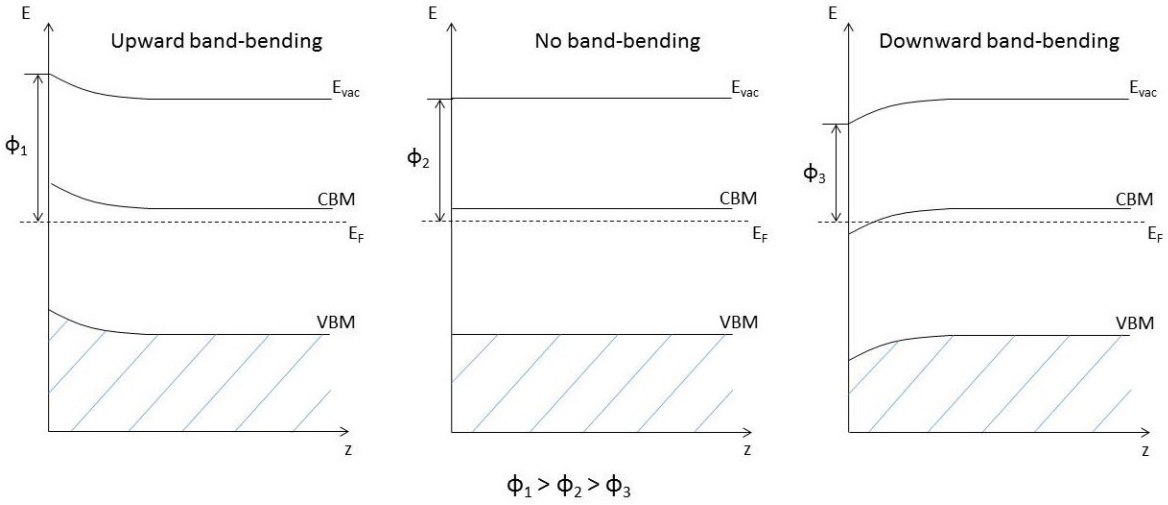

Figure 2. 18: Changes in work function ϕ with the different type of band bending in an n-type SC. E_{Vac} represents the Vacuum level.

In the case of an upward band bending, since the vacuum level is bended accordingly to the other bands, the work function measured is higher than the bulk work function. The opposite happens for a downward band bending. The work function measured with Kelvin probe needs to be considered as a surface measurement and not a clear indication of the bulk properties since the contact potential difference measured depends on E_F, adsorption layers (surface dipoles), surface states and doping.[36]

2.2.3.3. Kelvin probe (KP) measurements

The films were deposited on a conductive substrate in order to avoid charging effect during the measurement. The substrates used were all ITO on glass except for chapter 4 where silicon substrates had to be used under the annealing conditions. The instrument used for the measurement was a SKP5050 from KP Technology with a stainless steel tip.

The machine provides the difference between the work function of the tip and the work function of the sample and a reference is taken by performing the measurement on a silver sample. The own work function of silver is formerly measured before each KP measurement using photoelectron spectroscopy.[37]

2.2.4. Ultraviolet-Visible spectroscopy

In ultraviolet-visible (UV-Vis) spectroscopy, a monochromatic source is used to emit a light at a specific wavelength on a sample. The transmitted light is collected in a detector and the ratio between the intensity of the collected light and the intensity of the incident light (I_0) is calculated, it correspond to the transmission of the sample at this specific wavelength. The wavelength of the source is varied and the transmission spectrum is collected over the selected range of wavelengths. The amount of light transmitted through the sample is function of several parameters including reflections from the surfaces, scattering of the light and electronic transitions within the material. Considering this work is focused on semiconductors, the amount of light transmitted (or absorbed) is directly related to the band gap E_g of the material. If the incident light wavelength is low enough to cover the energy of the semiconductor optical band gap a part of the light is absorbed by the semiconductor.

In this work, the UV-vis spectroscopy technique is used to look at two aspects of our thin films; the amount of light transmitted in the visible region often used as a characterisation for TCOs and the determination of the band gap characteristic of the material. As SnO_2 is a direct band gap metal oxide, the optical band gap (E_g) metal oxide film can be calculated using the Tauc model, [38]

Equation 2.28
$$(\alpha h\upsilon)^2 = A\left(h\upsilon - E_g\right)$$

Where hν is the photon energy and A is a constant. The band gap can then be determined from the intercept of the extrapolated linear part of the curve with the energy axis. By plotting $(\alpha h\nu)^2$ function of the energy, we can extract the value of the band gap by extrapolating the linear part of the curve with the energy axis, Figure 2.19.

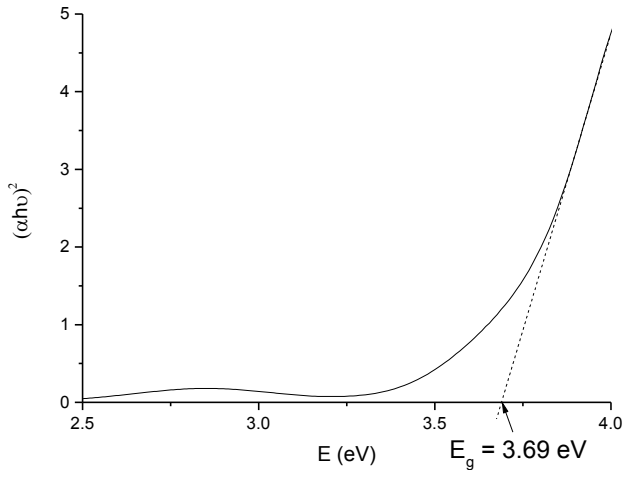

Figure 2. 19: Tauc plot for a SnO_2 film deposited by PLD at 600 °C and under 100 mTorr. The extracted E_g value is 3.69 eV.

The system used in this work was a Bentham 605 custom optical bench with a range of 250 to 800 nm and a 1 nm step size. The background was measured in air and the spot radius was about 2 mm. The data was collected using BenWin+ software.

2.2.5. Photovoltaic devices (PV)

Photovoltaic (PV) devices convert incident energy (light) into electrical energy. An incident light is absorbed by a photoactive material which generates charge carriers. These charge carriers are then separated and driven towards their respective electrodes due to the presence of an internal electric field. Due to the collection of charge carriers at the electrode, a potential difference at open circuit voltage (V=0) V_{oc} appears and a photocurrent density at short-circuit (J=0) J_{sc} is generated.

2.2.5.1. Measurement

The characteristics of a PV device are obtained by measuring the current density J function of an applied bias V in the dark and under illumination. The operation of a PV device under both conditions is displayed on Figure 2.20.

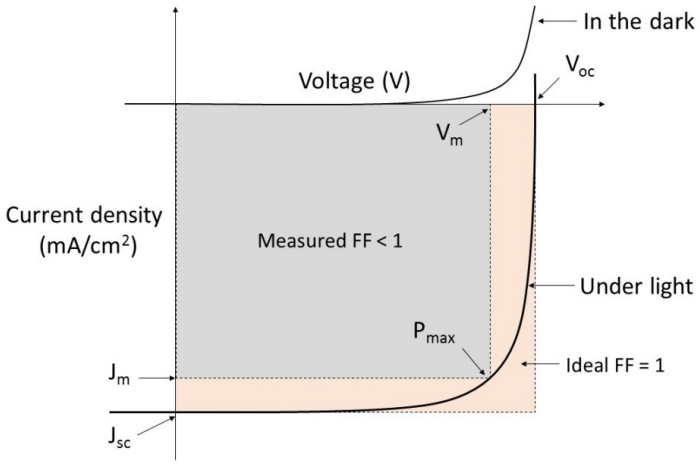

Figure 2. 20: J-V characteristics of an OPV device operating in the dark or under an incident light. V_{oc} is the open-circuit (J = 0 mA.cm^{-2}) voltage, J_{sc} the short-circuit (V = 0 V) current density and FF the fill factor (< 1 for a non-ideal device). P_{max} is the maximum power density and is given by the grey rectangle J_m x V_m.

In the dark the PV device behaves like a diode with a current flowing through only when the forward bias applied is above a threshold voltage. Under illumination, photocurrent is generated by the PV device. This photocurrent is directly proportional to the incident light intensity.

PV devices are generally represented by 4 main parameters: the open-circuit voltage V_{oc}, the short-circuit current J_{sc}, the fill factor FF and the efficiency η. V_{oc} reprensents the potential difference measured when J=0. It corresponds to the amount of bias created from the light generated current on the PV device. J_{sc} is the current density of the device when no bias is applied (V=0). It is due to the amount of charge carriers reaching successfully their respective electrode after being formed under illumination. J_{sc} represents the largest current density that can be produced by the device. Despite V_{oc} and J_{sc} being the maximum of respectively the voltage and photocurrent generated, the power density of the device at each of these point is 0 since the power density can be expressed as,[39]

Equation 2.29 $$P = J\,V$$

Where J is the current density measured and V the voltage applied. P_{max} is the maximum power density reached by the device, sown on Figure 2.20, and reaches a maximum at a given point.

Since the device is not ideal another parameter, the fill factor FF, has to be considered in the calculation of P_{max}. FF represent the 'squareness' of a PV's curve and is defined by,

Equation 2.30

$$FF = \frac{V_m J_m}{V_{oc} J_{sc}}$$

Where V_m and J_m are respectively the voltage and the current density corresponding to the point maximum power density. Knowing the fill factor it is possible to calculate P_{max} by,

Equation 2.31

$$P_{max} = V_{oc} J_{sc} FF$$

Finally the overall efficiency of the PV device is given by the ratio between the maximum power density generated and the incident light power density P_{in},

Equation 2.32

$$\eta = \frac{P_{max}}{P_{in}} = \frac{V_{oc} J_{sc} FF}{P_{in}}$$

In the case of non-deal PV devices, several factors influence the FF and therefore reduce the performance of the cell. By looking at the equivalent circuit for a PV device, Figure 2.21, we can observe the presence of two resistances: the series resistance R_s and the shunt resistance R_{sh}.

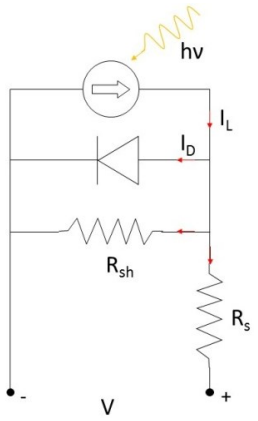

Figure 2. 21: Equivalent circuit of a photovoltaic device under incident light of energy hν. I_L is the photo-generated current, I_D the current of the device in the dark, V the voltage measured and R_s and R_{sh} the series and shunt resistance respectively.

These resistances do not affect the J_{sc} or the V_{oc} but they have a considerable impact on the FF and thus the overall efficiency. R_s affect the slope of the curve at the open circuit point and R_{sh} affects the slope of the curve at the short-circuit point. The series resistance R_s is due to the electrical resistance of the device, of the materials and at the interfaces, while the shunt resistance R_{sh} arises from leakage current in the device. Both R_s and R_{sh} can be evaluated by extrapolating the slope of the J-V curve at the point of short-circuit (a_{sc}) and at the point of open circuit (a_{oc}) respectively.[39]

Equation 2.33

$$R_s = \frac{1}{a_{sc} S} \quad \text{and} \quad R_{sh} = \frac{1}{a_{oc} S}$$

S is the surface of the active area under illumination, in this work S = 0.045 cm².

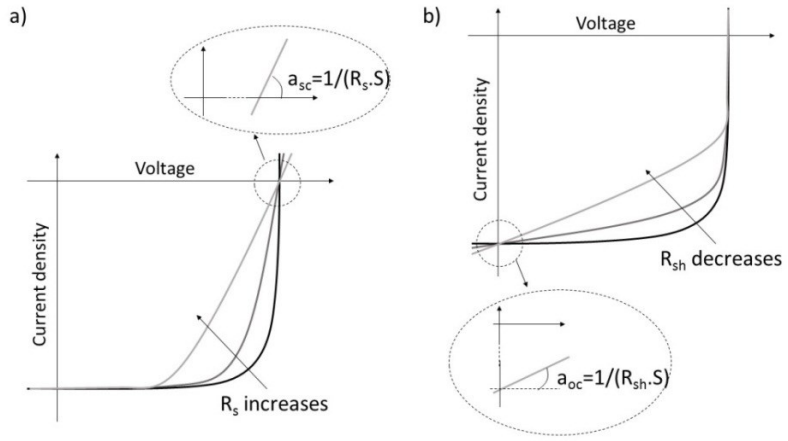

Figure 2. 22: J-V characteristics of PV devices under illumination when a) the series resistance Rs increases with an infinite shunt resistance R_{sh} and b) R_{sh} decreases with R_s fixe at zero. a_{sc} is the slope of the J-V curve in open circuit conditions (J=0) and a_{oc} is the slope of the J-V curve in short circuit conditions (V=0). S is the surface of the active area of the device.

2.2.5.2. Device structure and materials used

The architecture used in this work was an inverted structure as presented on Figure 2.21.[40]

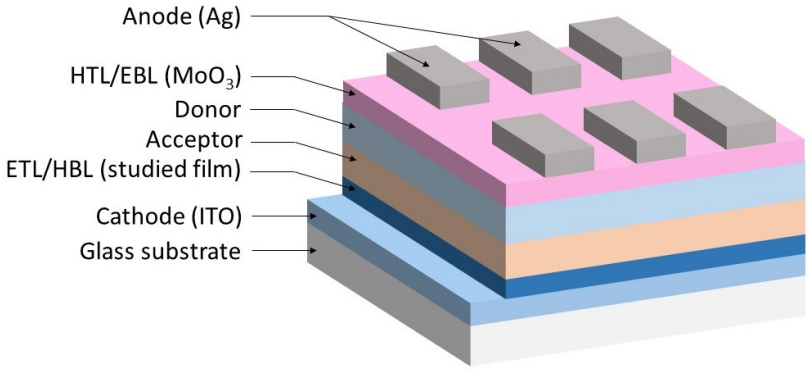

Figure 2. 23: Schematic of the type of OPV device used in this work. HTL and ETL being the hole and electron transporting layer respectively. HBL and EBL being the hole and electron blocking layer respectively.

The studied part of the device is the electron transporting layer (ETL) which was deposited by PLD on ITO/Glass substrates. The active layer was prepared from a 1:1 blend of P3HT:ICBA diluted at 40 mg/mL in chlorobenzene and spin coated at 2000 rpm and for 40 s on the ETL. Finally 10 nm of molybdenum oxide (MoO_3) as the hole transporting layer (HTL) and 100 nm of silver as the metallic contact were deposited by evaporation. The performances of the devices were measured using an AM1.5 Solar Simulator. The surface of the active area under illumination, in this work is S = 0.045 cm².

References

[1] H.M. Smith, A.F. Turner, "Vacuum Deposited Thin Films Using a Ruby Laser", Appl. Opt. 4 (1965) 3–4.

[2] G. Hass, J.B. Ramsey, "Vacuum Deposition of Dielectric and Semiconductor Films by a CO2 Laser", Appl. Opt. 8 (1969) 1115–1118.

[3] D. Dijkkamp, T. Venkatesan, X.D. Wu, S.A. Shaheen, N. Jisrawi, Y.H. Min-Lee, et al., "Preparation of Y-Ba-Cu oxide superconductor thin films using pulsed laser evaporation from high Tc bulk material", Appl. Phys. Lett. 51 (1987) 619.

[4] R. Eason, "Pulsed Laser Deposition of Thin Films: Applications-Led Growth of Functional Materials", John Wiley & sons, 2006.

[5] H. Krebs, M. Weisheit, S. Erik, T. Scharf, C. Fuhse, M. St, et al., "Pulsed Laser Deposition (PLD) - a Versatile Thin Film Technique UHV-chamber", Adv. Solid State Phys. 43 (2003) 505–517.

[6] M. V. Allmen, A. Blatter, "Laser-Beam interactions with materials: physical principles and applications", Springer S, 1995.

[7] H. Kim, R.C.Y. Auyeung, a. Piqué, "F-doped SnO2 thin films grown on flexible substrates at low temperatures by pulsed laser deposition", Thin Solid Films. 520 (2011) 497–500.

[8] S. Amirhaghia, V. Craciun, D. Craciuna, J. Elder, I.W. Boyda, "Low temperature growth of highly transparent by pulsed laser deposition c-axis oriented ZnO thin films", Microelectron. Eng. 25 (1994) 0–5.

[9] J. Kim, S. Lee, "The effect of target density and its morphology on TiO2 thin films grown on Si(100) by PLD", Appl. Surf. Sci. (1999) 6–16.

[10] C.R. Foschini, L. Perazolli, J.A. Varela, "Sintering of tin oxide using zinc oxide as a densification aid", J. Mater. Sci. 39 (2004) 5825–5830.

[11] J. Liu, W. Ning, "Influence of ZnO addition on the sintering properties of SnO2 electrode", J. Mater Sci. 44 (2009) 2520–2524.

[12] F. Claeyssens, A. Cheesman, S.J. Henley, M.N.R. Ashfold, "Studies of the plume accompanying pulsed ultraviolet laser ablation of zinc oxide", J. Appl. Phys. 92 (2002) 6886.

[13] L. Mcconville, N.J. Ianno, N. Shaikh, S. Pittal, P.G. Snyder, "Characterization of pulsed laser deposited zinc oxide", Thin Solid Films. 220 (1992) 92–99.

[14] V. Craciun, D. Craciun, "Evidence for volume boiling during laser ablation of single crystalline targets", Appl. Surf. Sci. 138-139 (1999) 218–223.

[15] K. Ellmer, A. Klein, B. Rech, "Transparent Conductive Zinc Oxide: Basics and Applications in Thin Film Solar Cells", 2007.

[16] K.R. Chen, J.N. Leboeuf, R.F. Wood, D.B. Geohegan, J.M. Donato, "Mechanisms affecting kinetic energies of laser-ablated materials", J. Vac. Sci. Technol. A Vacuum, Surfaces, Film. 14 (1996) 1111.

[17] H.S. Kwok, H.S. Kim, D.H. Kim, W.P. Shen, X.W. Sun, R.F. Xiao, "Correlation between plasma dynamics and thin film properties in pulsed laser deposition", Appl. Surf. Sci. 109-110 (1997) 595–600.

[18] G. Franceschinis, "Surface Profilometry as a tool to Measure Thin Film Stress, A

Practical Approach.", (2005). http://people.rit.edu/lffeee/stress_measurement.pdf.

[19] B.D. Cullity, "Elements of X-ray diffraction", 1953.

[20] D.K. Schroder, "MATERIAL AND DEVICE SEMICONDUCTOR MATERIAL AND DEVICE Third Edition", John Wiley & sons, 2006.

[21] E. Stefanaki, "Electron Microscopy : The Basics", (2008) 1–11.

[22] K. Kanaya, S. Okayama, "Penetration and energy-loss theory of electrons in solid targets", J. Phys. D. Appl. Phys. 5 (2002) 43–58.

[23] C. Nordling, S. Hagstrom, K.A.I. Siegbahn, "Application of Electron Spectroscopy to Chemical Analysis", Zeitschrift Fur Phys. 178 (1964) 433–438.

[24] R. Smart, S. McIntyre, M. Bancroft, I. Bello, "X-ray Photoelectron Spectroscopy", (n.d.). http://mmrc.caltech.edu/SS_XPS/XPS_PPT/XPS_Slides.pdf.

[25] C.G. Fonstad, R.H. Rediker, "Electrical Properties of High-Quality Stannic Oxide Crystals", J. Appl. Phys. 42 (1971) 2911.

[26] L.J. van der Pauw, "A method of measuring specific resistivity and Hall effect of discs of arbitrary shape", Philips Res. Reports. 13 (1958).

[27] K. Ellmer, "Characterization of Materials", Sons, John Wiley &, 2012.

[28] J. Lindemuth, S.-I. Mizuta, "Hall measurements on low mobility materials and high resistivity materials", Thin Film Sol. Technol. III. 8110 (2011) 81100I–81100I–7.

[29] J.S. Park, W.-J. Maeng, H.-S. Kim, J.-S. Park, "Review of recent developments in amorphous oxide semiconductor thin-film transistor devices", Thin Solid Films. 520 (2012) 1679–1693.

[30] H. Klauk, "Organic thin-film transistors.", Chem. Soc. Rev. 39 (2010) 2643–66.

[31] E. Fortunato, P. Barquinha, R. Martins, "Oxide semiconductor thin-film transistors: a review of recent advances.", Adv. Mater. 24 (2012) 2945–86.

[32] A. Bashir, "High-performance Zinc Oxide Thin-Film Transistors For Large Area Electronics", (2011).

[33] M. Nonnenmacher, M.P. O'Boyle, H.K. Wickramasinghe, "Kelvin probe force microscopy", Appl. Phys. Lett. 58 (1991) 2921.

[34] W. Melitz, J. Shen, A.C. Kummel, S. Lee, "Kelvin probe force microscopy and its application", Surf. Sci. Rep. 66 (2011) 1–27.

[35] Y. Rosenwaks, R. Shikler, T. Glatzel, S. Sadewasser, "Kelvin probe force microscopy of semiconductor surface defects", Phys. Rev. B. 70 (2004) 085320.

[36] H. Lüth, "Solid Surfaces, Interfaces and Thin Films", Springer, 2010.

[37] M.G. Helander, M.T. Greiner, Z.B. Wang, Z.H. Lu, "Pitfalls in measuring work function using photoelectron spectroscopy", Appl. Surf. Sci. 256 (2010) 2602–2605.

[38] Shimadzu, "Measurements of Band Gap in Compound Semiconductors - Band Gap Determination from Diffuse Reflectance Spectra", (n.d.) 2–3. http://www2.shimadzu.com/applications/UV/VIS/A428.pdf.

[39] T. Markvart, L. Castañer, "Practical Handbook of Photovoltaics: Fundamentals and Applications", Elsevier, 2003.

[40] T.-H. Lai, S.-W. Tsang, J.R. Manders, S. Chen, F. So, "Properties of interlayer for organic photovoltaics", Mater. Today. 16 (2013) 424–432.

Chapter 3: Study and control of intrinsic defects in undoped SnO_2

SnO_2 has been used in multiple applications such as conducting electrodes, transparent transistors, photovoltaics, sensors and LEDs[1–5] but the origin of its conductivity has yet to be fully understood. While several theoretical analyses were focused on the intrinsic defects responsible for its n-type conductivity, few studies correlate these results to the experimental work. This is particularly true in the development of p-type conductivity in SnO_2 where the formation of n-type defect must be controlled. Although p-type doping of SnO_2 using extrinsic dopants such as Al[6], Ga[7], In[8] and Zn[9] has been reported, few of these studies take in consideration the importance of controlling the growth environment and establishing "p-type compatible" conditions. The electrical performances of the films are highlighted rather than the defect mechanism behind it. The formation energy of defects is related to the amount of oxygen in the system and thus their control implies a regulation of the oxygen content during the deposition.

PLD is a versatile deposition technique suited for this type of study. As mentioned in section 2.1 it is a vacuum deposition technique, *i.e.* deposition in confined environment, and allows good control of the film growth through its variables such as temperature, oxygen pressure, laser fluence, repetition rate and pulse duration.[10,11] PLD has been used as a tool to deposit epitaxial or low resistivity SnO_2 thin films[1,12,13] however up to date no clear investigation on the origin of the variations in conductivity has been carried. This particular part is essential in the control of defect formation through the deposition parameters, be it for n-type TCOs where donor defects are required or for p-type doping where intrinsic donor defects must be limited. The study of point defects function of the environment has been mostly investigated theoretically while PLD offers efficient control over the deposition conditions.

The study in this chapter is split in 4 parts. A first preliminary investigation on primordial parameters such as laser fluence and sample positioning is carried out. The second and third parts are focused on the variation of simple deposition parameters such as deposition temperature (T_D) and oxygen pressure (P_D) to show relative control over defect formation can be achieved by carefully selecting them. Particular attention will be paid upon the determination of a "p-type compatible" environment for which T_D and P_D limit

the formation of n-type defects. Finally the interest is brought on the influence of the target composition on the properties of the films.

1. Determining optimum pulsed laser deposition parameters

1.1. General conditions

1.1.1. Target used

The preparation of pure SnO_2 ceramic targets for PLD using SnO_2 powders is known to be problematic.[14] Here, sintering tests were performed under different conditions (1000-1300 °C for 10h in air) however the densities of the targets were less than 50 % of the theoretical maximum density of SnO_2 (6.95 g/cm^3). Similar results have been reported by Lee *et al.*[15]. Sintering process such as 10 h at 1000 °C were applied to SnO_2 compacted powder, but they observed no densification occurred during the sintering, with densities between 33 and 55 % of the theoretical maximum of SnO_2. In this case, the use of additives or dopants is required to promote the densification. Zn has been identified as a densification aid for SnO_2 and this matter is discussed in appendix 1. Since the preparation of a pure SnO_2 target requires additives, a commercial target was used with a purity of 99.99 % and a density > 95 %.

1.1.2. Laser parameters

In the literature, the PLD of SnO_2 thin films performed with a KrF excimer laser has been reported at various laser fluences. The selection of the laser fluence generally varies with the repetition rate and pulse duration associated. Several reports associated a fluence between 4 and 6 J/cm^2 with a repetition of 30 Hz but a small pulse duration of 12 ns.[16–18] Other reports[19,20] mention a higher pulse duration (25 ns) associated with lower repetition rate (< 10 Hz) and fluence (1-2 J/cm^2) to avoid the projection of liquid droplet on the film from the melting of the target surface.[10] The laser system used in this work allows a pulse duration of 25 ns and a repetition rate between 1 and 10 Hz. In order to determine the optimum laser fluence for the depositions, the repetition rate was fixed at 8 Hz and the fluence varied between 1.6 and 3 J/cm^2. The films were deposited at a substrate temperature (T_D) of 300 °C and under a background oxygen pressure (P_D) of 50 mTorr. The SEM images shown on Figure 3.1 highlight the presence of micron size droplets ejected from the target during the deposition for films deposited at fluence > 2.4 J/cm^2.

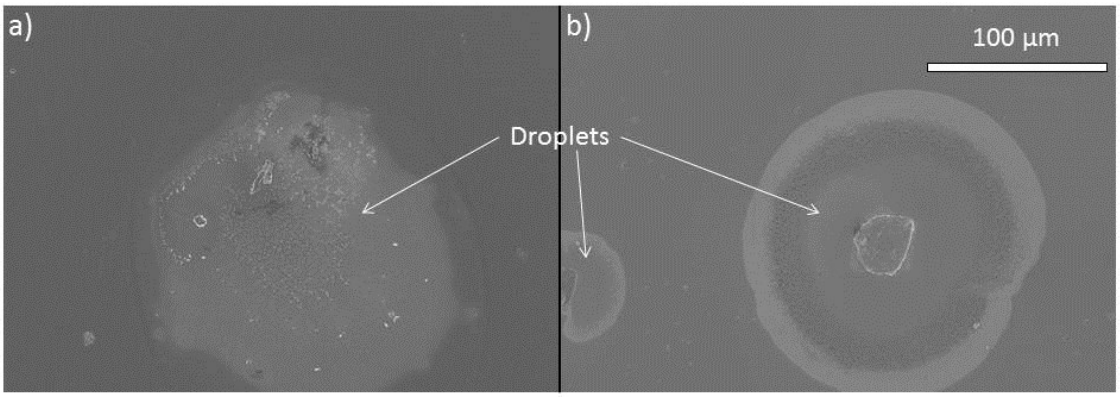

Figure 3. 1: Scanning electron microscope images of SnO_2 films deposited at 300 °C and under 50 mTorr displaying the presence of droplets on the surface of the films at laser fluence a) 2.7 J/cm² and b) 3 J/cm².

A fluence of 2.4 J/cm² appears to be the limit for the system used for the formation of surface droplets on the film. Therefore to avoid their formation the fluence corresponding to 2.2 J/cm² is used for all the experiments. This fluence is in agreement with some reports using similar pulse duration and repetition rates.[19,20] Even though the formation of droplets cannot be completely suppressed it can be limited by controlling the laser energy, in this case the fluence.[10]

1.1.3. Substrates

The SnO_2 films were deposited on three different substrates; i) 10 mm x 10 mm quartz, ii) single crystal (100) oriented silicon and iii) ITO coated glass.

i) 10 mm x 10 mm square quartz

These substrates were used to provide a non-conductive, symmetrical substrate for the Hall measurements using the Van der Pauw configuration. Quartz was selected for its transparency in the UV-visible region and for its thermal stability. It is not mentioned in this chapter but the quartz samples are also used to sustain high temperature annealing (up to 700 °C).

ii) Single crystal (100) oriented silicon

Silicon substrates were used to perform X-Ray diffraction (XRD) analysis without having the broad amorphous peak associated with the quartz substrate. They also provide a conductive base and are suited for X-ray Photoelectron spectroscopy (XPS). Their conductive behaviour is used in chapter 4 to perform KP as a conductive layer below the thin films is required to evacuate the electrons and ITO substrates do not resist high temperatures (above 700 °C).

iii) ITO coated glass

Commercial ITO coated glass samples of 12 mm x 12 mm with 12 mm x 8 mm active area were used for KPFM analysis as a conductive substrate is required to avoid any charging effect on the sample.

1.2. Effect of spatial distribution of the plasma plume

PLD is well known for its limitations in large area deposition and its non-uniformity in the spatial distribution of deposited material.[10] Due to the highly oriented plasma plume, more material is deposited at the centre of the plume.[21] However Hall measurement of thin films requires homogenous film thickness. In order to observe the spatial distribution of the plasma plume, SnO_2 thin films were deposited at 600 °C and 100 mTorr on glass, Si and ITO substrates. The substrates were distributed at defined positions on the sample holder (within a 5 cm diameter circular surface) allowing us to perform thickness, XRD and KPFM measurements. Series of 3000 laser pulses at 8 Hz were performed during each deposition (375 s). The thickness and work function spatial distributions are displayed in Figure 3.2. The work function (WF) represents the energy difference between the vacuum level and the Fermi level of the material.

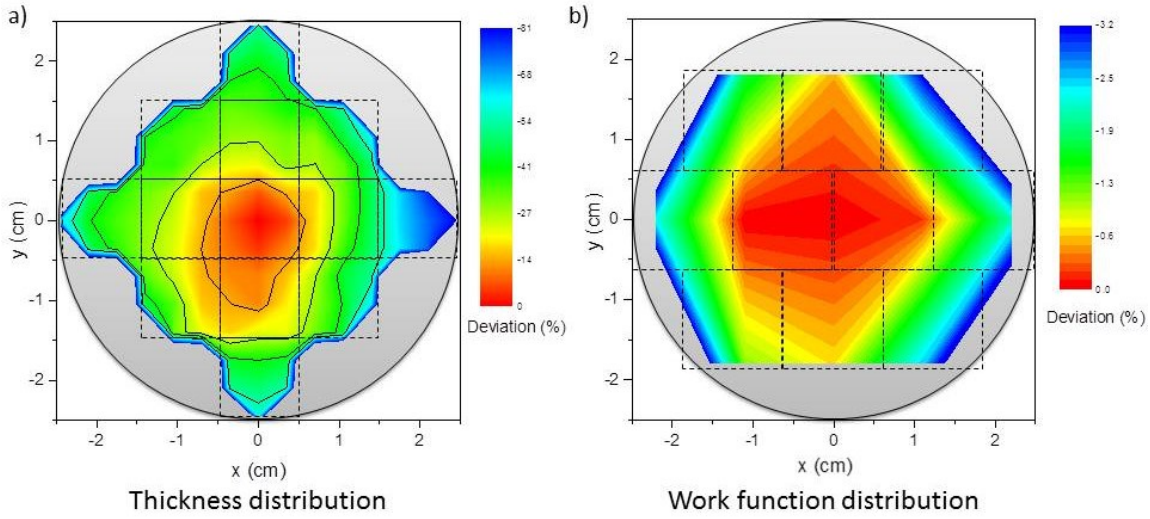

Figure 3. 2: Spatial distribution of SnO_2 films deposited at 600 °C and under 100 mTorr showing a) the film thickness across the sample holder (grey circle) and b) the work function (WF) of the samples. The scales show the deviations from the centre of the plume (x = y = 0). The point at the centre is represented by a thickness of 364 nm and a WF of 4.56 eV. The dotted squares represent the emplacements of the substrates.

In the case of the thickness distribution 13 glass substrates (dotted squares in Figure 3.2.a) were used with 9 points measured on each sample. Regarding the WF distribution, only 10 ITO substrates were used as they are larger (12 mm x 12 mm) and only one

measurement was performed on each sample due to averaging of the KP technique and the difficulty to position the probe at a specific area of the sample. The thickness profile shown on Figure 3.2.a shows a significant decrease of thickness from the centre (364 nm) to the edge (69 nm). This shows important differences in growth rate with the position of the sample. It varies from 0.97 nm/s in the centre to 0.17 nm/s at the edge. The most important drop in thickness seems to appear after the region [-0.5 cm < x < 0.5 cm] and [-1.5 cm < y < 0.5 cm]. Outside this region deviations above 20 % of the central thickness are observed. The most uniform region remains the core centre [-0.5 cm < x < 0.5 cm] and [-0.5 cm < y < 0.5 cm] where the deviations do not exceed 10 %. This region is identified as ideal for the deposition of the films on quartz substrate subject to Hall measurements as its shows the most homogenous thickness. However the centre of the plume is not necessarily at the centre of the substrate holder. It depends on the area of the target where the laser is focused, and on the surface of the target (if it is flat or not). For fresh targets the centre of the plume is generally the centre of the holder but for targets exposed to multiple laser pulses the centre of the plume moves away from the centre of the holder as the laser etches the target and its surface is not flat anymore.

Even though the non-uniformity of the spatial distribution of the deposited material in PLD is often correlated to a non-homogenous thickness profile it is not the main problem. As shown on Figure 3.2.b, not only the thickness is non-uniform but also the properties of the film, in this case the WF. Due to the non-homogeneity of the plume the kinetic energy form the species is different within the plume.[22] Changes in the particle energy are accompanied by systematic modification of texture and microstructure.[11] These changes induce variation of the properties of the film such as WF which is directly related to the Fermi level. The position of the Fermi level is known to be linked to the growth orientation of a material.[23]

The XRD data of SnO_2 films deposited at 600 °C and 100 mTorr with the substrate placed at the centre of the plume is shown in Figure 3.3.

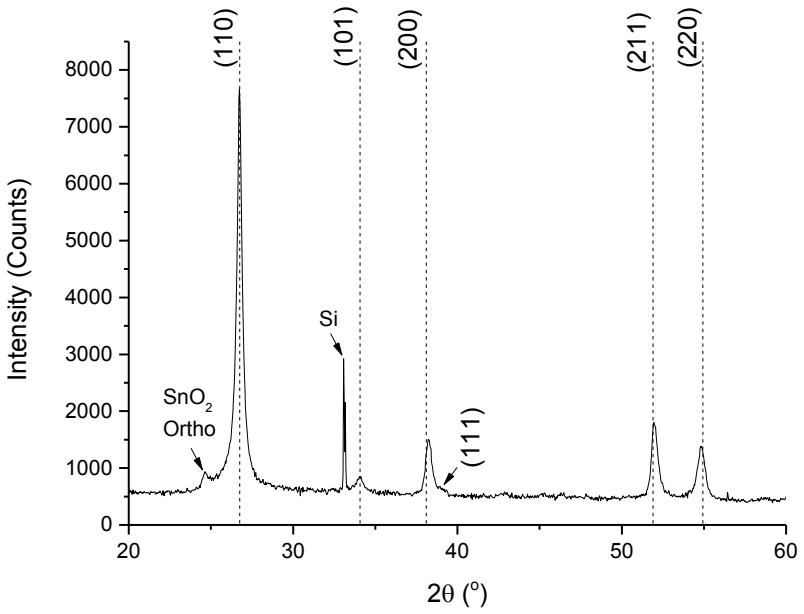

Figure 3. 3: X-Ray diffraction data of SnO_2 film deposited on Silicon substrate at 600 °C and under an oxygen background pressure of 100 mTorr. The main diffraction peaks from SnO_2 power pattern are represented by dotted lines.

Five main diffraction peaks appear at 2θ: 26.7, 34.1, 38.2, 52.0 and 54.9 °. The peak located at 33.1 ° belongs to the Silicon substrate. From the peak positions observed, it can be confirmed that SnO_2 films with a rutile structure were grown and the diffraction peaks belong respectively to the (110), (101), (200), (211) and (220) planes. A small presence of some (111) orientation can also be observed at 39 °. The films deposited are not purely formed of rutile SnO_2 as some trace characteristic of the (110) orthorhombic form of SnO_2 is detected at 24.6 °. Generally a single peak is not enough to characterize the presence of a structure but regarding the element present during the analysis, Sn, O and Si, only this plane matches the diffraction peak observed. Its presence is recurrent during the depositions and has also been observed in literature.[24] However the intensity of this peak is small compared to other diffraction peak and thus the orthorhombic phase is considered to be present in negligible quantities. All the properties of the films are attributed to the rutile phase observed.

In order to consider the impact of the non-uniformity of the plasma plume on the crystalline growth, the plume profile analysis has also been carried out through XRD. As the main orientation remains the (110) regardless of the substrate position and as the peak intensity is thickness related, the variation from the (101) to the (200) orientations were investigated. Figure 3.4 shows the spatial distribution of the ratio between the intensity of the (101) and the (200) diffraction peaks.

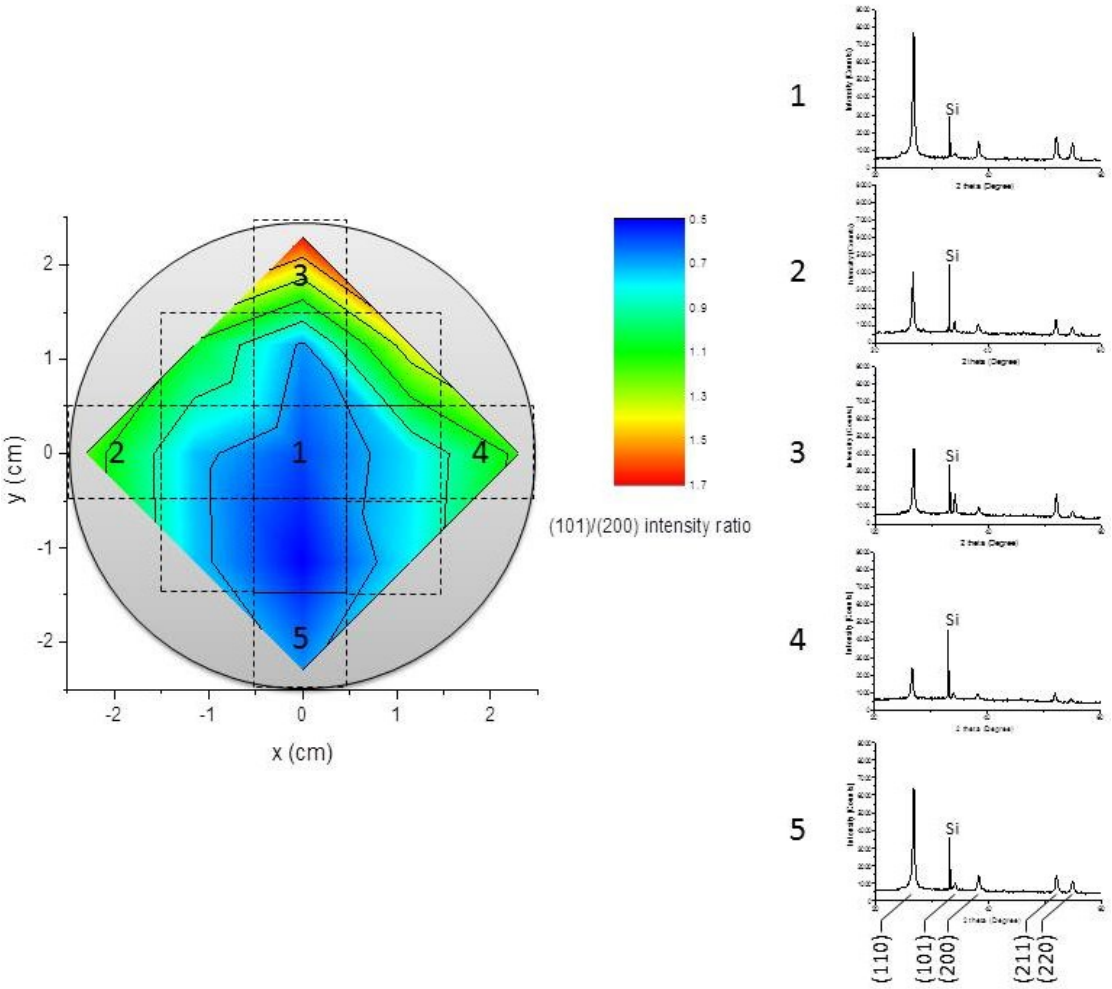

Figure 3. 4: Spatial distribution of SnO_2 films deposited at 600 C and under 100 mTorr showing intensity ratio between the (101) and the (200) diffraction peaks. The XRD data of several points (1-5) is displayed on the right. The dotted squares represent the emplacement of the Si substrates used.

13 Si substrates were used and since XRD scans the whole sample only one measurement per sample was performed. It can be observed from the WF distribution and from the secondary orientation intensity ratio that the deviation from the centre of the holder is less important than with the thickness profile. In the case of the WF profile the region of [-1 cm < x < 1 cm] and [-1 cm < y < 1 cm] shows the least deviation with only 5 % corresponding to a variation of 0.02 eV from the centre. The growth orientation of a wider region of [-1 cm < x < 1 cm] and [-2 cm < y < 1 cm] has been identified to contain the lowest deviation.

Considering these measurements it is fair to assume that the region [-0.5 cm < x < 0.5 cm] and [-0.5 cm < y < 0.5 cm] is the most uniform in term of thickness and film properties (considering only the WF and the growth orientation), and that the substrates used for the depositions should be placed in this particular region. Furthermore the shape of the plume

is subject to the oxygen background pressure used during the deposition and is known to be more compressed at higher P_D.[10] This leads to a more focused plume and an even larger non-uniformity of the material deposited, thus a larger error outside the centre of the plume.

2. Influence of deposition temperature on SnO_2 thin films

In order to observe the behaviour of intrinsic point defects in SnO_2 with the deposition temperature (T_D), the films were deposited under fixed oxygen background pressure of 100 mTorr while varying T_D between 300 and 700 °C. The films were deposited on quartz, silicon (100) and ITO covered glass substrates.

2.1. Crystalline structure

The XRD data for the SnO_2 films deposited between 300 and 700 °C is shown on Figure 3.5 along with the stick pattern corresponding to the SnO_2 diffraction peaks.

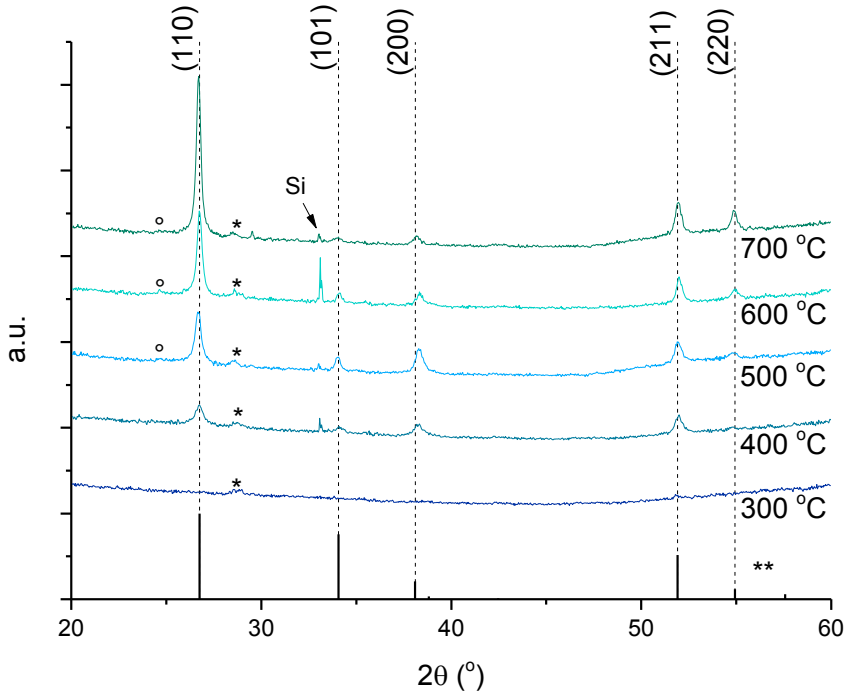

Figure 3. 5: XRD data for the SnO_2 films prepared at a fixed oxygen pressure of 100 mTorr with temperature varied from 300-700 °C. The major peaks identified belong to SnO_2 phase and are represented on experimental data with stick reference pattern (**) and dashed lines derived from ICDD 01-077-0452. The Si substrate peaks are clearly identified in addition to a small peaks attributed to a minor SnO phase (*) and a minor orthorhombic SnO_2 phases (o).

The films grown exhibit mainly the Cassiterite phase (rutile SnO_2) with some presence of orthorhombic SnO_2 and SnO at a 2θ angle of 24.6 and 29 °, respectively, but in very low quantity. The crystallinity seems to start only at T_D of 400 °C, below which the films are

amorphous. The crystalline films exhibit a strong (110) orientation with diffraction from the (101), (200) and (211) planes to different extents. The growth orientations obtained are coherent with the literature[25] and as expected from previous studies the crystallinity of the films, given by the intensity of the diffraction peaks, increases with temperature.[26]

Since the position of the plane's diffraction peaks is linked to the magnitude of the d-spacing between crystallographic planes, a shift of the peak position is attributed to a variation in the d-spacing size. When measuring the changes of 2θ of a diffraction peak, the error is reduced at higher angles as d-spacing varies as a function of 1/sinθ. Therefore a small variation of 2θ at small angles lead to a large variation of d, while at large angles the variation has much less impact on the d-spacing. For this reason the d-spacing was extracted from the (200) peak observed despite its lower intensity. Another reason is that in chapter 4, (200) is the dominant peak and the values are compared to this chapter. The variation of the (200) diffraction peak function of T_D are shown in Figure 3.6.a. The peak shifts observed are related to changes in the a-lattice parameter through the d-spacing. This can be calculated using Equation 3.1, here h, k and l are the Miller indexes of the diffracting planes:

Equation 3.1

$$\frac{1}{d^2} = \frac{h^2+k^2}{a^2} + \frac{l^2}{c^2}$$

The calculated a-lattice parameters are shown on Figure 3.6.b.

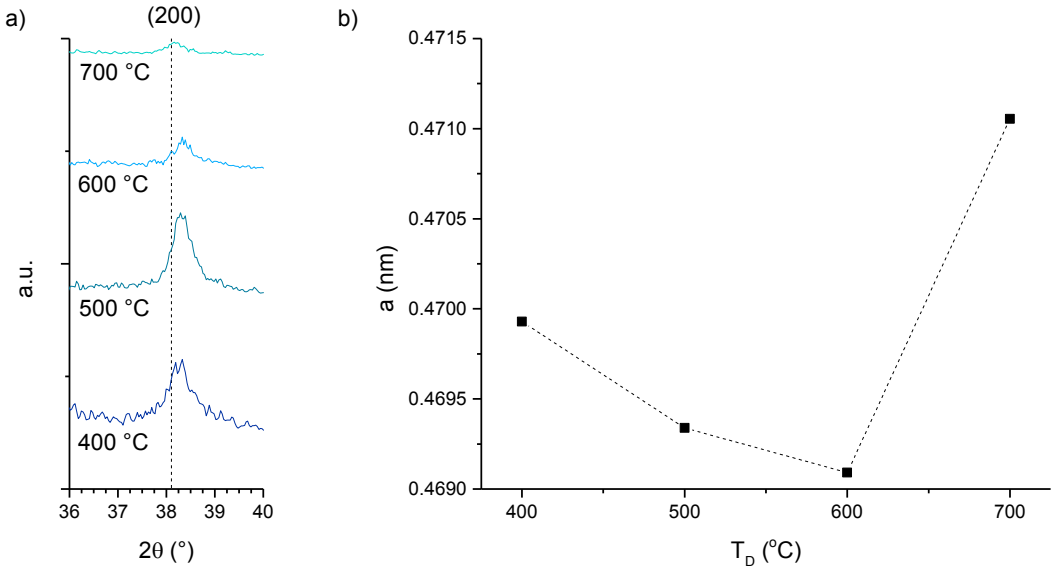

Figure 3. 6: a) XRD data of deposited SnO_2 under 100 mTorr showing the shift in (200) peak. b) Calculated a-lattice parameter from the XRD (200) peak shift function of the deposition temperature.

From 400 to 600 °C a shift of the (200) diffraction peak towards higher angles is observed. This is translated by a decrease of the lattice parameter a in this range of temperature however for the film deposited at 700 °C a shift towards lower angle appears and thus an important increase of the a-lattice parameter. Such changes are indicative of intrinsic point defects in the films. In section 1.2.2.1 the impact of the some defects on the strain in the lattice has been discussed. It has been noted that while tin interstitials induced an increase of the lattice size in its ionized form ($Sn_i^{\cdots}$), the presence of V_O can either compress or expand the lattice size function of its charge state. A doubly charged oxygen vacancy ($V_{\ddot{O}}$) increase the size of the lattice due to Coulombic repulsion but in the case of a neutral oxygen vacancy (V_O^x) the three nearest Sn atoms have been found to relax inwards, leading to a compression of the lattice.[27] Oxygen interstitials would also induce an increase of the lattice size.[28] In order to probe the origin of these lattice size variations, Hall measurements, KP and band gap extractions have been carried out in the next section.

2.2. Electrical properties and identification of defect species

The carrier concentrations of the deposited films have been extracted through AC Hall measurements and are shown in Figure 3.7.

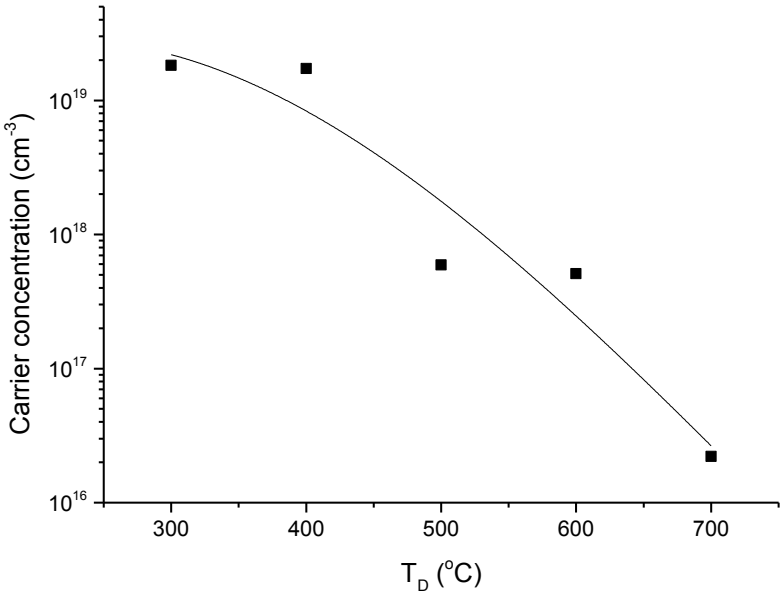

Figure 3. 7: Charge carrier (electron) concentrations of the SnO_2 films deposited over the temperature range 300–700 °C, measured by AC Hall effect.

The data indicates a clear reduction in the n-type charge carrier concentration by about 3-orders of magnitude (from 2 x 10^{19} to 2 x 10^{16} cm^{-3}) with increasing temperature. This suggests either the decrease of n-type donor defects (Sn_i and V_O) or the formation of p-

type acceptor defects (O_i). As the carrier concentration drops past 400 °C, the behaviour of the resistivity is partly ruled by it and the conductivity of the films decreases with increasing temperature as shown in Table 3.1.

Table 3. 1: Details of SnO_2 films thickness, sheet resistance, Hall resistivity, carrier concentration, Hall mobility, band gap (extracted by UV-Vis) and work function (WF). The dotted line above T_D of 300 °C separates films which are mostly amorphous to crystalline films.

T_D °C	Thickness nm	Hall resistivity Ω.cm	Carrier concentration cm^{-3}	Hall mobility $cm^2/(V.s)$	Band gap eV	WF eV
300	143	1.63	1.83×10^{19}	0.21	3.28	4.75
400	141	2.91×10^{-1}	1.73×10^{19}	1.24	3.64	4.58
500	136	2.12×10^{1}	5.92×10^{17}	0.50	3.64	4.54
600	130	1.44×10^{2}	5.11×10^{17}	0.09	3.65	4.55
700	127	2.93×10^{3}	2.21×10^{16}	0.10	3.69	--

The optical band gap (E_g) values of the films were extracted using the Tauc plot method for direct band gap semiconductors and are displayed alongside the WF measured by KP in Figure 3.8.

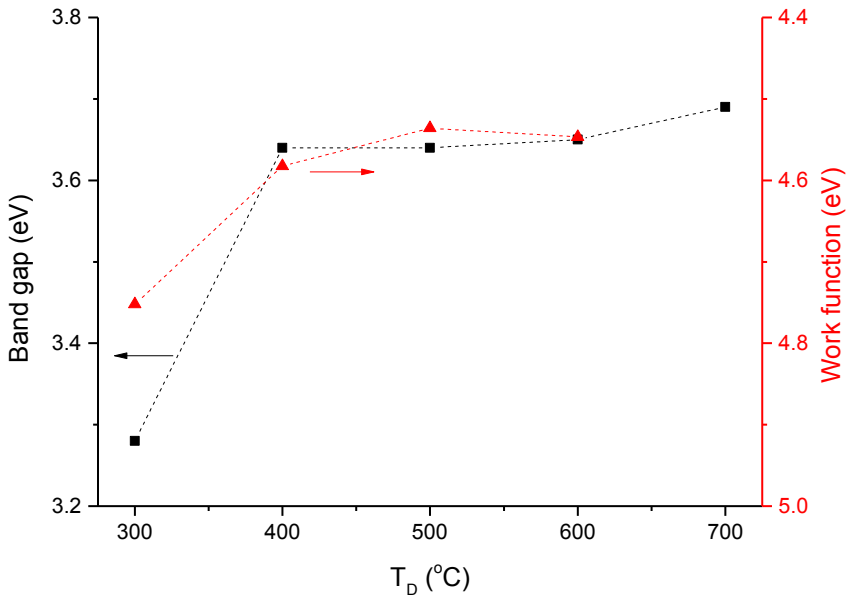

Figure 3. 8: Data of the optical band gap calculated from Tauc analysis of UV-Vis data and measured WF of the films deposited over the temperature range 300–700 °C measured by KP.

Above 400 °C, the E_g values are around 3.6 eV which is in agreement with results found in literature.[29] At 300 °C a drop of almost 0.4 eV is observed and E_g reaches its lowest value of 3.28 eV. Alongside the low value of E_g, the Fermi level (E_F) is found to drop at this

temperature as well (through the WF measurement). This has been attributed to a band tailing effect which is common in amorphous semiconductors.[30]. The WF position is a product of the electron chemical potential and surface dipole. The surface dipole is affected by the surface roughness of the film[31–33] and the most exposed crystal surface[23] which is the main crystalline orientation. Thin films deposited by PLD have been known for their low roughness.[10] The smoothness of the deposited films is apparent from the Fabry-Perot interference fringes[34] observed in Figure 3.9 showing the UV-Vis data and the band gap extraction of the films.

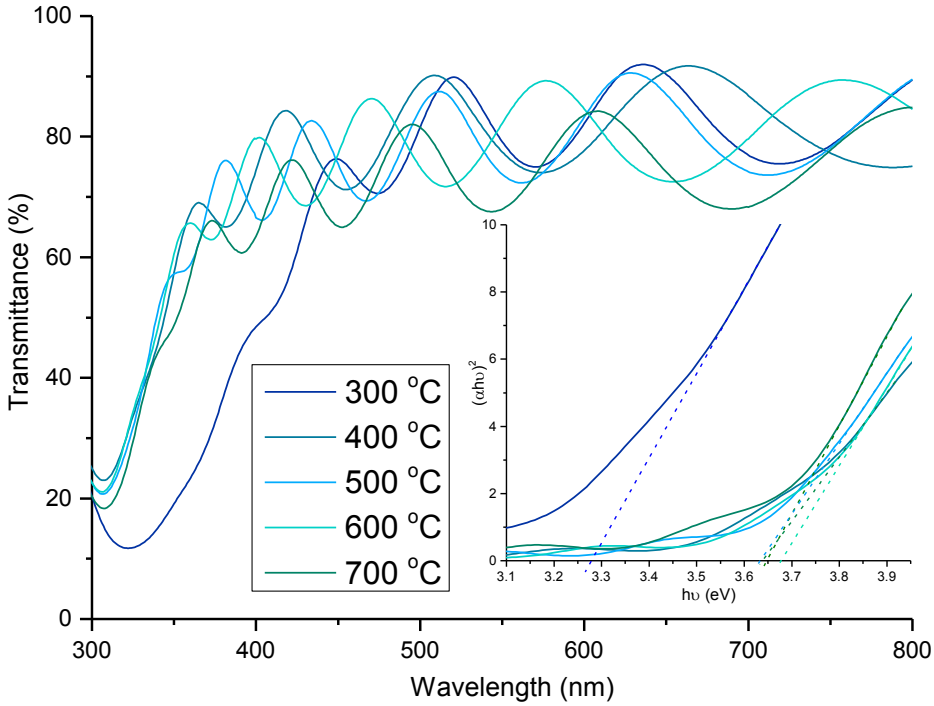

Figure 3. 9: UV-Visible spectroscopy of the SnO_2 films deposited within the range of temperature 300-700 °C and measured between 300 and 800 nm. The second data in the smaller Figure represents the Tauc plot to extract the values of E_g from the deposited films.

The deposited films present a remarkably flat surface and the main growth orientation remains along the (100) crystallographic plane over the range of T_D investigated. Based on this it seems reasonable to assume that the contribution from the surface dipole is negligible compared with the electron chemical potential which is directly influenced by the phase and structure of the films, their stoichiometry and the presence of defects.[35] More precisely, the existence of intrinsic or extrinsic defects is known to have a direct impact on the position of E_F.[36–38] They can form additional occupied or unoccupied states within or outside the band gap changing the carrier concentration and shifting the E_F consequently. In Figure 3.10 the energy levels of some crystalline point defects present in the SnO_2 system are shown. This diagram gathers the different defect transition levels,

ε(q/q') where q and q' are two charge states of the defect, extracted from literature calculations. In most models used in such calculations, *i.e.* local-density approximation (LDA)[39] or the hybrid density functional theory (DFT)[40], the value of the band gap is underestimated and the energy level of these defects is subject to variation. Therefore the defects energies represented in Figure 3.10 are an approximation of where their transition energy levels would lie.

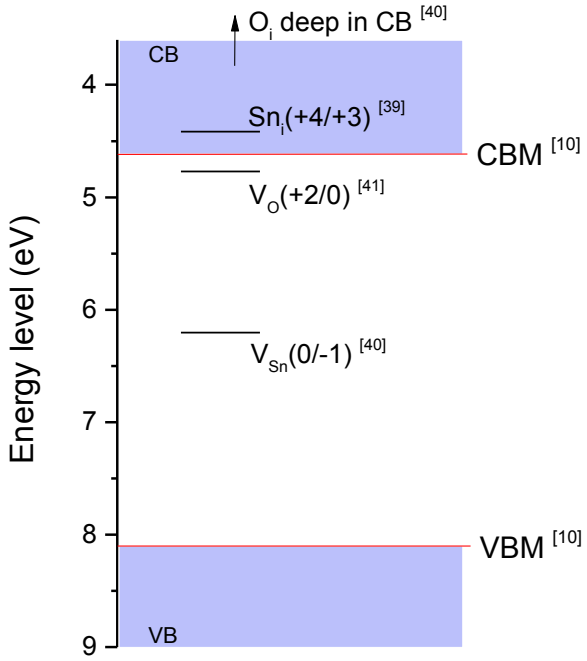

Figure 3. 10: Schematic representation of defect transition levels in SnO_2 in the form D(q/q') where D is the defect, q the charge of the defect below the transition level and q' the charge above it (values extracted from [39–41]. Valence band (VB) and conduction band (CB) represented in blue blocks. The Valence Band Maximum (VBM) and the Conduction Band Minimum (CBM) are represented by a red line. (values extracted from [10]).

As mentioned in chapter 1, the charge of the defect is defined by the position of the E_F related to its associated transition energy level ε(q/q'). Oxygen vacancies (V_O) have been found to create a donor level 0.115 eV below the conduction band minimum (CBM) for $\varepsilon_{V_O}(+2/0)$[39]. Therefore ionisation occurs only if E_F lies below this level, otherwise the defect remains neutral. Based on the literature, the SnO_2 CBM has been estimated to be around 4.5-4.6 eV[10,42] which would place the transition energy level of $V_O(+2/0)$ around 4.6-4.7 eV. The measurements of WF position, Figure 3.8, show that E_F lies above 4.6 eV, thus in the CB, for T_D above 400 °C. This means the V_O present in the films above 400 °C are likely to be in a neutral state. Therefore they would weakly contribute to the electrical conductivity of the film and another defect would be responsible for the loss in n-type charge carriers. Between 400 and 600 °C the decrease in a-lattice parameter, Figure 3.6, coupled with the drop in carrier concentration could correspond to a decrease of Sn_i in

the films. The final increase of a-lattice parameter at 700 °C could then be attributed to the increase of the amount of oxygen and thus a decrease of neutral V_O. The presence of oxygen interstitials (O_i) is a possibility when considering the increase of lattice size however they require an oxygen rich environment and their formation energies are higher than Sn_i or V_O. Tin vacancies, tin antisites and oxygen antisites have not been considered since their formation energy is too high.[40] Ke *et al.*[43] observed a decrease of the amount of V_O in SnO_2 films annealed at temperature higher than 500 °C attributed to an oxidation of the films. A similar behaviour of oxygen incorporation with increasing T_D in PLD has been described by Franklin[44] but in ZnO films. A compression of the c-lattice parameter indicated a decrease of the amount of Zn_i in the lattice.

Overall, the decrease of carrier concentration and resistivity with increasing T_D has been associated to an incorporation of more oxygen in the films and thus a decrease in donor type defects such as Sn_i and V_O. As T_D increases, Sn atoms possess enough energy to fully react with molecular oxygen which leads to SnO_2 films closer to stoichiometry.

Even though films deposited at 700 °C show the lowest carrier concentration observed, some problems have been encountered regarding the sample mounting and the thermal degradation of ITO (directly influencing the KP measurements). The deposition temperature of 600 °C is an appropriate balance between the processing restrictions and the limitation of donor defects, thus studies to invest the effect of the oxygen deposition pressure (P_D) were carried out at this temperature.

3. Influence of deposition oxygen pressure

To study the influence of the oxygen background pressure (P_D), SnO_2 films were deposited on quartz, Si (100) and ITO at a fixed T_D of 600 °C and under range of P_D from 5-300 mTorr.

3.1. Crystal structure

The XRD data of the deposited SnO_2 films function of the oxygen background pressure P_D is shown in Figure 3.11.

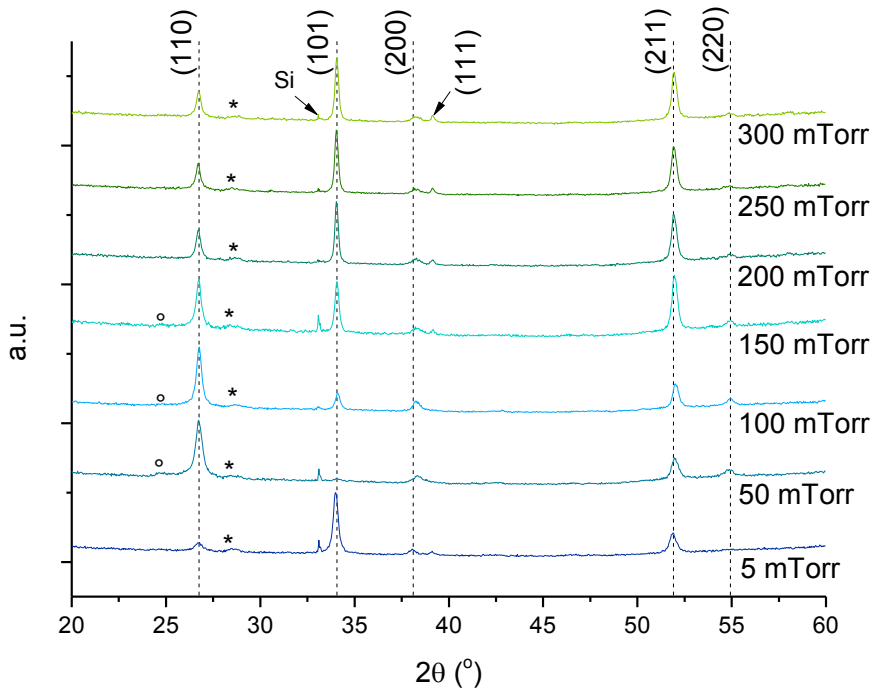

Figure 3. 11: XRD data for the SnO_2 films prepared at a fixed deposition temperature of 600 °C with deposition pressure varied from 5-300 mTorr. The major peaks identified belong to SnO_2 phase and are represented on experimental data with dashed lines derived from ICDD 01-077-0452, the Si substrate peaks are clearly identified in addition to small peaks attributed to a minor SnO phase (*) and a minor orthorhombic SnO_2 phases (o).

Similar to the temperature study the main phase present is the rutile SnO_2 with only a small amount of SnO at 29° 2θ. The films still exhibit a global (110) orientation, however the preferred orientation shifts as P_D varies. At low P_D the growth is dominated by the (101) orientation with a very small presence of the other peaks. As P_D increases to 50 mTorr the (101) preferred orientation almost disappears and leave the (110) as the main orientation with presence of (200) and (211) as well. Further increase in P_D leads to a decrease of the (110) diffraction intensity and the appearance of (101) and (211) as preferred orientations. The formation of the (101) orientation at very low P_D is characteristic of an oxygen-poor/tin-rich environment as this plane possess the lowest surface energy in these conditions.[29] This aspect is more developed in section 5.1.1. The (200) diffraction peak shifts can be observed in Figure 3.12 along with the calculated a-lattice parameter associated.

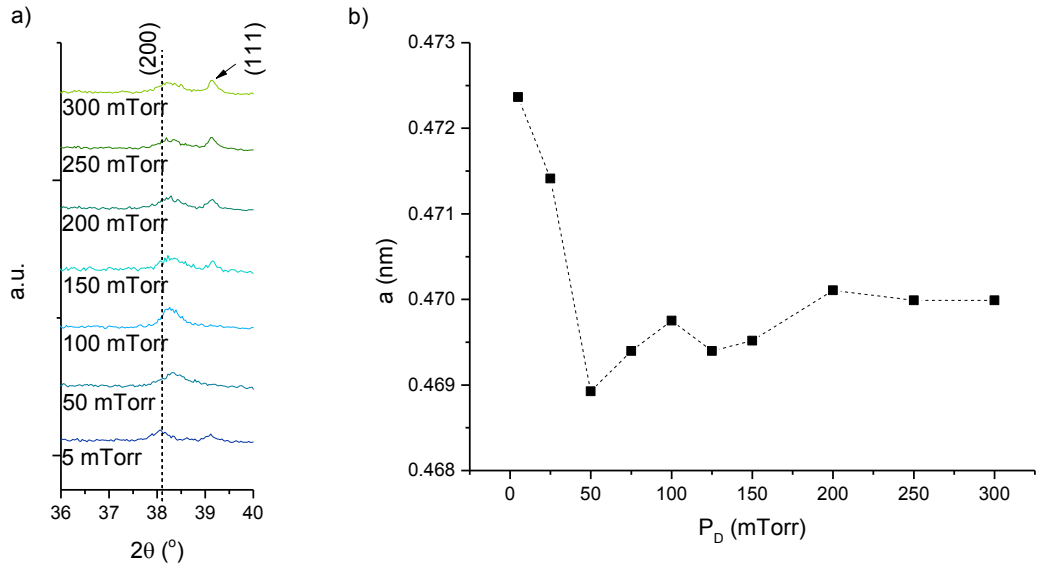

Figure 3. 12: a) XRD data of deposited SnO_2 at 600 °C showing the shift in (200) peak. b) Calculated a-lattice parameter from the XRD (200) peak shift function of oxygen deposition pressure (P_D).

A significant decrease of the a-lattice parameter is observed from 5-50 mTorr. A reduction of more than 0.3 Å is measured. Such change has been attributed to the highly energetic ablated species present in the plume as a result of the reduced interaction with the oxygen gas. In PLD the kinetic energies of the species in the ablation plume are sufficient to induce compressive stress on the films, leading to the displacement of some atoms and the formation of interstitials defects.[10,45] At such low oxygen pressure the interstitials formed cannot be from oxygen atoms. Therefore this shift of a-lattice parameter is attributed to a decrease of Sn_i defects. This theory is supported by Kiliç and Zunger[39], and Scanlon and Watson[40] who showed the formation energy of Sn_i decreases in oxygen-poor environment. Above 50 mTorr the lattice shows a subtle gradual increase until 200 mTorr which is investigated in the next part.

3.2. Electrical properties and defects involved

The evolution of the n-type charge carrier concentration can be observed in Figure 3.13. With increasing P_D an important three-order of magnitude drop of the charge carrier concentration is observed, from 1.3 x10^{19} to 1.1 x10^{16} cm^{-3}. The decrease of charge carrier concentration with increasing temperature and increasing oxygen content has also been reported in literature.[46] This results in an increase of the films resistivity as shown in Table 3.2. The decrease in carrier concentration is attributed to the incorporation of more oxygen in the films as P_D increases. This phenomenon is also observed in the shape of the plume. As P_D increases the plumes becomes more focused, this is due to more oxygen molecules interacting with the ionic species present in the plasma plume and thus more

oxygen being incorporated in the films. The plume narrowing effect has been mention in section 2.1.2.5 and illustrated with Figure 2.3. Four types of defect variation can be associated with the incorporation of more oxygen and the decrease of carrier concentration; i) a decrease of Sn_i, ii) a decrease of V_O, iii) an increase of O_i and iv) an increase of V_{Sn}.

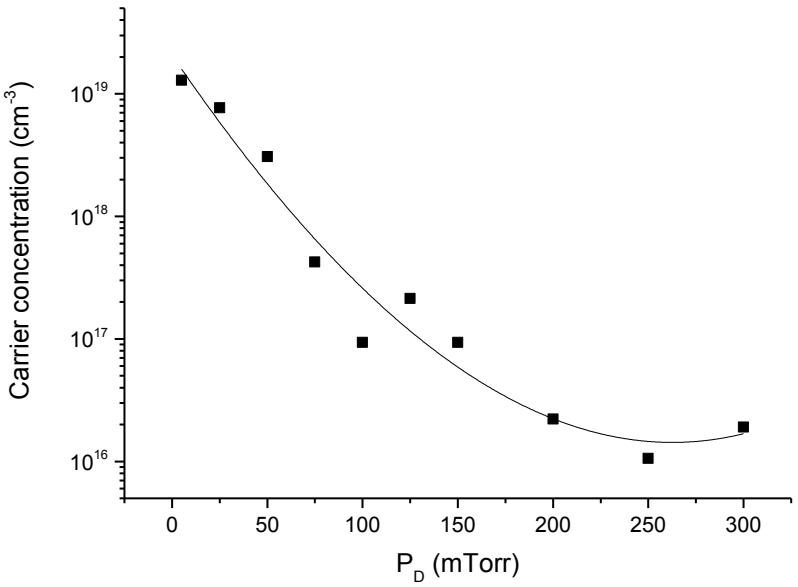

Figure 3. 13: Charge carrier (electron) concentrations of the SnO_2 films deposited over oxygen pressure range (P_D) 5-300 mTorr, measured by AC Hall effect.

The first decrease of carrier concentration from 5 to 50 mTorr has been attributed to a reduction in Sn_i. A decrease of the amount of V_O in the films is also expected as the growth environment goes from oxygen-poor to oxygen-rich. O_i and V_{Sn} are defects whose formation energy is lower under oxygen-rich environment. Although these intrinsic acceptor defects cannot be present in large quantity due to the easier formation of n-type defects (Sn_i and V_O) when E_F moves towards the valence band, they can still be present as a minority and contribute to the decrease in carrier concentration. No indications over the impact of a V_{Sn} on the lattice size have been found in the literature, however it is though that in its -4 charge state it would induce an increase of the lattice similarly to V_O. The increase in a-lattice parameter and the decrease of carrier concentration above 125 mTorr could then be attributed to the formation of V_{Sn} and O_i as secondary defects. These defects could act as traps in the films and explained the decrease in mobility observed in Table 3.2.

Table 3. 2 Details of SnO_2 films thickness, sheet resistance, Hall resistivity, carrier concentration, Hall mobility, band gap (extracted by UV-Vis) and WF function of the deposition oxygen pressure P_D.

P_D	**Thickness**	**Hall resistivity**	**Carrier concentration**	**Hall mobility**	**Band gap**	**WF**
mTorr	nm	Ω.cm	cm^{-3}	$cm^2/(V.s)$	eV	eV
5	227	2.47×10^{-2}	1.29×10^{19}	19.7	3.70	4.70
25	263	9.17×10^{-1}	7.70×10^{18}	8.84	3.74	4.60
50	301	2.01×10^{1}	3.08×10^{18}	0.10	3.62	4.66
75	301	1.44×10^{2}	4.23×10^{17}	0.10	3.67	4.65
100	300	1.10×10^{3}	9.34×10^{16}	0.06	3.69	4.68
125	298	1.88×10^{2}	2.14×10^{17}	0.16	3.72	4.67
150	302	3.19×10^{2}	9.36×10^{16}	0.21	3.71	4.68
200	310	9.24×10^{3}	2.22×10^{16}	0.03	3.66	4.87
250	315	2.68×10^{4}	1.06×10^{16}	0.02	3.65	4.87
300	318	2.60×10^{4}	1.91×10^{16}	0.01	3.69	4.87

The band gap and WF of the deposited films are shown in Figure 3.14. The E_g values for all P_D are around 3.6-3.7 eV and show no major changes. However a sharp increase in the WF is observed for P_D above 150 mTorr. This shift towards the centre of the band gap can be interpreted as a sign that the structure is moving towards stoichiometry as the E_F of a stoichiometric metal oxide semiconductor lies halfway between the top of the VB and the bottom of the CB.[37,47] The decrease of the amount of V_O in the SnO_2 films above 150 mTorr is confirmed through the shift in WF observed and the continuous decrease in carrier concentration in Figure 3.13. In the previous section, 3.2.2, the transition level for $V_O(+2/0)$ has been estimated to lie around 4.7 eV, Figure 3.10. While before 200 mTorr the V_O are most likely in a neutral state, the shift of WF observed below 4.8 eV indicates that the V_O would be in their +2 charge state above 200 mTorr and thus produce charge carriers. However no such increase in the carrier concentration is observed thus confirming the compensation of oxygen vacancies by the incorporation of more oxygen in the SnO_2 films.

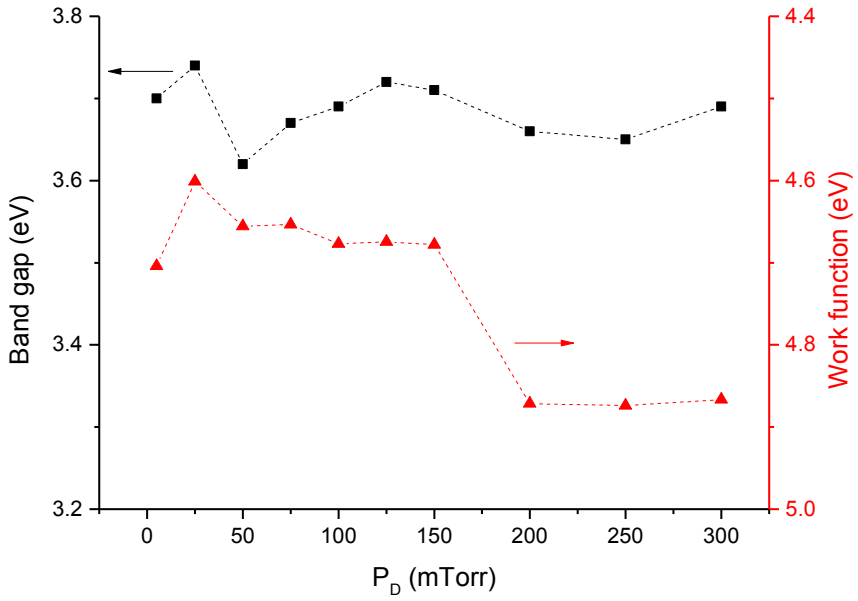

Figure 3. 14: Data of the optical band gap calculated from Tauc analysis of UV-Vis data and measured WF of the films deposited over the oxygen pressure (P_D) range 5-300 mTorr.

Globally the deposited films have been found to move closer to stoichiometry as more oxygen is incorporated in the reactive chamber mainly through a reduction of oxygen vacancies and tin interstitials. This is supported by Scanlon and Watson[40] who showed the formation energy of V_O and Sn_i increases in oxygen-rich environment. It is essential to identify the experimental conditions allowing the limitation of the formation of donor type defects when dealing with the development of p-type SnO_2. The elimination of n-type defects becomes a requirement to avoid charge compensation when p-type dopants are introduced. Even though they cannot be totally suppressed due to their low formation energy they can be limited. Based on the results presented it was considered that a deposition temperature of 600 °C and a background oxygen pressure of 250 mTorr are sufficient to significantly reduce the formation of Sn_i and V_O in the deposited SnO_2 films.

4. Influence of target composition

In this section the influence of the surface composition of the target is highlighted. This parameter is often neglected however it plays an essential role in the consistency of the film depositions. The composition of the target is controlled during the target preparation process, however the cation concentration may change after multiple laser ablation of the target surface. This phenomenon has been explained by Claeyssens *et al.*[48] who studied it in the ZnO system. They observed zinc enrichment on the surface of the target due to backscattering from the plasma plume and re-condensation on the target. In this process the least volatile element, Zn, condenses first which leads to a Zn accumulation on the

surface of the target. The target composition is therefore changing when used over extended periods. To avoid this effect the user can either increase the oxygen background pressure to compensate for the metal-rich conditions or polish the surface of the target regularly to keep the target composition un-changed. In the scope of this thesis, the polishing of the target between successive depositions has been performed to maintain the consistency of the experiments. However in order to investigate the changes induced by a target surface enrichment in SnO_2, the data shown previously is compared with films deposited in the same T_D and P_D conditions but using an unpolished target that was exposed to > 100,000 laser pulses. The temperature study is not repeated, the study is performed only on the pressure range 5-300 mTorr with T_D fixed at 600 °C.

4.1. Crystal structure

The XRD data of the films deposited with the exposed target is shown in Figure 3.15.a alongside with the variation in a-lattice parameter extracted from the (200) diffraction peak in Figure 3.15.b.

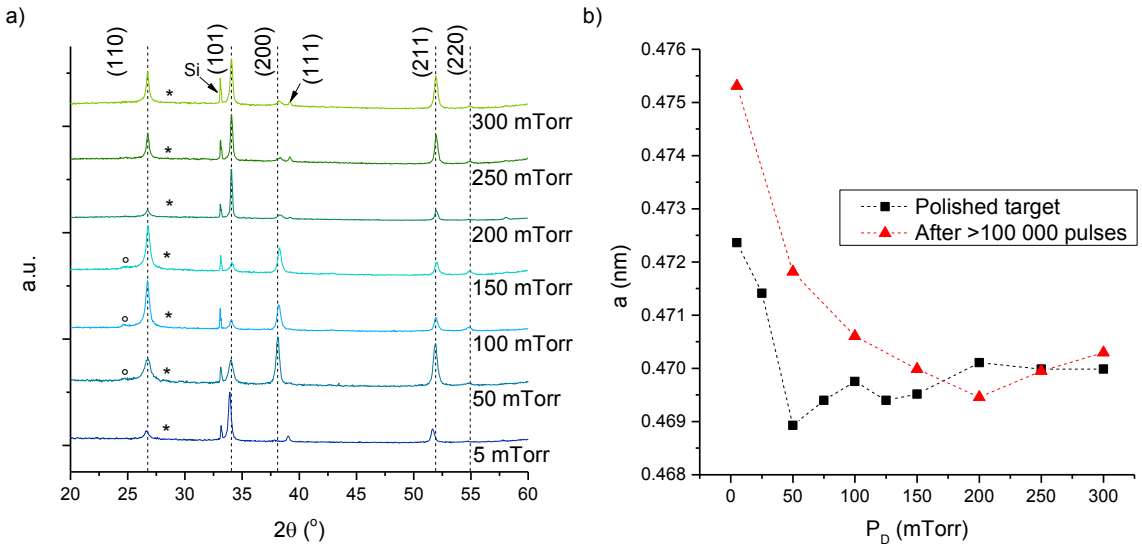

Figure 3. 15: XRD data for the SnO_2 films prepared using a SnO_2 target exposed to > 100,000 laser pulses at a fixed temperature of 600 °C with the oxygen pressure varied from 5-300 mTorr. The major peaks identified belong to SnO_2 phase and are represented on experimental data with dashed lines derived from ICDD 01-077-0452, the Si substrate peaks are clearly identified in addition to a small peak attributed to a minor SnO phase (*) and a minor orthorhombic SnO_2 phases (o).

The films deposited with the exposed target behave similarly as the films deposited with the polished target at low and high P_D with an almost exclusive (101) orientation at 5 mTorr and the presence of (101) and (211) as main orientation above 200 mTorr. The expected (110) main orientation expected between 50 and 150 mTorr only happens after

100 mTorr. In this range of pressure the (200) diffraction peak shows an important increase in intensity to the point of being the main orientation for films deposited at 50 mTorr. The presence of the (101) orientation in smaller proportions is also to be noted as this diffraction peak almost disappeared at 50 mTorr when using a polished target. This is thought to be due to the environment being more tin-rich and thus leading to the growth along oxygen-poor surfaces of SnO_2 such as the (101) and the (200) planes.[29] The a-lattice parameters variations observed in Figure 3.15.b show a larger displacement at 5 mTorr which is accounted for the introduction of more Sn_i from the Sn-rich environment combined with the high energy of the plume in these conditions. In the case of the polished target, a drop of the a-lattice parameter is measured from 5 to 50 mTorr however for the films deposited with the exposed targets this decrease continues until a P_D of 200 mTorr is reached. The cause of this difference may be related to the difference in environment, *i.e.* tin-rich/oxygen-poor in the case of the exposed target. The slower decrease in a-parameter could then be interpreted as a slower transition out of the Sn-rich environment towards an oxygen-rich environment. This hypothesis will be tested with the analysis of the electrical properties of the deposited films.

4.2. Electrical properties and differences in behaviour

The evolution of the carrier concentration and the WF of the SnO_2 films deposited with the exposed are shown in Figure 3.16 and are compared with the films deposited with the polished target.

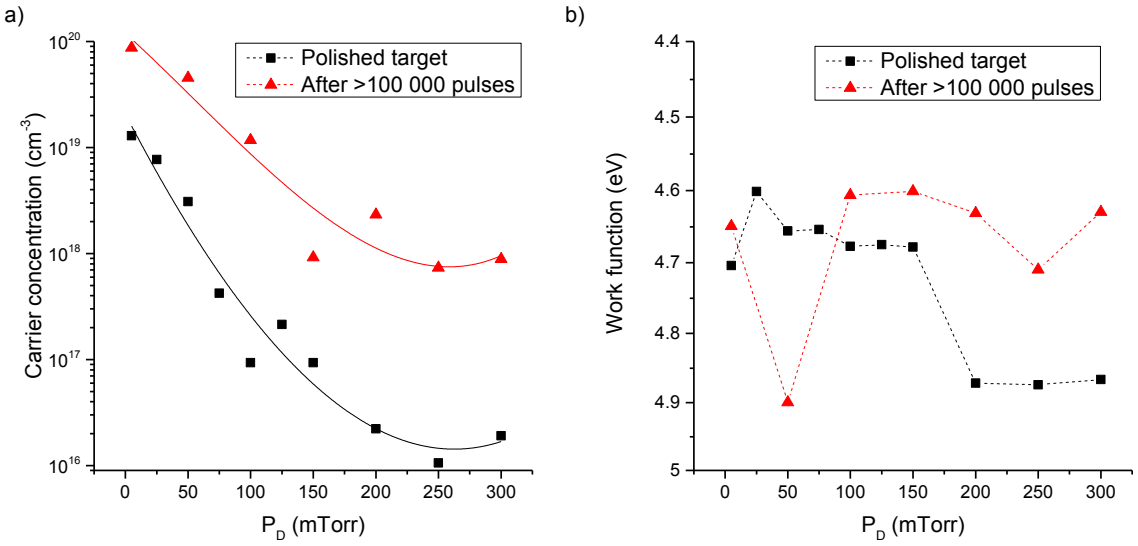

Figure 3. 16: Data of SnO_2 films deposited at 600 °C and under 5-300 mTorr comparing the films with a clean target and with the target exposed to > 100,000 laser pulses showing a) carrier concentration, and b) WF evolution.

Similarly to the polished target, the carrier concentration of the films deposited with the exposed target decreases when more oxygen is incorporated in the chamber. However the carrier concentration of the films deposited with the exposed target is significantly higher and the drop observed is only of two-orders of magnitude. The difference in environment is even more evident as the carrier concentration remains 10 to 100 times higher than in the case of the polished target. The drop in n-type charge carriers is attributed to a decrease of Sn_i and V_O similarly to the films deposited with the polished target. However the formation of acceptor defects even at P_D around 250 mTorr seems unlikely when the two levels of charge carrier concentration are compared together. This is supported by the level of the WF shown in Figure 3.16.b. Above 100 mTorr no consequent variations are measured and the drop present with the polished target at 200 mTorr is not observed in the case of the exposed target when a increase of WF would be expected if acceptor defects were to form. A possible explanation for the higher carrier concentration observed would be the presence of Sn_i from the tin-rich target. This theory coincides as well with the defect energy level of Sn_i defects located in the conduction band, Figure 3.10. The amount of oxygen required to compensate them is greatly increased as the target is tin-enriched after the multiple laser ablation exposures. Between 5 and 50 mTorr the WF displays some considerable variations, especially at 50 mTorr were the value drop to 4.9 eV compared with 4.65 and 4.6 eV at 5 and 100 mTorr respectively. Even though the value at 50 mTorr may appear to be an outlier it has been confirmed by several repeat measurements. This kind of shift could be characteristic of a change in the defect nature in the deposited films. A suggested mechanism is the presence of oxygen vacancies as main defect thus shifting the E_F below the conduction due to their lower defect energy level, Figure 3.10.

Based on the observed results it is clear that the composition of the surface of the target plays an essential role during the deposition and cannot be easily compensated through variation of oxygen pressure. The metal enrichment on the target induces films with more n-type charge carriers but also allows observing a more detailed transition from Sn-rich to O-rich environment. In the case of n-type TCOs this behaviour could allow increasing the formation of donor type defect and having a better control over them at low P_D. However in the domain of p-type SnO_2 this phenomenon has to be avoided as extra donor charge carriers are formed (10 to 100 times more) which could jeopardize the possible introduction of p-type conductivity.

5. Summary

In this chapter the effects of the deposition conditions during the PLD of undoped SnO_2 thin films were investigated. The studies carried allowed to identify some key points in the formation of main donor-type defects, such as oxygen vacancies and tin interstitials, and to limit their formation. It has also been noticed as mentioned in the literature that even under oxygen-rich conditions, the formation of donor type defects is still favoured compared to acceptor defects. Oxygen interstitials and tin vacancies may be present as secondary defects where they would compensate the electrons already present in the system, but they cannot lead to intrinsic p-type conductivity in SnO_2 as mentioned by Scanlon and Watson.[40] The key information extracted from the studies investigated in this chapter are gathered below.

- An increase in the substrate deposition temperature leads to a drop in the carrier concentration due to the compensation of Sn_i and V_O present in the film from the incorporation of more oxygen. The films get closer to stoichiometry as T_D is increased and 600 °C appears to be a relevant point of temperature at which a part of the Sn_i and V_o have been compensated.
- An increase in the amount of oxygen in the deposition chamber leads to a drop of carrier concentration. As expected Sn_i and V_O are compensated by the inclusion of more oxygen in the films. The presence of O_i and V_{Sn} is possible at high P_D (250 mTorr) however they do not appear as major defects. The deposition pressure 250 mTorr seems to be sufficient to limit the formation of a major part of the donor type defects in the films and to begin using extrinsic acceptor dopants for p-type doping.
- The process of laser ablation leads to an accumulation of metallic species at the surface of the target. If the target is not regularly polished major variations in the electrical properties (increase of n-type carrier concentration) appear due to the presence of a more Sn-rich environment.

References

[1] K.L. Chopra, S. Major, D.K. Pandya, "Transparent conductors—A status review", Thin Solid Films. 102 (1983) 1–46.

[2] H. Hartnagel, A.L. Dawar, A.K. Jain, C. Jagadish, "Semiconducting Transparent thin films", IOP Publishing Ltd., Bristol and Philadelphia, 1995.

[3] B.G. Lewis, D.C. Paine, "Applications and Processing of Transparent Conducting Oxides", MRS Bull. 25 (2000) 22–27.

[4] R.E. Presley, C.L. Munsee, C.H. Park, D. Hong, J.F. Wager, D.A. Keszler, "Tin oxide transparent thin-film transistors", J. Phys. D. Appl. Phys. 37 (2004) 2810–2813.

[5] N. Yamazoe, Y. Kurokawa, T. Seiyama, "Effects of Additives on Semiconductor Gas Sensors", Sensors Actuators B Chem. 4 (1983) 283–289.

[6] M.-M. Bagheri-Mohagheghi, M. Shokooh-Saremi, "The influence of Al doping on the electrical, optical and structural properties of SnO2 transparent conducting films deposited by the spray pyrolysis technique", J. Phys. D. Appl. Phys. 37 (2004) 1248–1253.

[7] T. Yang, X. Qin, H. Wang, Q. Jia, R. Yu, B. Wang, et al., "Preparation and application in p–n homojunction diode of p-type transparent conducting Ga-doped SnO2 thin films", Thin Solid Films. 518 (2010) 5542–5545.

[8] Z. Ji, Z. He, Y. Song, K. Liu, Z. Ye, "Fabrication and characterization of indium-doped p-type SnO2 thin films", J. Cryst. Growth. 259 (2003) 282–285.

[9] J.M. Ni, X.J. Zhao, J. Zhao, "Structural, Electrical and Optical Properties of p-Type Transparent Conducting SnO2:Zn Film", J. Inorg. Organomet. Polym. Mater. 22 (2011) 21–26.

[10] R. Eason, "Pulsed Laser Deposition of Thin Films: Applications-Led Growth of Functional Materials", John Wiley & sons, 2006.

[11] H. Krebs, M. Weisheit, S. Erik, T. Scharf, C. Fuhse, M. St, et al., "Pulsed Laser Deposition (PLD) - a Versatile Thin Film Technique UHV-chamber", Adv. Solid State Phys. 43 (2003) 505–517.

[12] J.E. Dominguez, X.Q. Pan, L. Fu, P.A. Van Rompay, Z. Zhang, J.A. Nees, et al., "Epitaxial SnO[sub 2] thin films grown on (1̄012) sapphire by femtosecond pulsed laser deposition", J. Appl. Phys. 91 (2002) 1060.

[13] L.C. Tien, D.P. Norton, J.D. Budai, "Epitaxial growth of transparent tin oxide films on (0001) sapphire by pulsed laser deposition", Mater. Res. Bull. 44 (2009) 6–10.

[14] E.R. Leite, J.A. Cerri, E. Longo, J.A. Varela, "Sintering of undoped SnO2", 49 (2003) 87–91.

[15] G.-G. Lee, S.-J.L. Kang, J. Kwon, D.S. Kim, "Effect of a Sintering Process on the Electrical Properties of SnO2 Gas Sensors", J. Nanosci. Nanotechnol. 10 (2010) 68–73.

[16] M.A. El Khakani, R. Dolbec, A.M. Serventi, M.C. Horrillo, M. Trudeau, R.G. Saint-Jacques, et al., "Pulsed laser deposition of nanostructured tin oxide films for gas sensing applications", Sensors Actuators B Chem. 77 (2001) 383–388.

[17] R. Dolbec, M.A. El Khakani, A.M. Serventi, R.G. Saint-Jacques, "Influence of the nanostructural characteristics on the gas sensing properties of pulsed laser deposited tin oxide thin films", Sensors Actuators B Chem. 93 (2003) 566–571.

[18] R. Dolbec, M.. El Khakani, A.M. Serventi, M. Trudeau, R.. Saint-Jacques, "Microstructure and physical properties of nanostructured tin oxide thin films

grown by means of pulsed laser deposition", Thin Solid Films. 419 (2002) 230–236.

[19] Z. Songqing, Z. Yueliang, W. Shufang, Z. Kun, H.A.N. Peng, "Effect of ambient oxygen pressure on structural , optical and electrical properties of SnO2 thin films", Rare Met. 25 (2006) 1–4.

[20] S.K. Sinha, R. Bhattacharya, S.K. Ray, I. Manna, "Influence of deposition temperature on structure and morphology of nanostructured SnO2 films synthesized by pulsed laser deposition", Mater. Lett. 65 (2011) 146–149.

[21] D.W. Kang, I.J. Jeon, J.S. Song, D. Kim, "Spatial and energy distribution of Co, Ag and Pt particles in pulsed laser deposition: in view of the fabrication of nanometer multilayer film", Appl. Phys. A Mater. Sci. Process. 77 (2003) 449–453.

[22] B. Verhoff, S.S. Harilal, R.J. Freeman, K.P. Diwakar, A. Hassanein, "Dynamics of femto- and nanosecond laser ablation plumes investigated using optical emission spectroscopy", J. Appl. Phys. 112 (2012) 93303–93309.

[23] R.W. Strayer, W. Mackie, L.W. Swanson, S. Admin-, "Work function measurements by the field emission retarding potential method", Surf. Sci. 34 (1973) 225–248.

[24] S. Tian, Y. Gao, D. Zeng, C. Xie, "Effect of Zinc Doping on Microstructures and Gas-Sensing Properties of SnO2 Nanocrystals", J. Am. Ceram. Soc. 95 (2012) 436–442.

[25] Z. Chen, J.K.L. Lai, C.H. Shek, H. Chen, "Synthesis and structural characterization of rutile SnO2 nanocrystals", J. Mater. Res. 18 (2003) 1289–1292.

[26] R. Khandelwal, A.P. Singh, A. Kapoor, S. Grigorescu, P. Miglietta, N.E. Stankova, et al., "Effects of deposition temperature on the structural and morphological properties of SnO2 films fabricated by pulsed laser deposition", Opt. Laser Technol. 41 (2009) 89–93.

[27] A.K. Singh, A. Janotti, M. Scheffler, C.G. Van de Walle, "Sources of Electrical Conductivity in SnO2", Phys. Rev. Lett. 101 (2008) 055502.

[28] P. Ágoston, C. Körber, A. Klein, M.J. Puska, R.M. Nieminen, K. Albe, "Limits for n-type doping in In2O3 and SnO2: A theoretical approach by first-principles calculations using hybrid-functional methodology", J. Appl. Phys. 108 (2010) 053511.

[29] M. Batzill, U. Diebold, "The surface and materials science of tin oxide", Prog. Surf. Sci. 79 (2005) 47–154.

[30] J. Lee, "Effects of oxygen concentration on the properties of sputtered SnO2:Sb films deposited at low temperature", Thin Solid Films. 516 (2008) 1386–1390.

[31] W. Li, D.Y. Li, "On the correlation between surface roughness and work function in copper.", J. Chem. Phys. 122 (2005) 064708.

[32] R. Smoluchowski, "Anisotropy of the Electronic Work Function of Metals", Phys. Rev. 60 (1941) 661–674.

[33] Y.-J. Lin, I.D. Baikie, W.-Y. Chou, S.-T. Lin, H.-C. Chang, Y.-M. Chen, et al., "Changes in surface roughness and work function of indium-tin-oxide due to KrF excimer laser irradiation", J. Vac. Sci. Technol. A Vacuum, Surfaces, Film. 23 (2005) 1305.

[34] Y. Guan, S. Yang, Y. Zhang, J. Xu, C.C. Han, N. a Kotov, "Fabry-Perot fringes and their application to study the film growth, chain rearrangement, and erosion of hydrogen-bonded PVPON/PAA films.", J. Phys. Chem. B. 110 (2006) 13484–90.

[35] M.T. Greiner, L. Chai, M.G. Helander, W.-M. Tang, Z.-H. Lu, "Transition Metal Oxide Work Functions: The Influence of Cation Oxidation State and Oxygen Vacancies", Adv. Funct. Mater. 22 (2012) 4557–4568.

[36] M.T. Greiner, Z.-H. Lu, "Thin-film metal oxides in organic semiconductor devices: their electronic structures, work functions and interfaces", NPG Asia Mater. 5

(2013) e55.

[37] M. Ohring, "The Materials Science of Thin Films", 1992.

[38] J.S. Blakemore, "Solid State Physics second edition", Cambridge university press, 1985.

[39] Ç. Kılıç, A. Zunger, "Origins of Coexistence of Conductivity and Transparency in SnO2", Phys. Rev. Lett. 88 (2002) 095501.

[40] D.O. Scanlon, G.W. Watson, "On the possibility of p-type SnO2", J. Mater. Chem. 22 (2012) 25236.

[41] S. Samson, C.G. Fonstad, "Defect structure and electronic donor levels in stannic oxide crystals", J. Appl. Phys. 44 (1973) 4618.

[42] X. Yong, M.A.A. Schoonen, "The absolute energy positions of conduction and valence bands of selected semiconducting minerals", Am. Mineral. 85 (2000) 543–556.

[43] C. Ke, W. Zhu, J.S. Pan, Z. Yang, "Annealing temperature dependent oxygen vacancy behavior in SnO2 thin films fabricated by pulsed laser deposition", Curr. Appl. Phys. 11 (2011) S306–S309.

[44] J.B. Franklin, Pulsed Laser Deposition of Zinc Oxide Thin Films for Optoelectronic Applications, Imperial College London, 2012.

[45] D.P. Norton, C. Park, J.D. Budai, S.J. Pennycook, C. Prouteau, "Plume-induced stress in pulsed-laser deposited CeO2 films", Appl. Phys. Lett. 74 (1999) 2134.

[46] I.H. Kim, J.H. Ko, D. Kim, K.S. Lee, T.S. Lee, J. -h. Jeong, et al., "Scattering mechanism of transparent conducting tin oxide films prepared by magnetron sputtering", Thin Solid Films. 515 (2006) 2475–2480.

[47] J.S. Blakemore, "Solid State Physics second edition", 1985.

[48] F. Claeyssens, A. Cheesman, S.J. Henley, M.N.R. Ashfold, "Studies of the plume accompanying pulsed ultraviolet laser ablation of zinc oxide", J. Appl. Phys. 92 (2002) 6886.

Chapter 4: Investigation of Zn as acceptor dopant in SnO_2

When doping a material, three factors should be considered: the dopant solubility in the host material, the ionisation level of the dopant defect and the compensation by native defects.[1] Amongst these the formation of compensation defects is the most critical one. The doping limits are defined by the n-type and p-type pinning energies of a material. They represent the range of energy between which E_F can move without causing the spontaneous formation of compensating defects. When considering p-type doping, the p-type pinning energy corresponds to the lowest position of E_F achievable, below it donor compensating defects possess a negative formation energy (*i.e.* they form spontaneously). The charge neutrality level (CNL) which defines the character of the defects function of E_F position generally lies in the middle of the n-type and p-type pinning energies as shown in Figure 4.1 from Robertson and Clark's work.[1]

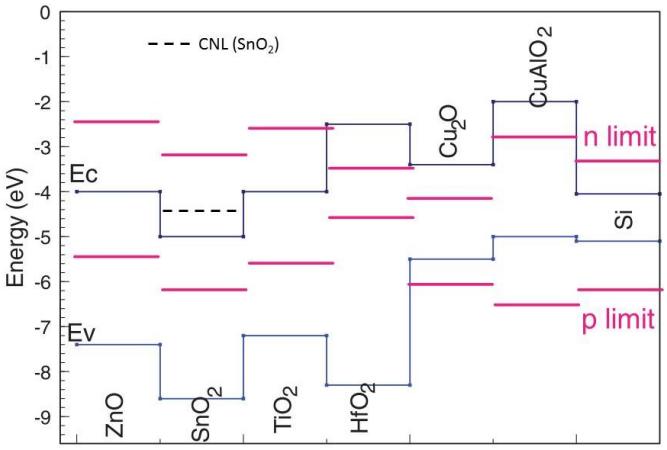

Figure 4. 1: Doping limits for several semiconductor including SnO_2 in O-poor environment. E_V and E_C represent the valence and the conduction band respectively while n limit and p limit represent the respective n-type and p-type pinning energies for the different oxide semiconductors. This diagram is taken from Robertson and Clark's work.[1]

The p-type doping of SnO_2 is limited by the p-type pinning energy lying in the middle of the band gap. However it should be taken into account that these pinning energies were calculated for an O-poor environment. Since the defects formation energy depends upon the growth environment, the pinning energy limits change accordingly. Scanlon and Watson[2] theoretically predicted it would be impossible to produce efficient p-type SnO_2 due to the spontaneous formation of donor defects before the Fermi level reaches the VBM

even in O-rich conditions. Some studies reported successful p-type doping in SnO_2 by either Zn, Ga, Al or In doping however the focus was not brought on these limiting factors.[3–8] The presence of compensating defects such as V_O and Sn_i is critical when trying to change the type of conductivity in SnO_2, and setting an optimum growth environment while considering the defect mechanisms is essential. Furthermore the large amount of dopant generally used (> 10 at.%) is likely to induce changes in the electronic structure and in the defect formation energies.

The aim of this chapter is to control the environment and determine the limitations of the formation of acceptor defects in SnO_2 when subject to p-type doping. The dopant selected here is Zn which is reported to act as a double acceptor when substituted on Sn site due to its lower valence. Studies involving Zn acceptor doping in SnO_2 reported successful p-type conductivity however they neglected to consider the role of compensating defects and growth environment on Zn behaviour in the system.[3–5] It is also important to note that Zn has been used as a dopant in SnO_2 where improved n-type electrical properties were reported.[9] Thus attention will be paid on the fact that Zn may not solely act as an acceptor dopant.

The interest will be brought on how Zn behaves in an environment supposedly favourable for the formation of acceptor defects and what the consequences are on the electrical properties of SnO_2. The study is split in two parts: studying the behaviour of 20 at.% Zn-doped SnO_2 (ZTO) films under T_D and P_D variations compared to undoped SnO_2, and the effect of annealing at high temperature and in oxidising conditions on ZTO films doped at different concentration of Zn (from 0-30 at.%). 20 at.% Zn was selected as the studied doping in the first part since it has been previously reported as the limit between n and p-type conductivity.[10] In these two parts the impact of Zn inclusion in SnO_2 system as an acceptor dopant will be analysed by defining specific sets of conditions favouring the activation of these acceptor defects and limiting intrinsic donor defects. Emphasis will be given on the effectiveness of Zn p-type doping reported in previous studies.[3,11]

In this chapter, Zn-doped SnO_2 thin films were deposited by PLD under various conditions. Unlike in chapter 3, the targets were prepared in our laboratory. ZnO powder (Mateck, purity 99.99 %, density > 95 %) was mixed with SnO_2 powder (> 99.99 %, trace metal basis, Sigma Aldrich). The amount of Zn doping is directly related to the ratio of ZnO to SnO_2 powder, thus the percentage of ZnO was controlled so that targets with compositions of 10, 15, 20, 25 and 30 at.% could be fabricated. Once mixed the powders are pressed into compact pellets by using a dye under a pressure of 1.2 tons. Finally the compact pellets

have been sintered in air at 1355 °C for 10 h and with a heat ramp of 5 °C/min. More information about the process of target preparation and characterisation can be found in Appendix 1. PLD using the freshly prepared ZTO targets and EDX analysis revealed that no Zn was actually incorporated in the films even though the targets' surfaces have been briefly polished. After investigation on the target via cross-section EDX, it was revealed that the Zn repartition in the target is inhomogeneous and that no Zn is present within the first 50 µm below the surface. Considering this, the targets were polished to remove the first layers and the expected Zn/Sn ratio of the target was achieved. This was monitored and controlled by performing film deposition with the targets after every polishing step and by analysing the film composition through EDX. More details about the target inhomogeneity can be found in Appendix 1. XRD analysis of the ZTO targets revealed a main SnO_2 rutile phase with an increased presence of the Zn_2SnO_4 phase as the Zn concentration increases. Slight signal from the $ZnSnO_3$ structure were also measured probably due to its decomposition into Zn_2SnO_4 and SnO_2 above 700 °C.[12] Even though the targets are not purely constituted of SnO_2 rutile phase it will not impact the phase of the deposited films due to the stoichiometric transfer of cations specific to PLD.[13]

In order to ensure the reproducibility of the deposited films, the amount of Zn incorporated in the films was monitored through EDX measurements. The extracted Zn doping from the analysis can be found in Appendix 2. Overall the analysis showed the films deposited with the 20 at.% ZTO target contained 20.0 ± 0.9 at.% Zn. As for the second part of the study where the Zn concentration is varied, the films deposited show concentration of 6.7 ± 0.8, 13.5 ± 1.2, 20.0 ± 0.7, 24.2 ± 1.3 and 30.1 ± 0.9 at.% Zn for the 10, 15, 20, 25 and 30 at.% ZTO targets respectively.

1. Effect of deposition parameters compared to undoped SnO_2

In this first part the interest is focused on the deposition conditions to limit the formation of donor defects intrinsic to SnO_2 as well as find optimum conditions for the formation of acceptor Zn_{Sn} defects. The study covered is similar to that on undoped SnO_2 performed in chapter 3 including a variation of T_D between 300-700 °C with P_D fixed at 100 mTorr, and a variation of P_D between 5-300 mTorr with T_D fixed at 600 °C. The laser parameters remain unchanged with a Fluence fixed at 2.2 J/cm^2 (400 mJ laser power), repetition rate of 8 Hz and pulse duration of 25 ns. The substrates do not change as well, 10 mm x 10 mm square quartz are used for Hall measurement, UV-Vis spectroscopy and EDX, Si (100) oriented for XRD and ITO covered glass substrates for KP measurements.

1.1. Deposition temperature variation

20 at.% ZTO films were deposited by PLD with oxygen pressure (P_D) fixed at 100 mTorr and substrate temperature (T_D) varied between 300 and 700 °C. The XRD data of the deposited films is shown in Figure 4.2.a.

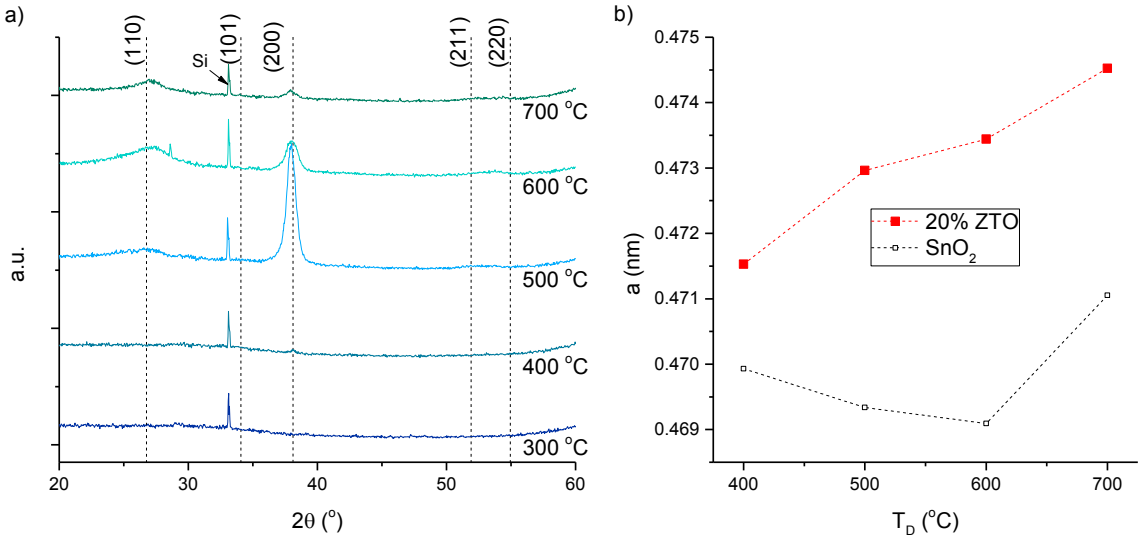

Figure 4. 2: a) XRD data for the 20 at.% ZTO films prepared at a fixed oxygen pressure of 100 mTorr with temperature varied from 300-700 °C. The major peaks identified belong to SnO_2 phase and are represented by dashed lines derived from ICDD 01-077-0452. b) Lattice parameter of the 20 at.% ZTO films (red) function of T_D at fixed P_D of 100 mTorr extracted for the (200) diffraction peak. The data is compared to the lattice parameter of undoped SnO_2 (black) extracted for the same deposition conditions and (200) diffraction peak.

The films deposited below 500 °C are mostly amorphous with only a small signal from the (200) diffraction plane at 400 °C. At $T_D \geq 500$ °C the ZTO films appear to crystallise with the SnO_2 rutile structure since two of its characteristic diffraction planes are measured, the (110) and the (200) orientations. Unlike what has been observed by Bilgin *et al.*[14] and Ko *et al.*[15] no diffraction plane characteristic of Zn_2SnO_4 or $ZnSnO_3$ was observed suggesting that the ZTO films possess a main rutile phase. Some Zn_2SnO_4 or $ZnSnO_3$ phase may exist but it was beyond detection limits. The crystalline ZTO films ($T_D \geq 500$ °C) seem to grow preferentially in the <200> direction unlike undoped SnO_2 films which grow preferentially along the <110>. It should also be noticed that for undoped SnO_2 the films started to crystallise at 400 °C (section 3.2.1) while in this case the ZTO films only show proper crystallisation only at 500 °C. The inclusion of Zn appears to change the growth orientation but also to act as thermal stabiliser. The lattice parameters extracted for the (200) plane function of T_D are shown in Figure 4.2.b and compared to the undoped SnO_2 values previously measured. The a-lattice parameter of the ZTO films (0.473-0.475 nm) appears to be significantly larger than the undoped films (0.470-0.471 nm). This would be

due to the difference in ionic radii between Sn^{4+} and Zn^{2+} with a coordination number of 6. Shannon[16] reported the ionic radii of Sn^{4+} and Zn^{2+} to be respectively 0.69 and 0.74 Å in these conditions. The larger lattice parameters observed with the Zn-doped films indicate that Zn has been successfully incorporated in SnO_2 lattice. Even though their ionic radii are close, the large amount of Zn used for the doping is accounted for this lattice distortion and thus supports the main SnO_2 rutile phase detected.

The 20 at.% ZTO films show an increase of the a-lattice parameter with increasing T_D. In the lattice, Zn can be in three different configurations: substitution on Sn site (Zn_{Sn}), interstitial (Zn_i) and antisite on O site (Zn_O). Zn_O defect is likely to possess, similarly to Sn_O, a very high formation energy thus limiting its presence.[17] Considering that each Sn atom is surrounded by 6 oxygen atoms (ideally), the substitution of Zn on Sn site would lead to the formation of 2 holes by extracting 2 electrons from the surrounding oxygen. However this process is expected to require a high energy owing to the high electronegativity of the oxygen (difficulty to remove electron from oxygen). In this case the formation of one or more oxygen vacancy would be more stable to the system leading to the formation of defect pair $\left(Zn_{Sn}^{//} - V_O^{\circ\circ}\right)^x$ where x is the charge of the defect complex. Such mechanism has been suggested by Scanlon and Watson[2] with the resulting redox equation in Kröger-Vink notations.

Equation 4.1
$$h^{\circ} + \frac{1}{2}O_O^x \rightarrow \frac{1}{2}V_O^{\circ\circ} + \frac{1}{4}O_2(g)$$

Zhu *et al.*[18] studied ZTO thin films deposited by PLD and with Zn doping between 10 and 30 at.%. They reported that the Zn coordination number does not exceed 4 however their study was limited to low temperature (< 400 °C) and oxygen-poor environment (P_D below 15 mTorr) thus highly favourable to the formation of donor defects such as V_O. Similar acceptor-donor defect pairing has been reported by Choudhurry *et al.*[19] and Islam *et al.*[20] in the TiO_2 system doped with Mn in +2 oxidation state. In their studies TiO_2 was in rutile structure similar to SnO_2. The Mn introduced was found to substitute on Ti site and form defect complex with V_O. Even though independently ionised V_O and Zn_{Sn} defects would cause an expansion of the lattice, the distortion would be reduced if those defects are paired due to Coulombic attraction due to their opposite charges.[21] The smaller lattice parameter measured at 400 and 500°C could therefore be the result of $\left(Zn_{Sn}^{//} - V_O^{\circ\circ}\right)^x$ defect pairs. It has been previously mentioned in section 3.2 that an increase of T_D in the case of undoped SnO_2 leads to the incorporation of more oxygen in the films. The increase in lattice parameter could be from the formation of Zn_{Sn} acceptor defects uncompensated by V_O or by the formation of Zn_i even though it would be more unlikely.

The Hall resistivity, carrier concentration and Hall mobility of the 20 at.% ZTO films are displayed in Figure 4.3 along with the values previously measured for undoped SnO_2 films in the same conditions. All the deposited films showed n-type conductivity.

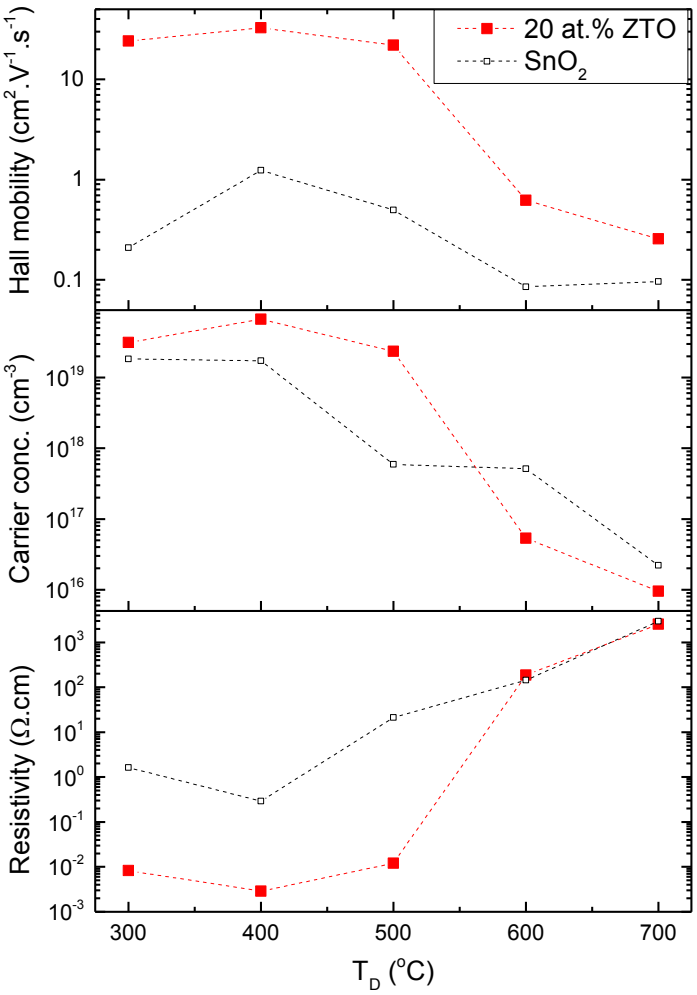

Figure 4. 3: Hall data showing the evolution of the Hall resistivity, the carrier concentration and the mobility of the 20 at.% ZTO films (in red) deposited at P_D 100 mTorr with T_D varying from 300-700 °C. The data is compared to that of the previously measured undoped SnO_2 films (in black) deposited under the same conditions.

The carrier concentration, the mobility and therefore the resistivity follow the same trend for ZTO films. While for the undoped films the carrier concentration decreases almost monotonously starting at 400 °C, in the case of the ZTO films it remains above 10^{19} cm^{-3} at $T_D \leq 500$ °C but above this temperature it drops dramatically until reaching 10^{16} cm^{-3} at 700 °C. At 600 °C the ZTO films show a carrier concentration one order of magnitude lower that the undoped ones. The drop of carrier concentration at T_D above 500 °C indicates that the increase in lattice parameter cannot be due to the presence of more Zn_i or Sn_i in the lattice. This behaviour is believed to originate from the formation of more Zn_{Sn} acceptor defect via the incorporation of more oxygen in the system. Considering the large

amount of Zn used for the doping (20 at.%) it would not be surprising that the defect formation energies would change from the undoped system despite retaining the rutile structure. At T_D below 500 °C V_O could form preferentially next to Zn_{Sn} defects to compensate for the high energy required for the formation of this acceptor defect. Zhu *et al.*[18] suggested that the V_O migrate from Sn to Zn in order to stabilise the system. Therefore the introduction of Zn would lower the formation energy of oxygen vacancies, accounting for the larger carrier concentration measured for ZTO films when compared to undoped films at low T_D. Above 500 °C the system is thought to possess enough energy to allow the formation of some uncompensated Zn_{Sn} acceptor defects explaining the sudden drop in electron carrier concentration. In the case of undoped SnO_2 the carrier concentration decrease was attributed to a limitation of the Sn_i and V_O however in this case the incorporation of more oxygen limits the formation of these donor defects but also introduces the formation of holes in the system.

The mobility of the films follows the same pattern as the carrier concentration with a sudden decrease above 500 °C. In SnO_2 the mobility is limited by different electron scattering mechanisms. Bruneaux *et al.*[22] reported two types of regime: at low carrier concentration (< 5 x10^{18} cm^{-3}) the conductivity is governed by the potential barrier at the grain boundaries with a drop of the mobility when the grains are fully depleted, and at high carrier concentration (> 5 x10^{18} cm^{-3}) the mobility is limited by scattered impurities but also by lattice scattering due to the high density of structural defects. In the case of the ZTO films the FWHM based on the (200) diffraction peak is 0.87, 1.11 and 0.97 ° at 500, 600 and 700 °C respectively, leading to crystallite size between 8-11 nm. As the carrier concentration decreases considerably with increasing temperature the depletion in the grain becomes more significant which would increase the height of the barrier at the grain boundaries thus limiting the mobility. However it is believed that some contribution from ionised impurity scattering may also have an effect on the lower mobility measured at high temperature. In the case of the formation of Zn_{Sn} defect in the system, these acceptor defects would constitute traps for the mobile electron as well as scattering centre and would limit the mobility.

The values of the resistivity, carrier concentration and Hall mobility, but also the thickness of the films, their band gap and work function (WF) extracted by KP can be found in Table 4.1. It should be noticed that the Zn-doped SnO_2 films exhibited surprisingly low resistivity and high mobility for T_D below 500 °C. This aspect of the Zn doping is more developed in chapter 5.

Table 4. 1: Details of 20 at.% ZTO function of T_D with P_D fixed at 100 mTorr showing the films thickness, sheet resistance, Hall resistivity, carrier concentration, Hall mobility, band gap and WF. The dotted line above T_D of 400 °C separates films which are mostly amorphous to crystalline films.

T_D	**Thickness**	**Hall resistivity**	**Carrier concentration**	**Hall mobility**	**Band gap**	**WF**
°C	nm	Ω.cm	cm^{-3}	$cm^2/(V.s)$	eV	eV
300	240	8.27×10^{-3}	3.13×10^{19}	24.1	3.29	4.93
400	236	2.86×10^{-3}	6.67×10^{19}	32.8	3.21	4.68
500	220	1.22×10^{-2}	2.34×10^{19}	21.9	3.56	4.45
600	224	1.86×10^{2}	5.36×10^{16}	0.6	3.53	4.34
700	242	2.54×10^{3}	9.54×10^{15}	0.3	3.58	4.32

The band gap of the ZTO films extracted by the Tauc plot method is about 0.1 eV smaller than for the undoped SnO_2 films. The low values measured at 300 and 400 °C are attributed to band tailing effect due to the films being mainly amorphous.[23] The evolution of the WF of the ZTO films function of T_D is shown in Figure 4.4 along with the undoped films.

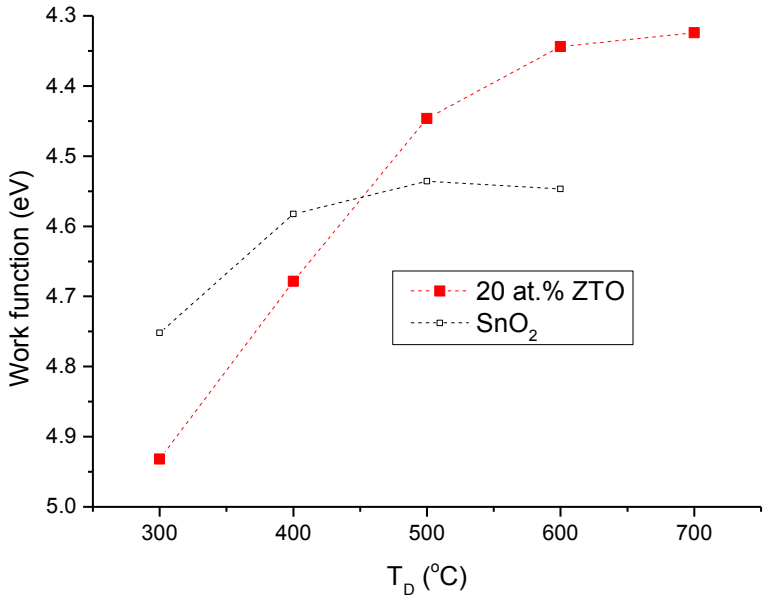

Figure 4. 4: Evolution of the work function (WF) of the 20 at.% ZTO (in red) and undoped SnO_2 (in black) measured by Kelvin probe for P_D of 100 mTorr and T_D between 300-700 °C.

The WF of the ZTO films measured by KP is found to decrease (move closer to the vacuum energy) as T_D increases. A similar trend could be observed for the undoped films, but the lower WF at 300 °C was thought to be pinned to the tail of the CB in the case of amorphous films.[24,25] The same effect is believed to happen for the ZTO films at 300 and 400 °C. Without considering the low WF at 300 °C in the case of undoped SnO_2, WF does not show significant variations and is rather contained within a 0.04 eV variation. However the ZTO

films show significantly lower WF compared to undoped SnO_2 at $T_D \geq 500$ °C and important decrease as the T_D increases with over 0.1 eV variations. Generally a decrease of WF (increase of the Fermi level) is attributed to an increase of the carrier concentration due to formation of donor defect levels close to or inside the CB. However in the present situation the carrier concentration follows the opposite behaviour of what is conventionally observed. It should be considered that KP is a surface sensitive technique subject to surface dipole as well as band bending. Both these effects influence the position of the Fermi level at the surface (work function) and the VBM (ionisation potential). Two kinds of mechanism could be suggested in the case of the reduced WF observed with the inclusion of Zn: a change in the ionisation potential resulting in a higher VBM and bending of the energy bands near the surface due to a space charged layer. Körber *et al.*[26] suggested the formation an upward band bending in Sb-doped SnO_2 due to the possible formation of Sn_{Sb} acceptor states. The inclusion of Sb with a +3 oxidation state on Sn would induce the formation of deep trap levels and thus an electron depleted zone near the surface. However SnO_2 is generally found to form a downward band bending at the surface from electrons accumulation. Vasheghani Farahani *et al.*[27] compared the E_F extracted via XPS to the theoretical position of the bulk E_F based on the carrier concentration from Hall measurements for undoped and Sb-doped SnO_2 films. In both cases they observed a downward band bending from an electron accumulation at the surface. Nagata *et al.*[28] also showed a downward band bending occurs at the surface of SnO_2, Sb-doped SnO_2 and even In-doped SnO_2 films where In was incorporated as an acceptor dopant. Therefore, even though the presence of Zn_{Sn} acceptor defects at the surface of the ZTO films could lead to an upward band bending similarly to what suggested Körber *et al.*[26], the presence of downward band bending due to electrons accumulation at the surface is more likely.

When T_D increases the work function decreases as well as the carrier concentration. This is characteristic of an increase of the space charge layer present in KP measurements due to less electrons present in the films. In the case of a downward band bending due to donor-like states at the surface, it would become more important at high T_D. The lower WF measured at the surface would therefore account for a decrease of the Fermi level in the bulk (increase in WF). E_F would consequently lie deeper in the band gap when T_D is increased above 500 °C. As a result the low WF measured is attributed to the formation of Zn_{Sn} acceptor defects at higher T_D decreasing the amount of electron charge carrier. However the KP data alone is not enough to explain the behaviour of the ZTO films at high

temperature and complementary XPS measurements need to be performed. This matter is discussed in section 5.1.3.

1.2. Oxygen pressure variation

In this section T_D was kept constant at 600 °C and P_D varied between 5-300 mTorr for the 20 at.% ZTO films similarly to what has been performed in chapter 3 with undoped SnO_2. The thickness of the deposited films was kept around 200 nm. The XRD data of the deposited ZTO films is shown in Figure 4.5.a. The diffraction peaks observed corresponds to the rutile structure of SnO_2 with no apparent secondary phases. The growth orientations appear to change with the oxygen pressure. At low P_D (5 mTorr) the growth in the <101> direction is clearly favoured considering the high intensity of the diffraction peak which is also observed for the undoped films (Figure 3.11). However the orientations of the films diverge at 50 mTorr where in the case of the ZTO films the (200) plane is favoured until 200 mTorr where the main orientation switches to the (110). Unlike undoped SnO_2 no major (101) orientation is observed at high P_D (> 200 mTorr).

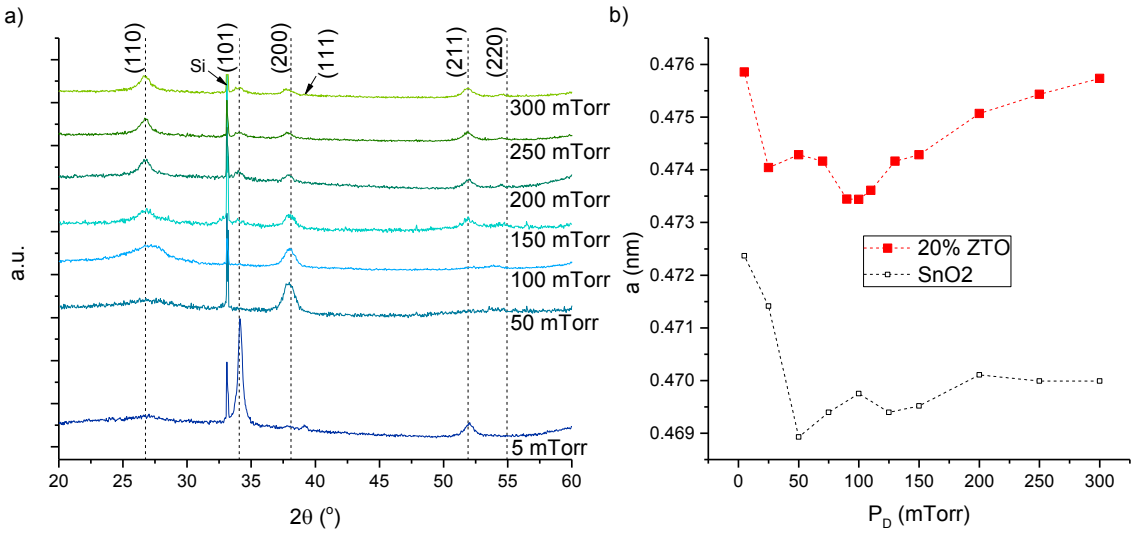

Figure 4. 5: a) XRD data for the 20 at.% ZTO films prepared at a fixed T_D of 600 °C with P_D varied between 5-300 mTorr. b) Lattice parameter of the 20 at.% ZTO films (in red) function of P_D at fixed T_D of 600 °C extracted for the (200) diffraction peak. The data is compared to the lattice parameter of undoped SnO_2 (in black) extracted for the same deposition conditions and (200) diffraction peak.

The evolutions of the a-lattice parameter with and without Zn-doping extracted from the (200) plane are shown in Figure 4.5.b. Similarly to the previous section a larger lattice parameter is observed when 20 at.% Zn are added to the system suggesting that Zn has been successfully incorporated and does not form secondary phases.

From 5 to 100 mTorr the lattice parameter of the 20 at.% ZTO films decreases considerably. In undoped SnO_2 this change has been attributed to the decrease of Sn_i present at low P_D due to the O-poor environment. A similar change of defect can be assumed for the ZTO films with the presence of less Sn_i or Zn_i as P_D increases up to 100 mTorr. In the previous section it has been suggested that at T_D = 600 °C and P_D = 100 mTorr Zn_{Sn} acceptor might be formed, which corresponds to the minimum lattice parameter measured with varying P_D. Above 100 mTorr the lattice parameter increases considerably up to 300 mTorr. Considering undoped SnO_2 this regime was attributed to a decrease of donor defect such as Sn_i and V_O and to the possible formation of V_{Sn} and O_i leading to a small increase of the lattice parameter. However in the case of ZTO, the increase observed is much larger suggesting a different defect mechanism occurs in the films. Han and Shao[29] examined the theoretical acceptor doping of Zn in TiO_2. They estimated the Zn substitution on Ti site leading to acceptor states would be energetically unstable in oxygen-poor condition. Under these conditions the formation of Zn_i or Zn_{Ti}-V_O defect pair is expected to be preferred. Under O-rich conditions, even though Zn_{Ti}-V_O neutral defect pair can be energetically favoured over the charge state, Zn_{Ti} acceptor defects would form preferentially due to lower formation energy. Zn_i are thought to be very limited due to their increased formation energy in this environment. This theoretical investigation would suggest that the increase in lattice parameter measured in the ZTO films at high P_D is due to the formation of more Zn_{Sn} acceptor defects. However that Hall measurements performed on the ZTO samples prove otherwise as shown in Figure 4.6.

It should be noted that all the deposited films were measured to be n-type. The deposition pressures used were originally intended to be spaced by 50 mTorr steps but considering the surprisingly low carrier concentration measured at 100 mTorr, complementary points had to be included. Therefore the step has been narrowed to 20 mTorr between 50 and 150 mTorr. The carrier concentration of the ZTO films decreases accordingly with the undoped SnO_2 films between 25 and 100 mTorr. This behaviour suggests a similar decrease of Sn_i and V_O occurs when P_D is increased. Above 100 mTorr the carrier concentration of the ZTO films diverges completely from the undoped films with an increase back to 10^{19} cm^{-3}. The carrier concentration then decreases gradually down to 10^{18} cm^{-3} until 300 mTorr. A variation from 10^{16} to 10^{19} cm^{-3} cannot be due to the formation of Zn_{Sn} acceptor defects. This behaviour corresponds to a sudden increase in donor defects in the ZTO film despite the increasing oxygen pressure. No reports have yet signalled this behaviour in SnO_2. As P_D increases the possible amount of V_O around the Zn_{Sn} defects would decrease due to more oxygen incorporated in the films. This would lead to

an increasing formation of acceptor Zn_{Sn}, however this defect might cost a lot of energy to the system with the removal of two electrons from the surrounding oxygen. Therefore with increasing P_D the system is thought to meet a threshold at which the energy to form more Zn_{Sn} acceptor defects is too high. This would lead to either the compensation of this defect or a different incorporation of Zn in the lattice.

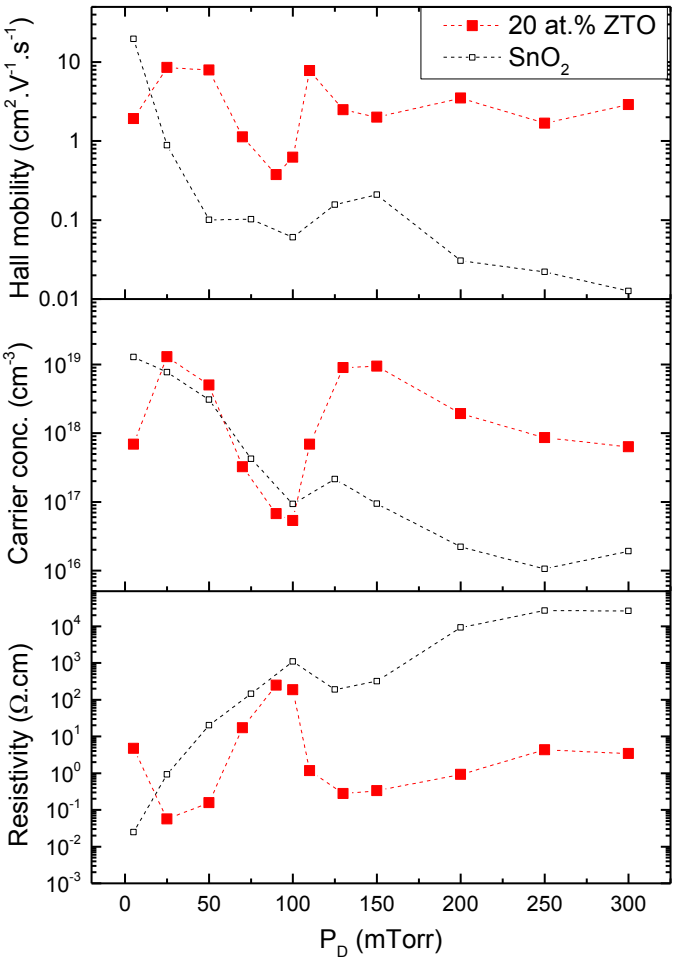

Figure 4. 6: Hall data showing the evolution of the Hall resistivity, the carrier concentration and the mobility of the 20 at.% ZTO films (in red) deposited at T_D 600 °C with P_D varying from 5-300 mTorr. The data is compared to that of the previously measured undoped SnO_2 films (in black) deposited under the same conditions.

Several compensation mechanisms have been reported in the development of p-type doping in semiconductors, among them two are particularly relevant to this study. The first is the formation of Zn_i (donor defect), it is a possibility as it would explain the increase in lattice parameters and in carrier concentrations at high P_D (> 150 mTorr). Singh *et al.*[30] showed group-IIIA acceptors dopants such as In and Ga possess a low formation energy on the interstitial site however this occurs only under Sn-rich conditions. When moving away from O-poor conditions the formation energy of such compensating defects is expected to increase. A second mechanism is the formation of AX

centres. This type of defect originates from the restructuration around an acceptor defect to form a donor. This effect has been reported in the p-type doping of ZnO and II-VI semiconductors.[31,32] In these cases two anion-cation bonds are broken next to the acceptor structure to form an anion-anion bond and two electrons are released from the net loss of one bond changing the A^- defect into AX^+ donor.[33] Such change involves a large relaxation of the lattice which would account for the enlarged lattice parameter measured in the ZTO films. This type of compensation for the p-type doping of SnO_2 has also been suggested by Singh *et al.*[30]. Even though the mechanism is not certain, the Zn acceptor doping in SnO_2 is clearly less efficient at high P_D. Singh *et al.* suggested the existence of optimum growth conditions at which the formation energy of the acceptor defect would be low enough and the formation energy of compensating defects high enough to achieve p-type conductivity in SnO_2. Even though p-type conductivity is far from being achieved, here the narrow conditions window at 600 °C and 100 mTorr appears to represent the point of lowest formation energy for Zn_{Sn} acceptor defects without thermal annealing. It should be noted that the measurements at 90 and 100 mTorr were particularly difficult to achieve. The Hall effect measurements which allows the determination of the carrier concentration and Hall mobility by using the resistivity measured by Van der Pauw method showed large variations to the point where the error was too high. The errors of the measurements (V_H error) are detailed in Table 4.2.

Table 4. 2: Details of 20 at.% ZTO function of P_D with T_D fixed at 600 °C showing the films thickness, sheet resistance, Hall resistivity, carrier concentration, Hall mobility, band gap, work function (WF) and Hall voltage (V_H) error.

P_D	**Thickness**	**Resistivity**	**Carrier concentration**	**Hall mobility**	**Band gap**	**WF**	**V_H error**
mTorr	nm	Ω.cm	cm^{-3}	$cm^2/(V.s)$	eV	eV	%
5	186	4.69	6.92×10^{17}	1.9	3.69	4.44	40.5
25	220	5.62×10^{-2}	1.30×10^{19}	8.6	3.54	4.43	0.3
50	200	1.57×10^{-1}	5.03×10^{18}	7.9	3.47	4.48	14.4
70	200	1.71×10^{1}	3.24×10^{17}	1.1	3.50	4.47	8.9
90	200	2.48×10^{2}	6.73×10^{16}	< 1	3.54	4.43	328
100	224	1.86×10^{2}	5.36×10^{16}	< 1	3.53	4.34	143
110	200	1.16	6.91×10^{17}	7.8	3.55	4.35	5.5
130	200	2.78×10^{-1}	9.01×10^{18}	2.5	3.51	4.38	26.1
150	200	3.30×10^{-1}	9.42×10^{18}	2.0	3.59	4.45	24.3
200	210	9.25×10^{-1}	1.93×10^{18}	3.5	3.60	4.61	0.1
250	220	4.31	8.63×10^{17}	1.8	3.62	4.67	3.7
300	220	3.41	6.34×10^{17}	2.9	3.60	4.84	2.3

The Hall voltage (V_H) is used for the calculations of the carrier concentration and the mobility (see section 2.2.2.1). The absolute error was calculated by taking the ratio between the variance of the V_H measured and its average, and is expressed as a percentage. Since the error is too large at 90 and 100 mTorr it would not be right to consider their carrier concentration however the resistivity which presents a much lower error (< 1 %) shows the same behaviour with P_D showing the consistency of the data.

Similarly to the investigation of T_D, a decrease of the carrier concentration leads to a drop of mobility. The evolution of the mobility of the ZTO films with increasing P_D is very close to the variations of the carrier concentration. The drop of mobility at 100 mTorr is likely to be due to an increase of grain boundary scattering as the size of the grains is about 10 nm (FWHM close to 1 ° for the (200) peak) and the carrier concentration is considerably decreased (below 10^{17} cm^{-3}). However the possibility of Zn_{Sn} trap states acting as scattering centre is not excluded. The band gap measured for the ZTO films is generally 0.1 eV lower than that of the undoped films (section 3.3.2).

The evolution of the WF measured by KP function of P_D is shown in Figure 4.7 along with the variations obtained with the undoped films from section 3.3.2. The local minimum of WF observed at 100 mTorr is similar to the behaviour of the carrier concentration on Figure 4.6. This support the hypothesis of a downward band bending in the ZTO films due to donor-like states at the surface which becomes more important as the carrier concentration drops. The drop of carrier concentration would result in a decrease of the Fermi level in the band gap, but it has yet to be confirmed (section 4.1.3).

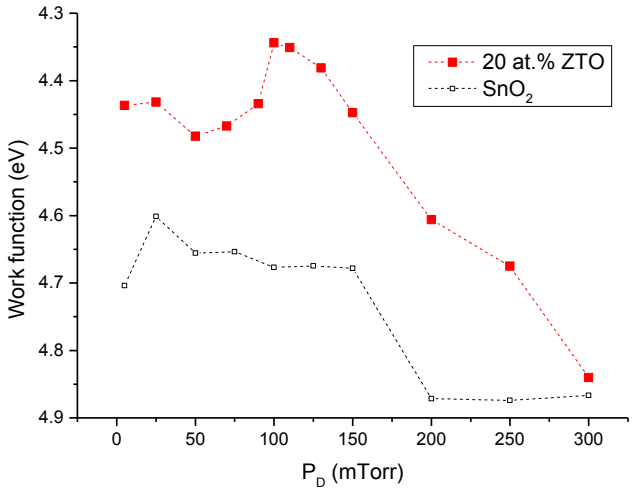

Figure 4. 7: Evolution of the WF of the 20 at.% ZTO (in red) and undoped SnO_2 (in black) measured by Kelvin probe for T_D of 600 °C and P_D between 5-300 mTorr.

Above 100 mTorr the WF drops dramatically reaching the level of undoped films at 300 mTorr. This effect is assigned to the sudden increase in carrier concentration above 100 mTorr leading to a reduction of the band bending. However this effect alone is not enough to explain the increase observed as it shift deeper than the WF measured for the films deposited at 5 mTorr for similar carrier concentrations. In the previous chapter this behaviour was assigned to the films being more stoichiometric as a result of more oxygen being incorporated. Another possible explanation is a change of the VBM with increasing P_D as observed for undoped films where WF increases by 0.2 eV. This eventuality is discussed in the next section.

1.3. Impacts on Fermi level and VBM

XPS analysis of the valence band onset and of the Fermi edge have been performed on undoped and 20 at.% Zn-doped SnO_2 films deposited at T_D of 600 °C and P_D of 100 and 250 mTorr. The aim of these measurements is to detect changes in the valence band position and compare the WF extracted to the WF measured by KP.

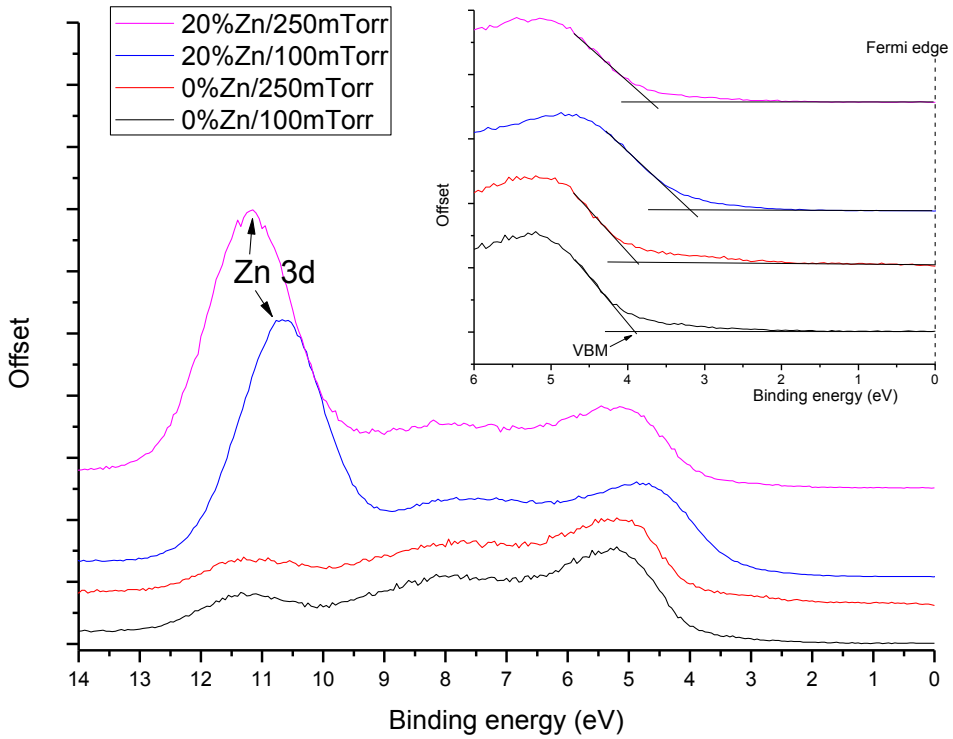

Figure 4. 8: Valence band onset measured by XPS of undoped and 20 at.% Zn-doped SnO_2 films deposited at 600 °C and under P_D of 100 and 250 mTorr on Si substrates. All the measurements were normalised to the gold reference.

The VB onset measured for the undoped samples coincides with the features generally observed for SnO_2.[34,35] In the case of the 20 at.% Zn-doped films the features between binding energies of 4-9 eV follow that of SnO_2 but an intense peak can be notice at 11 eV

which does not correspond to SnO_2. This peak is specific of the Zn 3d in the films.[36] The peak shift observed from the 20 at.% ZTO films between 100 and 250 mTorr corresponds to a shift of the Fermi edge towards the valence band at 100 mTorr which is discussed below. The energy difference between the VBM and E_F has been extracted from Figure 4.8 and the position of E_F related to the vacuum energy (WF) was determined by Fermi edge analysis and allowed to position the VBM energetically. Gold was used as a reference for these measurements. Finally the CBM was positioned using the values of the optical band gap measured. The energy position of the VBM, CBM, and Fermi level measured from XPS and KP are all displayed in Figure 4.9.

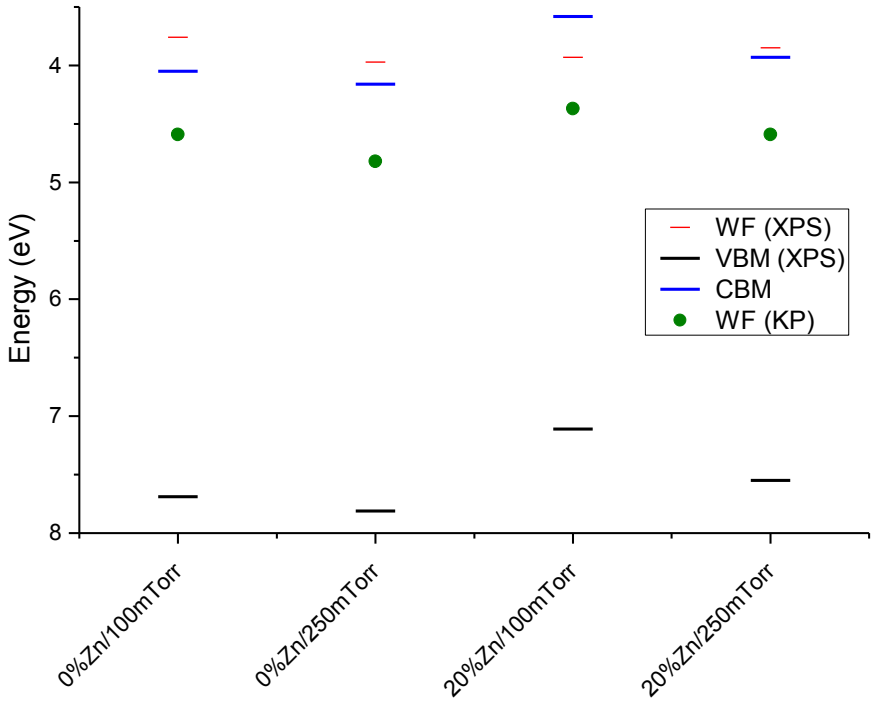

Figure 4. 9: Diagram representing the position of the Fermi level (red) and VBM (black) measured by XPS, the Fermi level measured by kelvin probe (KP) (green dot), and the CBM (blue) extracted by applying the measured optical band gap to the VBM. These level are compared between undoped and 20 at.% Zn-doped SnO_2 films and deposited at T_D 600 °C but under two different P_D of 100 and 250 mTorr.

The first noticeable effect is the evolution of the VBM position. Either for undoped or Zn-doped films, when P_D is increased (from 100 to 250 mTorr) the VBM moves deeper in energy (higher ionisation potential). This phenomenon has been reported by several authors. An increase of the ionisation potential as well as the work function was observed when moving to more oxidising conditions.[37–39] The variations when increasing the oxygen content of the environment were attributed to changes of surface terminations such as the presence of more Sn^{4+} states in oxygen-rich conditions.[26] This induces a modification of the surface dipole which impacts both the VBM and E_F position. When

comparing the undoped and Zn-doped films the VBM is clearly raised with the inclusion of Zn in SnO_2. This change is also considered to be due to a change in the oxidising environment but not directly linked to the amount of oxygen during the deposition. Zn when introduced in the SnO_2 is in a +2 charge state which is reducing compared to the +4 charge state of Sn. It should also be noted that the VBM of ZnO is about 7.4 eV while that of SnO_2 lies deeper around 8 eV.[40]

The energy difference ξ between the VBM and E_F (measured by XPS) changes with the doping and the experimental conditions. ξ represents the relative position of the Fermi level with respect to the VBM and is therefore influenced by the electron concentration and the type of defects present in the films. When varying P_D from 100 to 250 mTorr only a slight decrease of ξ is observed but when Zn is introduced in SnO_2 at 100 mTorr ξ is much smaller, see Figure 4.8. This significant drop of E_F relative to the VBM is attributed to the presence of more acceptor states such as Zn_{Sn} with the formation of energy states towards the VBM. At 250 mtorr ξ increases for the ZTO films which accounts for the significant increase in carrier concentration above 100 mTorr and justify the formation of donor states close to the CBM. The Fermi levels measured by KP are significantly deeper (larger WF) than those measured by XPS. While XPS was performed in ultra-high vacuum (UHV), KP was performed in air leaving the surface of the sample more oxidised and subject to contamination. Therefore the difference in Fermi level is partially due to the difference in environment in which the measurements have been carried and thus to a difference in surface potential.[41] Another reason behind the difference of E_F measured is believed to be the depth sensitivity of the two techniques. XPS is a tool that can be used to probe the first nanometers (depending on the X-ray energy) of the surface but in the case of KP only the first atomic layer are analysed leaving the depth sensitivity of this technique to about a few angstroms.[42] Therefore a band bending effect would result in different WF measured as it varies with the depth in the sample from its surface. Figure 4.10 shows the changes in band bending intensity with a decreasing carrier concentration. The CNL is the charge neutrality limit which pins to the neutral level of the surface density of states at the surface. As E_F decreases due to a reduced amount of electrons in the system, the amount of unoccupied (charged) donor-like states increases and thus more electrons are necessary to compensate the charge. As a consequence the band bending is increased.

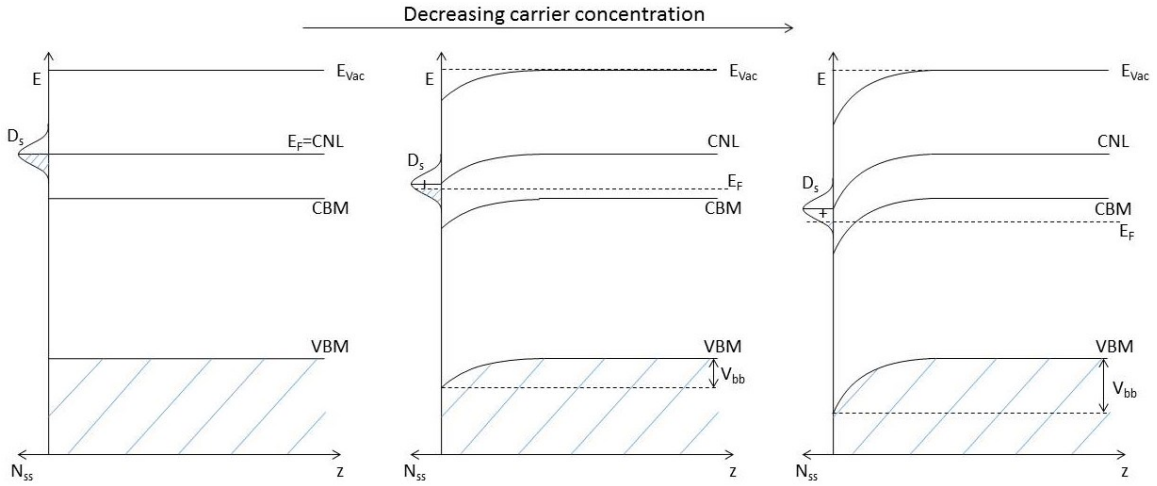

Figure 4. 10: Band diagram showing the influence of Fermi level position (E_F) and carrier concentration on the intensity of downward band bending (V_{bb}) present at the surface of an n-type semiconductor. As the carrier concentration decreases the density of unoccupied surface states increases leading to larger band bending. N_{ss} is the surface density of states and z the depth within the sample from the surface. Figure taken from Ref [27].

Considering the band bending behaviour reported by Farahani *et al.*[27] illustrated in Figure 4.10, it is fair to infer that a more intense band bending is present a 100 mTorr for the ZTO doped films. This could confirm the formation of more Zn_{Sn} acceptor defects states in these conditions as the Fermi level moves deeper in the band gap. Unlike KP and XPS, the Hall measurements give information about the entire film (surface and bulk). It is essential to consider the difference in the type of information extracted from each analytical technique. In this case XPS and KP are used in parallel with the Hall Effect to estimate the position of E_F in the bulk and how it influences the band structure near the surface.

In this first section the behaviour of 20 at.% ZTO films function of the deposition temperature and the oxygen pressure were studied. The initial "p-type compatible" conditions (T_D = 600 °C and P_D = 250 mTorr) established in chapter 3 to limit the formation of donor-type defects in undoped SnO_2 were not effective with the introduction of Zn and showed a higher degree of charge carriers in the films. Zn appeared to influence greatly the formation energy of intrinsic defects in SnO_2 due to the instability of the Zn_{Sn} acceptor defect. The lowest carrier concentration achieved, supposedly corresponding to the lowest formation energy of the acceptor defects, was achieved at 600 °C and 100 mTorr. However this study cannot be solely limited to the deposition conditions as a post deposition thermal treatment is often required to achieve the energy necessary for the acceptor defect activation. To continue, two sets of optimum conditions are selected: T_D = 600 °C and P_D = 250 mTorr from the undoped SnO_2 study, and T_D = 600 °C and P_D = 100

mTorr from this study. Under these conditions the Zn doping will be varied and thermal annealing under oxidising environment will be carried.

2. Impact of thermal annealing

In this section the effect of Zn doping variation and thermal annealing on the properties of the films are studied. In the process of p-type doping, thermal annealing and oxidising conditions are often required to activate the acceptor defects as discussed in section 1.2.4.[43,44] To compare the impact of the deposition conditions after annealing, the two sets of conditions selected previously (600 °C/100 mTorr and 600 °C/250 mTorr) were subject to thermal annealings at temperature of 600 and 700 °C during 3 h under continuous flow of oxygen (1 bar). These conditions have been set for two reasons: to increase the concentration of acceptor defects and to limit the formation energy of donor compensating defects by placing the system in extreme oxidising environment. The Zn doping is varied between 0-30 at.%. The films were deposited on quartz and (100) oriented silicon substrates. The KP measurements were performed with Si substrates due to the thermal degradation of ITO.

2.1. Film structure

The XRD data recorded for all the ZTO films deposited and annealed at 600 and 700 °C are shown in Figure 4.11. Without annealing the inclusion of Zn does not appear to induce the formation of secondary phase even at 30 at.% Zn. The main structure of the films remains the rutile form of SnO_2. As mentioned in section 1.2.5 secondary phases such as $ZnSnO_3$ and Zn_2SnO_4 have been reported to form more above 30 at.% doping.[45,46] However given the poor crystallinity of the films at 250 mTorr it is not excluded that some secondary phase exists either in small amount or in an amorphous state. Upon annealing at 600 and 700 °C no major changes are observed on the structure apart from the detection of a Zn_2SnO_4 phase at 34.6 ° 2θ. The intensity of the diffraction peak remains small compared to the SnO_2 ones therefore its contribution to the film structure is considered to be minor.

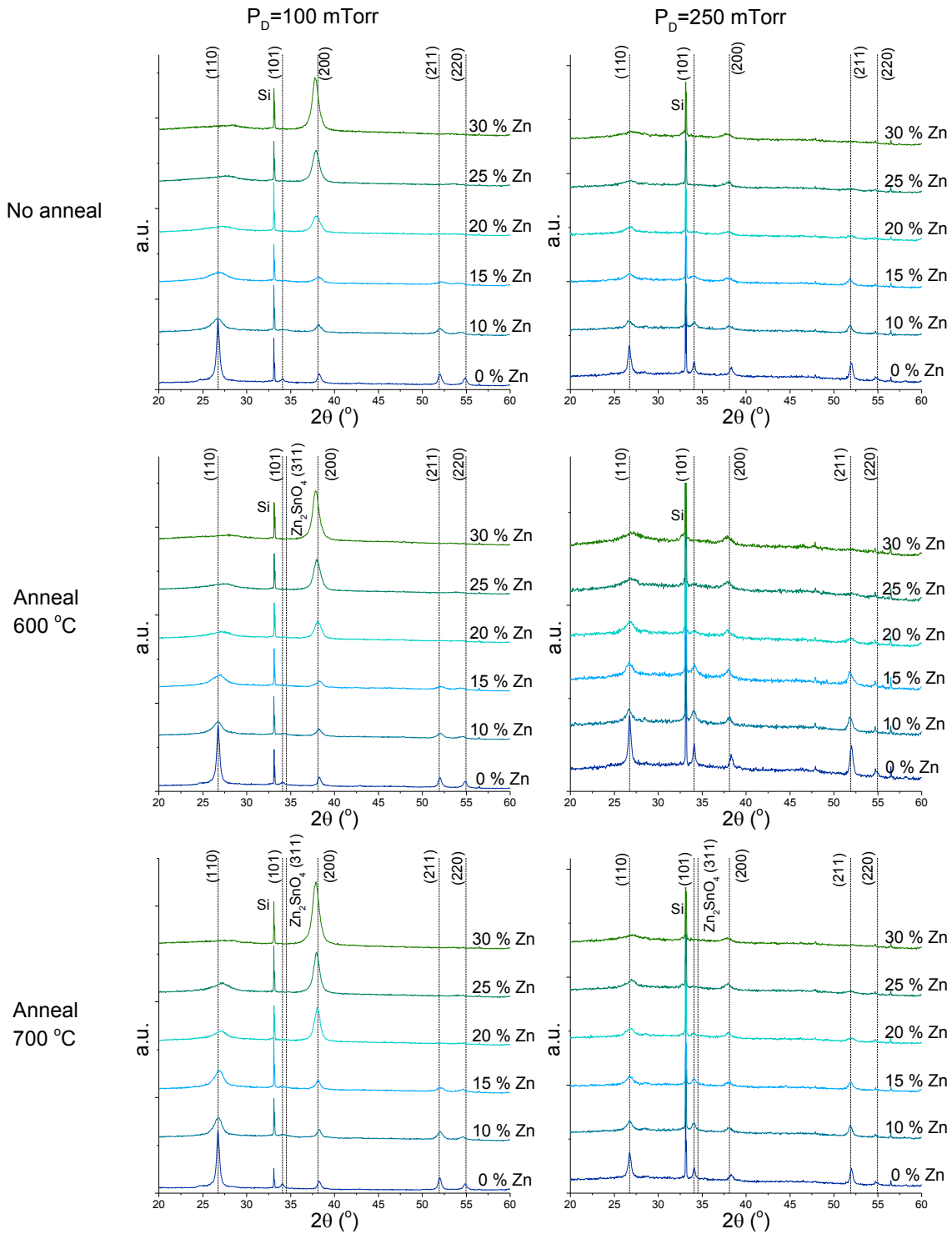

Figure 4. 11: XRD data of SnO_2 thin films doped with 0-30 at.% Zn deposited on Si substrates at 600 °C, under P_D of 100 and 250 mTorr, and annealed at 600 and 700 °C in O_2 atmosphere.

The a-lattice parameter of the different films was extracted from the (200) diffraction peak position and is shown in Figure 4.12. The lattice parameter increases when more Zn is added to the system. This confirms the integration of Zn in SnO_2 and the limitation of secondary phases. At higher P_D (250 mTorr) the lattice parameter appears to be larger for

Zn-doped samples which is coherent with what has been previously observed when the environment becomes oxygen-rich. This was attributed to the formation of compensating donor defects such as AX or Zn_i. As the films are annealed the trend of increased lattice parameter with increasing amount of Zn is conserved however the lattice parameter appears to reduce after the films have been annealed. This overall behaviour is observed for Zn doping higher than 10 at.% Zn. This slight change is interesting as previously the lowest lattice parameter observed when varying P_D was assigned to an increased concentration of acceptor defects and a decreased amount of compensating donor defects. The variations are more consequent in the case of the films deposited under 100 mTorr.

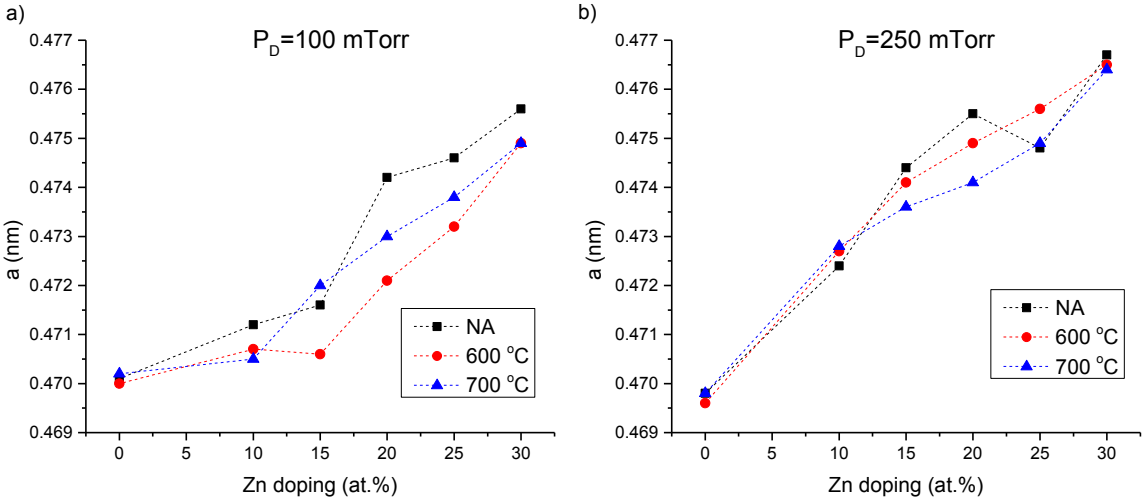

Figure 4. 12: a-lattice parameter extracted from the (200) diffraction plane for ZTO films with Zn doping from 0-30 at.% deposited at 600 °C, under a) 100 and b) 250 mTorr, not annealed (NA) and annealed in oxygen at 600 and 700 °C.

The thermal annealing in oxidising conditions did not considerably change the structure of the films, however the a-lattice parameter revealed a possible increase of acceptor defects, this will be investigated in the next section.

2.2. Electrical properties

2.2.1. Effect of Zn variation without annealing

The carrier concentration measured by Hall effect for the ZTO films with Zn variation and at different P_D is shown in Figure 4.13. The data corresponds to the properties of the films before thermal annealing. All the films measured showed n-type conductivity, this is later confirmed by the use of TFT devices in section 5.2.2.2.

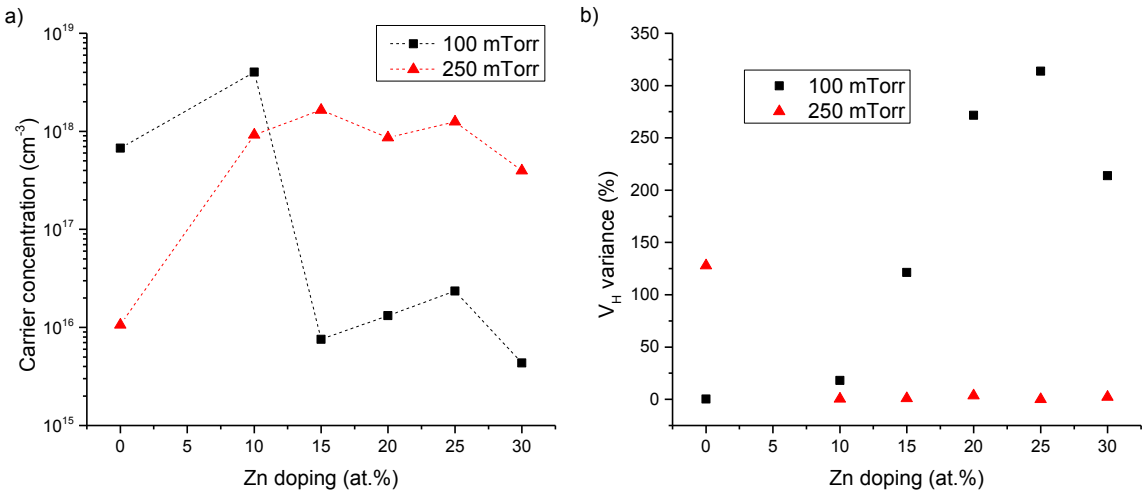

Figure 4. 13: Data of the films with Zn between 0-30 at.% deposited at 600 °C and under 100 and 250 mTorr NA showing a) the carrier concentration and b) the variance of the measured Hall voltage (V_H).

At P_D of 100 mTorr, the carrier concentration suddenly drops when the Zn doping exceed 10 at.%. Between 15 and 30 at.% Zn the carrier concentration remains about 10^{16} cm^{-3} without significant changes with respect to the lattice parameter evolution. However in this range of doping the measurement error was particularly high. As mentioned in the previous part, at 100 mTorr the 20 at.% ZTO this film were particularly hard to analyse due to high variation during the Hall effect measurements. The absolute errors are shown in Figure 4.13.b and were calculated based on the Hall voltage V_H. The error (V_H variance in %) represents the ratio between the variance of the V_H measured and their average. The larger deviations observed are a consequence of the low mobility of the films. The measurements show the more important deviations above 15 at.% Zn for the films deposited under 100 mTorr, therefore the carrier concentration cannot be fully trusted. However the Hall resistivity which is measured by Van der Pauw method possesses a much lower error (< 2 %), thus its variations can be used to describe the evolution of the carrier concentration in Figure 4.15.a.

Above 10 at.% doping the resistivity is much higher at 100 mTorr than at 250 mTorr, which is in agreement with the variations observed with the carrier concentration. When P_D is set at 100 mTorr the resistivity increases by two orders of magnitude in this range of doping. No trend can be observed with increasing doping at this pressure although the lattice parameter keeps increasing. The differences measured between the two P_D confirm the formation of more acceptor-like defects such as Zn_{Sn} at 100 mTorr and seem to appear above a certain doping threshold, 10 at.% Zn in this case. The WF measured by KP in Figure 4.14.b is consistent with the behaviour observed in the previous section as above 10 at.% Zn, WF is smaller at P_D 100 mTorr than at 250 mTorr while the carrier

concentration follows the opposite trend. As discussed previously this could be due to an increased band bending effect due to E_F moving into the band gap coupled with a higher position of the VBM at 100 mTorr.

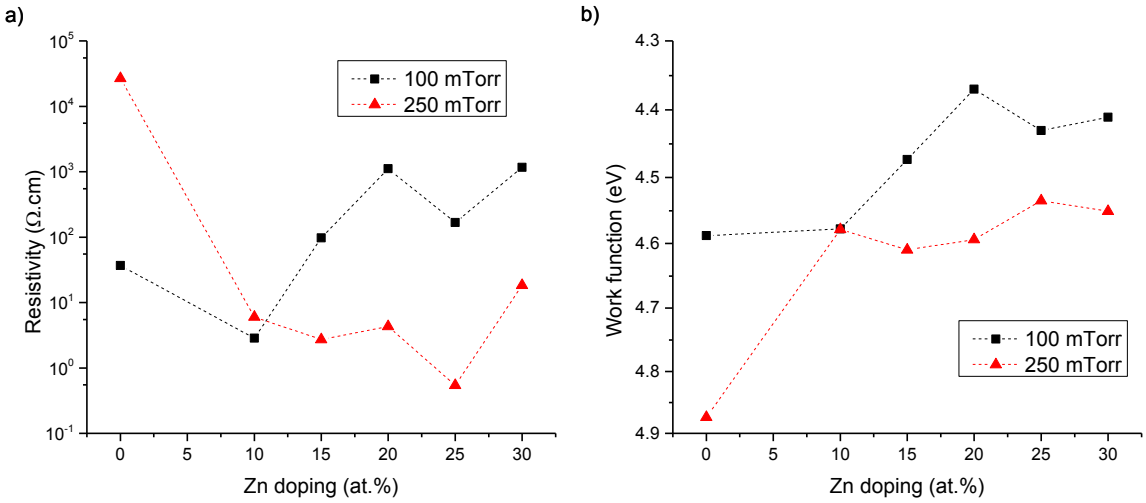

Figure 4. 14: Data of ZTO films with Zn between 0-30 at.% deposited at 600 °C and under 100 and 250 mTorr NA showing a) the Hall resistivity and b) the WF variations.

2.2.2. Thermal annealing and limitations

As the error during the Hall effect measurement becomes more predominant with high resistivity samples, the limit of the instrument was reached when analysing annealed samples.

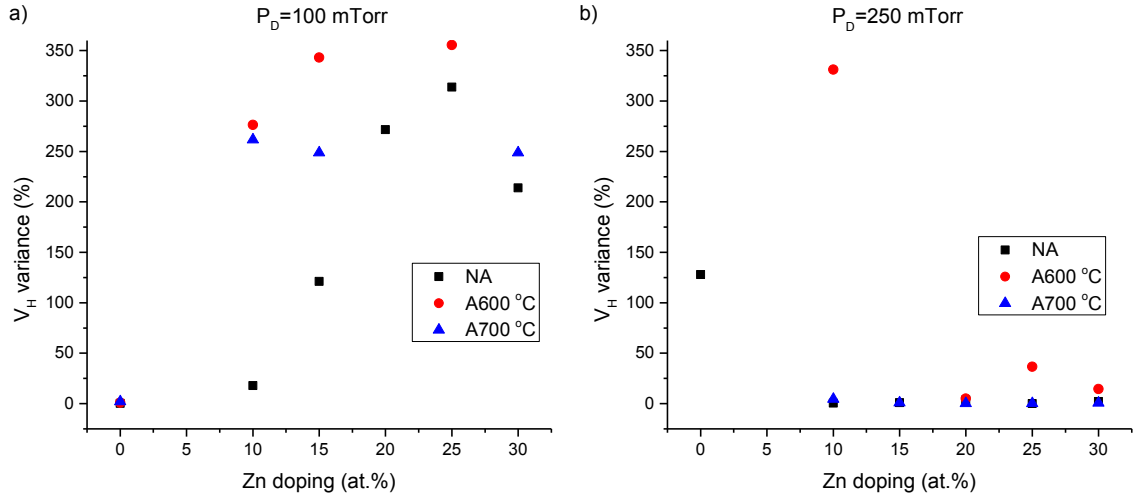

Figure 4. 15: Variance of the Hall voltage (V_H) from Hall effect measurements on ZTO films with Zn-doping between 0-30 at.%, deposited at 600 °C, under 100 and 250 mTorr, and under different annealing: none (NA), 600 °C (A600 °C) and 700 °C (A700 °C).

The variance of the Hall voltage (V_H) displayed in Figure 4.15 shows the deviations are too large to even consider the values measured for the carrier concentration. However the

error on the resistivity from the Van der Pauw measurements remained low for the analysed samples (< 3 %) and thus is more suited to compare the electrical behaviour. Some samples could not be measured, this was a combination of bad contact (schottky) and large resistivity exceeding the limits of the instrument.

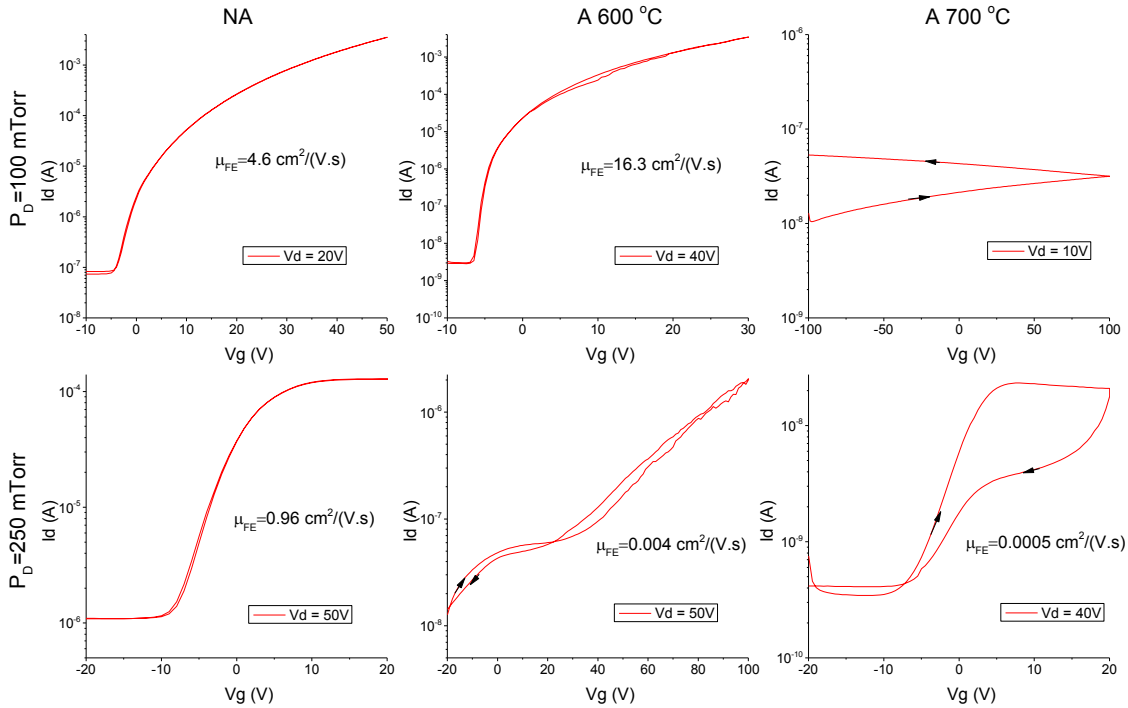

Figure 4. 16: Transfer curve of 20 at.% ZTO films deposited on Fraunhofer OFET substrates at 600 °C, under 100 and 250 mTorr, not annealed (NA) and annealed at 600 and 700 °C in oxygen. The transfer curves were measured in saturation mode and represent the drain current (Id) function of the gate voltage (Vg) at fixed drain voltage (Vd). The channel width was fixed at 2 mm and its length was 20 µm for the NA and 600 °C annealed samples, and 10 µm for the 700 °C annealed samples. μ_{FE} represents the saturation field effect mobility extracted from the transfer curves.

Due to the large errors present in the measurements, especially at 100 mTorr, the nature of the conductivity could not be fully determined by this method. Therefore films were deposited on TFT substrates (with a Si as gate contact, SiO_2 as dielectric, and ITO and Gold layers as top contacts) and annealed in the same conditions. The transfer curves corresponding to the 20 at.% ZTO films are shown in Figure 4.16. The transfer curves for the 10, 15, 25 and 30 at.% ZTO films are shown in Appendix 3 (Figures S3.1 and S3.2). All the films were found to be n-type semiconductor as the transistor channel starts to let current flow when the gate voltage is increased (from negative to positive). The increased annealing temperature affected the quality of the transistor. Since the top electrodes are made of gold and ITO layers they may be damaged at elevated temperatures, *i.e.* 700 °C. The larger hysteresis observed with increasing annealing temperature is attributed to either an increase of the traps in the films, a higher leakage current or the deterioration of

the electrodes. The resistivity of the ZTO films with and without annealing is shown in Figure 4.17.

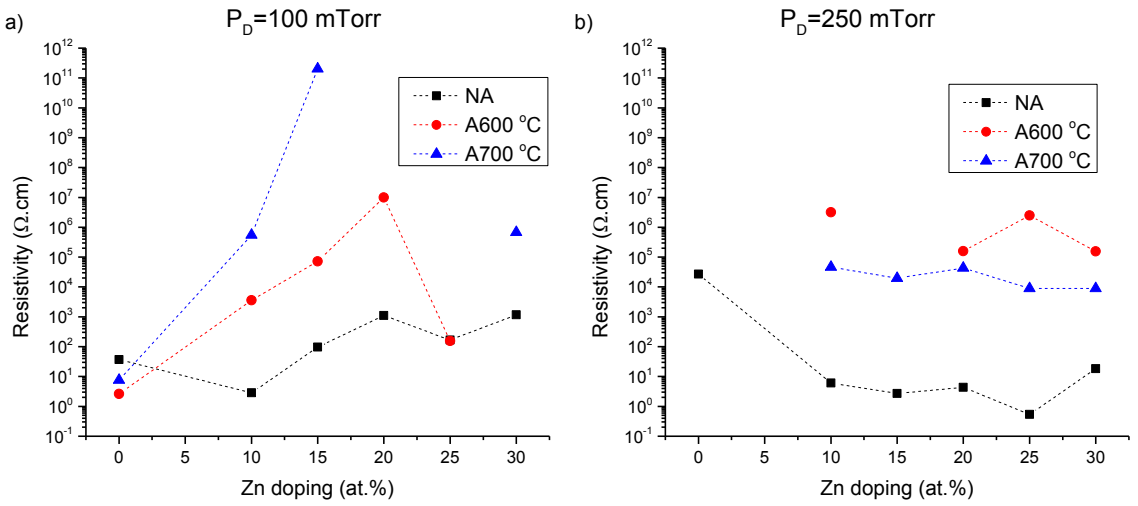

Figure 4. 17: Hall resistivity for ZTO films with Zn doping from 0-30 at.% deposited at 600 °C, under a) 100 and b) 250 mTorr, not annealed (NA) and annealed in oxygen at 600 and 700 °C.

After annealing at 600 and 700 °C, the resistivity of the samples increased dramatically. The difference between the NA and the annealed samples is more than 4-orders of magnitude. Even though the mobility has a direct contribution to the resistivity the variations encountered cannot be solely due to it and therefore the annealing step involved a consequent drop in the carrier concentration. Considering the undoped SnO_2 films, the annealing does not have a considerable impact on the resistivity of the films. The films deposited at 100 mTorr show a first increase of resistivity when annealed at 600 °C (apart from the 25 at.% Zn film) of about 3 order of magnitude then a considerable second increase when annealed at 700 °C. This suggests the formation of more Zn_{Sn} defects in the films, however since the type of conductivity did not change, the amount of donor or compensating defect remains larger. The films with 15, 20 and 25 at.% Zn under 100 mTorr and when annealed at 700 °C are considered to show the largest concentration of acceptor as they exceed the limit of the instrument. In the case of the films deposited at 250 mTorr, the increase in resistity is about 4-5 orders of magnitude but remain constant with increasing doping. Only the samples with 10 and 15 at.% Zn showed difficulty in the measurements, the rest of the samples showed an variance below 50 % with Hall mobilities in the range of 1-10 $cm^2/(V.s)$. The monotonous increase of the lattice parameter indicates that above 10 at.% doping, the Zn incorporated forms either neutral defects or electrically active defects (either donor, Zn_i, or acceptor, Zn_{Sn}) but which are immediately compensated since no considerable variation in the resistivity is observed.

Despite the difficulty to discuss accurately defect formation, it is clear that the Zn forms some acceptor defects under annealing treatment. The increase of resistivity cannot be attributed to a sheer decrease of intrinsic donor defects as the undoped SnO_2 films do not show such variations at 100 mTorr. Therefore it is suggested that the thermal annealing provides the system enough energy to activate more Zn_{Sn} acceptor defects in the lattice, compensating a part of the intrinsic donor defects. The deposition conditions also seem to affect the electrical properties after annealing since with P_D of 250 mTorr no considerable variations of resistivity were measured above 10 at.% while with 100 mTorr the resistivity clearly increases up to 20-25 at.% Zn. At 100 mTorr the changes in resistivity are more consequent, especially when annealed at 700 °C. The Hall measurements of the films were mostly impossible to achieve after annealing, only the films deposited at 250 mTorr showed easy measurements with reduced errors. This confirms that the choice of the deposition conditions prior-annealing has a great impact on the film properties. Under no circumstances the type of conductivity changes from n to p-type. The main problem is the compensation of the acceptor defects formed. Either the acceptor defect relaxes into a donor (AX defect) or the formation energy of intrinsic donor defects is considerably lowered when the Fermi level move closer to the VB.

2.3. Impact on Fermi level and VBM

The WF measured by KP of the ZTO films with and without annealing are shown in Figure 4.18.

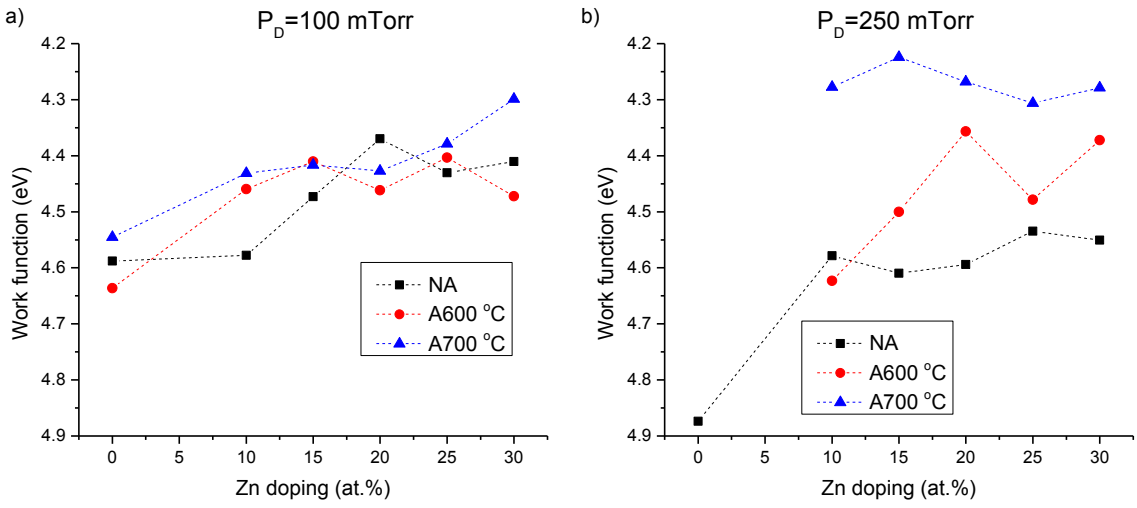

Figure 4. 18: WF measured by KP for ZTO films with Zn doping from 0-30 at.% deposited at 600 °C, under a) 100 and b) 250 mTorr, not annealed (NA) and annealed in oxygen at 600 and 700 °C.

The trends in WF measured by KP can be clearly seen in Figure 4.18 with a general decrease of WF with the introduction of Zn. The difference between NA and annealed

samples is particularly important for the ZTO films deposited under 250 mTorr. This is thought to be due to the large difference in acceptor defects as without annealing the Zn_{Sn} seems to transform into donor complex AX. As more energy is given to the system through the annealing, more Zn_{Sn} defects can be formed. However as mentioned in the previous sections, several mechanisms influence the WF measured by KP, including a change in the VBM position (surface dipole). A comparison between the E_F measured by XPS and KP along with the VBM extracted from valence band onset measurement via XPS is shown in Figure 4.19. The band gap used for the positioning of the CBM along with the valence band onset of the ZTO films can be found in Appendix 3 (Figures S3.3 and S3.4).

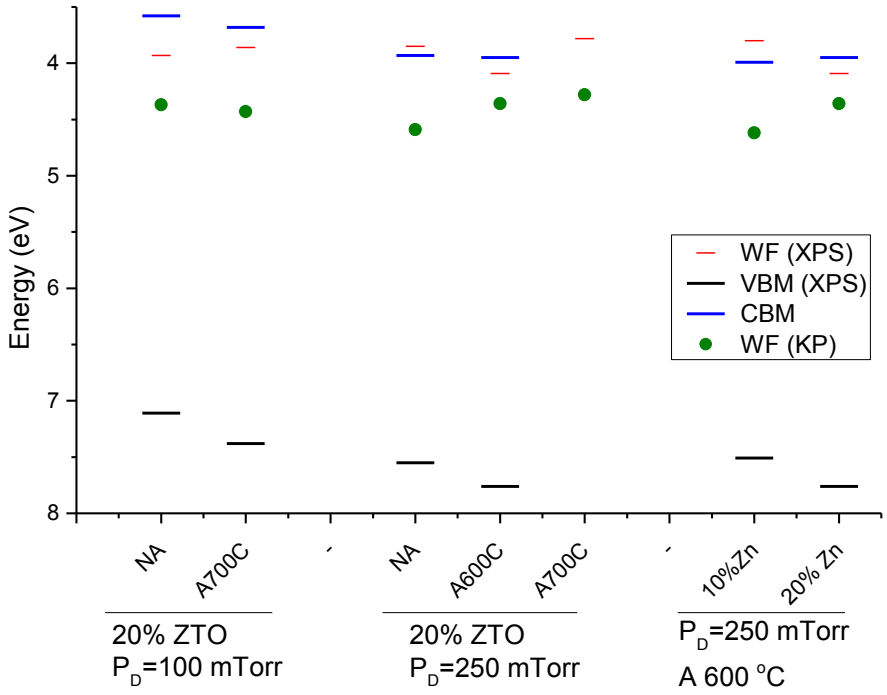

Figure 4. 19: Diagram representing the position of the Fermi level (red) and VBM (black) measured by XPS, the Fermi level measured by kelvin probe (KP) (green dot), and the CBM (blue) extracted by applying the measured optical band gap to the VBM. These level are compared between annealings (NA, A600C and A700C), P_D (100 and 250 mTorr) and Zn doping (10-20 at.%). The VBM for the 20 at.% ZTO film deposited at 250 mTorr and annealed at 700 °C could not be extracted.

The first observation is a decrease of the VBM when the samples are annealed. This is attributed to a more oxidising environment as the annealing has been performed at high temperature and under oxygen atmosphere.[37–39] As such change would be induced by a different surface dipole, the Fermi level is shifted accordingly. Another main element is ξ the energy difference between the VBM and E_F measured by XPS. ξ is seen to increase or remain constant after annealing of the films while the conductivity (carrier concentration) decreases dramatically. Such change is not coherent with the position of E_F in the bulk

which is expected to be lower due to the loss in charge carriers. Only two explanations are possible in this case: an upward surface band bending or an extension of the space charge layer causing the downward band bending. The upward band bending would be caused by charged surface acceptor defects such as Zn_{Sn} and lead to an electron depletion zone near the surface. However this possibility was discussed previously and Nagata *et al.*[28] showed a more intense downward band bending with In-doped SnO_2 where In was used as an acceptor dopant similarly to Zn. The second possible mechanism which is the increased band bending effect with decreasing carrier concentration agrees with what has been demonstrated by Vasheghani Farahani *et al.*[27] and Nagata *et al.*[28] and is illustrated in Figure 4.20.

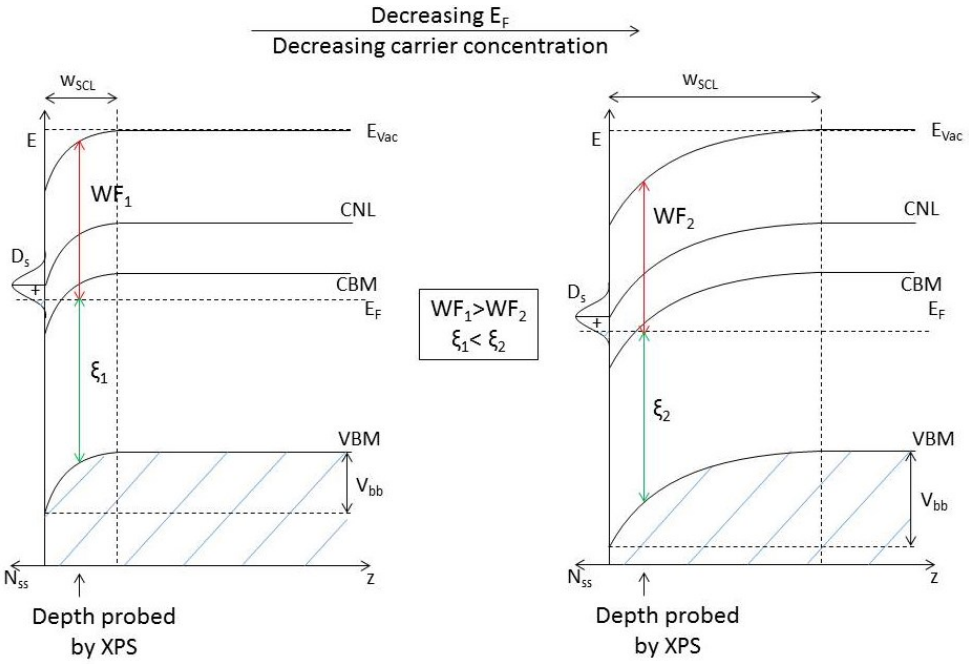

Figure 4. 20: Band diagram showing the influence of Fermi level position (E_F) and carrier concentration on the intensity of downward band bending (V_{bb}) and the width of the space charge layer (w_{SCL}) present at the surface of an n-type semiconductor. WF is the work function and ξ the energy difference between the VBM and the Fermi level E_F at the depth probed by XPS.

The VBM have been taken at the same level to simplify the discussion. When the carrier concentration decreases, the Fermi level moves in the band gap towards the valence band as fewer donor states below or in the CB are formed. Considering only the bulk of the sample, the work function would be larger when E_F is the lowest (closest to VBM) and ξ would be smaller. However the situation changes near the surface. The lower position of E_F induces the formation of more charged surface donors and the amount of electrons present to compensate the existing charges on the surface is reduced. Therefore the width of the SCL is increased and the band bending is more intense (larger V_{bb}). Considering the

depth probe by XPS which is a few nm, the WF and VBM measured by XPS would be at a much different depth in the SCL due to the increase in its width. While the measurement would appear near the end of the SCL at large electron concentration, it may only be the beginning of it at lower carrier concentration leading to a larger energy difference between the VBM and E_F. The same situation is thought to happen between 10 and 20 at.% ZTO films deposited under 250 mTorr and annealed at 600 °C. The energy difference between the VBM and E_F is slightly larger in the case of the 10 at.% ZTO films (3.71 eV against 3.67 eV for the 20 at.% ZTO films). Furthermore the resistivity measured with the 10 at.% Zn films is larger than with the 20 at.% ones and the measurement error is significantly higher as well suggesting the presence of a lower carrier concentration leading to larger band bending. At 250 mTorr the lowest resistivity achieved, supposedly thought to correspond to the highest concentration of acceptor defects, is between 10 and 15 at.% Zn doping. At 100 mTorr this "optimum acceptor doping" seems to occur at higher doping, between 20-25 at.% Zn and at higher annealing temperature of 700 °C.

As the ZTO films have been annealed, more acceptor defects were activated. Accurate measurements of the electrical properties could not be performed as the limits of the instrument were reached leaving only an insight on the resistivity of the films. However the high resistivity achieved and brief XPS analysis of the valence band onset and Fermi edge allowed to suggest the presence of a more prominent band bending as the films are annealed owned to the formation of more acceptor defects while remaining an n-type semiconductor.

3. Summary

In this study Zn was introduced in SnO_2 as an acceptor dopant. The aim was not to focus on turning the films p-type but to understand the deposition conditions and their effect on the formation energy of the acceptor defects. The growth environment was set such that the formation energy of compensating donor defect would be increased while that of Zn substitutional acceptor defect on Sn sites would remain low enough to be formed. Most studies on p-type doping of SnO_2 do not even consider the environment in which the films are grown with respect to the formation of compensating defects.[4,7,47] This part showed p-type conductivity could not be achieved in SnO_2 by doping with Zn. Below are summered several main points highlighted in this study.

- By carefully setting the growth environment to favour the formation of Zn_{Sn} acceptor defects a clear reduction of the conductivity after annealing at 700 °C was observed however the conductivity does not changes from n to p-type. Unlike the

p-type ZTO films reported in literature it was found to be impossible to switch the conductivity in SnO_2 with Zn.[3–5,11] The Zn_{Sn} acceptor defects formed are compensated by the formation of either AX centres, Zn_i or intrinsic donor defects.

- The lowest formation energy for Zn_{Sn} is thought to be achieved at 100 mtorr corresponding to an intermediated oxygen pressure between oxygen-poor and oxygen-rich environments. Unlike what has been shown in chapter 3 the largest P_D of 250 mTorr limiting the formation of intrinsic donor defect showed larger electron carrier concentration attributed to the formation of AX defect centres.
- Even though the annealing conditions were the same, the deposition conditions were found to influence greatly the amount of acceptor defect formed as lower conductivity (supposedly lower Fermi level) were achieved at P_D of 100 mTorr where the formation energy of these defect was the lowest.
- The carrier concentration, therefore the Fermi level position, impacts the intensity of the band bending observed in ZTO films and the width of the space charge layer. The presence of band bending was suggested through phenomenon already reported in the literature. Even though the data follows the suggested hypothesis more analysis could be performed to confirm it such as angle-resolved XPS.
- The introduction of Zn in SnO_2 induces a more reducing environment and lead to an increase of the VBM (consequently E_F) due to a change in the surface dipole. This behaviour is reversed as the films are exposed to extreme oxidising conditions lowering the VBM level.
- It is thought that the introduction of Zn as acceptor dopant in the optimum conditions lowers the position of the Fermi level through compensation of intrinsic donor defects and the formation of energy states close to VB. However the Fermi level is believe to be “stuck” in the band gap as suggested by Scanlon and Watson[2] and shown by Nagata *et al.*[28] due to the spontaneous formation of donor defects (negative formation energy) compensating the holes created even though the formation energy of acceptor defect is lowered in oxygen-rich environment.

Even though Zn was originally introduced as a p-type dopant this study showed the improvement of electrical properties at low temperature. This matter is studied in the next chapter of this thesis.

References

[1] J. Robertson, S.J. Clark, "Limits to doping in oxides", Phys. Rev. B - Condens. Matter Mater. Phys. 83 (2011) 1–7.

[2] D.O. Scanlon, G.W. Watson, "On the possibility of p-type SnO2", J. Mater. Chem. 22 (2012) 25236.

[3] J.M. Ni, X.J. Zhao, J. Zhao, "Structural, Electrical and Optical Properties of p-Type Transparent Conducting SnO2:Zn Film", J. Inorg. Organomet. Polym. Mater. 22 (2011) 21–26.

[4] K. Ravichandran, K. Thirumurugan, N. Jabena Begum, S. Snega, "Investigation of p-type SnO2:Zn films deposited using a simplified spray pyrolysis technique", Superlattices Microstruct. 60 (2013) 327–335.

[5] K. Thirumurugan, K. Ravichandran, "Role of solvent volume on the structural and transparent conducting properties of SnO2:Zn films", J. Mater. Sci. Mater. Electron. 25 (2014) 3594–3600.

[6] T. Yang, X. Qin, H. Wang, Q. Jia, R. Yu, B. Wang, et al., "Preparation and application in p–n homojunction diode of p-type transparent conducting Ga-doped SnO2 thin films", Thin Solid Films. 518 (2010) 5542–5545.

[7] M.-M. Bagheri-Mohagheghi, M. Shokooh-Saremi, "The influence of Al doping on the electrical, optical and structural properties of SnO2 transparent conducting films deposited by the spray pyrolysis technique", J. Phys. D. Appl. Phys. 37 (2004) 1248–1253.

[8] Z. Ji, Z. He, Y. Song, K. Liu, Z. Ye, "Fabrication and characterization of indium-doped p-type SnO2 thin films", J. Cryst. Growth. 259 (2003) 282–285.

[9] J.H. Ko, I.H. Kim, D. Kim, K.S. Lee, T.S. Lee, J.H. Jeong, et al., "Effects of ZnO addition on electrical and structural properties of amorphous SnO2 thin films", Thin Solid Films. 494 (2006) 42–46.

[10] K. Ravichandran, K. Thirumurugan, N. Jabena Begum, S. Snega, "Investigation of p-type SnO2:Zn films deposited using a simplified spray pyrolysis technique", Superlattices Microstruct. 60 (2013) 327–335.

[11] J. Ni, X. Zhao, J. Zhao, "P-type transparent conducting SnO2:Zn film derived from thermal diffusion of Zn/SnO2/Zn multilayer thin films", Surf. Coatings Technol. 206 (2012) 4356–4361.

[12] Y.S. Shen, T.S. Zhang, "Preparation, Structure and Gas-Sensing Properties of Ultramicro ZnSno3 Powder", Sensors and Actuators B-Chemical. 12 (1993) 5–9.

[13] R. Eason, "Pulsed Laser Deposition of Thin Films: Applications-Led Growth of Functional Materials", John Wiley & sons, 2006.

[14] V. Bilgin, S. Kose, F. Atay, I. Akyuz, "The effect of Zn concentration on some physical properties of tin oxide films obtained by ultrasonic spray pyrolysis", Mater. Lett. 58 (2004) 3686–3693.

[15] J.H. Ko, I.H. Kim, D. Kim, K.S. Lee, T.S. Lee, B. Cheong, et al., "Transparent and conducting Zn-Sn-O thin films prepared by combinatorial approach", Appl. Surf. Sci. 253 (2007) 7398–7403.

[16] R.D. Shannon, "Revised Effective Ionic Radii and Systematic Studies of Interatomie Distances in Halides and Chaleogenides", Acta Cryst. 32 (1976) 751–767.

[17] Ç. Kılıç, A. Zunger, "Origins of Coexistence of Conductivity and Transparency in SnO2", Phys. Rev. Lett. 88 (2002) 095501.

[18] Q. Zhu, Q. Ma, D.B. Buchholz, R.P.H. Chang, M.J. Bedzyk, T.O. Mason, "Structural and physical properties of transparent conducting, amorphous Zn-doped SnO2 films", J. Appl. Phys. 115 (2014) 033512.

[19] B. Choudhury, A. Choudhury, "Oxygen vacancy and dopant concentration dependent magnetic properties of Mn doped TiO2 nanoparticle", Curr. Appl. Phys. 13 (2013) 1025–1031.

[20] M.M. Islam, T. Bredow, "Rutile Band-Gap States Induced by Doping with Manganese in Various Oxidation States", J. Phys. Chem. C. 119 (2015) 5534–5541.

[21] E. Jedvik, A. Lindman, M.Þ. Benediktsson, G. Wahnström, "Size and shape of oxygen vacancies and protons in acceptor-doped barium zirconate", Solid State Ionics. 275 (2015) 2–8.

[22] J. Bruneaux, H. Cachet, M. Froment, "Correlation Between Structural and Electrical Properties of Sprayed Tin Oxide Films With and Without Fluorine Doping", Thin Solid Films. 197 (1991) 129–142.

[23] J. Lee, "Effects of oxygen concentration on the properties of sputtered SnO2:Sb films deposited at low temperature", Thin Solid Films. 516 (2008) 1386–1390.

[24] A. Madan, M.P. Shaw, "The Physics and Applications of Amorphous Semiconductors", Academic Press, Inc., 1988.

[25] W. Hu, R.L. Peterson, "Charge transport in solution-processed zinc tin oxide thin film transistors", J. Mater. Res. 27 (2012) 2286–2292.

[26] C. Körber, P. Ágoston, A. Klein, "Surface and bulk properties of sputter deposited undoped and Sb-doped SnO2 thin films", Sensors Actuators B Chem. 139 (2009) 665–672.

[27] S.K. Vasheghani Farahani, T.D. Veal, J.J. Mudd, D.O. Scanlon, G.W. Watson, O. Bierwagen, et al., "Valence-band density of states and surface electron accumulation in epitaxial SnO2 films", Phys. Rev. B. 90 (2014) 155413.

[28] T. Nagata, O. Bierwagen, M.E. White, M.Y. Tsai, Y. Yamashita, H. Yoshikawa, et al., "XPS study of Sb-/In-doping and surface pinning effects on the Fermi level in SnO2 (101) thin films", Appl. Phys. Lett. 98 (2011) 232107.

[29] X. Hana, G. Shao, "Theoretical prediction of p-type transparent conductivity in Zn-doped TiO2", Phys. Chem. Chem. Phys. (2013) 9581–9589.

[30] A.K. Singh, A. Janotti, M. Scheffler, C.G. Van de Walle, "Sources of Electrical Conductivity in SnO2", Phys. Rev. Lett. 101 (2008) 055502.

[31] C.H. Park, S.B. Zhang, S.-H. Wei, "Origin of *p* -type doping difficulty in ZnO: The impurity perspective", Phys. Rev. B. 66 (2002) 073202.

[32] D.J. Chadi, E. Si, "Predictor of p -type doping in II-VI semiconductors", 59 (1999) 181–183.

[33] K. Biswas, M.-H. Du, "AX centers in II-VI semiconductors: Hybrid functional calculations", Appl. Phys. Lett. 98 (2011) 181913.

[34] R.G. Egdell, J. Rebane, T.J. Walker, D.S.L. Law, "Competition between initial- and final-state effects in valence- and core-level x-ray photoemission of Sb-doped SnO2", Phys. Rev. B. 59 (1999) 1792–1799.

[35] J.-M. Themlin, M. Chtaib, L. Henrard, P. Lambin, J. Darville, J. Gilles, "Characterization of Tin Oxides by X-ray-Photoemission Spectroscopy", Phys. Rev. B. 46 (1992) 2460–2466.

[36] M. Krzywiecki, L. Grządziel, A. Sarfraz, D. Iqbal, A. Szwajca, A. Erbe, "Zinc oxide as a defect-dominated material in thin films for photovoltaic applications –

experimental determination of defect levels, quantification of composition, and construction of band diagram", Phys. Chem. Chem. Phys. 17 (2015) 10004–10013.

[37] A. Klein, C. Körber, A. Wachau, F. Säuberlich, Y. Gassenbauer, R. Schafranek, et al., "Surface potentials of magnetron sputtered transparent conducting oxides", Thin Solid Films. 518 (2009) 1197–1203.

[38] J. Montero, C. Guillen, C.G. Granqvist, J. Herrero, G.A. Niklasson, "Preferential Orientation and Surface Oxidation Control in Reactively Sputter Deposited Nanocrystalline SnO2:Sb Films: Electrochemical and Optical Results", ECS J. Solid State Sci. Technol. 3 (2014) N151–N153.

[39] C. Körber, J. Suffner, A. Klein, "Surface energy controlled preferential orientation of thin films", J. Phys. D. Appl. Phys. 43 (2010) 055301.

[40] X. Yong, M.A.A. Schoonen, "The absolute energy positions of conduction and valence bands of selected semiconducting minerals", Am. Mineral. 85 (2000) 543–556.

[41] M.M. Beerbom, B. Lagel, A.J. Cascio, B. V. Doran, R. Schlaf, "Direct comparison of photoemission spectroscopy and in situ Kelvin probe work function measurements on indium tin oxide films", J. Electron Spectros. Relat. Phenomena. 152 (2006) 12–17.

[42] H. Lüth, "Solid Surfaces, Interfaces and Thin Films", Springer, 2010.

[43] T. Aoki, Y. Shimizu, A. Miyake, A. Nakamura, Y. Nakanishi, Y. Hatanaka, "p-type ZnO layer formation by excimer laser doping", Phys. Status Solidi Basic Res. 229 (2002) 911–914.

[44] C. Morhain, M. Teisseire, S. Vézian, F. Vigué, F. Raymond, P. Lorenzini, et al., "Spectroscopy of Excitons, Bound Excitons and Impurities in h-ZnO Epilayers", Phys. Status Solidi B. 229 (2002) 881–885.

[45] T. Minami, S. Takata, H. Sato, H. Sonohara, "Properties of transparent zinc-stannate conducting films prepared by radio frequency magnetron sputtering", J. Vac. Sci. Technol. A. 13 (1995) 1095.

[46] Y. Hayashi, K. Kondo, K. Murai, T. Moriga, I. Nakabayashi, H. Fukumoto, et al., "ZnO-SnO2 transparent conductive films deposited by opposed target sputtering system of ZnO and SnO2 targets", Vacuum. 74 (2004) 607–611.

[47] C.-Y. Tsay, S.-C. Liang, "Fabrication of p-type conductivity in SnO2 thin films through Ga doping", J. Alloys Compd. 622 (2015) 644–650.

Chapter 5: Use of Zn to improve electrical properties of SnO_2

ZnO was first combined with SnO_2 by Enoki *et al.*[1] in 1992 and later investigated by Minami *et al.*[2,3] to improve the n-type conductivity. In these study the amount of Zn used was too high to be considered doping, the resulting material was neither SnO_2 nor ZnO but a new multicomponent oxide ZnO-SnO_2. Depending on the concentration of Zn used two ternary compounds could be formed $ZnSnO_3$ or Zn_2SnO_4. Minami *et al.* considered these oxides to be promising for the development of new TCOs with resistivity as low as 4 $x10^{-3}$ Ω.cm[4]. Despite a lot of research performed on this matter, few studies have been done on Zn-doping of SnO_2 to improve its electrical conductivity while maintaining the SnO_2 rutile structure. The structure has been reported to diverge above 30 at.% Zn doping[4,5] but some reports[6] observed slight formation of Zn_2SnO_4 even though the films were mainly constituted of SnO_2 rutile structure.

The original aim for the incorporation of Zn in SnO_2 is the formation of acceptor defects to push the system towards p-type conductivity. However this state of conductivity in SnO_2 has been found to be unstable and limited by the presence of the CNL in the CB.[7,8] (See chapter 4) The formation of acceptor defects is unfavoured which leads to the compensation or the rearrangement of the defects. In the case of Zn doping, a different configuration is assumed to be adopted at low deposition temperature leading to the formation of more V_O as shown by Zhu *et al.*[9]. As only few reports mention the use of Zn in SnO_2, some properties of the films have been discussed but the results are scattered and generally incomplete.

The aim of this study is to highlight the potential of Zn as a n-type dopant in SnO_2 and discuss its possible integration in applications. Low resistivity ZTO films were observed in the chapter 4 at T_D < 500 °C. This section focuses on the use of Zn-dopant at relatively low temperature (≤ 400 °C). The films were deposited on quartz, Si (100) oriented and ITO covered glass substrates. The ZTO targets used are the same as in chapter 4 and the Zn doping was controlled by EDX, see Appendix 2. The Zn content in the films for the 10, 15, 20, 25 and 30 at.% ZTO targets were 7.3 ± 1.6, 14.7 ± 1.26, 19.37 ± 1.47, 25.2 ± 1.1 and 28.6 ± 1.1 at.% Zn respectively.

1. Influence of Zn doping variation

In this section the influence of Zn addition to SnO_2 is investigated, with an objective of improving electrical properties, *i.e.* conductivity, of the as-deposited thin films. The amount of Zn is varied between 0 and 30 at.% and the targets used are the same as that in chapter 4. Three different conditions were investigated, high temperature to set the environment more in Zn acceptor conditions (T_D = 600 °C and P_D = 75 mTorr), intermediate temperature to increase conductivity but keep good crystallinity (T_D = 400 °C and P_D = 50 mTorr), and low temperature to maintain low resistivity but move towards an amorphous system (T_D = 200 °C and P_D = 25 mTorr). All the films were deposited on quartz, ITO and (100) orientated silicon substrates. The thicknesses of the films deposited were 224 ± 23, 226 ± 10 and 213 ± 15 nm at 600, 400 and 200 °C respectively.

1.1. Growth orientation and crystallinity

XRD data of the ZTO films deposited at 400 °C and 50 mTorr, and at 600 °C and 75 mTorr are displayed on Figure 5.1. The data from the low temperature series (200 °C/25 mTorr) shows only a low degree of crystallinity below 15 at.% Zn and thus is not displayed here.

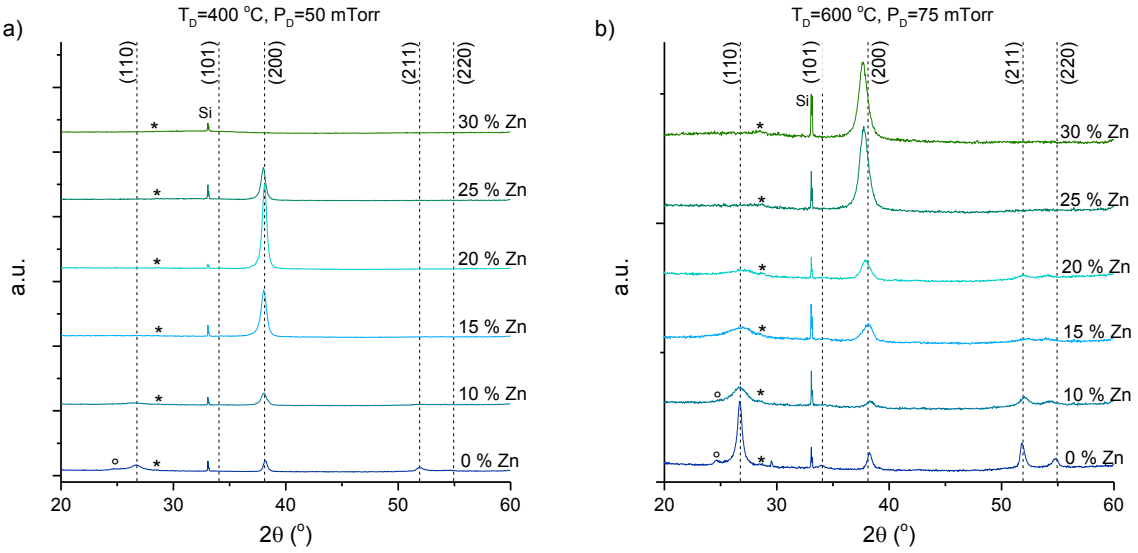

Figure 5. 1: XRD data of SnO_2 films doped with Zn between 0 and 30 at.% deposited on Si at a) temperature (T_D) of 400 °C and oxygen pressure (P_D) of 50 mTorr and b) T_D of 600 °C and P_D of 75 mTorr. The major peaks identified belong to SnO_2 phase and dashed lines derived from ICDD 01-077-0452. The Si substrate peaks are clearly identified in addition to a small peaks attributed to a minor SnO phase (*) and orthorhombic SnO_2 phases (o).

All films show a tetragonal rutile SnO_2 phase with the presence of a minor SnO phase observed and orthorhombic SnO_2 phase at some conditions. No additional phases, *i.e.* $ZnSnO_3$ or Zn_2SnO_4, were been observed despite the high amount of Zn doping. While the undoped SnO_2 films show polycrystalline growth with main orientations (110) and (200),

the introduction of Zn in the system appears to modify the growth in the <200> direction. The intensity of the other diffraction peaks such as (110) and (211) decreases to the profit of the (200) orientation. Such changes in orientation with the addition of Zn in the system have previously been reported by Vijayalakshmi *et al.*[10] and Bilgin *et al.*[11]. Even though Vijayalakshmi *et al.* observed the growth orientation changes as more Zn was added (0 - 25 at.%), the shift was not as predominant as in this study using a PLD system. The change of orientation towards the (200) plane is rather uncommon since most of the reports mentioned a shift to the (101) plane instead.[12–15] Jiang *et al.*[16] mentioned the possibility of a decrease of the surface energies of various crystalline planes but no further explanation has been suggested. In order to understand the origin of this change it is necessary to look at the type of environment required for such orientated growths. As mentioned in section 2.1.1.2 the surface energy of crystallographic plane needs to be lower than the others to be formed preferentially. Batzill and Diebold[17,18] calculated the surface energies of the (110), (101) and (100) surfaces in both stoichiometric and reduced conditions. The resulting energies and the detailed crystallographic surfaces are highlighted in Figure 5.2.

The stoichiometric forms of the different surfaces discussed here are composed of oxygen terminations leaving the surface Sn in a +4 oxidation state. However in their reduced form the surfaces are depleted of oxygen and thus the surface Sn are in a +2 oxidation state. At high oxygen chemical potential (μ_O) the stoichiometric forms of the surfaces are more stable, due to the lower surface energy than their respective reduced form. The opposite happens at low μ_O (oxygen-poor environment) where the oxygen depleted surfaces become more stable with lower surface energies.[18] According to calculations[17] the reduced (101) surface is more stable at low oxygen content due to the presence of more Sn^{2+} atoms while the stoichiometric (110) surface is more stable at high oxygen content. In this diagram the (100) surface does not seem to be predominant in any conditions. Some studies[19,20] experimentally show the transition from (101) to (110) orientation relating to the theoretical calculations from Batzill and Diebold, but no preferential (200) growth was mentioned. However, the XRD data of the undoped SnO_2 films deposited at 600 °C and under different oxygen pressure from chapter 3 (sections 3.3.1 and 3.4.1) proves otherwise.

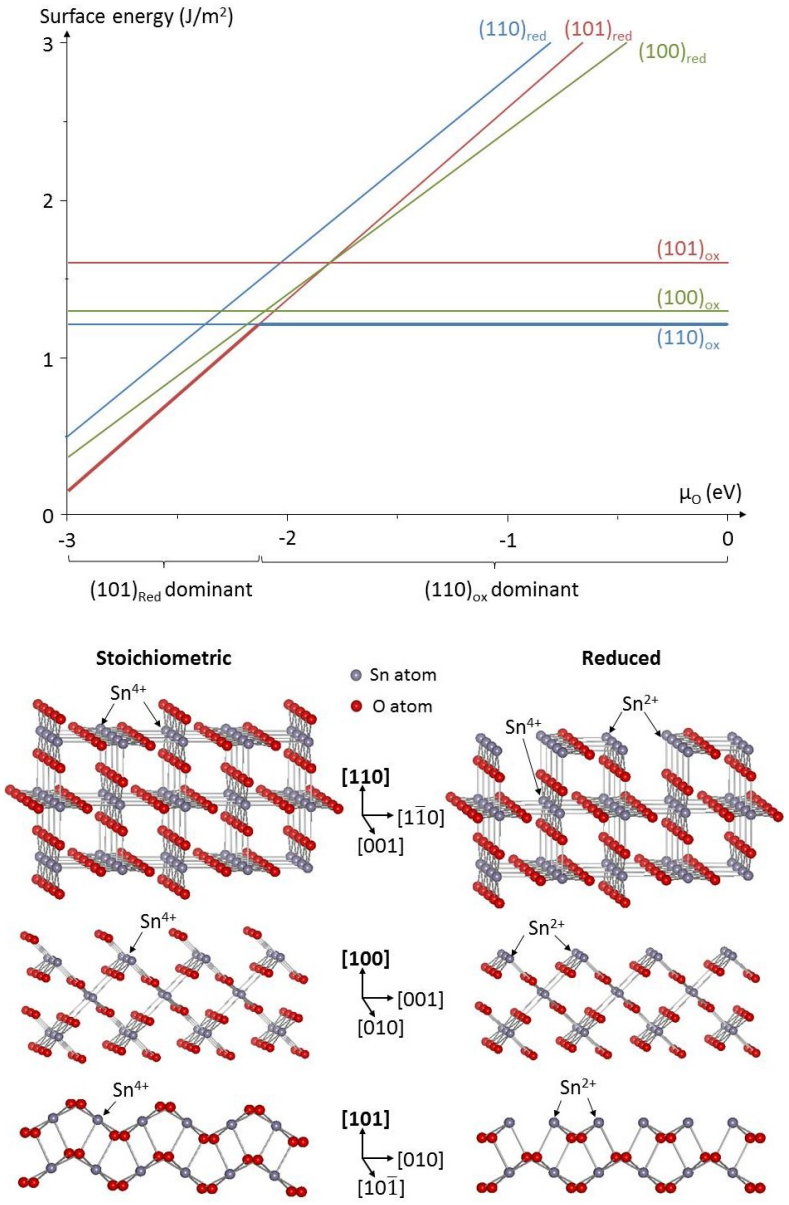

Figure 5. 2: (top) Surface energy of the three main surface orientations observed in SnO_2 thin films (110), (101) and (100), function of the oxygen chemical potential (μ_O). Low μ_O indicate an oxygen-poor environment while high μ_O (0 eV) represents an oxygen-rich environment. The signs red and ox represent the reduced and oxidised (stoichiometric) forms of the surfaces respectively. (bottom) Ball-and-stick models of SnO_2 showing the bulk termination of the (110), (100) and (101) surfaces. Stoichiometric terminations are represented on the left surfaces with reduced oxygen concentration are shown on the right. Data gathered and representation adapted from Batzill and Diebold calculations.[17]

To demonstrate it, the texture coefficients TC(hkl) of the SnO_2 films deposited with and without polished target were calculated for each of the diffraction planes using the formula,[21]

Equation 5.1

$$TC(hkl) = \frac{I(hkl)/I_0(hkl)}{(1/N)\sum I(hkl)/I_0(hkl)}$$

Where TC(hkl) is the texture coefficient of the hkl plane concerned, I(hkl) is the integrated area of the peak, I_0(hkl) the corresponding standard intensity from the ICDD data (01-077-0452) and N the number of diffraction peak observed. The calculated texture coefficients are shown in Figure 5.3.

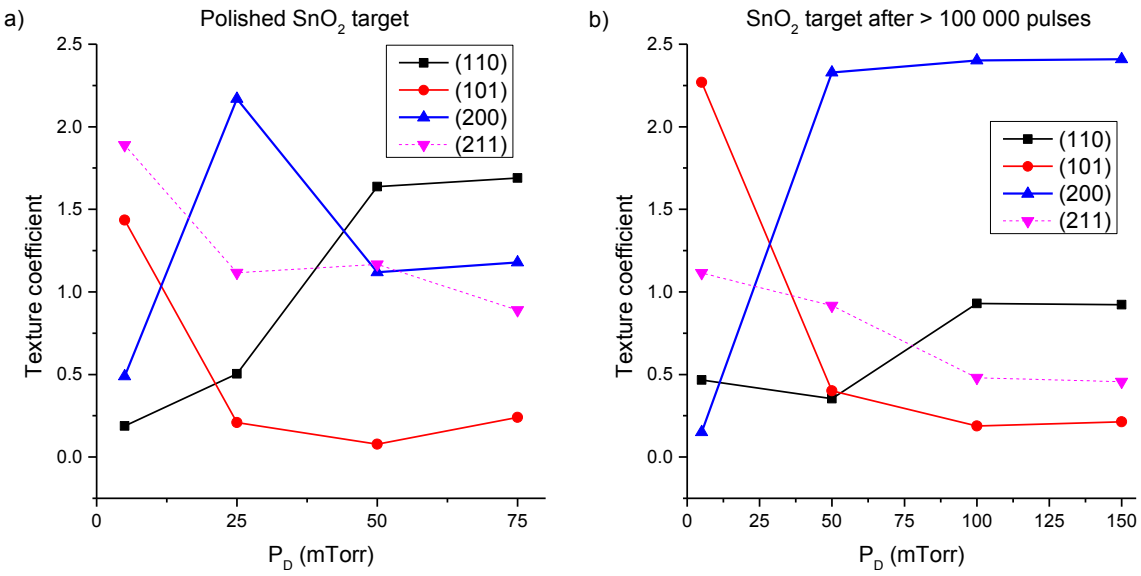

Figure 5. 3: Texture coefficient of the SnO_2 films deposited at 600 °C and under various oxygen pressure P_D, calculated from the XRD data found in 3.3.1 and 3.4.1. a) Texture coefficient of the films deposited with a polished SnO_2target and b) texture coefficient of the films deposited with SnO_2 target exposed to > 100 000 laser pulses.

With the polished SnO_2 target the (101) orientation is grown at 5 mTorr and the (110) at 50 mTorr which accounts for the change in environment with the increase in P_D. However at 25 mTorr the orientation showing the most texture is the (200). This feature may place the (200) surface as an intermediate surface between the (101) formation in heavily oxygen deficient conditions and the (110) formation in higher oxygen environment. What is observed here is the reduced form of the (200) surface since the environment is more towards oxygen-poor (25 mTorr). Therefore as the amount of oxygen (oxygen chemical potential) increases SnO_2 would preferentially grow along the $(101)_{red}$, $(200)_{red}$ and finally the $(110)_{ox}$ showing the existence of a narrow window for the preferential formation of the (200) plane. The TC calculated for the SnO_2 target exposed to > 100 000 laser pulses support this hypothesis. Since the target has been exposed to multiple laser pulses, the growth environment has been pushed towards Sn-rich/O-poor and highly favours the growth of reduced surfaces. The $(101)_{red}$ is more textured at 5 mTorr but between 50 and 150 mTorr the films are clearly more $(200)_{red}$ oriented. Therefore the (200) orientation can be formed preferentially and seems to appear under oxygen-poor conditions due to the higher stability and surface energy of its reduced form.

The TC of the ZTO films with doping variation from 0-30 at.% Zn based on the XRD presented in Figure 5.1 are displayed in Figure 5.4.

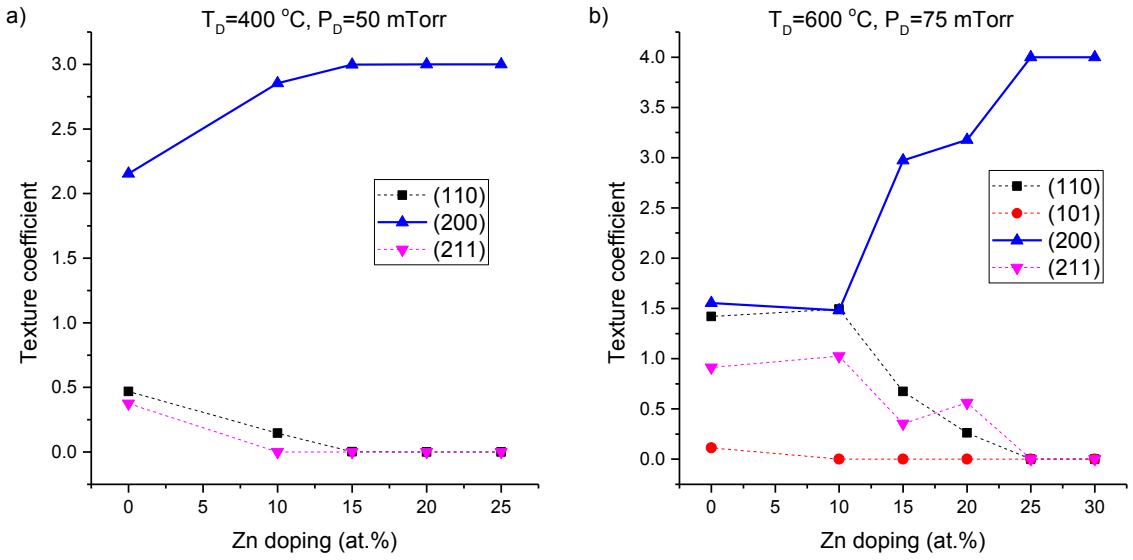

Figure 5. 4: Texture coefficient of the Zn-doped SnO_2films with amount of Zn between 0 and 30 at.% calculated from data found in figure 5.1.

The films grown clearly show an increased (200) orientation as the Zn doping increases. The effect is even more significant on the films deposited at 600 °C with the decrease of the (110), (101) and (211) intensities. The films change from a polycrystalline to single orientation along the (200) with the addition of Zn. The origin of such change is thought to be due to the oxidation state of Zn^{2+}. The (200) surface is more stable in its reduced form where the surface tin are in a +2 states. Therefore the introduction of Zn with +2 oxidation state could force the formation of a reduced surface, in this case the (200). This hypothesis supports the idea suggested in chapter 4 that the introduction of Zn induces a more oxygen deficient environment. This preferential orientation is surprising as most of the result in literature observe a (101) shift. However it is believed to be due to the technique used. It should be noted that despite the preferential orientation reported with the introduction of Zn, it has never been reported to such an extent with singly oriented films without epitaxial growth. The best result is found at 400 °C and 50 mTorr for a Zn doping of 20 at.% where the (110), (101) and (211) orientation disappear and the (200) presents its highest diffraction peak intensity for comparable thicknesses between the different dopings.

Along with this change of growth, a change in the crystallinity is observed while adding Zn to the SnO_2 system. The XRD data for the ZTO films deposited at 200 °C and 25 mTorr, and

the crystallite size of the ZTO films extracted with the Scherrer's equation on the FWHM of the (200) diffraction peak are shown on Figure 5.5.

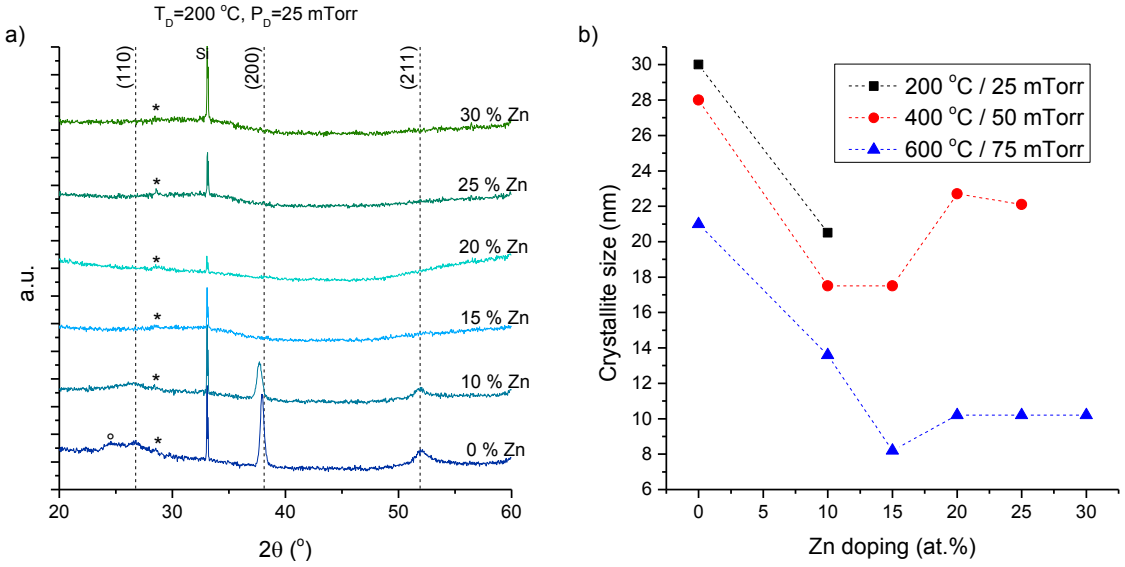

Figure 5. 5: a) XRD data of SnO_2 films doped with Zn amount between 0 and 30 at.% deposited on Si at 200 °C and 25 mTorr. The Si substrate peaks are clearly identified in addition to a small peaks attributed to a minor SnO phase (*) and a minor orthorhombic SnO_2 phases (o). b) Crystallite size of the ZTO films deposited under various conditions calculated with the Scherrer's equation based on the FWHM of the (200) diffraction peak.

It can be noted from Figure 5.1 that the crystallinity of the films decreases after a certain amount of Zn is added. The intensity of the (200) diffraction peak at 400 °C increases until 20 at.% Zn, above this point the intensity drops dramatically leading to nearly amorphous films at 30 at.%. This limit seems to be function of the growth conditions. At high T_D, the maximum diffraction peak intensity reached is between 25-30 at.% Zn while at 200 °C, Figure 5.5.a, the crystallinity already decreases at 10 at.% Zn and the films become amorphous at higher doping. The decay of crystallinity can also be noticed in the crystallite size evolution on Figure 5.5.b. The crystallite size is reduced with addition of Zn compared to the undoped SnO_2 films with grains size down to 10 nm at 600°C above 15 at.% Zn doping. However the values extracted with the Scherrer's method do not reflect completely the crystallite size due to possible strain effects in the films. Considering the large level of dopant used (20 at.% Zn) the repartition of Zn in SnO_2 lattice is unlikely to be homogenous and therefore would lead to different lattice sizes, thus variations of strain in the films. The resulting effect is a broadening of the diffraction peak which influences the calculation of crystallite size. Under normal circumstances the crystallite sizes extracted from XRD are compared to the size of the grains measured using SEM, however the shape of the grains could not be observed under SEM. The degradation of crystallinity with inclusion of Zn dopant in SnO_2 has been reported by several authors.[13–15] In these

studies the intensity of the diffraction peaks decreases along with the size of the crystallite. Tian *et al.*[14] suggested that the addition of Zn accelerates the rate of nucleation during the crystallisation. After the nucleation a part of the Zn^{2+} ions would move to the surface and block the coalescence of small SnO_2 crystallites. This hypothesis supports the idea that Zn^{2+} ions decrease the surface energy of the (200) reduced surface and allow the film to grow along this orientation.

In summary, when large amounts of Zn are used to dope SnO_2 (10-30 at.%) the films require higher deposition temperatures to reproduce the level of crystallinity observed in the undoped films, which may be associated with the additional energy required to incorporate Zn(II). However Zn allows the growth of highly (200) oriented films to the detriment of crystalline quality with smaller crystallite size observed.

1.2. Electrical and optical properties

Analysis of the electrical characteristics of the films prepared using AC Hall under the different conditions investigated is shown in Figure 5.6. The case of T_D = 600 °C and P_D = 75 mTorr is similar to the case studied in chapter 4 at 600 °C and 100 mTorr where the addition of Zn above 15 at.% leads to a dramatic drop in carrier concentration supposedly due to compensation of charge carriers through the formation of acceptor defects. The focus is brought to the ZTO films deposited at 200 and 400 °C which show surprisingly low resistivities. As the amount of Zn dopant is increased, the carrier concentration would be expected to decrease due to Zn substitution on Sn site leading to the formation of 2 holes and compensating the existing electrons (which happens at higher temperature). However the results on Figure 5.6 demonstrate the opposite. No dramatic drop of charge carrier concentration is observed, instead the evolution with increasing Zn is steady and even increases slightly at 400 °C up to 20 at.% Zn. Above this amount of doping the carrier concentration starts to decrease but not significantly. A change in behaviour of Zn under these conditions may be responsible for the difference observed. Zhu *et al.*[9] studied the environment around Sn and Zn in amorphous ZTO thin films deposited by PLD with Zn doping between 0 - 30 at.%. By using X-ray absorption techniques (X-ray absorption near edge structure and extended X-ray absorption fine structure) they were able to determine the coordination number (CN) of Sn and Zn in the films. While Sn CN is slightly below 6 due to the presence of V_O, Zn showed a surprising CN of 4 and less. This indicated that under these conditions, Zn would adopt a coordination of 4 oxygen atoms when substituting on Sn site inducing the formation of 2 oxygen vacancies. The resulting defect would not be $Zn_{Sn}^{//}$ but a new defect complex in the form of $\left(Zn_{Sn}^{//} - V_O^{\circ\circ}\right)^x$. Zhu *et al.*

identified the structure around Sn in the amorphous ZTO films to be similar to amorphous and crystalline typical SnO_2 structure. Even though a large amount of the oxygen vacancy formed is expected to be in neutral state, they suggested the conductivity is still governed by the oxygen vacancy positively charged due to the high concentration formed through Zn doping. The lower coordination of Zn and the apparition of oxygen vacancies to avoid the formation of holes in these conditions could explain why the carrier concentration shown in Figure 5.6 does not decrease dramatically.

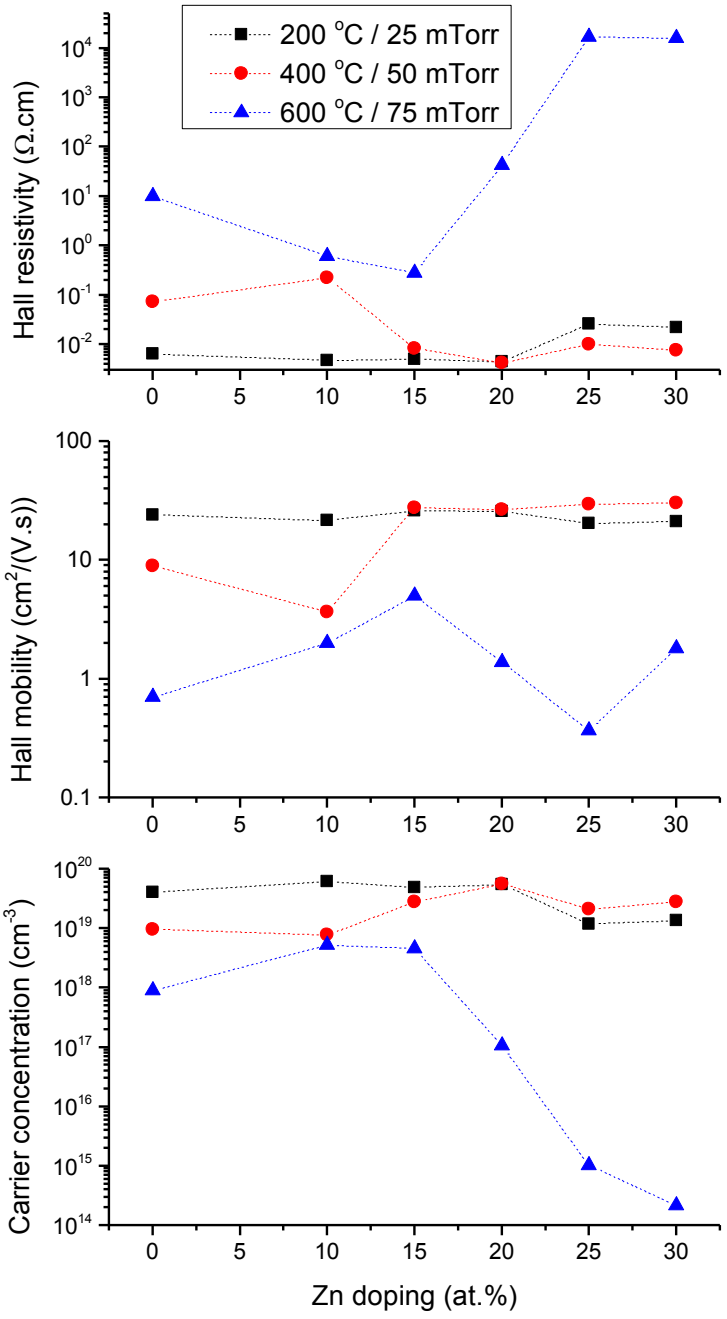

Figure 5. 6: Hall data of ZTO films deposited under different conditions showing the evolution of the Hall resistivity, Hall mobility and carrier concentration as function of the Zn doping.

The mobility also displays interesting behaviour while doping with Zn. At 400 °C, the mobility shows an increase from 8.9 $cm^2/(V.s)$ at 0 at.% Zn to 27.5 $cm^2/(V.s)$ at 15 at.% Zn. Above 15 at.% the mobility seems to stabilise around 30 $cm^2/(V.s)$. At 200 °C the mobility does not vary consequently and lies between 20-26 $cm^2/(V.s)$ with the highest values obtained at 15-20 at.% Zn. Even though the crystallinity of the samples changes with doping it does not seem to have a huge impact on the resulting mobility. Based on the evolution of the crystallite size shown on Figure 5.5.b, the mobility does not appear to be limited by grain boundary scattering. The addition of Zn in SnO_2 when processing at low temperature seems to stabilise and even increase the mobility of the charge carriers. This feature may be unique among TCOs while doping to such high levels. The highest mobility reported by Zhu *et al.*[9] was about 22 $cm^2/(V.s)$ and prior to their study, Ko *et al.*[22] already obtained mobility of 30 $cm^2/(V.s)$ with 20 at.% Zn doping and for films annealed at 450 °C. In both cases they observed an overall increase and stabilisation of the mobility with increasing Zn doping.

While the Zn doping is increased up to 30 at.% Zn the transparency of the films is maintained either at low (200 °C) or high (600 °C) temperatures as shown in Figure 5.7.

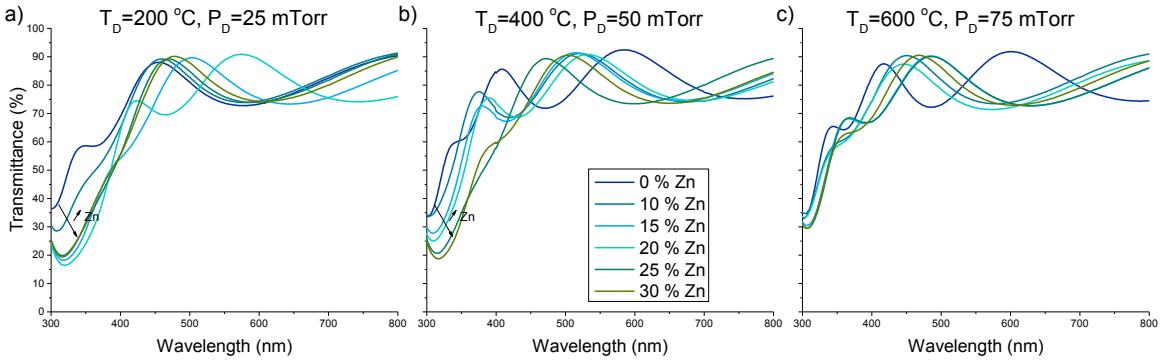

Figure 5. 7: UV-Vis transmission data measured between 300 and 800 nm wavelengths of the ZTO films deposited at a) 200 °C and 25 mTorr, b) 400 °C and 50 mTorr, and c) 600 °C and 75 mTorr.

The transmission in the visible range (400-800 nm) is about 80 % for all the films. No considerable change is observed in the transparency. The associated band gaps have been extracted and plotted in Figure 5.8.

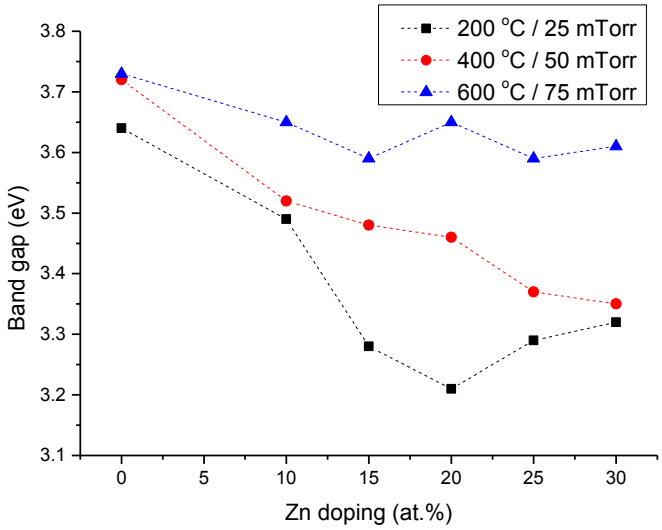

Figure 5. 8: Band gap of the deposited ZTO films extracted using the Tauc plot method.

Overall the band gaps obtained with the ZTO films are smaller than the undoped SnO_2 films. The difference is less important at higher temperature where at 600 °C E_g is only 0.05-0.1 eV below the value at 0 at.% Zn without showing significant changes at higher doping. The possibility of quantum size confinement effect on E_g due to the small size of the crystallite (about 10 nm at 600 °C) has been excluded since a drop in crystalline size would induce an increase of the band gap. However despite E_g being higher for the films at 600 °C than at 400 °C, the value of E_g are still lower than with 0 at.% Zn in the films even though the crystallite size at this doping is doubled (20 nm). Also no major change with increasing doping is observed while the crystallite size shows important variations. The films deposited at 400 °C show a more important decrease of E_g with increasing Zn doping than those deposited at 600 °C. The case of band gap narrowing with increasing amount of Zn has been previously reported by Vijayalakshmi *et al.*[15] in which they attributed it to the large difference in band gap between ZnO and SnO_2. Since the Zn present in the SnO_2 films deposited at 400 °C might mostly be surrounding by only 4 oxygen atoms (and 2 V_O) which is the same coordination as in the ZnO structure, it would not be surprising that with increasing amount of Zn more contribution of the 4-fold coordinated Zn would appear in the band gap of the films. The decrease of E_g observed in the films deposited at 200 °C is thought to be mainly due to the disorder present in the films. Disorder in amorphous films induces localised energy states at the band edge (just above the VBM and just below the CBM), these are called band tail states.[23] Due to their presence the resulting optical band gap is smaller since the localised states participate to the optical absorption and are located in the band gap. This phenomenon is called band tailing effect and has been previously noted to appear in SnO_2 thin films.[24,25]

The ZTO films showed good electrical performances while maintaining their optical transparency in the visible range. The band gap was varied between 3.2-3.7 eV with the lowest value at 3.4 eV for crystalline films and 3.2 eV for amorphous films. Such changes could be used in band gap tailoring applications, furthermore the films showed low resistivity at the lowest band gap. The best electrical performances were observed at Zn doping of 20 at.% which also correspond to the highest (200) plane diffraction intensity recorded without other secondary orientations. Therefore this amount of Zn doping has been selected for the conductivity improvement.

2. Conductivity improvements at fixed Zn doping

In the following section the amount of doping has been fixed at 20 at.% Zn. The films have been deposited on Si (100) oriented substrates for XRD and quartz for AC Hall and UV-vis analysis, and the deposition temperature T_D does not exceed 400 °C.

2.1. Achievement of lowest resistivity

Three temperatures, 200, 300 and 400 °C, with P_D varying between 5-100 mTorr have been used during the deposition of the 20 at.% Zn-doped SnO_2 films. The XRD data in Figure 5.9 shows XRD data obtained for the films.

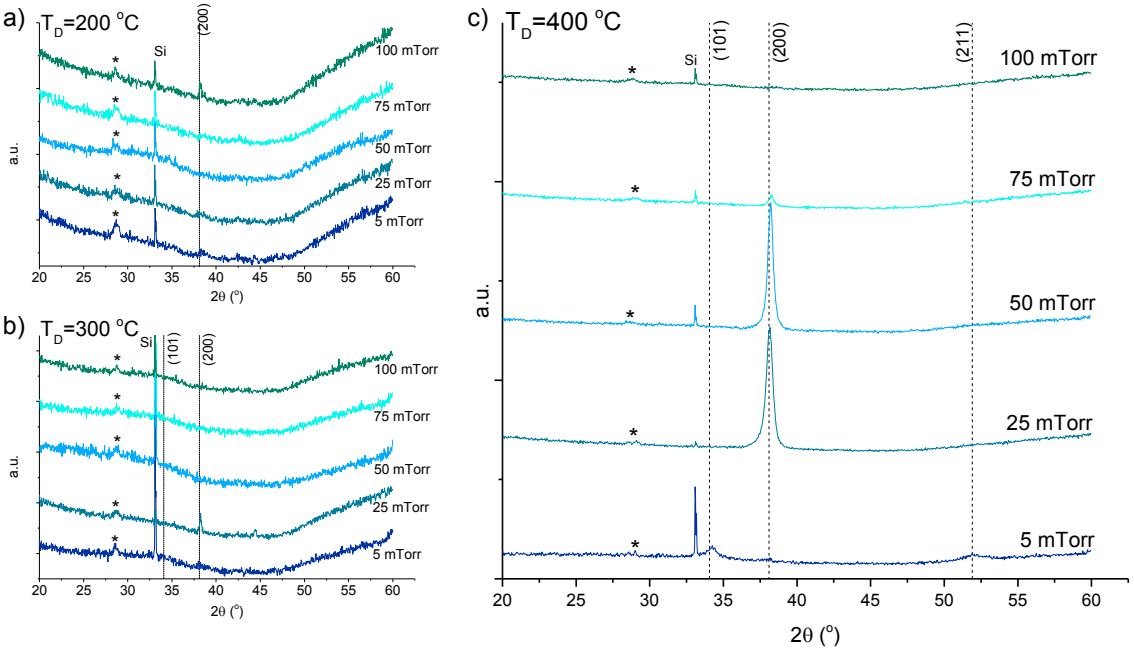

Figure 5. 9: XRD data of the 20 at.% ZTO deposited films on Si under pressure between 5-100 mTorr and at a) 200 °C, b) 300 °C, and c) 400 °C. The Si substrate peaks are identified in addition to a small peaks attributed to a minor SnO phase (*).

While the films deposited at 200 and 300 °C are mostly amorphous, crystallisation is apparent at 400 °C with strongly (200) oriented films at P_D of 50 mTorr. This observation confirms that the introduction of Zn in SnO_2 induces a thermal stabilisation of the films as the crystallisation of undoped SnO_2 is generally observed around 200-300 °C depending on the P_D applied. (Figure 5.6.a) As T_D decreases the minor SnO phases is more present in the XRD data which could be attributed to the lower temperature and oxygen environment required to the formation of the SnO phase.[26–28] At 400 °C the films show a change in orientation from weak (101) diffraction peak observed at 5 mTorr to a strong (200) intensity at 25 mTorr. This change is a consequence of the (101) surface being more stable in very low oxygen environment stated in section 5.1.1. The decrease of crystallinity as P_D increases is attributed to the decrease of energy in the plasma plume as more oxygen species are present to interact with the plume species.[29] This leads to a lower energy to allow the crystallisation of the films at this temperature.

The electric performances of the deposited films measured by Hall are shown in Figure 5.10. The Hall resistivity measured cover a wide range with values from 7.8 $x10^2$ to as low as 2.9 $x10^{-3}$ Ω.cm. As T_D is increased, the resistivity stabilises between 10^{-2}-10^{-3} Ω.cm with variations of only a factor 10 at 400 °C despite the variation in P_D. This can be explained by evaluating the evolution of the carrier concentration with changes in T_D. As the temperature increases the carrier concentration increases owning to the increased energy brought to the system enabling the formation of more donor defects. The deposition parameters required to give enough energy for the creation of these defects are generally a compromise between the deposition temperature and the oxygen pressure directly influencing the plume energy. As it can be observed, the highest carrier concentration achieved at 200 and 300 °C corresponds to a P_D of 25 mTorr. Above this pressure the plume does not give the system enough energy while below it (at 5 mTorr) the growth conditions start to favour the formation of SnO[26,27], *i.e.* the drop in carrier concentration observed. This phenomenon is more detailed in section 5.2.2. The values of the thickness, sheet resistance, resistivity, carrier concentration and mobility of the 20 at.% ZTO films are reported in table 5.1. At 400 °C while the carrier concentration does not show consequent variation with the change in P_D, the mobility increases between 5 and 25 mTorr from 2.2 to 23.3 $cm^2/(V.s)$ respectively. The bad crystallinity of the films at 5 mTorr with low diffraction intensity of the (101) and (211) orientations is believed to be the reason behind the difference in mobility.

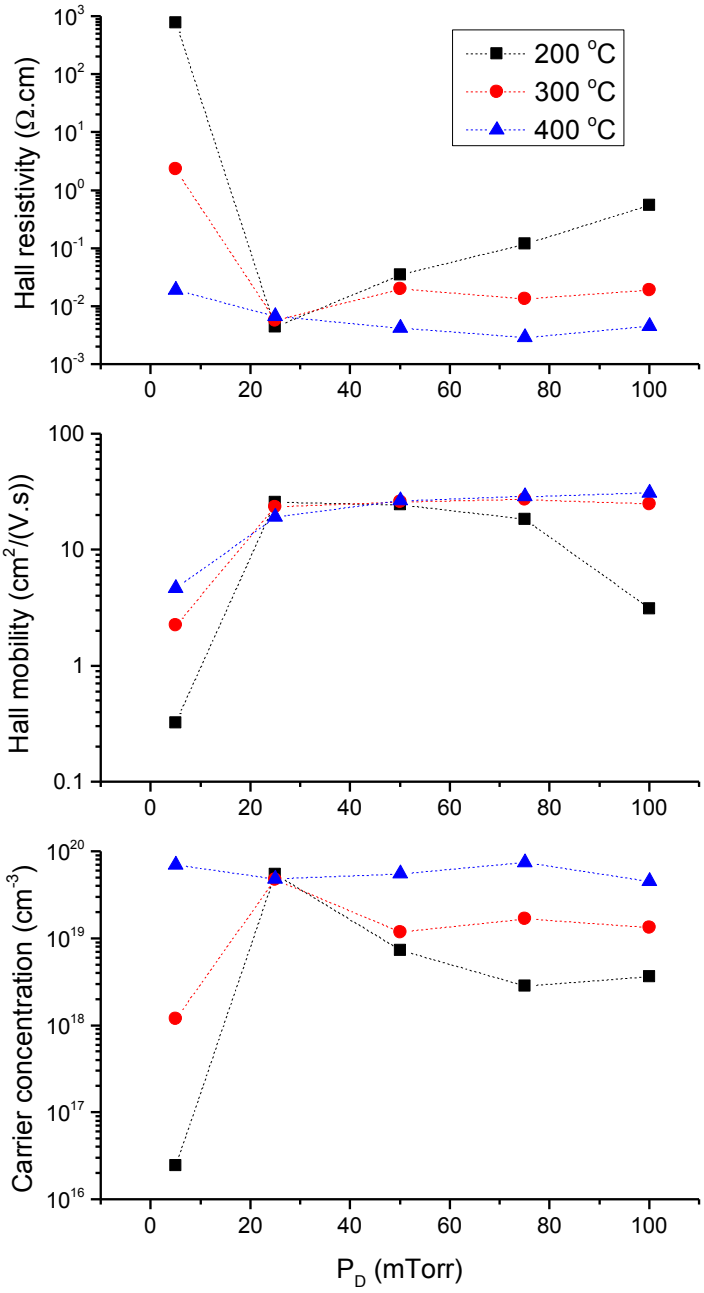

Figure 5. 10: Hall data of 20 at.% ZTO films deposited under different conditions under P_D between 5-100 mTorr and at T_D between 200-400 °C showing the evolution of the Hall resistivity, Hall mobility and carrier concentration.

The lowest resistivity achieved is 2.9 x10^{-3} Ω.cm at 400 °C and 75 mTorr, and 4.5 x10^{-3} Ω.cm at 200 °C and 25 mTorr. Even though these resistivities are still higher than the lowest achieved through F or Sb doping (2-3 x10^{-4} Ω.cm)[30–32], they are close to the values generally reached through Sb doping. Reports of ATO films deposited by PLD generally mention resistivity about 1-3 x10^{-3} Ω.cm[33,34] which is also the case for other deposition technique such as magnetron sputtering[35], CVD[36] and spray pyrolysis[37,38]. Some F-doped SnO_2 studies also report resistivity in this range[37,39,40]

but overall SnO_2 doping with F induces lower resistivities. The main limitation in these doping is the mobility. The mobility obtained with ATO films is generally about 10 $cm^2/(V.s)$[34,35,41] while FTO films exhibit mobilities of 20 $cm^2/(V.s)$ or higher.[42,43] The main difference between Sb/F doping and the Zn doping presented in this study is that Sb or F directly influences the amount of charge carriers by creating an extra electron to the system when substituting on Sn or O site respectively. Zn incorporation on Sn site is likely to lead to the formation of more oxygen vacancy, however these defects are not necessarily charged and consequently the charge carrier concentration barely increases.[9] The mobility of the ZTO films deposited do not reach the improved mobility of CVD deposited FTO films (77.5 $cm^2/(V.s)$)[43] however it is above the value generally reported in the literature of 10-20 $cm^2/(V.s)$ for Sb and F doped SnO_2 films. Furthermore the addition of Zn in SnO_2 does not induce a decay of the mobility, but instead an improvement from 10 to 30 $cm^2/(V.s)$ (section 5.1.2) is observed while the introduction of Sb as a dopant can cause a decrease of the mobility.[41,44]

Table 5. 1: Details of 20 at.% ZTO function of T_D and P_D showing the films thickness, sheet resistance, Hall resistivity, carrier concentration and Hall mobility.

T_D	**P_D**	**Thickness**	**Sheet resistance**	**Hall resistivity**	**Carrier concentration**	**Hall mobility**
°C	mTorr	nm	Ω/square	Ω.cm	cm^{-3}	$cm^2/(V.s)$
200	5	245	$3.2x10^7$	$7.8\ x10^2$	$2.5\ x10^{16}$	0.3
	25	227	$2.0x10^2$	$4.5\ x10^{-3}$	$5.5\ x10^{19}$	25.6
	50	220	$1.6\ x10^3$	$3.5\ x10^{-2}$	$7.3\ x10^{18}$	24.6
	75	243	$4.9\ x10^3$	$1.2\ x10^{-1}$	$2.9\ x10^{18}$	18.4
	100	240	$2.3\ x10^4$	$5.5\ x10^{-1}$	$3.7\ x10^{18}$	3.1
300	5	249	$9.4\ x10^4$	2.3	$1.2\ x10^{18}$	2.2
	25	233	$2.4\ x10^2$	$5.6\ x10^{-3}$	$4.7\ x10^{19}$	23.3
	50	228	$8.9\ x10^2$	$2.0\ x10^{-2}$	$1.2\ x10^{19}$	26.1
	75	244	$5.6\ x10^2$	$1.4\ x10^{-2}$	$1.7\ x10^{19}$	27.4
	100	247	$7.7\ x10^2$	$1.9\ x10^{-2}$	$1.3\ x10^{19}$	24.8
400	5	251	$7.7\ x10^2$	$1.9\ x10^{-2}$	$7.0\ x10^{19}$	4.6
	25	235	$2.9\ x10^2$	$6.7\ x10^{-3}$	$4.8\ x10^{19}$	19.3
	50	222	$1.9\ x10^2$	$4.3\ x10^{-3}$	$5.6\ x10^{19}$	26.5
	75	246	$1.2\ x10^2$	$2.9\ x10^{-3}$	$7.4\ x10^{19}$	29.0
	100	245	$1.8\ x10^2$	$4.5\ x10^{-3}$	$4.5\ x10^{19}$	30.8

Despite the changes in resistivity as the P_D increases, the mobility shows remarkable stability. Between 25 and 75 mTorr the mobility lies between 20 and 30 $cm^2/(V.s)$ even though the carrier concentration drops in some cases. This is thought to be due to the films becoming more amorphous. In TCOs with a conduction band minimum mostly localised on metal s state (such as SnO_2 and ZnO) the disorder in the film have a very low

impact on the electrical properties. Since s orbitals are spherical the angular disorder has no effect, and the large metal ion radius imply that the metal-metal atom distance stays relatively constant.[23] Therefore the effects of disorder on s-shape conduction band are very small and the transport properties are not altered.[45] This leads to the potential use of amorphous ZTO films with the highest mobility of 30.8 $cm^2/(V.s)$ at 400 °C and 100 mTorr. The effect of the amorphous state of the films on the band gap can be observed in Figure 5.11.

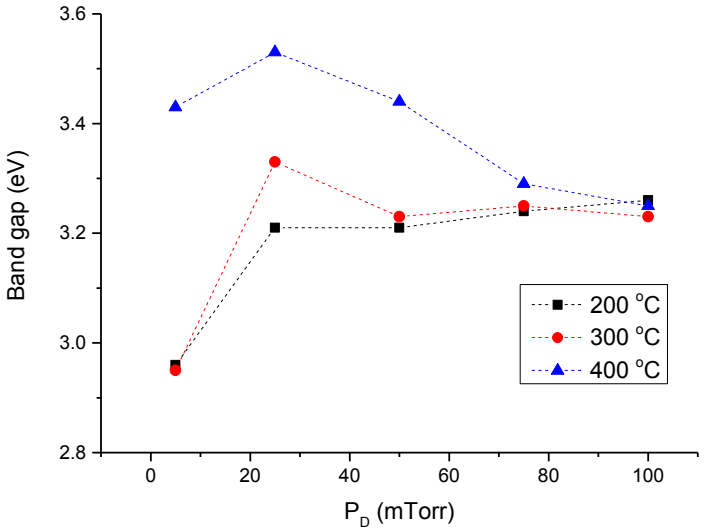

Figure 5. 11: Band gap of the 20 at.% ZTO films deposited at T_D between 200-400 °C and P_D between 5-100 mTorr.

The crystalline 20 at.% ZTO films deposited at 400 °C between 5-50 mTorr display optical band gaps about 3.4-3.5 eV which is about 0.2 eV lower than with undoped SnO_2. A second plateau is observed at 3.2 eV which corresponds to the films in an amorphous state owning to band tail states (most likely about the valence band). Finally a third set of band gaps can be notice slightly below 3 eV for the films deposited at 200 and 300 °C, and under 5 mTorr. This large difference is thought to be due to the presence of Sn^{2+} states in the films (also responsible for the decrease in mobility and carrier concentration) which is interpreted in the next part.

2.2. Amorphous ZTO films

In order to observe the limitations of the electronic properties in amorphous Zn-doped SnO_2 films, 20 at.% ZTO films were deposited at temperatures below 200 °C. T_D was varied between 50 and 150 °C with P_D between 5 and 50 mTorr. One of the main reasons behind this study was to maintain the low resistivity of the films while decreasing the deposition temperature used. The AC Hall resistivity, AC Hall mobility and carrier concentrations of the deposited films are shown in Figure 5.12.

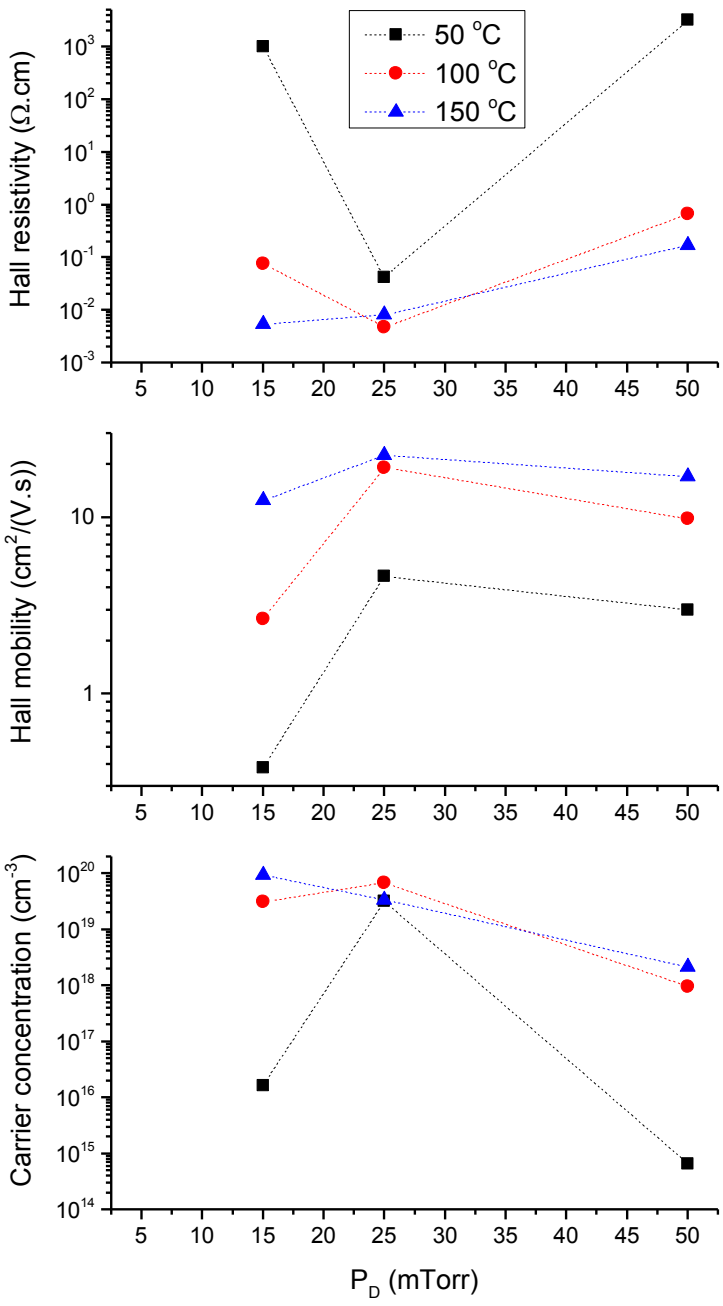

Figure 5. 12: Hall data of 20 at.% ZTO films deposited under different conditions under P_D between 5-50 mTorr and at T_D between 50-150 °C showing the evolution of the Hall resistivity, Hall mobility and carrier concentration.

It can be observed that as the temperature is increased, the resistivity is less influenced by the changes in P_D. The lowest resistivity achieved was at 100 °C and 25 mTorr with 4.74 x10^{-3} Ω.cm. This value is only slightly higher than the lowest obtained for the 20 at.% Zn doping but has been achieved by using a deposition temperature 300 °C lower thus allowing possible deposition on flexible substrates. Even though the mobility decreased down to 19.2 cm²/(V.s) the loss was compensated by the amount of charge carrier created by the oxygen poor environment (25 mTorr). The highest mobility obtained was at 150 °C and 25 mTorr where it reached 22.5 cm²/(V.s). While decreasing the deposition

temperature below 200 °C despite the increase in resistivity the mobility could be maintained about 20 $cm^2/(V.s)$ in some cases. At 150 °C and 15 mTorr the film display a lower resistivity despite the decrease of mobility (12.5 $cm^2/(V.s)$. This is due to the increase in charge carrier since less oxygen is used during the deposition, increasing the plume energy and favouring the formation of donor type defects. 100 °C seems to be the limit to produce 20 at.% films with resistivity below 10^{-2} Ω.cm, below this deposition temperature, *i.e.* at 50 °C, the mobility of the films decreases consequently followed by the carrier concentration. The only deposition pressure at which the film deposited at 50 °C shows a resistivity below 10^{-1} Ω.cm is 25 mTorr which also represents the P_D corresponding to the lowest resistivity achieved at 100 °C. It is believed that this point of pressure for $T_D \leq 100$ °C represents a compromise between the environment having too much oxygen for the formation of donor defects (lower energy of the plume) and the growth conditions being too oxygen-poor favouring the formation of the SnO phase. Figure 5.12 does not show the data for the films deposited at 5 mTorr and the reason behind this lies on the impossibility to perform Hall measurement on the samples. The resistivity of the deposited films was too high and the measurements not stable enough to extract information about the electrical properties. The band gap of the 20 at.% ZTO films deposited between 50 and 150 °C, and a picture of the samples are shown in Figure 5.13.

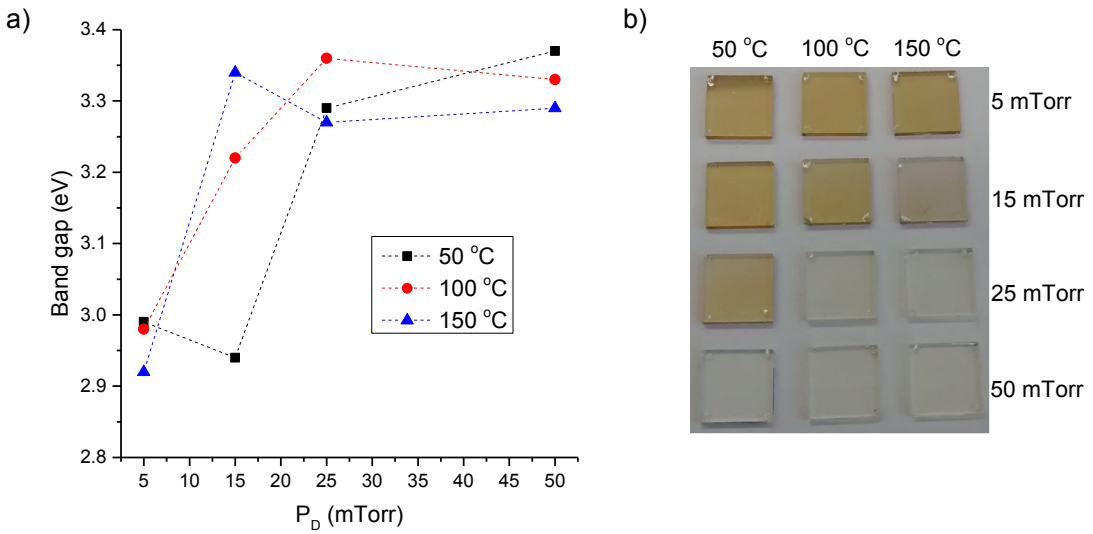

Figure 5. 13: a) Band gap of the 20 at.% ZTO films deposited at T_D between 200-400 °C and P_D between 5-100 mTorr. b) Picture of the samples deposited on quartz showing the "brownish" tint as P_D and T_D decreases.

The XRD data is not displayed here but all the films were found to be amorphous (presumably SnO_2 phase) with minor SnO phase. Therefore the values of the band gap around 3.2-3.4 eV were to be expected due to the presence of disorder in the films causing band tailing effect. However for all the films deposited at 5 mTorr and the film deposited

at 50 °C and 15 mTorr, the band gaps fall below 3 eV. In the previous sections such a low value was attributed to the presence of Sn^{2+} in the film. By observing Figure 5.13.b it can be noticed that the concerned films show a "brownish" tint which fades as P_D increases to lead to the anticipated appearance of the film, *i.e.* no colour change, at 50 mTorr. The apparition of a "brownish" tint on Zn-doped films has been previously reported in the literature by Ko *et al.*[25] and Zhu *et al.*[9]. The sample coloration was observed at very low oxygen pressure and low deposition pressure similarly to this case. While Ko *et al.* suggested it to be from mixed phases of SnO and Sn_3O_4, Zhu *et al.* confirmed the presence of tin in oxidation state +2 instead of the +4 originally found in SnO_2. In both cases the presence of some 4-fold coordinated Sn^{2+} ions in the films led to a degradation of the electrical properties. Large presence of Sn^{2+} would indicate that the structure differs from the SnO_2 structure and thus decrease greatly the mobility. Similar behaviour was observed in the deposited films, which as P_D decreases when $T_D \leq 100$ °C showed both a decrease in mobility and carrier concentration (probably due to the compensation of the charge carriers by the SnO phase). A way to distinguish Sn^{2+} from Sn^{4+} is to analyse the valence band of the materials. Figure 5.14 shows the valence band onsets analysed by XPS for two 20 at.% ZTO films, one presenting the brownish tint (50 °C and 5 mTorr) and one without (600 °C and 100 mTorr).

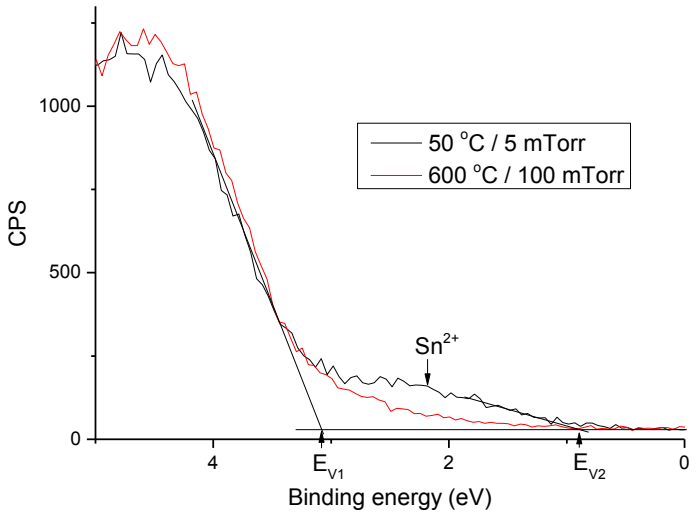

Figure 5. 14: Valence band onset measured by XPS of the 20 at.% ZTO films deposited at 50 °C and 5 mTorr, and 600 °C and 100 mTorr. The film deposited at 50 °C and 5 mTorr shows a shoulder characteristic of SnO phase. The intensity of the signal is measured in counts per second (CPS).

While SnO_2 has a characteristic valence band onset about 4 eV, the onset of SnO is at a lower binding energy (about 2 eV) due to the Sn 5s states constituting the valence band.[17,46] The films deposited at 50 °C and 5 mTorr show two valence band offset (E_{V1}

and E_{V2}), however the film deposited at 600 °C and 100 mT without brownish tint shows only one (about the same level as E_{V1}). The presence of the second onset E_{V2} in the film with the brownish tint is attributed to the presence of SnO or SnO_x phase as the peak match the characteristic VB onset of SnO. A study reporting the presence of SnO phase after the sputtering of a SnO_2 surface showed similar changes in the VB onset.[47] The presence of the second onset at lower binding energy confirm the presence of Sn^{2+} ions in the films deposited at 5 mTorr and explain the increase in resistivity. The second onset also shows that additional states have been formed above the VBM with the apparition of Sn^{2+} leading to the decrease observed in the band gap. Similar observations were reported by Körber *et al.*[48] with undoped and Sb-doped SnO_2 deposited under reducing conditions. Along with the coloration of the samples the transparency of the films in the visible range decreases from about 80 % and higher to less than 70 % as shown in Figure 5.15.

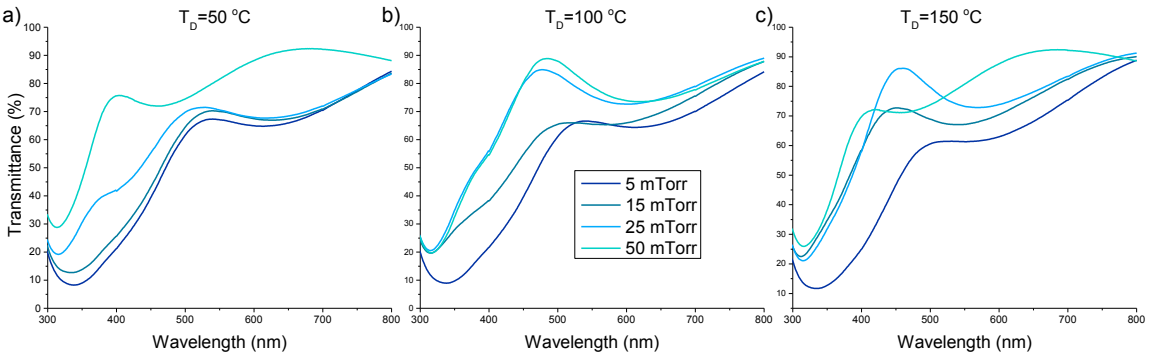

Figure 5. 15: UV-Vis transmission data measured between 300 and 800 nm wavelengths of the 20 at.% ZTO films deposited at a) 50 °C, b) 100 °C, and c) 150 °C.

The amorphous state of the films does not have a great impact on the transmission in the visible range which globally stays above 80 %. Similarly a low resistivity was maintained as the deposition temperature was decreased down to 100 °C by adjusting the oxygen pressure. However the formation of Sn^{2+} states at very low P_D constitutes a limitation to the electrical and optical performances of the films.

Low resistivity 20 at.% ZTO films were successfully deposited at T_D below 200 °C. Resistivity of 4.74 x10^{-3} Ω.cm and mobility of 19.2 $cm^2/(V.s)$ were achieved using only 100 °C as T_D by adjusting P_D. At low resistivity the optical transparency in the visible range was maintained (around 80 %) however under very low P_D (function of T_D) the transparency falls to 60-70 % and the resistivity dramatically increases. This has been attributed to the formation of Sn^{2+} states in the films compensating the charge carriers and decreasing the E_g down to 3 eV. For the other films the E_g was maintained between 3.2-3.4 eV.

2.3. Impact of thickness in SnO_2/ZTO

Undoped SnO_2 and 20 at.% Zn-doped SnO_2 films have been deposited on quartz at 400 °C and 50 mTorr. The thickness was controlled through the amount of laser pulses delivered and varied between 5 and 200 nm. Figure 5.16.a and b show the XRD data of the undoped and Zn-doped films respectively. The diffraction peaks only appeared for thicknesses above 50 nm. Below 50 nm the films were too thin to give a diffraction signal intense enough to be detected, except for the undoped films where a weak signal could be measured on films down to 20 nm thick. Even though the crystallisation at low thicknesses could not be confirmed, the comparison between undoped and Zn-doped at 200 nm emphasizes the preferred (200) orientation with the introduction of Zn (section 5.1.1). The homogenous coating of the film on the substrates was confirmed by SEM.

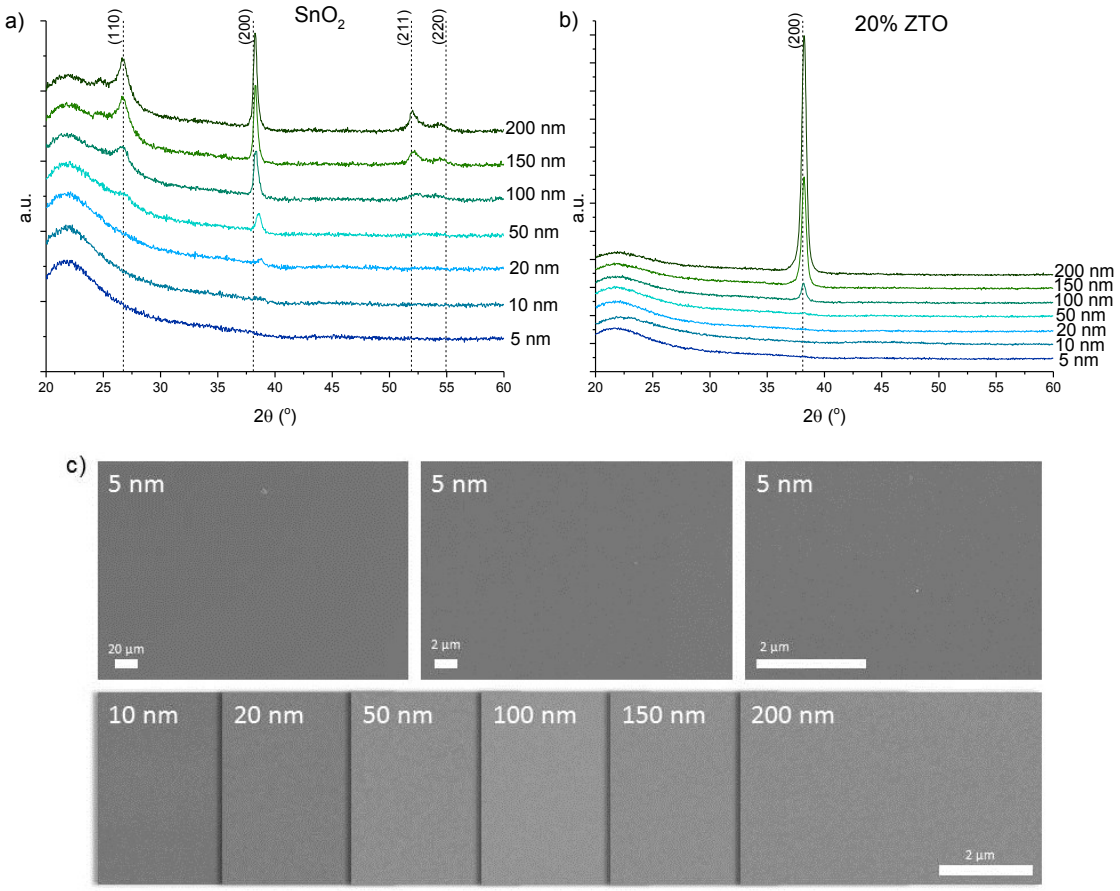

Figure 5. 16: XRD data of a) SnO_2 and b) 20 at.% ZTO thin films deposited at 400 °C and 50 mTorr with different thicknesses from 5-200 nm. c) SEM micrograph of the SnO_2 deposited films displaying the homogenous covering of the films on the substrate.

Figure 5.16.c shows the continuity of the deposited SnO_2 films even with a thickness as low as 5 nm. No pinholes or islands were observed regarding of the thickness deposited which

account for the uniformity of the films. The electrical properties of the films have been measured by Hall and displayed in Figure 5.17.

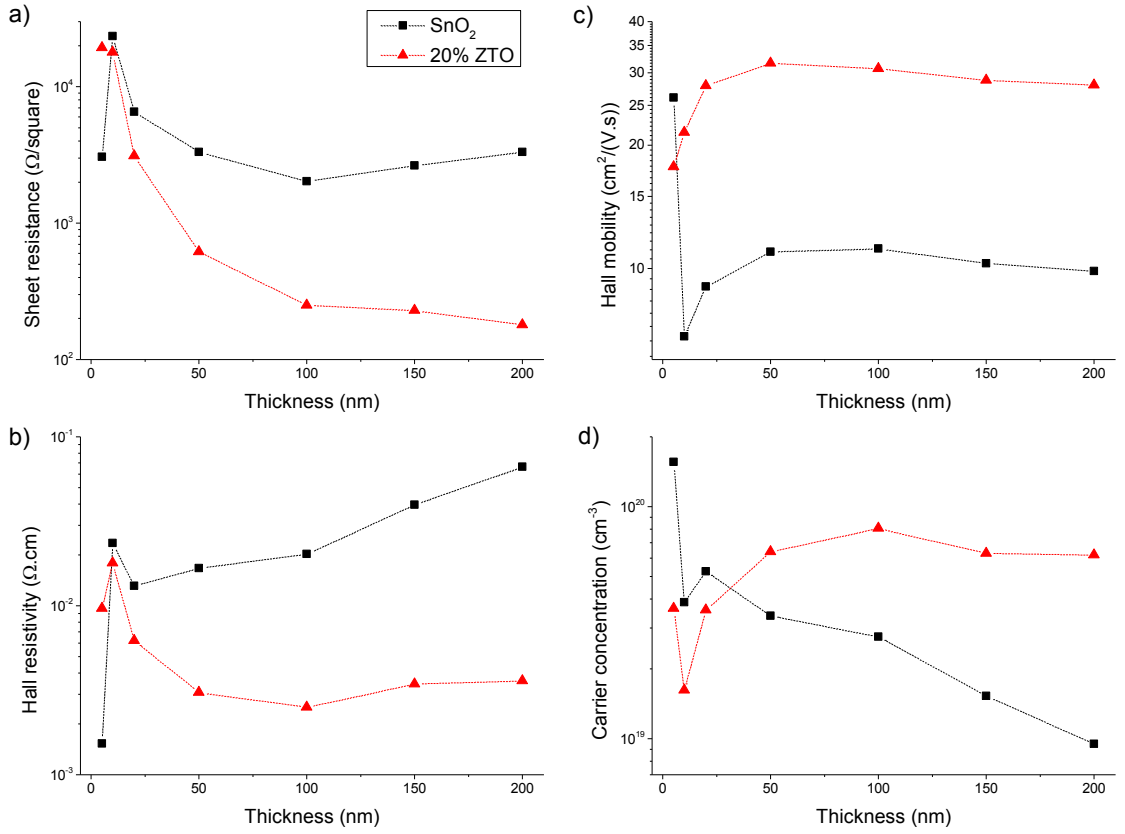

Figure 5. 17: Hall measurements performed on SnO_2 and 20 at.% ZTO films deposited at 400 °C and 50 mTorr, with thicknesses ranging from 5-200 nm showing the evolution of a) the sheet resistance, b) the Hall resistivity, c) the Hall mobility, and d) the carrier concentration.

As shown on Figure 5.17.a, the sheet resistance remains relatively stable, at around 2000 Ω/sq for the undoped films. The same phenomenon has been observed by Casey and Stephenson[49] where they suggested the presence of a highly conductive surface layer in SnO_2. This results in an increase of the resistivity ρ when the thickness t increases since ρ = R_{sq}/t with R_{sq} the sheet resistance. The slight decrease observed in the sheet resistance is associated to the evolution of the mobility which, unlike what Casey and Stephenson reported, shows a clear increase with increasing thickness up to 50 nm (excluding the film of 5 nm thickness). Takwale and Bhide[50] associated this increase in mobility to a reduction of surface scattering. The existence of a surface conductive layer is confirmed by the nearly monotonous decrease in carrier concentration with increasing thicknesses. The conductivity would therefore be dominated by a surface channel of constant thickness while the bulk brings a significantly lower contribution to the conductivity hence the rather constant sheet resistance.[49,51] Since the main increase of resistivity with the

increased thickness is due to the decrease of carrier concentration, it can be expected that the surface conductive channel is due to a donor defect accumulation on the surface of the sample (such as V_O and Sn_i). The SnO_2 films deposited with a 5nm thickness shows remarkably better mobility and carrier concentration. This leads to the lowest resistivity achieved in this study (1.53 $x10^{-3}$ Ω.cm) considering the very low thickness of the films. With the 5 nm SnO_2 films exhibiting such different electrical behaviour than the 10 nm films, it is believed that the thickness of the surface channel would be between around 5 nm.

The addition of Zn seems to change the overall conductivity behaviour in SnO_2. The sheet resistance decreases as the thickness increases. The resulting resistivity shows a gradual decrease up to 50 nm thicknesses where it stabilises around 3 $x10^{-3}$ Ω.cm. Jiang *et al.*[16] associated the improvement of the electrical properties of Zn-doped SnO_2 compared to undoped samples with the presence of the surface interstitial cations hence increasing the conductivity in the surface conductive channel. However this interpretation might be wrong since the carrier concentration of the 20 at.% ZTO films increases with increasing thickness and stabilises at thicknesses of 50-100 nm. The increase/stabilisation observed is a sign that the amount of charge carriers (not the concentration) is continuously improved as the thickness increases. Therefore the Zn-doping acts in the bulk of the film by creating more charge carriers and balances the highly conductive surface layer towards a more homogenous repartition of the conductivity in the material (surface and bulk). The same effect has been observed by Casey and Stephenson[49] while doping SnO_2 with Mo.

2.4. Summary

Over the course of this work the deposition of 20 at.% ZTO films have been covered over a wide range of conditions with T_D extending from 50-600 °C and P_D from 5-300 mTorr. The conductivity of the films varied between 2.9 $x10^{-3}$ to over 10^3 Ω.cm showing a 6-order of magnitude change within a single material. Along with the range of deposition conditions covered the work function (WF) also showed important changes as displayed in Figure 5.18.

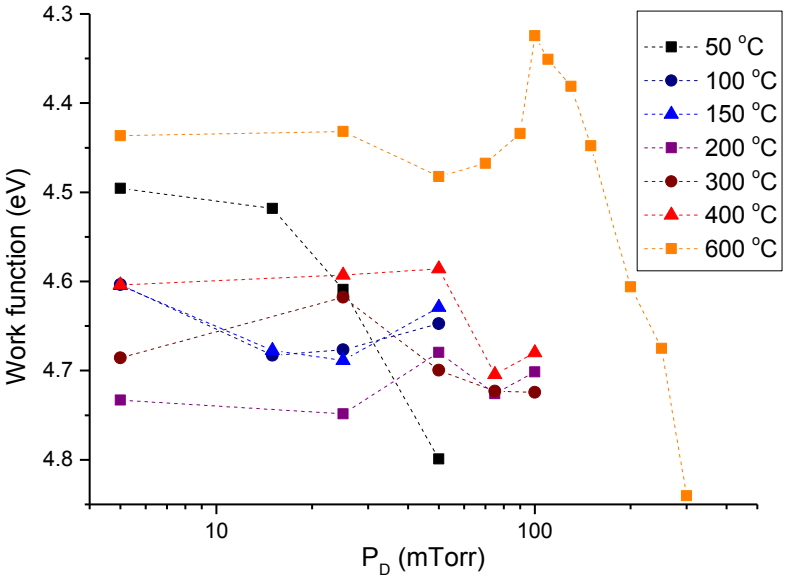

Figure 5. 18: WF of 20 at.% ZTO films deposited over 50-600 °C and 5-300 mTorr.

The values of WF extend between 4.3 - 4.8 eV by controlling the T_D and P_D. A part of these variations is thought to be due to an effect of band bending happening at the surface of the films and thus decreasing the work function. Such variation could be explored as electron transporting layer in OPV device.

3. Test in solar cells as electron transporting layer (ETL)

In order to improve the power conversion efficiency of OPVs, charge extracting interlayers are generally used between the bulk heterojunction layer and the electrodes. In the case of the electron collecting electrode (the cathode) the materials generally used possess a work function much deeper than the LUMO of the organic's acceptor leading to a loss in energy (Δ_{LUMO}) during the charge transfer as shown in Figure 5.19. The introduction of an electron transporting layer (ETL) with a WF closer to the LUMO of the acceptor can reduce the amount of carrier recombination and current loss, but also improves the open-circuit voltage (V_{OC}).[52]

SnO_2 as a buffer layer is mostly used in CdTe/CdS solar cells.[53,54] However since the expertise in the research group was focused on OPVs and especially the P3HT/ICBA BHJ, and considering the toxicity of Cd the study was performed using P3HT as a donor and ICBA as an acceptor. The energy levels of the HOMO and LUMO of P3HT, ICBA and PCBM extracted from ref [55] are shown in Figure 5.20 along with their HOMO levels measured by photoelectron spectroscopy and the chemical formula.

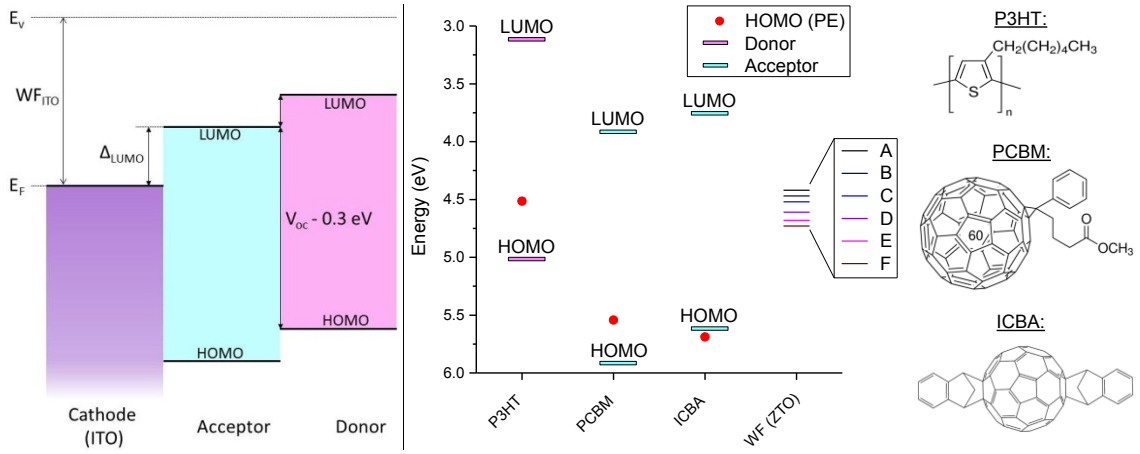

Figure 5. 19: (left) Band diagram showing the energy offset (Δ_{LUMO}) between the cathode (ITO) and the acceptor in a photovoltaic device. (middle) HOMO and LUMO energy levels of P3HT, PCBM and ICBA extracted from [55]. The HOMO levels represented by the red dots have been measured by Photoemission spectroscopy in air. The work functions (WF) of the 20 at.% ZTO films used as ETL are represented by bars of different colours labelled A, B, C, D, E and F corresponding respectively to the T_D/P_D: 600 °C/25 mTorr, 600 °C/75 mTorr, 600 °C/50 mTorr, 50 °C/25 mTorr, 100 °C/15 mTorr and 200 °C/75 mTorr.

The most commonly used cathode, ITO, generally possesses a work function about 4.7-4.8 eV. Considering the HOMO level of the P3HT (5 eV) and the LUMO level of the ICBA (3.7 eV), the energy offset at the cathode for the electron transfer is considerably large and the HOMO of the P3HT might pin to the ITO Fermi level. ZnO is a common material used as ETL with devices adopting the structure ITO/ETL/ICBA (or PCBM)/P3HT/HTL/Metal. Due to its low WF about 3.7-4 eV, ZnO allows good improvements of the efficiency of the devices along with V_{OC} between 0.7-0.8 V.[56,57] Even though the 20 at.% ZTO films could not achieve such values, WF between 4.4 and 4.7 eV can still be controlled as to observe the effect on the efficiency of the charge transfer.

The solar cells were fabricated using inverted device structure (cathode on bottom, anode on top) with the layers: ITO/20 at.% ZTO/ICBA/P3HT/MoO3/Ag. The interest was brought upon the variations of the work function, therefore deposition conditions have been chosen such that the WF changes but the resistivity remains of the same order of magnitude (about 0.1 Ω.cm). Five conditions of T_D/P_D have been selected: 600 °C/25 mTorr (WF = 4.43 eV), 600 °C/50 mTorr (WF = 4.48 eV), 50 °C/25 mTorr (WF = 4.61 eV), 100 °C/15 mTorr (WF = 4.68 eV) and 200 °C/75 mTorr (WF = 4.73 eV). Finally a last condition was picked with a low WF but a higher resistivity: 600 °C/75 mTorr (WF = 4.44 eV). The ZTO films thickness was fixed to 100 nm as it can be observed in Figure 5.20 showing a cross-section SEM micrograph of two devices with different ETLs. To simplify the notations, the 20 at.% ZTO films used as ETL are represented labelled A, B, C, D, E and F corresponding respectively to the T_D/P_D: 600 °C/25 mTorr, 600 °C/75 mTorr, 600 °C/50

mTorr, 50 °C/25 mTorr, 100 °C/15 mTorr and 200 °C/75 mTorr. Their WF is displayed in Figure 5.19 with respect to the ICBA energy levels.

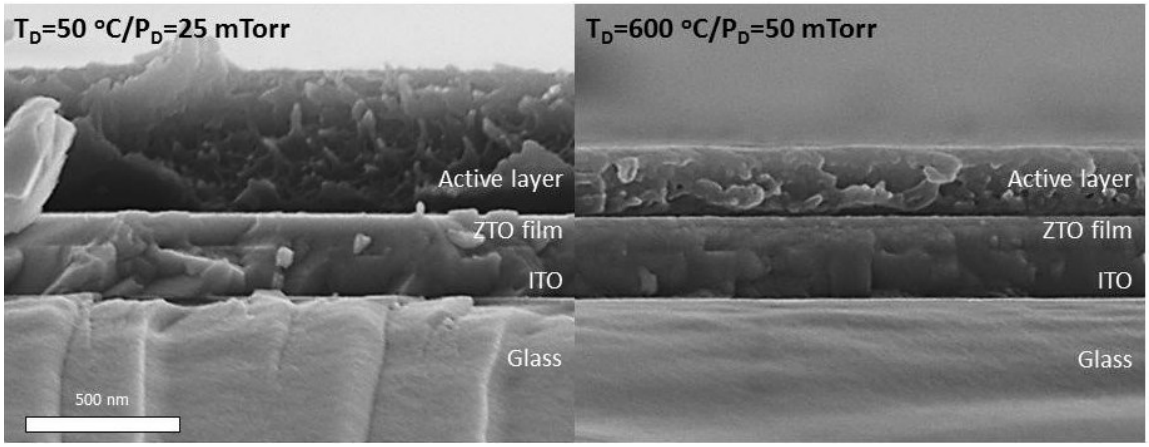

Figure 5. 20: Cross-section SEM images of the photovoltaic devices containing (ITO/ZTO/ICBA/P3HT/MoO_3/Ag) with different 20 at.% ZTO layer used. ZTO layers deposited at a) 50 °C and 25 mTorr, and b) 600 °C and 50 mTorr.

The cleavage of the samples was performed by dipping the device in liquid nitrogen before cutting to avoid delamination of the active layer. The two different ZTO layers picked for the cross-section imaging are in different states, the films deposited at 50 °C are amorphous while the films deposited at 600 °C are crystalline. No particular differences were noticed on the layer superposition. In both cases the ZTO layer covers uniformly the ITO layer. The delamination observed at 50 °C of the polymer is due to the splitting of the device.

The current-voltage characteristics of the fabricated devices are shown in Figure 5.21.a. Devices without ETL (only ITO) were also deposited however none of the cells showed a measureable photovoltaic effect and no efficiency could be recorded. The V_{OC} recorded for devices are plotted alongside the WF of the 20 at.% ZTO ETL in Figure 5.21.b. While the device with low WF ETL were easily measurable, the devices with larger WF ETL (T_D from 50 to 200 °C) showed very low efficiency with a large part of them being non-measurable. Despite two points differing (A and D), the trend followed by the WF of the ETL is found in the V_{OC} which increases with lower WF. Even though the devices with the ETL A (600 °C/25 mTorr) showed a slight difference in V_{OC} the value is still in the range expected. A decrease of the WF of the ETL therefore leads to lower energy lost during the charge transfer to the electrode. As the WF becomes deeper the V_{OC} but also the overall performances of the device decrease dramatically. This effect has been highlighted by Greiner *et al.*[58] who investigated the impact of the work function of ETL/HTL in OPV.

They suggested that if the WF of the electrode in contact with the organics (ETL) exceeds a certain threshold, the HOMO level becomes pinned to the Fermi level of the electrode inducing a reduced V_{OC}. The HOMO energy level of the P3HT lies about 5 eV, relatively close to the range of WF covered by the ZTO films. A pinning of the HOMO of the P3HT as the WF increase above 4.6 eV is a possible explanation for the lowered V_{OC} measured. The performances of the devices are detailed in Table 5.2.

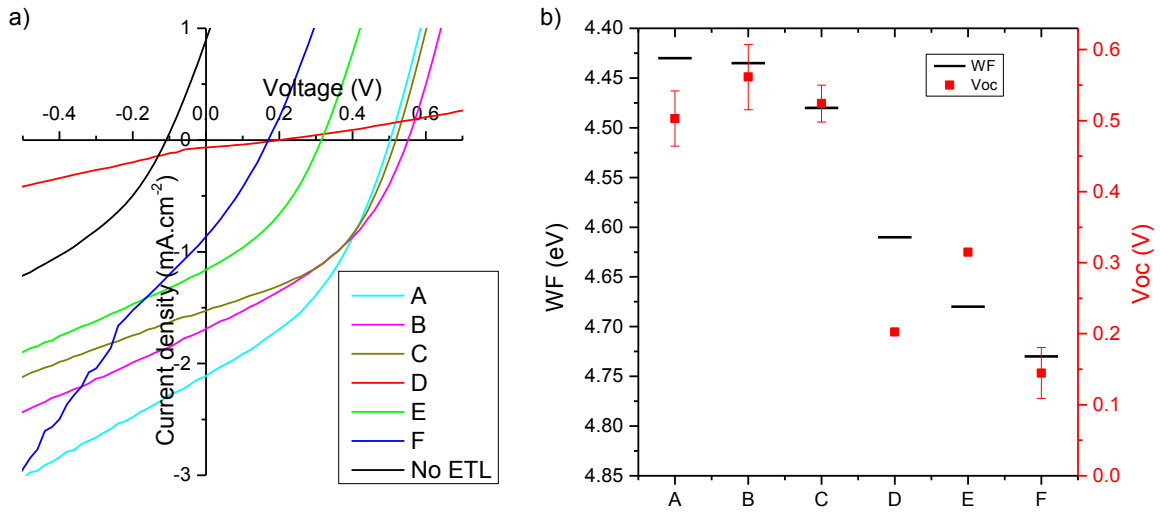

Figure 5. 21: a) Current – Voltage characteristics of the photovoltaic devices with different deposition temperature and pressure for the 20 at.% ZTO films, labelled from A to F, and one device without ETL layer. b) Comparison between the evolution of the work function (WF) of the 20 at.% ZTO films and the V_{oc} obtained in the devices.

The devices fabricated showed an overall lower efficiency than what can be achieved with an ICBA/P3HT BHJ.[59] The main problem seem to come from the short-circuit current (J_{SC}) and the fill factor (FF) which are too low, values around -9 mA.cm^{-2} and 50-60% respectively should be expected. A possible explanation is the presence of charge recombinations at the interface ETL/organic. Another explanation lies within the level of the WF. An important requirement for a good ETL is its low WF to match the LUMO of the organic and to stop the holes from being collected at the cathode. ITO is a material that can be used either as a cathode or as an anode depending on the device structure. This is due to its deep WF (4.8 eV). Therefore if the WF of the ETL is too deep, it cannot block the holes efficiently and recombinations with electrons occur at the cathode reducing the J_{SC} and the FF. The ETL with a higher WF show the highest J_{SC} and FF measured.

Table 5. 2: List of the characteristics of the measured devices for the different 20 at.% ZTO layer used (labelled T_D/P_D). Voc is the open circuit voltage, Jsc the short circuit current density, FF the fill factor, PCE the power conversion efficiency, Rs the series resistance and Rsh the shunt resistance.

ETL		Voc	Jsc	FF	PCE	R_s	R_{sh}
Label	T_D/P_D	(V)	$mA.cm^2$	%	%	Ω	Ω
A	600 °C/25 mTorr	0.50	-2.13	40	0.44	4.17	24.1
B	600 °C/75 mTorr	0.56	-1.32	43	0.29	4.75	28.5
C	600 °C/50 mTorr	0.52	-1.61	45	0.38	4.41	41.4
D	50 °C/25 mTorr	0.20	-0.07	30	0.004	101.1	189.1
E	100 °C/15 mTorr	0.31	-1.16	36	0.13	5.65	26.5
F	200 °C/75 mTorr	0.14	-0.84	28	0.03	6.31	12.7

Even though the PCE of the measured cells, about 0.4 %, is much lower than the 4 % generally achieved with other ETL[59], the V_{OC} clearly translates the impact of the WF of the ETL. As the WF gets closer to the LUMO of the acceptor, the energy loss decreases and the hole barrier is higher. However if the WF is too high, the HOMO of the donor becomes pinned to the Fermi level decreasing dramatically the V_{OC} and also the energy of the hole barrier.

4. Summary

In this section the properties of Zn-doped SnO_2 thin films deposited at relatively low temperatures were highlighted. Contrary to what has been studied in chapter 4, here the Zn doping is used to improve the electrical properties even though it was originally meant as an acceptor dopant. The incorporation of Zn did not only impact the conductivity of SnO_2 but also its structural and optical properties. The study in this chapter therefore led to some unique features of the ZTO material which are listed below.

- The introduction of Zn in SnO_2 induces a crystallisation along the (200) plane. Past a certain doping (function of deposition conditions) the films become singly (200) oriented with no other diffraction plane measured by XRD without using epitaxial growth. This selective growth was attributed to the Zn^{2+} ions which would favour the formation of oxygen deficient surfaces such as (200) which possess Sn^{2+} states.
- Zn unexpectedly increases the charge carrier concentration at low temperature most likely by forcing the formation of oxygen vacancies. The mobility of the films was also found to be stabilised with the incorporation of Zn. Resistivity as low as 2.9 $x10^{-3}$ Ω.cm could be achieved with mobility as high as 30 $cm^2/(V.s)$ (higher than undoped SnO_2). Amorphous films with conductivity of 4.74 $x10^{-3}$ Ω.cm and mobility of 22 $cm^2/(V.s)$ were deposited at temperature of 100 °C.

- Low temperature (below 200 °C) and highly oxygen deficient environment favours the formation of SnO phase with the introduction of Sn^{2+} states in the films. Their presence led to a dramatic decay of the electric properties along with a brown coloration of the samples and a decrease of the optical band gap.
- Undoped SnO_2 films possess a highly conductive surface channel, however the introduction of Zn induces the formation of donor defects in the bulk of the film and lead to a more homogenous repartition of the conductivity in the films.
- A range of 0.3 eV of WF could be covered with 20 at.% ZTO films of similar resistivity to investigate the impact as ETL in OPV device. The changes in WF are directly linked to the measured V_{OC}. WF too deep are likely to lead to a high amount of carrier recombination due to low energy of the hole blocking layer.

References

[1] H. Enoki, T. Nakayama, J. Echigoya, "The Electrical and Optical Properties of the ZnO-SnO2 Thin Films Prepared by RF Magnetron Sputtering", Phys. Stat. Sol. 129 (1992) 181.

[2] T. Minami, H. Sonohara, S. Takata, H. Sato, "Highly Transparent and Conductive Zinc Stannate Thin Films Prepared By Rf Magnetron Sputtering", Jpn. J. Appl. Phys. 33 (1994) L1693–L1696.

[3] T. Minami, "Transparent and conductive multicomponent oxide films prepared by magnetron sputtering", J. Vac. Sci. Technol. A Vacuum, Surfaces, Film. 17 (1999) 1765.

[4] T. Minami, S. Takata, H. Sato, H. Sonohara, "Properties of transparent zinc-stannate conducting films prepared by radio frequency magnetron sputtering", J. Vac. Sci. Technol. A. 13 (1995) 1095.

[5] Y. Hayashi, K. Kondo, K. Murai, T. Moriga, I. Nakabayashi, H. Fukumoto, et al., "ZnO-SnO2 transparent conductive films deposited by opposed target sputtering system of ZnO and SnO2 targets", Vacuum. 74 (2004) 607–611.

[6] V. Bilgin, S. Kose, F. Atay, I. Akyuz, "The effect of Zn concentration on some physical properties of tin oxide films obtained by ultrasonic spray pyrolysis", Mater. Lett. 58 (2004) 3686–3693.

[7] B. Falabretti, J. Robertson, "Electronic structures and doping of SnO2, CuAlO2, and CuInO2", J. Appl. Phys. 102 (2007) 123703.

[8] J. Robertson, S.J. Clark, "Limits to doping in oxides", Phys. Rev. B - Condens. Matter Mater. Phys. 83 (2011) 1–7.

[9] Q. Zhu, Q. Ma, D.B. Buchholz, R.P.H. Chang, M.J. Bedzyk, T.O. Mason, "Structural and physical properties of transparent conducting, amorphous Zn-doped SnO2 films", J. Appl. Phys. 115 (2014) 033512.

[10] S. Vijayalakshmi, S. Venkataraj, M. Subramanian, R. Jayavel, "Physical properties of zinc doped tin oxide films prepared by spray pyrolysis technique", J. Phys. D. Appl. Phys. 41 (2008) 035505.

[11] V. Bilgin, S. Kose, F. Atay, I. Akyuz, "The effect of Zn concentration on some physical properties of tin oxide films obtained by ultrasonic spray pyrolysis", Mater. Lett. 58 (2004) 3686–3693.

[12] A. Tripathi, R.K. Shukla, "Blue shift in optical band gap of sol–gel derived Sn1−xZnxO2 polycrystalline thin films", J. Mater. Sci. Mater. Electron. 24 (2013) 4014–4022.

[13] J. Zhao, J. Ni, X. Zhao, Y. Xiong, "Preparation and characterization of transparent conductive zinc doped tin oxide thin films prepared by radio-frequency magnetron sputtering", J. Wuhan Univ. Technol. Sci. Ed. 26 (2011) 388–392.

[14] S. Tian, Y. Gao, D. Zeng, C. Xie, "Effect of Zinc Doping on Microstructures and Gas-Sensing Properties of SnO2 Nanocrystals", J. Am. Ceram. Soc. 95 (2012) 436–442.

[15] S. Vijayalakshmi, S. Venkataraj, M. Subramanian, R. Jayavel, "Physical properties of zinc doped tin oxide films prepared by spray pyrolysis technique", J. Phys. D. Appl. Phys. 41 (2008) 035505.

[16] Y. Jiang, W. Sun, B. Xu, M. Yan, N. Bahlawane, "Unusual enhancement in electrical conductivity of tin oxide thin films with zinc doping.", Phys. Chem. Chem. Phys. 13 (2011) 5760–5763.

[17] M. Batzill, U. Diebold, "The surface and materials science of tin oxide", Prog. Surf. Sci. 79 (2005) 47–154.

[18] M. Batzill, K. Katsiev, J.M. Burst, U. Diebold, A.M. Chaka, B. Delley, "Gas-phase-dependent properties of SnO2 (110), (100), and (101) single-crystal surfaces: Structure, composition, and electronic properties", Phys. Rev. B. 72 (2005) 165414.

[19] J. Montero, C. Guillen, C.G. Granqvist, J. Herrero, G.A. Niklasson, "Preferential Orientation and Surface Oxidation Control in Reactively Sputter Deposited Nanocrystalline SnO2:Sb Films: Electrochemical and Optical Results", ECS J. Solid State Sci. Technol. 3 (2014) N151–N153.

[20] C. Körber, J. Suffner, A. Klein, "Surface energy controlled preferential orientation of thin films", J. Phys. D. Appl. Phys. 43 (2010) 055301.

[21] C.S. Barrett, T.B. Massalski, "Structure of metals: crystallographic methods, principles and data", 3rd rev. e, Oxford: Pergamon, n.d.

[22] J.H. Ko, I.H. Kim, D. Kim, K.S. Lee, T.S. Lee, J.H. Jeong, et al., "Effects of ZnO addition on electrical and structural properties of amorphous SnO2 thin films", Thin Solid Films. 494 (2006) 42–46.

[23] D.S. Ginley, H. Hosono, D.C. Paine, eds., "Handbook of Transparent Conductors", Springer, 2011.

[24] J. Lee, "Effects of oxygen concentration on the properties of sputtered SnO2:Sb films deposited at low temperature", Thin Solid Films. 516 (2008) 1386–1390.

[25] J.H. Ko, I.H. Kim, D. Kim, K.S. Lee, T.S. Lee, B. Cheong, et al., "Transparent and conducting Zn-Sn-O thin films prepared by combinatorial approach", Appl. Surf. Sci. 253 (2007) 7398–7403.

[26] J.A. Caraveo-Frescas, P.K. Nayak, H.A. Al-Jawhari, D.B. Granato, U. Schwingenschlogl, H.N. Alshareef, "Record mobility in transparent p-type tin monoxide films and devices by phase engineering", ACS Nano. 7 (2013) 5160–5167.

[27] S. Cahen, N. David, J.M. Fiorani, A. Maitre, M. Vilasi, "Thermodynamic modelling of the)-Sn system", Thermochim. Acta. 403 (2003) 275–285.

[28] H. Yabuta, N. Kaji, R. Hayashi, H. Kumomi, K. Nomura, T. Kamiya, et al., "Sputtering formation of p-type SnO thin-film transistors on glass toward oxide complimentary circuits", Appl. Phys. Lett. 97 (2010).

[29] R. Eason, "Pulsed Laser Deposition of Thin Films: Applications-Led Growth of Functional Materials", John Wiley & sons, 2006.

[30] E. Elangovan, K. Ramamurthi, "A study on low cost-high conducting fluorine and antimony-doped tin oxide thin films", Appl. Surf. Sci. 249 (2005) 183–196.

[31] H. Kim, R.C.Y. Auyeung, A. Piqué, "Transparent conducting F-doped SnO2 thin films grown by pulsed laser deposition", Thin Solid Films. 516 (2008) 5052–5056.

[32] A.V. Moholkar, S.M. Pawar, K.Y. Rajpure, C.H. Bhosale, J.H. Kim, "Effect of fluorine doping on highly transparent conductive spray deposited nanocrystalline tin oxide thin films", Appl. Surf. Sci. 255 (2009) 9358–9364.

[33] G.W. Kim, K.Y. Park, M.S. Anwar, Y.J. Seo, C.H. Sung, B.H. Koo, et al., "Preparation and properties of Sb2O3-doped SnO2 thin films deposited by using PLD", J. Korean Phys. Soc. 60 (2012) 1548–1551.

[34] I.A. Petukhov, L.S. Parshina, D.A. Zuev, A.A. Lotin, O.A. Novodvorsky, O.D. Khramova, et al., "Transport properties of thin SnO2⟨Sb⟩ films grown by pulsed laser deposition", Inorg. Mater. 49 (2013) 1123–1126.

[35] B. Bissig, T. Jäger, L. Ding, A.N. Tiwari, Y.E. Romanyuk, "Limits of carrier mobility in

Sb-doped SnO2 conducting films deposited by reactive sputtering", APL Mater. 3 (2015) 062802.

[36] J. Kane, H.P. Schweizer, W. Kern, "Chemical Vapor Deposition of Transparent, Electrically Conductive Tin Oxide Films Formed from Dibutyl Tin Diacetate", J. Electrochem. Soc. 122 (1975) 1144.

[37] H. Bisht, H.-T. Eun, a Mehrtens, M.. Aegerter, "Comparison of spray pyrolyzed FTO, ATO and ITO coatings for flat and bent glass substrates", Thin Solid Films. 351 (1999) 109–114.

[38] A.R. Babar, S.S. Shinde, A. V. Moholkar, C.H. Bhosale, K.Y. Rajpure, "Structural and optoelectronic properties of sprayed Sb:SnO2 thin films: Effects of substrate temperature and nozzle-to-substrate distance", J. Semicond. 32 (2011) 102001.

[39] S. Shanthi, C. Subramanian, P. Ramasamy, "Preparation and properties of sprayed undoped and fluorine doped tin oxide films", Mater. Sci. Eng. B. 57 (1999) 127–134.

[40] S. Wu, Y. Li, J. Luo, J. Lin, Y. Fan, Z. Gan, et al., "Pr and F co-doped SnO_2 transparent conductive films with high work function deposited by ion-assisted electron beam evaporation.", Opt. Express. 22 (2014) 4731–7.

[41] Y.J. Seo, C.H. Sung, M.S. Anwar, S.N. Heo, G.W. Kim, B.H. Koo, et al., "Structure and properties of transparent conductive Sb2O5-doped SnO2 thin films fabricated by using pulsed laser deposition", J. Korean Phys. Soc. 60 (2012) 1543–1547.

[42] H. Kim, G.P. Kushto, R.C.Y. Auyeung, A. Piqué, "Optimization of F-doped SnO2 electrodes for organic photovoltaic devices", Appl. Phys. A Mater. Sci. Process. 93 (2008) 521–526.

[43] I. Masanobu, I. Toru, O. Junichi, O. Takuji, S. Eiji, O. Hidefumi, et al., "Improving Mobility of F-Doped SnO 2 Thin Films by Introducing Temperature Gradient during Low-Pressure Chemical Vapor Deposition", Jpn. J. Appl. Phys. 51 (2012) 95801.

[44] M.E. White, O. Bierwagen, M.Y. Tsai, J.S. Speck, "Electron transport properties of antimony doped SnO[sub 2] single crystalline thin films grown by plasma-assisted molecular beam epitaxy", J. Appl. Phys. 106 (2009) 093704.

[45] H. Hosono, "Recent progress in transparent oxide semiconductors: Materials and device application", Thin Solid Films. 515 (2007) 6000–6014.

[46] "Tin - Interpretation of XPS spectra", (n.d.). http://xpssimplified.com/elements/tin.php.

[47] S. Kumar, C. Mukherjee, D.M. Phase, "Valence Band Onset and Valence Plasmons of SnO2 and In2-xSnxO3 Thin Films", arXiv:1406.3211. (2014).

[48] C. Körber, P. Ágoston, A. Klein, "Surface and bulk properties of sputter deposited undoped and Sb-doped SnO2 thin films", Sensors Actuators B Chem. 139 (2009) 665–672.

[49] V. Casey, M.I. Stephenson, "A study of undoped and molybdenum doped, polycrystalline, tin oxide thin films produced by a simple reactive evaporation technique", J. Phys. D. Appl. Phys. 23 (2000) 1212–1215.

[50] M.G. Takwale, V.G. Bhide, "Correlation between the structural and electrical transport properties of Sn02 films", J. Mater. Sci. 24 (1989) 2628–2636.

[51] V. Casey, M.I. Stephenson, "Investigation of enhanced conductivity in dye-coated tin oxide thin films using Hall voltage measurements", J. Phys. D. Appl. Phys. 26 (1993) 89–92.

[52] D. Konios, G. Kakavelakis, C. Petridis, K. Savva, "Highly e ffi cient organic photovoltaic devices utilizing work-function tuned graphene oxide", J. Mater. Chem.

A Mater. Energy Sustain. 00 (2016) 1–12.

[53] B. a. Korevaar, a. Halverson, J. Cao, J. Choi, C. Collazo-Davila, W. Huber, "High efficiency CdTe cells using manufacturable window layers and CdTe thickness", Thin Solid Films. 535 (2013) 229–232.

[54] O. Vigil-Galán, D. Jiménez-Olarte, G. Contreras-Puente, M. Courel, "SnO2 buffer layer deposition for thin film solar cells with superstrate configuration", J. Renew. Sustain. Energy. 7 (2015) 013115.

[55] H. Xin, S. Subramaniyan, T.W. Kwon, S. Shoaee, J.R. Durrant, S. a. Jenekhe, "Enhanced open circuit voltage and efficiency of donor-acceptor copolymer solar cells by using indene-C60 bisadduct", Chem. Mater. 24 (2012) 1995–2001.

[56] B.A. MacLeod, B.J. Tremolet de Villers, P. Schulz, P.F. Ndione, H. Kim, A.J. Giordano, et al., "Stability of inverted organic solar cells with ZnO contact layers deposited from precursor solutions", Energy Environ. Sci. 8 (2015) 592–601.

[57] R. Geethu, C. Sudha Kartha, K.P. Vijayakumar, "Improving the performance of ITO/ZnO/P3HT:PCBM/Ag solar cells by tuning the surface roughness of sprayed ZnO", Sol. Energy. 120 (2015) 65–71.

[58] M.T. Greiner, Z.-H. Lu, "Thin-film metal oxides in organic semiconductor devices: their electronic structures, work functions and interfaces", NPG Asia Mater. 5 (2013) e55.

[59] X. Zhou, X. Fan, X. Sun, Y. Zhang, Z. Zhu, "Enhanced efficiency of inverted polymer solar cells by using solution-processed TiOx/CsOx cathode buffer layer", Nanoscale Res. Lett. 10 (2015) 29.

Conclusions and future work

This study has been focused on the deposition of SnO_2 thin films by PLD. The emphasis was on the precise control of the deposition environment provided by this method. The study of SnO_2 prior doping allowed a better understanding behind the mechanics of preferential intrinsic defect formation and how to control them. The incorporation of Zn did not act as an efficient acceptor dopant but rather as an "electron killer" as predicted by Scanlon and Watson[1], and in some conditions improved the n-type conductivity of SnO_2. The main points developed in this thesis are highlighted below along with improvements and future work that could be done.

i) Exploring intrinsic defects in undoped SnO_2

In the third chapter, undoped SnO_2 was investigated in order to understand the preferential formation of intrinsic defects while changing deposition parameters. The aim was to limit the amount of donor defects formed and set a "p-type compatible" environment for eventual acceptor doping. The variation of simple parameters such as the deposition temperature (T_D) and the oxygen background pressure (P_D) demonstrated that increased T_D led to the incorporation of more oxygen in the films and similarly so does an increase in P_D. The presence of more oxygen in the films means a decreased concentration of donor defects such as V_O and Sn_i echoed in the drop in carrier concentration observed due to the films being closer to stoichiometry. The main defects responsible for SnO_2 n-type conductivity have been identified to be Sn_i as V_O ionisation energy level lies below the CBM. The study showed the growth environment could be controlled via T_D and P_D but also through the target composition.

The PLD system allows stoichiometric cation transfer between the target and the films, however the oxygen composition of the target greatly influences the film properties. Claeyssens *et al.*[2] showed the presence of metal enrichment at the surface of the target after laser exposure. In this chapter the consequences on the film electrical properties have been clearly observed with the environment changing towards oxygen-poor as the surface of the target is enriched in Sn from the plasma plume backscattering. The excess of Sn is difficult to compensate with the background gas, thus different types of environment can be set by controlling the composition of the target surface. For the deposition of highly conductive n-type films, improved control of the Sn-rich environment is favoured.

Therefore the increased formation of donor defects is achieved with Sn-rich target surface while to limit these defects an O-rich/stoichiometric target surface is necessary.

ii) Limitations of Zn as acceptor dopant in SnO_2

Chapter 4 focused on the introduction of Zn as an acceptor dopant and the type of environment required for the formation of acceptor defects. Based on the results from chapter 3, optimum limitation of donor defects was found to occur at high T_D and high P_D however the behaviour of point defects changes with the introduction of Zn in SnO_2. As T_D increases the system possesses more energy to activate Zn_{Sn} acceptor defects leading to a decrease of the electron carrier concentration. However above a certain threshold the increase of P_D supposedly lowering the formation energy of acceptor defects led to an increase in donor defects instead. The mechanism behind this change is likely due a lack of energy to form the Zn_{Sn} defects and thus a rearrangement of Zn in the lattice either in interstitial or as AX donor centre.

Upon thermal annealing in oxidising conditions more Zn_{Sn} acceptor defects were activated and the resistivity increased consequently. However the conductivity remains n-type and the Zn acceptor dopant only acts as an "electron killer". This limitation is in agreement with what Scanlon and Watson[1] predicted. The growth environment is essential to consider when trying to induce the formation of p-type defects, however even though the p-type pinning energy is lowered in O-rich conditions, it remains above the VBM and thus limits the formation of p-type SnO_2.

The use of Zn as a dopant induced an increase of the VBM towards the vacuum level. The drop in electron carrier concentration with the activation of Zn_{Sn} acceptor defects is thought to increase the downward band bending effect present in SnO_2. Such effect could be confirmed by using angle-resolved XPS technique to probe at different depths of the surface. In addition of forming acceptor defect and self-compensating centres, Zn is thought to induce the formation of oxygen vacancies neighbour to the Zn_{Sn} defect at low temperature inducing an increase in n-type conductivity.

iii) Improvement of n-type electrical properties by Zn doping in SnO_2

Chapter 5 focused on the use of Zn to improve the n-type electrical properties of SnO_2. ZTO films showed preferential growth in the <200> direction especially at 400 °C and 50 mTorr where highly (200) oriented films without secondary orientations were obtained. Zn is thought to decrease the surface energy of the reduced (200) surface by replacing the Sn^{2+} states. These highly oriented films deposited on quartz or Si can be used as seed layer

to induce preferential growth of SnO_2. Nakao *et al.* reported the use of TiO_2 seed layers to induce the growth of (200) oriented Ta-doped SnO_2[3] and W-doped SnO_2[4]. The induced (200) orientation increased the films mobility from 25 $cm^2/(V.s)$ for the Ta-doped SnO_2 deposited on glass to 80 $cm^2/(V.s)$. The ZTO films could be used to improve the (200) orientation of SnO_2 films. Furthermore improvements can be made to the crystallinity by varying the laser parameter, *e.g.* the pulse frequency to induce a more ordered growth.

The use of Zn showed improved electrical properties of the SnO_2 films despite the large dopant concentration used (10-30 at.% Zn). This phenomenon was attributed to the formation of V_O defects next to the Zn_{Sn} substitution sites to stabilise the system as Zn normally adopt a coordination 4. Undoped SnO_2 films have been shown to possess a surface conductivity channel. The fact that the incorporation of Zn in the SnO_2 leads to a more homogenous repartition of the conductivity in the bulk of the sample support the hypothesis of the formation of more V_O around Zn_{Sn} sites. Resistivity as low as 2.9 $x10^{-3}$ Ω.cm and high Hall mobility of 30 $cm^2/(V.s)$ were obtained with 20 at.% ZTO films while maintaining the optical transparency in the visible range.

The optical band gap was found to decrease with the introduction of Zn at low temperature. Undoped SnO_2 showed E_g around 3.6-3.7 eV while with the addition of Zn, E_g was decreased to 3.4 eV with single oriented (200) films and as low as 3.2 eV for amorphous films. Such variations could find an application in band gap tailoring. Ganose and Scanlon[5] recently reported the potential use of Pb in SnO_2 to decrease the E_g down to 3.17 eV by lowering the CBM while maintaining the optical transparency. This type of band gap modulation would provide significant advantages in organic solar cells where the alignment of the WF between the cathode and the hole injection layer are essential. Even though the ZTO films show reduced E_g it is yet unclear if it is from a lowering of the CBM, an increase of VBM or both. WF (from KP) of about 4.7-4.8 eV suggests improvement can be done and the incorporation of the films in devices should be investigated.

The mobility of the ZTO films does not seem to depend on the crystallinity of the films as mobility of 30 $cm^2/(V.s)$ were obtain for both crystalline and amorphous films. The high conductivity and large mobility of the films were successfully preserved as the deposition temperature was decreased. 20 at.% ZTO films deposited at 100 °C showed resistivity of 4.7 $x10^{-3}$ Ω.cm and mobility of 19 $cm^2/(V.s)$ showing potential application to flexible substrates or for deposition on organic materials. The development of low temperature processed ZTO films was limited under very low T_D and P_D by the formation of Sn^{2+} states compensating the charge carriers and compromising the optical transparency.

Appendix 1: Targets preparation and characterisation

The use of dense targets in PLD is required to avoid particulates expulsion on the substrate.[6] The sintering of pure SnO_2 powder has been reported difficult as no significant macroscopic shrinkage has been observed through constant heating sintering even with temperatures up to 1500 °C.[7] The sintering of SnO_2 is controlled by a non-densifying mechanism which happens above 1200 °C. SnO_2 has been found to decompose and condense above this temperature into SnO and O_2. The simplified equation for the mechanism is generally written as,

Equation S1.1 $$SnO_{2\,(s)} \xrightarrow{1200\,^{\circ}C} SnO_{(g)} + 1/2O_{2\,(g)}$$

However the full decomposition mechanism of SnO_2 at 1200 °C can be described by either S1.2 or S1.3 detailed below.[8]

Equation S1.2 $$SnO_2 \xrightarrow{1200\,^{\circ}C} Sn_{Sn}^{x} + O_O^{x} + V_O^{x}\left(V_O^{\circ\circ} + 2e^{/}\right) + 1/2O_2(\uparrow)$$

Equation S1.3 $$2SnO_2 \xrightarrow{1200\,^{\circ}C} Sn_{Sn}^{x} + 3O_O^{x} + V_O^{x} + V_{Sn}^{x} + SnO(\uparrow)$$

The poor sinterability of SnO_2 requires the use of sintering aids to help the densification process. Due to its close ionic radii, Zn is a good choice for the sintering of SnO_2. The use of Zn promotes the densification of SnO_2 by inducing the formation of oxygen vacancies in the structure.

Equation S1.4 $$ZnO \xrightarrow{SnO_2} Zn_{Sn}^{//} + V_O^{\circ\circ} + O_O^{x}$$

The mechanism responsible for the densification is the suppression of the decomposition of SnO_2 at high temperature (Equation S1.1) and the formation of $ZnSnO_3$ or Zn_2SnO_4 phases at the grain boundaries.[8,9] The segregation of Zn at the grain boundaries of the SnO_2 structure has been reported in several studies[8,10] and is found to help the densification of SnO_2 during the sintering process.

Zn as a densification aid in SnO_2 has been successfully reported with Zn concentration about 0.25-9 at.% and at sintering temperature between 1200 and 1500 °C.[8,10–12] The relative density obtained were above 95 % of the maximum density of the material.

Therefore Zn has been used to promote the fabrication of dense SnO_2 targets. A dilatometric study on a 30 at.% Zn in SnO_2 powder mix was done to find the optimum sintering parameter and a series of Zn-doped SnO_2 targets with Zn content between 10 and 30 at.% were prepared.

1. Target preparation

The pure SnO_2 target was commercially purchased (Mateck, purity 99.99 %, density > 95 %) since the sintering was not possible. For the Zn-doped SnO_2 (ZTO) targets ZnO powder (99.99 %, trace metal basis, Sigma Aldrich) was mixed in the desired proportion (between 10 and 30 at.% Zn) with SnO_2 powder (> 99.99%, trace metal basis, Sigma Aldrich). The powders used for the ZTO targets were ball milled during 48 h in methanol to have a uniform mixing of the powder. The mix was then dried and pressed into compact pellet using a dye under a pressure of 1.2 tons. The pressed powder pellets were then ready for either dilatometry analysis or sintering process.

The dilatometric analysis was performed on the highest concentration of Zn used, e.g. 30 at.% Zn. Two steps were required to determine the optimum sintering temperature, a sintering ramp up to 1500 °C to find the highest shrinkage rate $\frac{d\Delta l/l_0}{dT}$ while measuring the linear shrinkage of the ceramic $\Delta l/l_0$, where l is the measured length of the sample varying with the temperature T and l_0 is the initial length of the sample. After this step a isotherm at the chosen temperature is required to establish the duration of sintering and to confirm the densification of the target. The sintering ramp up to 1500 °C with a heating rate of 10 °C/min of the 30 at.% Zn-doped SnO_2 target is shown on Figure S1.1.

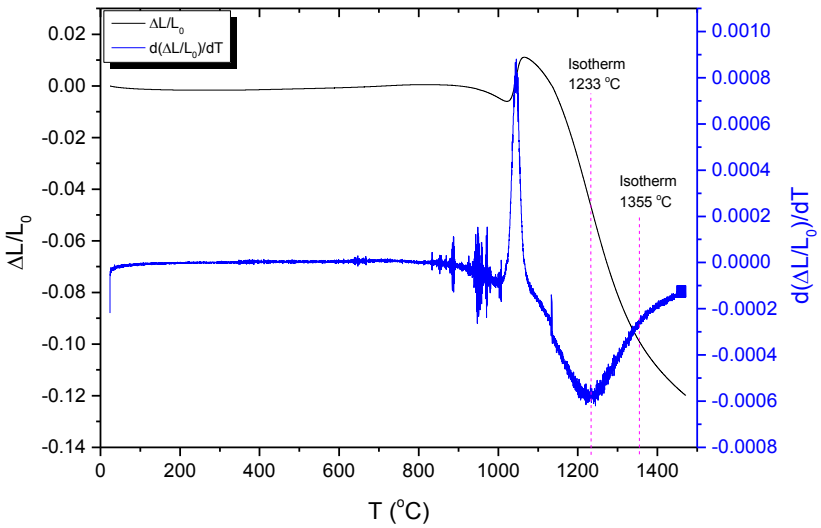

Figure S1. 1: Linear shrinkage (black) and shrinkage rate (blue) of a 30 at.% ZTO target sintering ramp up to 1500 °C at 10 °C/min.

The highest shrinkage rate measured was at 1233 °C, however the resulting density if the target was too low and a second temperature of 1355 °C was selected for the isotherm presented on Figure S1.2.

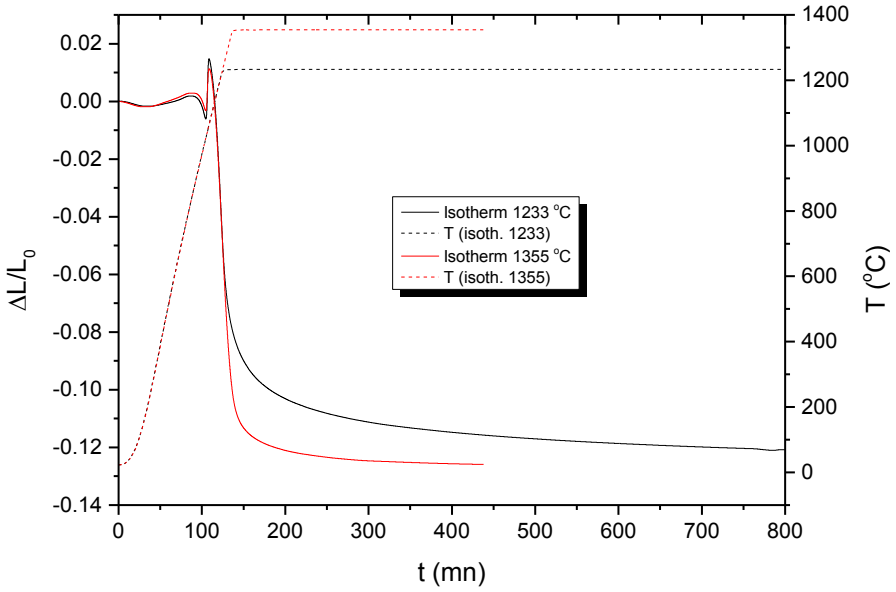

Figure S1. 2: Isotherm of the 30 at.% ZTO target done at 1233 °C (in black) and 1355 °C (red).

In order to calculate the referential density (d_0) of a mix of component, the rule of mixture is applied as d_0 vary with the composition. In the case of a powder mix between two components the total density d_0 can be expressed as,

Equation S1.5
$$d_0 = d_1\left(\frac{w_1 d_2}{w_1(d_2-d_1)+d_1}\right) + d_2\left(1-\frac{w_1 d_2}{w_1(d_2-d_1)+d_1}\right)$$

Where d_1 and d_2 the density of the two components and w_1 the weight percentage of component 1 in the mix. The experimental density (d) is extrapolated by measuring the weight and the volume of the cylindrical target, d is then compared to d_0 and expressed as a percentage. Based on this equation the respective theoretical density could be calculated in the case of the 30 at.% ZTO mix and it was found that at 1355 °C the target shows a much higher densification (90 %) than at 1233 °C (71.8 %). The densification is also faster at 1355 °C since only 5 h were necessary to reach 90 % density while at 1233 °C it took 13h to obtain 72 % density. The XRD analysis of the target was performed and is shown in Figure S1.3.

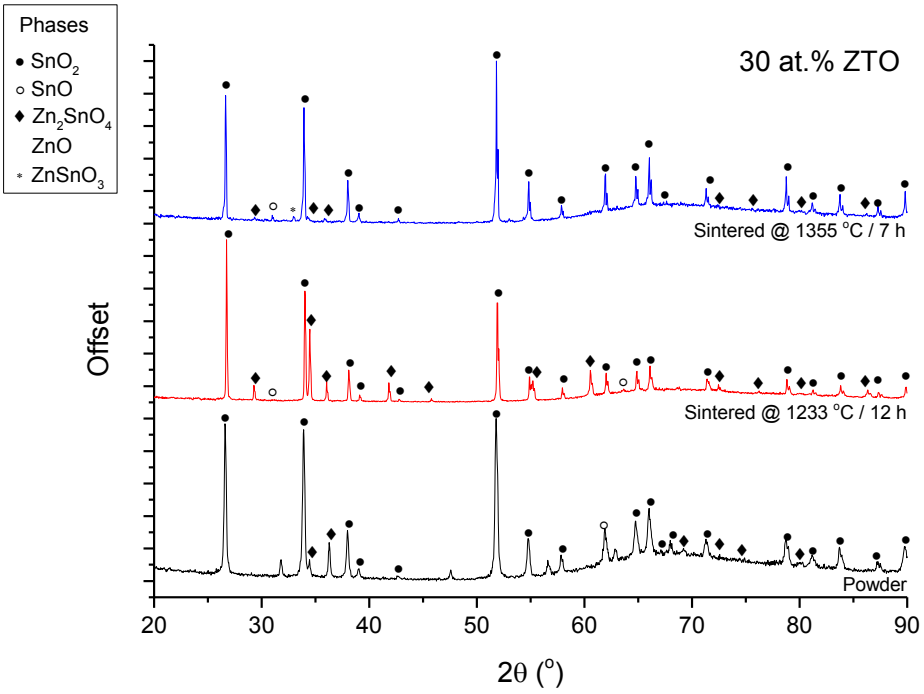

Figure S1. 3: XRD data of the 30 at.% ZTO powder and sintered targets at 1233 and 1355 °C respectively. The different phases are indicated by several signs on the corresponding peaks.

It can be observed that after sintering the target does not show ZnO phase (only in very small quantity). The only phases present are SnO_2 rutile, Zn_2SnO_4 and a small amount of $ZnSnO_3$. The presence of the $ZnSnO_3$ and Zn_2SnO_4 indicates that Zn has successfully helped the densification of SnO_2 since a density of 90 % was reached. The presence of phases other than SnO_2 is not a concern since the PLD process does not take into account the phases but the cation ratio in the target.

The optimum sintering temperature has been found to be 1355 °C with density up to 90 % for only 5h of sintering. Therefore this temperature was used for the preparation of the ZTO targets, however the duration of sintering was pushed to 10 h to slightly improve the densification. The sintering was done in air in a furnace with a heating rate of 5 °C/min. The list of target sintered is presented in table S1 along with their respective densities.

Table S1. 1: List of ZTO target prepared with Zn at.% between 10 and 30 and their respective experimental and theoretical densities (d and d_0 respectively).

Zn dopant at.%	**d** g.cm^{-3}	**d_0** g.cm^{-3}	**d/d_0** %
10	6.43	6.85	93.9
15	6.50	6.81	95.5
20	6.39	6.76	94.6
25	5.86	6.70	87.4
30	5.87	6.66	88.1

The lower density observed compared to the dilatometry is due to the larger size of the sample (5 mm diameter for the dilatometry against 22 mm diameter for the target sintering. The XRD data of the different targets is shown in Figure S1.4.

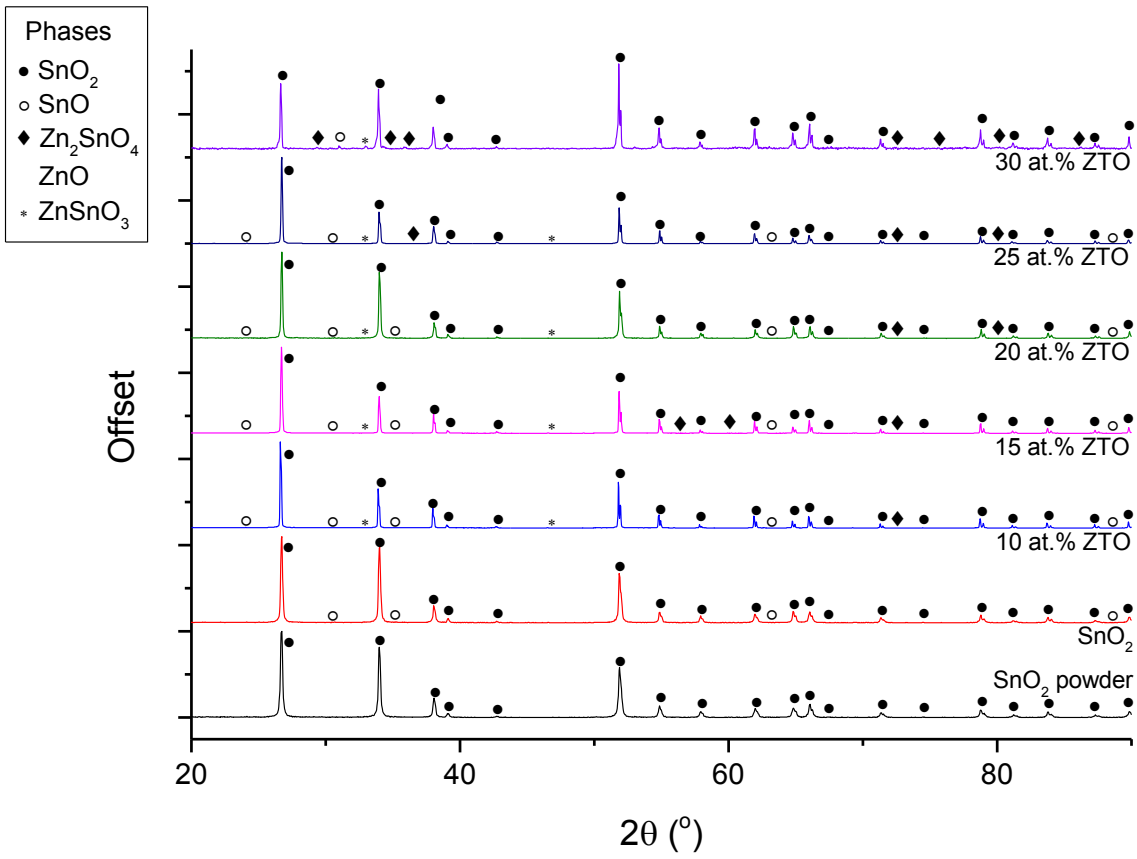

Figure S1. 4: XRD data of the ZTO targets sintered at 1355 °C during 10 h in air.

The ZTO targets all show presence of $ZnSnO_3$ and Zn_2SnO_4 which accounts for the densification displayed in table S1.1. All the target densities are about 90 % and higher which is considered enough to be used in PLD.

2. Non-homogeneity of Zn in the targets

In order to confirm the incorporation of the right amount of Zn in the target, EDX analysis were performed to determine the Zn/Sn ratio. However, surprisingly the targets showed no presence of Zn in the first analysis. A cross-section EDX of the 30 at.% ZTO target revealed that the surface contains only SnO_2 while Zn accumulates at the centre of the target as shown in Figure S1.5.

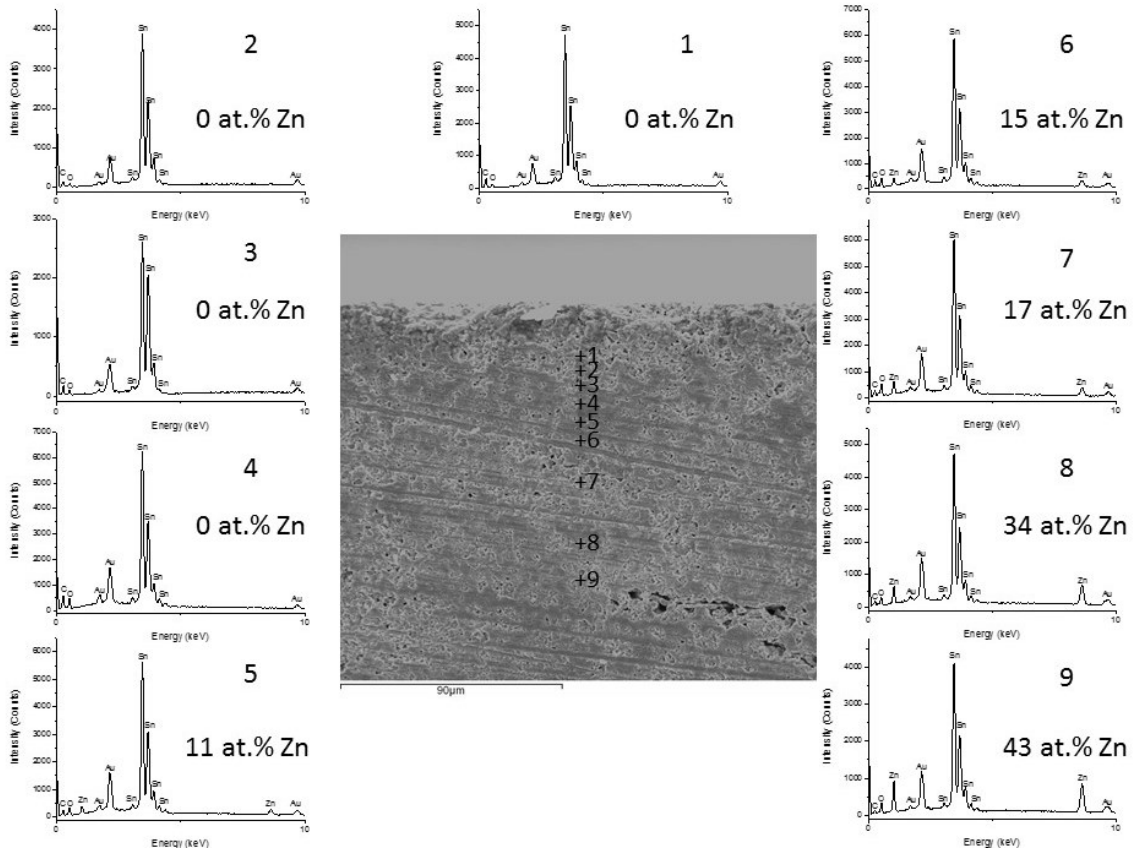

Figure S1. 5: SEM cross-section image of the 30 at.% ZTO target coupled with EDX point analysis at different locations referred by their number (from 1 to 9, 1 being closer to the surface and 9 towards the centre of the target).

The analysis showed no presence of Zn was measured within the first 40-50 µm of the target. An gradual increase of Zn at.% is observed towards the centre of the target. The Zn concentration even exceed 30 at.% therefore the Zn incorporation in the films must be carefully monitored after each deposition. The Zn depletion at the surface of the target can be clearly observed in Figure S1.6.

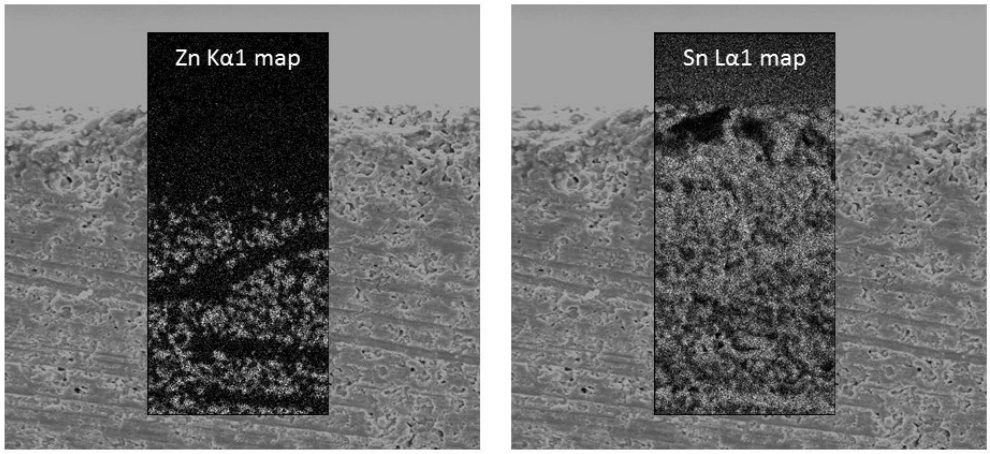

Figure S1. 6: EDX map of the Zn Kα1 and Sn Lα1 displayed in the dark rectangle. The background in light grey represent the SEM of the cross-section of the 30 at.% ZTO target.

Since Zn is not present within the first 50 µm of the target and also not homogenously distributed in the target, the targets had to be carefully polished until the required doping is reached. The Zn doping was controlled after every set of depositions to avoid any inconsistency in the study.

Appendix 2: Assessment of Zn doping through EDX measurements

Over the different sets of deposition achieved, the amount of doping was regularly assessed via EDX as to ensure the right amount of Zn was incorporated in the films. Considering the thickness of the films (about 200 nm) the signals from Zn and Sn are rather weak compared to the substrate. Therefore quartz samples had to be used to obtain a clear signal from the films. Each analysed sample was averaged by two to three measurements at different zones. All films were coated with 5-10 nm of gold and the measurements were performed over an area of 200 µm x 200 µm. The data shown below is separated in two part: films with 20 at.% Zn and films with varying Zn doping.

1. 20 at.% ZTO

As mentioned in appendix 1, the repartition of Zn in the targets is not homogenous and thus must be monitored after the depositions. Figure S2.1 represent a typical EDX data obtained for a 20 at.% ZTO film (deposited at 600 °C and 100 mTorr).

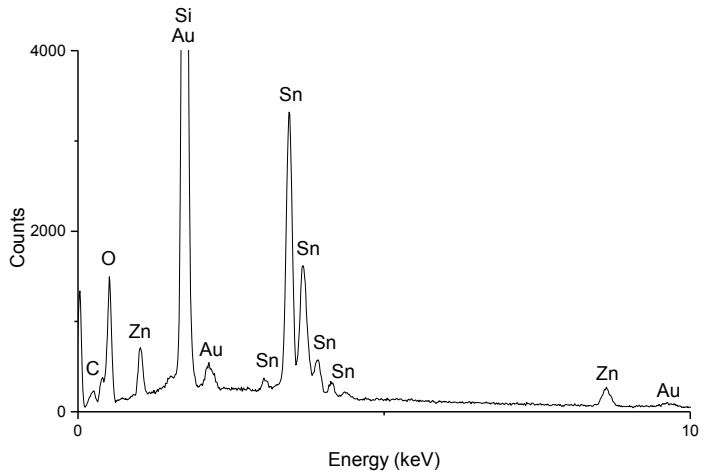

Figure S2. 1: EDX data of a 20 at.% ZTO film deposited at 600 °C and 100 mTorr on quartz substrate. The emission peaks are labelled to their respective element.

Several elements can be observed from this measurement. The most intense peak at 1.74 eV corresponds to the Si present in large quantity in the substrate. The peaks present at 2.15 and 9.63 eV but also part of the peak at 1.74 eV corresponds to the gold present on the surface. Some traces of carbon can be found at 0.25 eV and the peak at 0.51 eV is attributed to the oxygen. However the oxygen peak cannot be used to determine the

amount of oxygen in the films as the substrates also contain some. Finally the main peaks of interest are the pack of peaks between 3-4.4 eV which corresponds to the Sn element and the peaks at 1.02 and 8.63 eV arise from the presence of Zn in the films. The atomic ratios are calculated by the software which takes into account all the elements indicated and finally the atomic ratio between Zn and Sn can be extracted.

Regarding the 20 at.% ZTO films deposited in Chapter 4, the overall measurements showed the films contained 20.0 ± 0.8 at.% Zn. The deviation is less than 1 at.% and shows the reproducibility of the doping despite the initial large variations within the target. Similar doping was used in Chapter 5 and the measurements showed the amount of Zn incorporated remains similar with 19.9 ± 0.6 at.% Zn even though the depositions were note performed during the same period of time. This consistency is attributed to the careful adjustments of the amount of Zn incorporated in the films from the target after multiple target polishing and laser ablation.

2. Zn doping variation

The amount of Zn incorporated in the films while using different target compositions was monitored in two sections referring each to two different studies, respectively chapter 4 and chapter 5.

Figure S2.2.a shows the evolution of the EDX data with increasing doping regarding the films deposited in chapter 4. The energy displayed in the graph has been cut to 5 eV since the interest is brought on the Zn peak at 1.02 eV. The peak at 8.63 eV is too shallow to bring specific visual information. As the amount of Zn increases in the target the Zn peak intensity increases accordingly with as well a decrease of the Sn peak intensity. The mean value of the atomic ratios of Zn extracted with the EDX measurements along are presented in Figure S2.2.b along with their respective standard deviations.

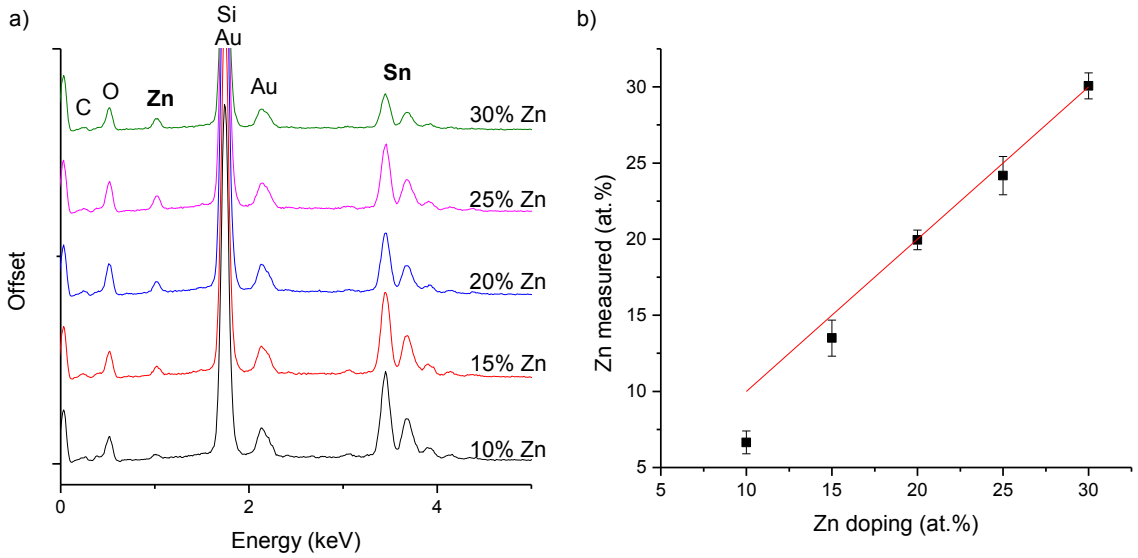

Figure S2. 2: a) EDX data of the ZTO films deposited at 600 °C and 100 mTorr on quartz with Zn doping varying between10-30 at.%. b) Graph showing the amount of dopant measured by EDX function of the amount of Zn initially put in the ZTO target. The red line represents the function y = x.

The measurements report a Zn content on the same order that of the Zn in the target, except for the 10 at.% ZTO target where the content is clearly lower (about 7 at.% Zn). The films deposited with 15 and 25 at.% targets shows Zn content slightly off what was expected however the standard deviation do not exceed 1.5 at.% in the worst case.

Concerning the films deposited in Chapter 5, their EDX measurements and the mean amount of Zn doping can be found in Figure S2.3.

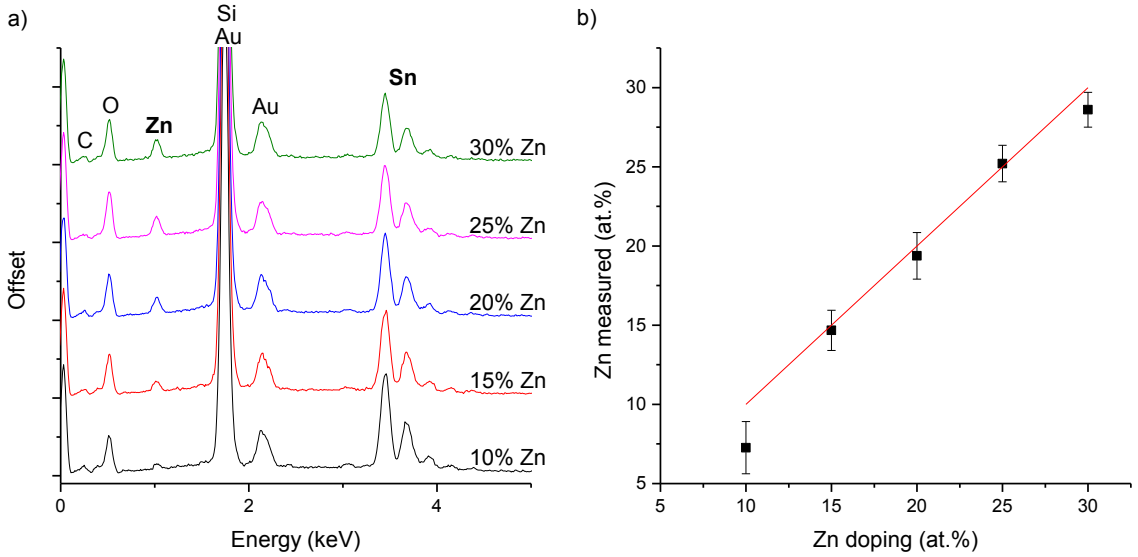

Figure S2. 3: a) EDX data of the ZTO films deposited at 400 °C and 50 mTorr on quartz with Zn doping varying between10-30 at.%. b) Graph showing the amount of dopant measured by EDX function of the amount of Zn initially put in the ZTO target. The red line represents the function y = x.

The measurements still show an increase of the Zn peak and decrease of Sn peaks as more dopant is added. However slight deviations persist from the content measured in Figure S2.2. The films deposited with the 30 at.% ZTO target show lower concentration of Zn while those deposited with the 15 at.% target display higher concentrations. But the concentrations of Zn in the films remain of the same order to those deposited previously. The same lower doping was measured for the films deposited with the 10 at.% ZTO target.

Finally the overall Zn doping averaged for all the samples analysed gathering those from chapter 4 and 5 is shown in Figure S2.4.

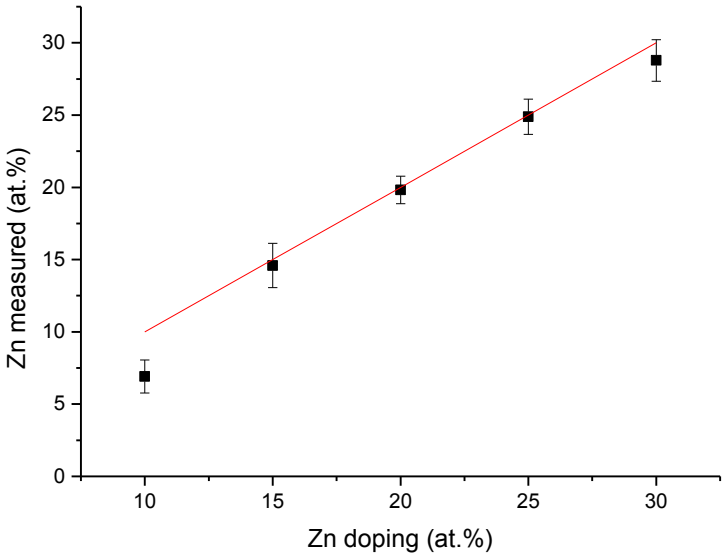

Figure S2. 4: Average amount of Zn measured across all the films measured function of the initial Zn concentration in the target.

Due to the control of the amount of Zn at the surface of the target, via polishing, the Zn content can be adjusted in the films to the value required. Overall the doping present in the films is similar to those in the prepared targets apart from the 10 at.% target which shows lower doping in the films. However this is not problematic since the amount of Zn incorporated remained rather constant over the various depositions.

Appendix 3: Complementary data

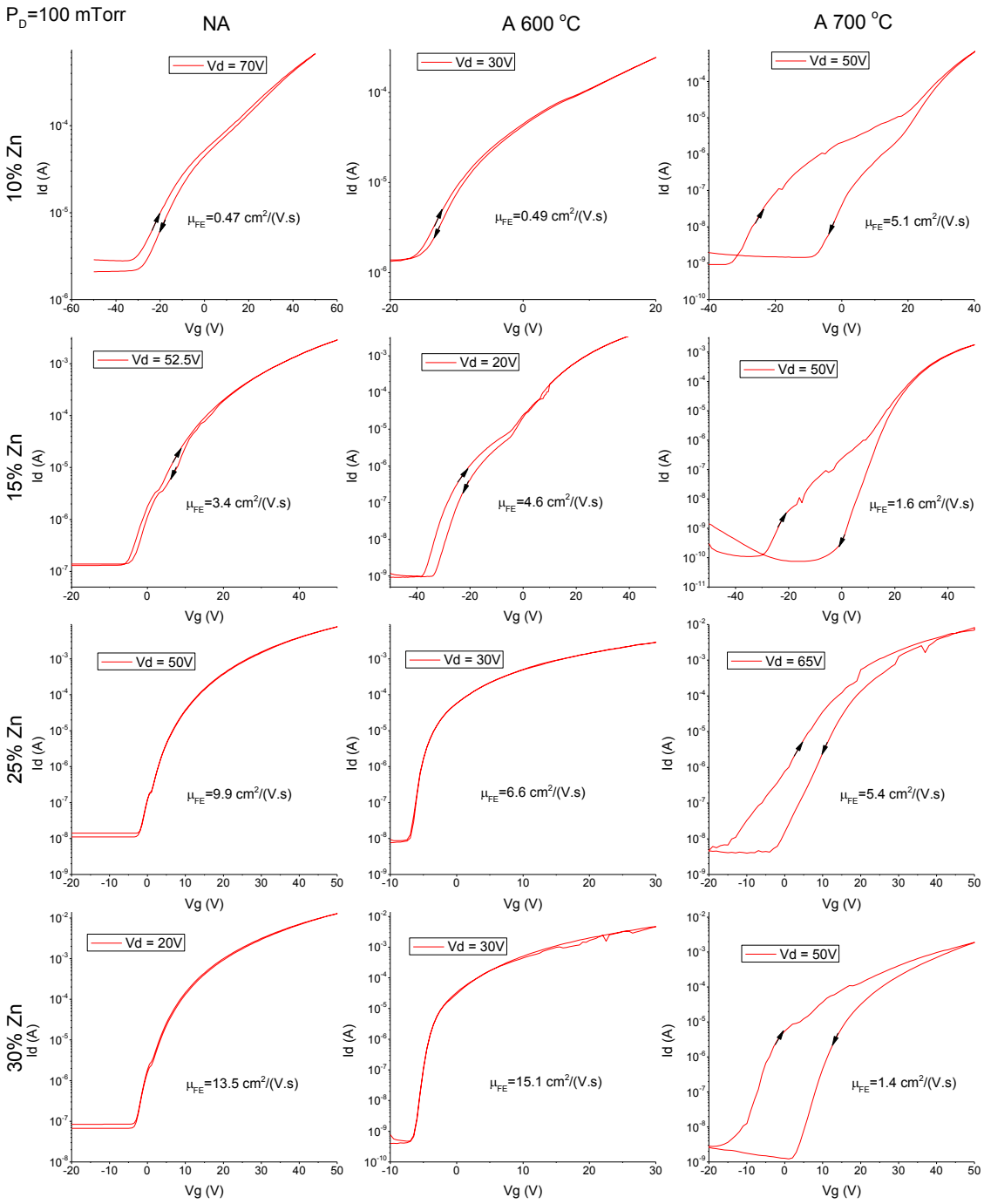

Figure S3. 1: Transfer curve of 10, 15, 25 and 30 at.% ZTO films deposited on Fraunhofer OFET substrates at 600 °C, under 100 mTorr, not annealed (NA) and annealed at 600 and 700 °C in oxygen. The transfer curves were measured in saturation mode and represent the drain current (Id) function of the gate voltage (Vg) at fixed drain voltage (Vd). The channel width was fixed at 2 mm and its length was 20 µm for the NA and 600 °C annealed samples, and 10 µm for the 700 °C annealed samples. μ_{FE} represents the saturation field effect mobility extracted from the transfer curves.

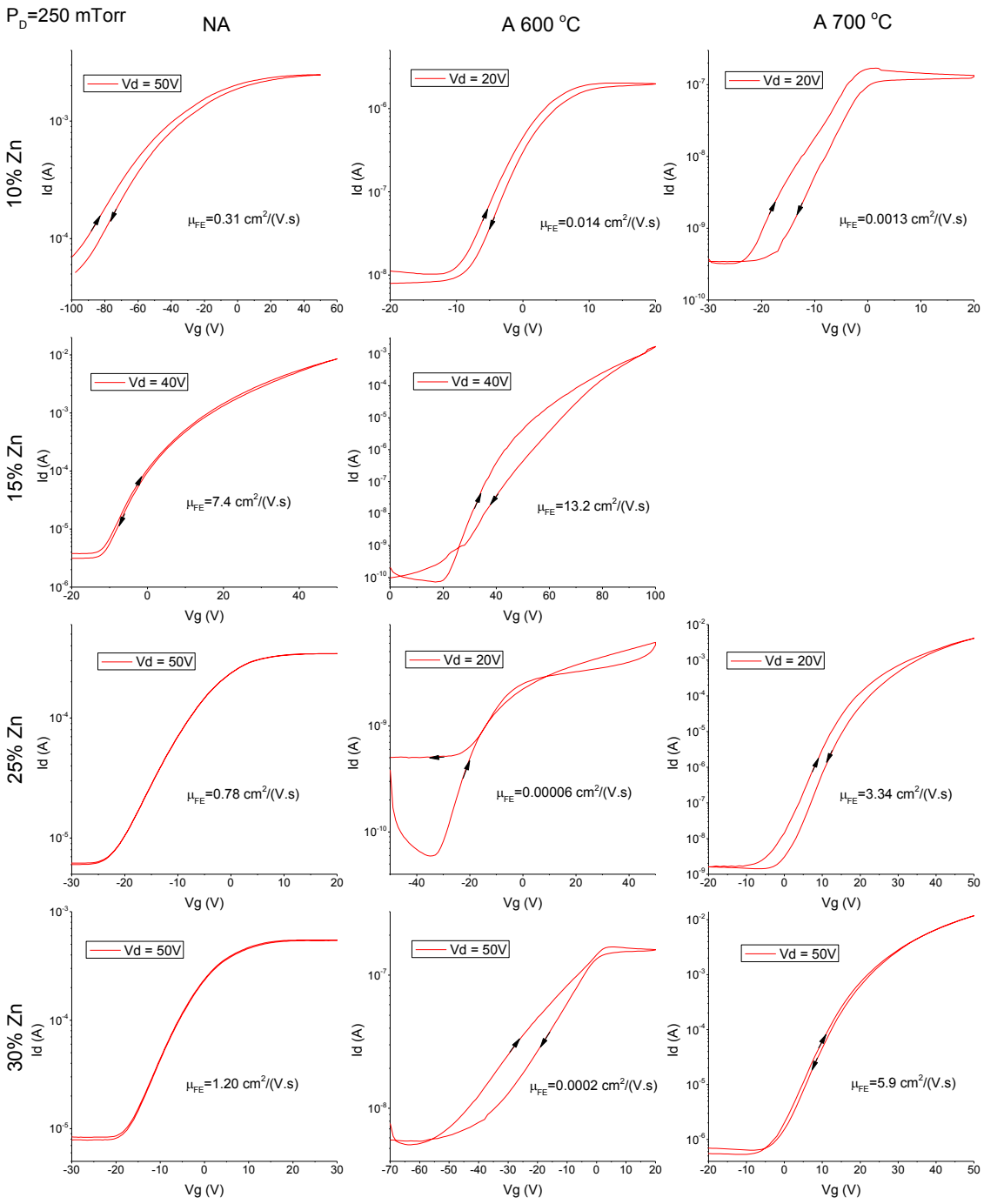

Figure S3. 2: Transfer curve of 10, 15, 25 and 30 at.% ZTO films deposited on Fraunhofer OFET substrates at 600 °C, under 250 mTorr, not annealed (NA) and annealed at 600 and 700 °C in oxygen. The transfer curves were measured in saturation mode and represent the drain current (Id) function of the gate voltage (Vg) at fixed drain voltage (Vd). The channel width was fixed at 2 mm and its length was 20 µm for the NA and 600 °C annealed samples, and 10 µm for the 700 °C annealed samples. μ_{FE} represents the saturation field effect mobility extracted from the transfer curves.

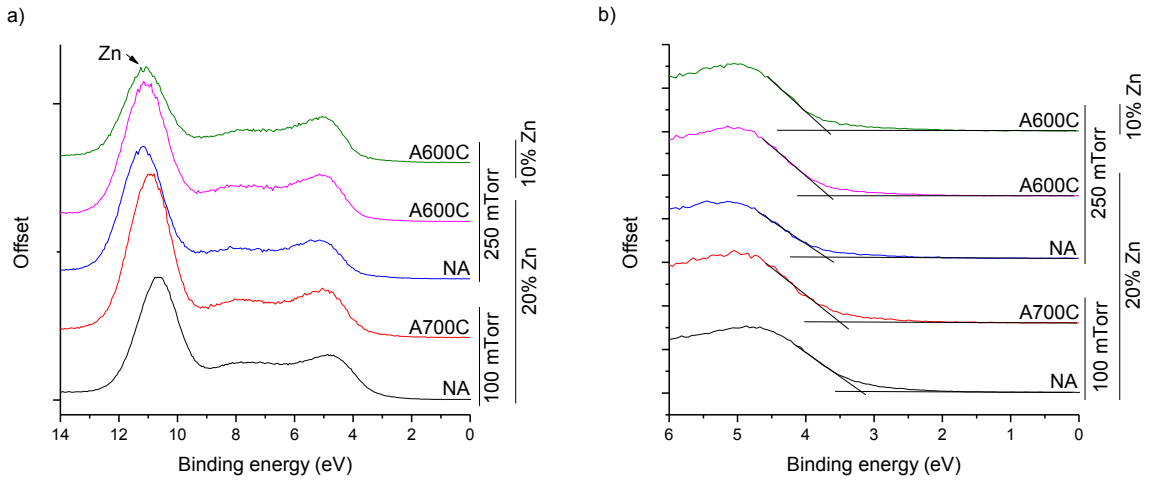

Figure S3. 3: Valence band Onset measured by XPS of. The VB onset is shown for different annealings (NA, A600C and A700C), P_D (100 and 250 mTorr) and Zn doping (10-20 at.%). a) General VB onset and b) determination of the VBM position related to the Fermi edge (0 eV).

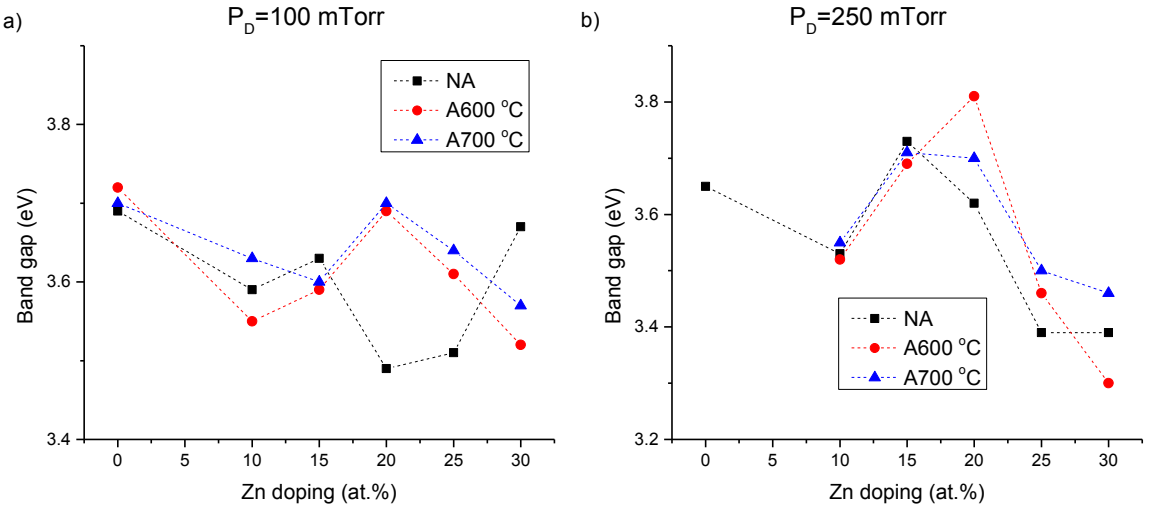

Figure 4. 21: Band gap extracted via the Tauc plot method for ZTO films with Zn doping from 0-30 at.% deposited at 600 °C, under a) 100 and b) 250 mTorr, not annealed (NA) and annealed in oxygen at 600 and 700 °C.

References

[1] D.O. Scanlon, G.W. Watson, "On the possibility of p-type SnO2", J. Mater. Chem. 22 (2012) 25236.

[2] F. Claeyssens, A. Cheesman, S.J. Henley, M.N.R. Ashfold, "Studies of the plume accompanying pulsed ultraviolet laser ablation of zinc oxide", J. Appl. Phys. 92 (2002) 6886.

[3] S. Nakao, N. Yamada, T. Hitosugi, Y. Hirose, T. Shimada, T. Hasegawa, "High Mobility Exceeding 80 cm 2 V -1 s -1 in Polycrystalline Ta-Doped SnO 2 Thin Films on Glass Using Anatase TiO 2 Seed Layers", Appl. Phys. Express. 3 (2010) 031102.

[4] S. Nakao, N. Yamada, T. Hitosugi, Y. Hirose, T. Shimada, T. Hasegawa, "Fabrication of transparent conductive W-doped SnO2 thin films on glass substrates using anatase TiO2 seed layers", Phys. Status Solidi Curr. Top. Solid State Phys. 8 (2011) 543–545.

[5] A.M. Ganose, D.O. Scanlon, "Band gap and work function tailoring of SnO_2 for improved transparent conducting ability in photovoltaics", J. Mater. Chem. C. (2016).

[6] H. Krebs, M. Weisheit, S. Erik, T. Scharf, C. Fuhse, M. St, et al., "Pulsed Laser Deposition (PLD) - a Versatile Thin Film Technique UHV-chamber", Adv. Solid State Phys. 43 (2003) 505–517.

[7] E.R. Leite, J.A. Cerri, E. Longo, J.A. Varela, "Sintering of undoped SnO2", 49 (2003) 87–91.

[8] I. Sakaguchi, N. Sakamoto, M. Hashiguchi, H. Yurimoto, S. Hishita, N. Ohashi, "Characterization of oxygen defect and zinc segregation in the dense tin dioxide ceramics added with zinc oxide", J. Ceram. Soc. Japan. 121 (2013) 956–959.

[9] M. Hashiguchi, I. Sakaguchi, S. Hishita, N. Ohashi, "Zn and Sb interaction and oxygen defect chemistry in dense SnO2 ceramics co-doped with ZnO and Sb2O5", J. Ceram. Soc. Japan. 122 (2014) 421–425.

[10] J. Liu, W. Ning, "Influence of ZnO addition on the sintering properties of SnO2 electrode", J. Mater Sci. 44 (2009) 2520–2524.

[11] C.R. Foschini, L. Perazolli, J.A. Varela, "Sintering of tin oxide using zinc oxide as a densification aid", J. Mater. Sci. 39 (2004) 5825–5830.

[12] M.A.L. Margionte, A.Z. Simões, C.S. Riccardi, F.M. Filho, A. Ries, L. Perazolli, et al., "WO3 and ZnO-doped SnO2 ceramics as insulating material", Ceram. Int. 32 (2006) 713–718.